University of Calgary

PRISM Repository **https://prism.ucalgary.ca**

The Vault Open Theses and Dissertations

2023-12-14

Advanced MRI methods for probing disease severity and functional decline in multiple sclerosis

Oladosu, Olayinka Adeoluwa

Oladosu, O. A. (2023). Advanced MRI methods for probing disease severity and functional decline in multiple sclerosis (Doctoral thesis, University of Calgary, Calgary, Canada). Retrieved from https://prism.ucalgary.ca.

https://hdl.handle.net/1880/117738

Downloaded from PRISM Repository, University of Calgary

UNIVERSITY OF CALGARY

Advanced MRI methods for probing disease severity and functional decline in multiple sclerosis

by

Olayinka Adeoluwa Oladosu

A THESIS

SUBMITTED TO THE FACULTY OF GRADUATE STUDIES

IN PARTIAL FULFILMENT OF THE REQUIREMENTS FOR THE

DEGREE OF DOCTOR OF PHILOSOPHY

GRADUATE PROGRAM IN NEUROSCIENCE

CALGARY, ALBERTA

DECEMBER, 2023

© Olayinka Adeoluwa Oladosu 2023

Abstract

Multiple sclerosis (MS) is a chronic and severe disease of the central nervous system characterized by complex pathology including inflammatory demyelination and neurodegeneration. MS impacts >2.8 million people worldwide, with most starting with a relapsing-remitting form (RRMS) in young adulthood, and many of them worsening to a secondary-progressive course (SPMS) despite treatment. So, there is a clear need for improved disease characterization. MRI is an ideal tool for non-invasive assessment of MS pathology, but there is still no established measure of disease activity and functional consequences. This project aims to overcome the challenge by developing novel imaging measures based on brain diffusion MRI and phase congruency texture analysis of conventional MRI. Through advanced modeling and analysis of clinically feasible brain MRI, this thesis investigates whether and how the derived measures differentiate MS pathology types and disease severity and predict functional outcomes in MS. The overall process has led to important technical innovations in several aspects. These include: innovative modeling of simple diffusion acquisitions to generate high angular resolution diffusion imaging (HARDI) measures; new optimization and harmonization techniques for diffusion MRI; innovative neural network models to create new diffusion data for comprehensive HARDI modeling; and novel methods and a graphic user interface for optimizing phase congruency analyses. Assisted by different machine learning methods, collective findings show that advanced measures from both diffusion MRI and phase congruency are highly sensitive to subtle differences in MS pathology, which differentiate disease severity between RRMS and SPMS through multi-dimensional analyses including chronic active lesions, and predict functional outcomes especially in physical and neurocognitive domains. These results are clinically translational and the new measures and techniques can help improve the evaluation and management of both MS and similar diseases.

Preface

We thank all the participants involved in the clinical studies of the thesis, and the HBI MS clinical research team for their strong support. All studies were approved by the Conjoint Health Research Ethics Board at the University of Calgary, and all participants provided written informed consent.

This thesis made use of the HELIX and ARC high-performance computing resources available through the Research Computing Services at the University of Calgary.

This thesis took advantage of several locally-acquired datasets including brain MRI as part of different funded studies. This includes a pilot clinical study funded by MS Canada known as Measures of Corpus Callosum Function (MCCF, PI: Dr. Lenora Brown), a Pilot Trial of Domperidone in Relapsing-Remitting Multiple Sclerosis (PI: Dr. Luanne Metz, clinicaltrials.gov identifier NCT02493049) as part of a provincial team grant from Alberta Innovates (CRIO, PI: Dr. V Wee Yong; co-I: Dr. Metz), as well as an ongoing national clinical study named Canadian Prospective Cohort (CanProCo) study supported by MS Canada, Brain Canada, Roche, Biogen-Idec, and the Government of Alberta (PI: Oh).

Studies in this thesis also made partial use of data from the Human Connectome Project, WU-Minn Consortium (PIs: David Van Essen and Kamil Ugurbil; 1U54MH091657) funded by the 16 NIH Institutes and Centers that support the NIH Blueprint for Neuroscience Research; and by the McDonnell Center for Systems Neuroscience at Washington University.

Part of Chapter 3 of this thesis has been published with myself as a co-first author. The citation is: Cayden Murray, Olayinka Oladosu, Manish Joshi, Shannon Kolind, Jiwon Oh, and Yunyan Zhang. "Neural Network Algorithms Predict New Diffusion MRI Data for Multi-Compartmental Analysis of Brain Microstructure in a Clinical Setting." Magnetic Resonance Imaging, April 2023. https://doi.org/10.1016/j.mri.2023.03.023. For detailed author contributions, see the published articles. This work was supported by the University of Calgary, and (in part) by MS Canada, HBI MS Brain and Mental Health Team, and Canadian Institutes of Health Research (PI: Zhang), with data acquired from the CanProCo study and Human Connectome Project.

Part of Chapter 4 of this thesis has been published with myself as the leading author as follows. Oladosu, Olayinka, Wei-Qiao Liu, Bruce G. Pike, Marcus Koch, Luanne M. Metz, and Yunyan Zhang. "Advanced Analysis of Diffusion Tensor Imaging Along With Machine Learning Provides New Sensitive Measures of Tissue Pathology and Intra-Lesion Activity in Multiple Sclerosis." Frontiers in Neuroscience 15 (May 7, 2021). https://doi.org/10.3389/fnins.2021.634063. For detailed author contributions, see the published articles. This work was supported by MS Canada (PI: Zhang) for study operation and disseminating results. This research benefited from personnel awards from the Alberta Innovates and Canadian Network for MS Clinics (WQL) and made use of data acquired from the Domperidone and Human Connectome Project studies.

Chapter 5 of this thesis has been published with myself as the leading author as follows. Oladosu, Olayinka, Wei-Qiao Liu, Lenora Brown, Bruce G. Pike, Luanne M. Metz, and Yunyan Zhang. "Advanced Diffusion MRI and Image Texture Analysis Detect Widespread Brain Structural Differences between Relapsing-Remitting and Secondary Progressive Multiple Sclerosis."

Frontiers in Human Neuroscience 16 (August 12, 2022). https://doi.org/10.3389/fnhum.2022.944908. For detailed author contributions, see the published articles. This study was supported by MS Canada (PI: Zhang) for operating the study and disseminating results. This research was benefited from personnel awards from the Alberta Innovates and Canadian Network for MS Clinics (Liu W-Q) and made use of data acquired from the Domperidone and MCCF studies.

Chapter 6 of this thesis is under preparation for publication as a manuscript as follows. Olayinka Oladosu, Yunyan Zhang. "Advanced brain imaging measures based on diffusion MRI and texture analysis predict functional outcomes in MS and control participants." OO: study design, data analysis & interpretation, and manuscript draft & edit. LB: data acquisition. YZ: study design, data acquisition & interpretation, and manuscript draft and edit. This study was supported by MS Canada (PI: Zhang) for operating the study and disseminating results. This study made use of data acquired from the MCCF study.

Acknowledgements

I want to thank my supervisor, Dr. Yunyan Zhang, for allowing me to pursue this opportunity in her lab. From your encouragement and challenging me in my research to the many opportunities you have provided me to grow and achieve more in this program, I am forever grateful. You have been a strong supporter through every step of the degree and experience it has brought my way. I am genuinely thankful to have worked with you.

I am also very grateful to my committee members, Dr. Manish Joshi and Dr. Jeff Dunn, for their guidance and support throughout my program. You have challenged me to delve deeper into the questions upon which this work was built, and I thank you for your patience and kindness.

I am thankful for the scholarship support from the NSERC CREATE I3T program, Bonvicini Neuroscience Scholarship, the Government of Alberta Queen Elizabeth II Graduate Scholarship, and Alberta Graduate Education Scholarships which supported the research in this thesis and provided access to opportunities to share my work, expand my knowledge, and connect with the network of individuals in associated research fields.

To my fellow lab members, thank you for your continued feedback, ideas, and suggestions. Along with my thanks to the undergraduate trainees whose work encouraged me to develop many of the approaches I used in my work, you all excited me to explore new things. I am also thankful to the collaborators who have been critical to obtaining the data used for my studies.

Finally, I would like to thank my parents, Michael and Lydia Oladosu, and my brother and sisters, Ademola, Olamide, and Ayooluwa Oladosu, for your unwavering support and encouraging me to seek out success in my education. You provided constant encouragement throughout this pursuit and kept my spirits high.

Dedication

This work is dedicated to my parents, Michael and Lydia Oladosu for their unwavering support has been my rock. Your tireless dedication to my dreams, your boundless encouragement, and your unwavering belief in my abilities have fueled my determination and provided me with the strength to overcome every obstacle. It is your love that has provided the foundation upon which my academic pursuits have flourished.

Table of Contents

List of Tables

List of Figures

Abbreviations

AD	–	Axial Diffusivity
AMICO	–	Accelerated Microstructure Imaging via Convex Optimization
ART	–	Automatic Registration Toolbox
BBB	–	Blood Brain Barrier
BET	–	Brain Extraction Tool
CNS	–	Central Nervous System
CSF	–	Cerebrospinal Fluid
DTI	–	Diffusion Tensor Imaging
DWI	–	Diffusion Weighted Imaging
EDSS	–	Expanded Disability Status Scale
FA	–	Fractional Anisotropy
FDi	–	Fiber Density Index
FLAIR	–	Fluid Attenuated Inversion Recovery
FMRIB	–	Functional Magnetic Resonance Imaging of the Brain
FSL	–	FMRIB Software Library
FTi	–	Fiber Termination Index
Gd	–	Gadolinium
HARDI	–	High Angular Resolution Diffusion Imaging
ICVF	–	Intracellular Volume Fraction
MD	–	Mean Diffusivity
MRI	–	Magnetic Resonance Imaging
MS	–	Multiple Sclerosis

NAWM	–	Normal Appearing White Matter
NODDI	–	Neurite Orientation Dispersion and Density Index
ODF	–	Orientation Distribution Function
ODI	–	Orientation Dispersion Index
PPMS	–	Primary-Progressive Multiple Sclerosis
PRMS	–	Progressive-Relapsing Multiple Sclerosis
RRMS	–	Relapsing-Remitting Multiple Sclerosis
SPMS	–	Secondary-Progressive Multiple Sclerosis
RD	–	Radial Diffusivity
ROI	–	Region of Interest
TE	–	Echo Time
TR	–	Repetition Time

Chapter 1: Introduction

1.1 Overview of research

Multiple sclerosis (MS) is a chronic and severe disorder of the central nervous system (CNS) characterized by inflammatory demyelination and neurodegeneration (1–3). There is still no cure. MS is complex in both pathology and clinical manifestations. Most people begin MS with a relapsing-remitting clinical form (RRMS) during young adulthood (4) and therefore MS is literally a life-long disease. Without appropriate management, over half of the people with MS will suffer from progressive functional decline including being wheelchaired or bed-bound (5–7). The etiology of MS is not completely clear, and both environmental and genetic factors among others may play a role (8). However, MS is seen primarily distributed in northern latitudes such as North America, and Canada has one of the highest prevalence rates of MS in the world (9). Further, MS is highly imbalanced in sex with ≥3X more presentation in women than men in many regions globally (9). Development of a cure for MS individuals requires a clear understanding of disease activity and the associated pathology, along with the ability to measure them non-invasively.

Focal lesions are hallmarks of MS pathology. There are different types of MS lesions which may feature different degrees of pathologies that lead to different consequences. In addition, MS pathology not only occurs as focal lesions but also presents in non-lesion areas such as normal-appearing white matter (NAWM) and diffusely-abnormal white matter (DAWM) (10). While the underlying mechanisms remain unclear, it is commonly considered that MS pathology is an immune-mediated process that often varies between individuals, and between structures (4,8). Immune processes cause a variety of tissue damage including loss of myelin, and with dysregulation of axonal membrane and eventual disruption of cellular activity, loss of axons (11).

With time, the resulting damages can worsen, leading to clinically significant increases in severity and eventually transformation of disease phenotype.

For people with RRMS, the natural consequence of their disease is converting to the secondary progressive form (SPMS) (1–3,12–14,8). A progressive functional decline characterizes SPMS for which no effective disease-modifying therapy is available. In MS, progression frequently occurs due to clinical relapses but also because of other factors, including age at diagnosis and subclinical disease activities. Specifically, long-term disability in MS has been linked to the frequency of lesion development and lesion load in early disease stages (15). Further, the presence and amount of chronic active lesions, typically characterized by ongoing tissue damage, are associated with an increased likelihood of disease progression (15,16). The conversion from RRMS to SPMS is associated with a shift to reduced inflammatory activity despite progressive loss of mobility and function (15,17). Current understanding of disease mechanisms suggest that the shift from an inflammatory to progressive disease pattern in MS is accompanied by a notable degree of neural degeneration such as axonal loss, as evidenced by the correlation between brain atrophy and disease progression (3,15,18). However, the change in disease forms is not always clear clinically, and when it becomes clear, irreversible damage may have occurred and it may be too late to intervene. The availability of methods that help identify the pathological changes early would be critical for early disease management.

Disease development will unavoidably lead to worsened functional performance (5). Consequences of MS include negative impact to different functional areas such as physical disability and cognitive impairment (19). There are different approaches developed for assessing

functional performance for people with MS, including clinical exams (e.g. Extended Disability Status Scale, EDSS) and neuropsychological batteries (6,20). Nonetheless, many of these clinical assessment tools may not be sensitive enough to detect subclinical changes, which typically occur earlier than clinical manifestations (21). As such, robust assessment methods for early identification of functional wellbeing would also be crucial for improving outcomes of MS individuals.

Magnetic resonance imaging (MRI) serves as a pivotal tool in the diagnosis, monitoring, and management of MS. Conventional MRI is instrumental in clinical imaging, including utilities in quantifying the number and volume of MS lesions, and identifying new and existing lesion activity (18,22,23). By direct observation or software assisted quantification, conventional MRI also offers the ability to estimate the changes in gross neural structure in MS such as atrophy. However, conventional MRI alone is limited by its ability to characterise specific processes of tissue pathology (22). Moreover, while relationships between lesion load and functional outcomes have been frequently documented in MS, the importance of specific lesion types such as chronic active lesions and their compositional characteristics in pathology are not intuitive to detect using conventional MRI, further confounding its use (24–26).

Advanced MRI has improved specificity to MS pathology and has the potential to overcome some of the challenges mentioned above. While not routinely in clinical use, multiple advanced MRI methods have been developed. Myelin water imaging and magnetization transfer imaging have been investigated to quantify myelin integrity using measures such as myelin water fraction (MWF) and magnetization ratio (MTR), highly applicable in MS (27,28). In addition,

susceptibility-weighted imaging is a method sensitive to iron accumulation and is useful for inferring inflammatory activities as well as identifying chronic active lesions as detected by a paramagnetic rim in MS (16,22,29). Diffusion MRI is capable of providing information related to both myelin and axonal changes with competitive sensitivity and specificity (22,30,31). Assisted by different modeling approaches, a range of advanced imaging measures can be developed using clinically applicable diffusion MRI, which helps identify lesion formation and intra-lesion activity (32,33). Further, in combination with physiological modeling, diffusion MRI measures have also shown the likelihood of characterizing chronic active lesions in MS (33). Despite the promises, robust MRI measures of whole brain pathology is still lacking in MS.

In addition to the above, advanced analysis of already acquired MRI data serves as an alternative method for improved characterization of disease activity including those in MS. These types of methods are under the scope of image postprocessing. With the focus of characterizing image patterns and trends associated with individual people, these methods also have the option to take advantage of the new artificial intelligence (AI) technologies such as machine learning/deep learning. Texture analysis is a pattern recognition method. By assessing the distribution of voxel signals voxels in an image, texture analysis methods can identify different tissue integrity characteristics invisible to human eyes (34). Applied to MS, texture analysis measures based on conventional MRI have shown the utility to assess pathological changes associated with de- and remyelination (35,36). Phase congruency is one such texture analysis method. Unlike many other methods, phase congruency extract image features using frequency domain information and therefore is robust to variations in image intensity and contrast (37). Machine learning is an approach that builds models automatically based on samples of data to learn patterns to enable it

to make predictions and classifications to unseen data (38). Combining with texture analysis methods, machine learning has the power to improve the pattern recognition and disease characterization abilities in various disorders including MS, in addition to their competitive ability to handle high dimensional datasets (33,39,40).

The main goal of this project is to advance our understanding of the neuroscience mechanisms underlying disease severity and brain function alterations in MS bolstered by innovations in data science methods. To achieve this objective, I take advantage of recent advances in the fields especially those on cutting-edge diffusion MR imaging, image processing and analysis such as image texture analysis, and machine learning/deep learning. These processes are based largely on archived data acquired from people with different types of MS as part of at least three well-characterized clinical studies.

1.2 Hypothesis and Aims

Current MS research is challenged by the lack of connections between MRI-measured disease activity and patient outcome. One critical factor is the lack of methods that reliably detect clinically relevant information of MS pathology. I hypothesize that brain diffusion MRI and phase congruency texture analysis will provide new micro- and macro-scale measures of MS pathology that in combination with novel data science algorithms, will facilitate advanced classification of injury patterns across brain areas, differentiation of phenotypes with different disease severity, and correlation with functional outcomes in MS. Diffusion MRI has shown considerable potential in assessing changes in tissue microstructure in numerous studies. Phase congruency, on the other hand, can detect signal intensity patterns that are difficult to assess using conventual MRI but that

may be critical for additional probing of pathological and functional integrity. The overall goal of this project is to establish methods that are sensitive to MS pathology, disease severity, and functional changes based on innovative brain diffusion MRI and phase congruency analyses. Specifically, this work will establish measures that detect tissue structural changes in both focal MS lesions and non-lesion areas, particularly those associated with critical tracts of brain white matter, to advance the specificity and clinical relationship of the methods. Moreover, this study will apply novel data augmentation and model optimization procedures with diffusion MRI, and integrate machine learning techniques into the analyses with both types of imaging where applicable to improve the applicability of the techniques to clinical data. Collectively, this thesis includes 3 specific aims:

Aim 1: Identify advanced imaging measures that are sensitive to pathological changes in MS based on brain diffusion MRI and texture analysis along with machine learning.

Aim 2: Discover key imaging measures that differentiate disease severity between RRMS and SPMS based on important brain diffusion MRI and phase congruency measures.

Aim 3: Assess the relationships of advanced imaging measures based on brain diffusion MRI & phase congruency with functional outcomes in RRMS and SPMS participants versus controls.

1.3 Thesis Organization

To address the problem of missing tools and measures that link tissue structural changes to disease activity and functional changes in MS, this thesis has taken a stepwise approach. Ranging from an

overview and literature review to method developments, evaluation, and application, and then to conclusion, this thesis includes 7 chapters.

Chapter 1 introduces major topics concerning this thesis and provides a general highlight and contextualization of the problem addressed by the investigations of the thesis. Background information includes an overview of MS, the concerns of disease pathology, phenotypes and severity, and functional performance, the challenges and potential of different types of MRI especially that pertaining to MS, and the potential of image postprocessing techniques including texture analysis such as phase congruency and machine learning as alternative methods of advanced imaging investigations.

Chapter 2 gives a more thorough literature review of topics pertinent to this project. It provides an overview of MS epidemiology, pathology, and clinical understandings, as well as current knowledge and gaps on tissue pathophysiology and their relationship with function. The chapter then gives an overview of a range of imaging techniques and outcomes, including the benefits they offer and limitations they may have, that guide their current and potentially future use in the research and clinical management of MS. The range of offerings by diffusion MRI and phase congruency texture analysis are specifically explored in depth along with methods employed in this project to advance their application such as machine learning/deep learning. A highlight of these methods for their potential to enhance our study of the structural and functional relationships is also included.

Chapter 3 outlines knowledge developments with regards to new methodologies implemented in this thesis. These developments cover explorations made for both diffusion MRI and phase congruency analyses. For diffusion MRI, I outline innovations in obtaining novel measures using diffusion orientation distribution function and tractography models. Further, I present the contributions of some of the orientation modelling approaches to harmonizing diffusion MRI data between samples, and then provide an overview of a relevant experiment. This experiment involves development of competitive neural network models for predicting new copies of diffusion MRI data not typically acquired in clinical imaging such as diffusion scans with a high b-value. Based on both the newly predicted data and original data, this study then shows the feasibility of reconstructing high-quality diffusion metrics equivalent to those derived using purely original data in high angular resolution diffusion imaging (HARDI) for advanced analysis of brain microstructure. In addition, I also present a framework including a graphic user interface established for improved understanding and investigation of phase congruency parameters. This interface allows the identification of optimal settings needed for desired analysis of tissue structural properties using conventional MRI in this project.

Chapter 4 presents the initial investigation and selection of advanced brain diffusion MRI and textural phase congruency outcomes in the context of measurement sensitivity to MS pathology associated with lesion formation and intra-lesion activity, assisted by a recognized, supervised machine learning technique known as support vector machine. Experiments include comparisons of lesions and NAWM regions of the brain, and lesion cores versus lesion rims. Regarding diffusion MRI, this chapter involves the study of measures obtained through multiple modeling approaches based on a single-shelled diffusion MRI acquisition with relatively high numbers of

diffusion acquisition directions (single-shell diffusion MRI). For phase congruency, outcomes are calculated based on systemic tests of associated parameters from multiple mathematical functions. In particular, the parameters are tuned in a way that the eventual phase congruency measures can detect structural changes in a spatial scale range of MS lesions, and that the measures are sensitive to local pattern changes in tissue structure according to experiments with known structural characteristics. The tuning processes are done based on empirical heuristics or prior lab experiences. The derived brain diffusion MRI and phase congruency outcomes are dimensionality reduced by a recursive feature elimination method as part of the support vector machine modelling.

Chapter 5 goes one step further, which focuses on investigating the potential of the associated brain diffusion MRI and phase congruency measures for differentiating disease severity, based on data from new cohorts of people with RRMS and SPMS. For maximal understanding, this chapter takes a systemic approach that includes investigations of disease pathology across the whole brain at different scales. This involves analyses of whole-brain NAWM pathology using histogram approaches, tract-based lesion and NAWM analysis, and along-tract analysis based on critical brain white matter tracts commonly affected in MS: corpus callosum, cerebrospinal tracts, and optic radiation tracts. Further, given the importance of chronic active lesions, this chapter has developed a novel method for assessing the activity of these MS lesions based on diffusion MRI followed by cohort comparisons between RRMS and SPMS. Furthermore, built upon contemporary advances in AI, this chapter also employs new deep learning models developed in tandem with this thesis to improve the calculation of several advanced diffusion MRI measures using only single-shell diffusion data.

Chapter 6 represents the culmination of the development based on advanced diffusion MRI and textural phase congruency methods. The overall goal is to assess whether and how the advanced imaging measures under study predict functional outcomes of RRMS and SPMS participants. This Chapter proceeds with the imaging measures that have shown significance in differentiating MS phenotypes (Chapter 5), particularly measures out of the lesion and non-lesion areas of the aforementioned brain white matter tracts. To further reduce potential 'noises' in the data, recursive feature elimination processes are taken such that only imaging measures that are most relevant are chosen for subsequent functional predictions. The prediction models are implemented based on a different machine learning method, Ridge Regression, and the prediction is done for each of the identified functional outcomes that span physical, neurocognitive, and affective domains. Similar to the above, to minimize variances, only functional outcomes that show significant differences between MS participants and matched controls are used in the prediction. Using a competitive method, the strength of the prediction models is also compared quantitatively to maximize understanding in each study group: MS, healthy control, and both.

Chapter 7 presents an overall summary of the investigations and research findings accompanied by a discussion of the results with respect to current literature. Finally, limitations of the current research are discussed, future steps are suggested, and significance is provided.

Overall, this project is expected to discover new knowledge and novel technologies for advanced probing of MS pathology and function that can further enhance our disease evaluation and management abilities for people with MS and similar diseases.

Chapter 2: Literature Review

As listed in Chapter 1, this Chapter provides a detailed review of the literature directly associated with this thesis project. The main topics include disease overview, pathology, measurement methods from clinical, neuropsychological, and imaging perspectives, advancement of data analysis methods along with artificial intelligence technologies, and summary.

2.1 Multiple Sclerosis

2.1.1 Overview

Multiple sclerosis (MS) is a severe and common disorder of the brain and spinal cord, affecting >2.8 million people worldwide. The disease begins primarily at young adulthood, for many at 20-40 years old, and has a notable sex bias. Depending on geographic locations, the female versus male ratio ranges from 2:1 to 4:1 and this skew is observed to be increasing in some regions of the world (4,9,41). Different opinions exist on the inciting cause of this disease. Common considerations include environmental factors (e.g. place of residence prior to age 15, latitude, and vitamin D levels), genetics (HLA haplotype, relationship risk factors), and the presence of underlying infections (1). In general, MS is manifest with a range of symptoms including visual dysfunction, loss of balance and coordination, cognitive decline, and mood dysfunction, making MS diagnosis a process of elimination sometimes (26,42,43). In pregnant women, MS symptoms sometimes exhibit a remission pattern likely attributed to the elevation of the hormone prolactin during the period (44). Diagnostic tests include physical examinations for clinical outcomes, cerebrospinal fluid analysis for cellular and molecular activity, and MRI for subclinical changes such as lesions (22,42,45,46).

MS presents with several phenotypes clinically, including primary-progressive (PPMS) and progressive-relapsing (PRMS), besides RRMS and SPMS (8,15). The patterns of presentation differ significantly between these forms, where progressive MS often demonstrates progressive physical disability in the absence of acute attacks, while the relapsing forms typically show intermittent development of neurological deficits with partial or complete recovery (Figure 2.1) (15). Current therapies are most efficient in managing the inflammatory processes of MS as seen primarily in RRMS; for PPMS and SPMS, treatment availability has improved with the promising results of B-cell therapies and some immunomodulatory medications for active SPMS patients, though for some managing symptoms is the main form of treatment (8,15,47–49). To improve the management strategy and patient outcome, accurate understanding of tissue pathology is critical.

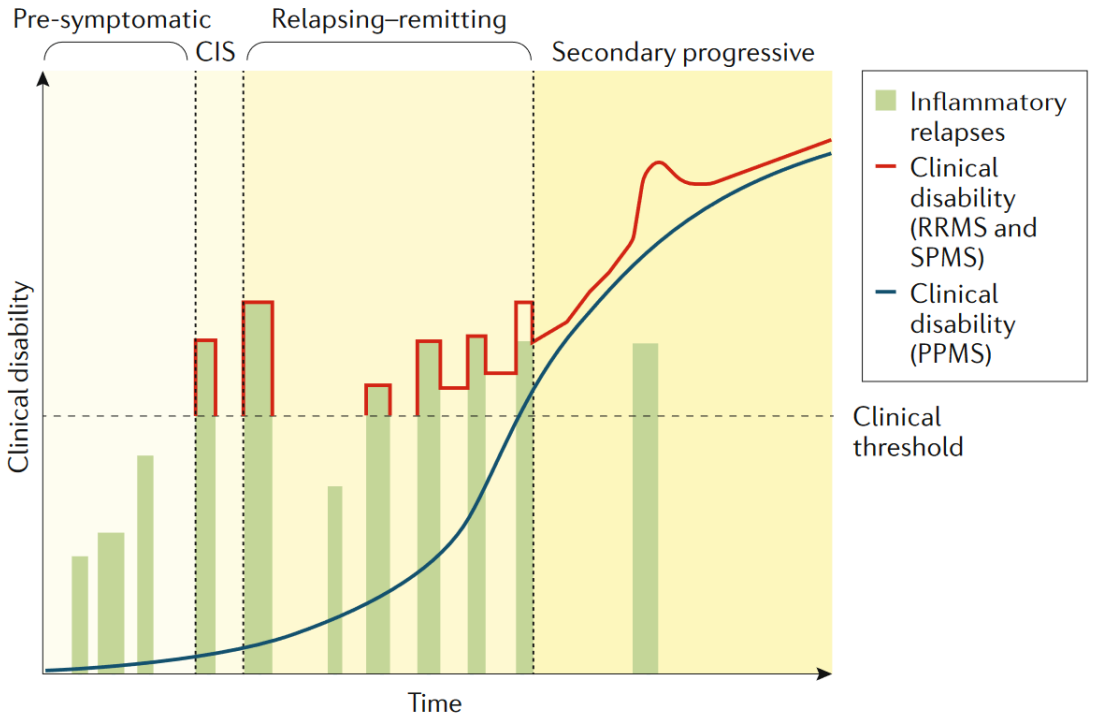

Figure 2.1: Relapse and disability progression in RRMS and SPMS clinical courses. The greater relative frequency of relapses in RRMS than SPMS phenotypes is seen alongside a difference in persistence and severity of clinical disability. (Adapted from Filippi *et al*., 2018) (4).

2.1.2 MS Pathology

Demyelination, axonal degeneration, and certain degrees of remyelination and gliosis mark the key histological characteristics of MS pathology (2). Microstructural damages underlying much disease activity in MS are mediated by inflammatory processes that involve different cell types including atypical microglia and lymphocytes, and the inflammatory intensity varies depending on disease course, occurrence of relapses, and the activity or type of lesions (1–3,50,51). Increased inflammatory activity causes damages to myelin-forming oligodendrocytes (1–3). Myelin injury in turn can cause axonal damage as well as dysregulation of axonal membrane components, including ion channels which makes axons become more vulnerable to homeostatic changes and subsequent injury (2,3,15). Axonal damage has also been suggested to occur through other mechanisms other than demyelination, suggesting the complexity of the disease (3,52).

MS pathology is seen most prominently within lesions of the white and gray matter but also extends into areas with no visible lesions such as the diffusely-abnormal (DAWM) and normal-appearing white matter (NAWM) of the brain (10). The pathology is spatially and temporally heterogeneous both within and across patients (42), presenting in different patterns including those characterized by macrophage associated injury, antibodies and complement or apoptosis of oligodendrocytes (Figure 2.2), and with lesion frequencies that vary by disease phenotype (1,2,51,53,54), making disease activity and functional outcomes highly unpredictable. Focal lesions may accompany temporary functional impairment during relapses as commonly seen in RRMS presentations. Progressive forms of MS exhibit mostly continuous progression in disability in conjunction with slow lesion growth leading to the formation of confluent lesions (1,18,55,56). Nonetheless, the lack of clear association between patterns of lesion development and functional

loss may suggest the importance of investigating the seemingly lesion-free regions, such as the anatomically critical NAWM areas including the corpus callosum and corticospinal tracts. Indeed, strong evidence indicate that microstructural changes within non-lesion regions have significant functional consequences (10). As such, understanding the exact patterns of tissue damage associated with different disease phenotypes such as RRMS and SPMS would be critical for improved disease evaluation and treatment for people with MS.

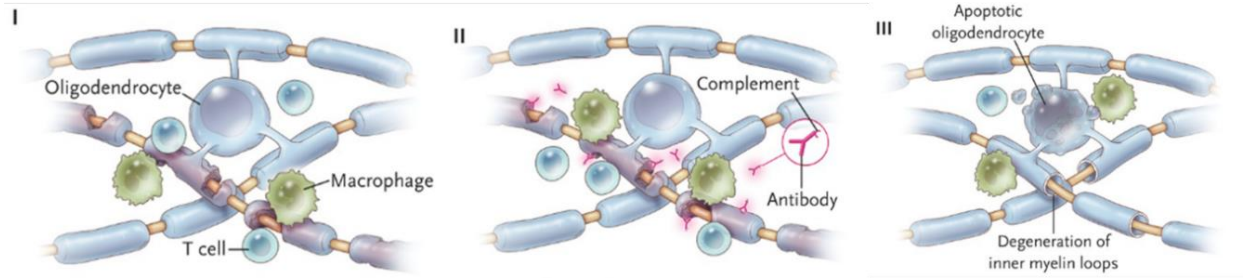

Figure 2.2: Immunologic patterns of acute white matter lesions. Shown are three types of tissue damage underlying lesion pathogenesis: T-cell infiltration and macrophage injury (Type I), mediation of immune interactions by antibody and complement (Type II), and dysfunction and apoptosis of oligodendrocytes (Type III) (Adapted from Reich *et al*., 2018) (8).

2.2 RRMS and SPMS

RRMS is the most common form of MS, accounting for 85% of the initial MS diagnoses, and RRMS and SPMS are two disease course classifications on a continuum of disease activity and accumulation (1,2,7,57). RRMS is characterized by ongoing inflammation and frequent active lesion development during relapses, much more than the progressive MS forms (57). In addition, given the heterogeneity of RRMS from mild to severe presentations, it is thought that many RRMS cases may go undiagnosed (50,57). With a diagnosis, people with RRMS also face a number of uncertainties including the temporal onset and debilitating effects of future relapses, and the likelihood of transition to the hardly manageable SPMS phenotype. SPMS is diagnosed following

an initial diagnosis of RRMS presenting with relentless decline in function. Patients who commence with RRMS vary in the duration of relapses, time between relapses, and timing of progression to SPMS. About 15% of those with RRMS experience only one incident of relapse without further disease worsening while in others, they may begin to experience continuous functional decline after a single relapse attack (57). Approximately 65% of those with RRMS will develop SPMS after 10 to 20 years of disease presentation (51,57,58). Clinically, relapse frequency is a primary classifier of RRMS disease activity, and the conversion from RRMS to SPMS marks the beginning of progressive disability although the conversion point is often far from being clear (2,14).

Mechanisms underlying the ongoing disability and the shift from a relapsing to progressive presentation in MS are not fully understood despite the link between disability accumulation and relapse-associated worsening and progression independent of relapse activity (17,51,59). Ongoing pathological processes including axonal degeneration and oxidative injury are commonly considered to be drivers of disease progression, but disability outcomes have also been attributed to lesion load and the frequency of chronic active lesions in people with MS (15,16,24,60). The lack of knowledge on disease progression mechanisms limits the ability to discover new measures and new effective therapies for MS patients. Given the unique association between RRMS and SPMS, further understanding of the pathological characteristics of these phenotypes and the patterns of abnormalities that differentiate them would be invaluable. Achieving this goal would require competitive in vivo measures of disease outcome for people with MS.

2.3 Methods for assessing disease outcome in MS

2.3.1 Clinical Assessments

Different measures exist for assessing clinical outcomes of MS. Common measures of function include expanded disability status scale (EDSS) and multiple sclerosis functional composite (MSFC) assessments (45,61). The EDSS primarily focuses on the presence of physical disabilities (6). With a score range of 0 to 10, the EDSS assessment covers several functional systems including cerebral, brainstem, cerebellar, pyramidal, visual, sensory, bowel and bladder function, and other systems. A score of 0 represents no disability, 1-3 reflect mild to moderate impairment of one or two functional systems, 4-5.5 reflect changes in mobility and more severe functional impairments, 6 indicates the requirement for unilateral or bilateral support for ambulation, 8 refers to bed- or wheelchair-bound with some independence, and 10 indicates death due to MS. People with RRMS generally rank lower in this scale (1 – 4.5) than those with SPMS. Notably, the EDSS score faces multiple challenges, such as its accuracy in measuring changes over a short time period, repeatability across raters, and completeness in function representations (50,62). The MSFC is a combined measure of physical and cognitive function and is expected to provide more accurate assessments of disease outcomes than EDSS (63). This assessment includes three components: 25-foot walk for assessing lower limb function, 9-hole pegboard test for upper limb function, and paced auditory serial addition test (PASAT)-3 for cognitive function.

2.3.2 Neuropsychological Assessments

Various neuropsychological evaluations are available for characterizing the cognitive and affective outcomes of MS people, such as fatigue, executive function, and depression for the latter (24–26,53,64,65). Similar to physical functions, affective states and executive functions wane with the

progression of disease severity (25). The number of assessments is more expansive than the above as made available through the minimal assessment of cognitive function in MS (MACFIMS) and the brief international cognitive assessment for MS (BICAMS) (66,67). Among these neuropsychological batteries, the brief visuospatial memory test and symbol digit modalities test are specifically used to assess information processing and working memory abilities (26,50,62). Common tests of affective symptoms include Beck's depression inventory and modified fatigue impact scale to assess function in the associated domains (65,66,68). In addition to accurate functional assessment, understanding the underlying mechanisms causing functional alterations is also crucial for MS individuals, where the availability of robust imaging methods is fundamental.

2.3.3 Imaging Assessments

MRI is an exquisite tool that allows non-invasive detection of multiple types of tissue structural changes in people with MS. Most conventional MRI methods can provide information sensitive to the anatomy and gross structural changes of MS individuals useful for clinical management and trials, such as that of focal lesions (14,22). But these methods lack the ability to detect minute changes in a tissue. Advanced MRI methods, based on competitive image acquisitions or post-processing technologies, appear to be more specific to pathological alterations than conventional MRI (Figure 2.3) (27,28,55,69). The sections below will give a brief overview of methods related to these entities.

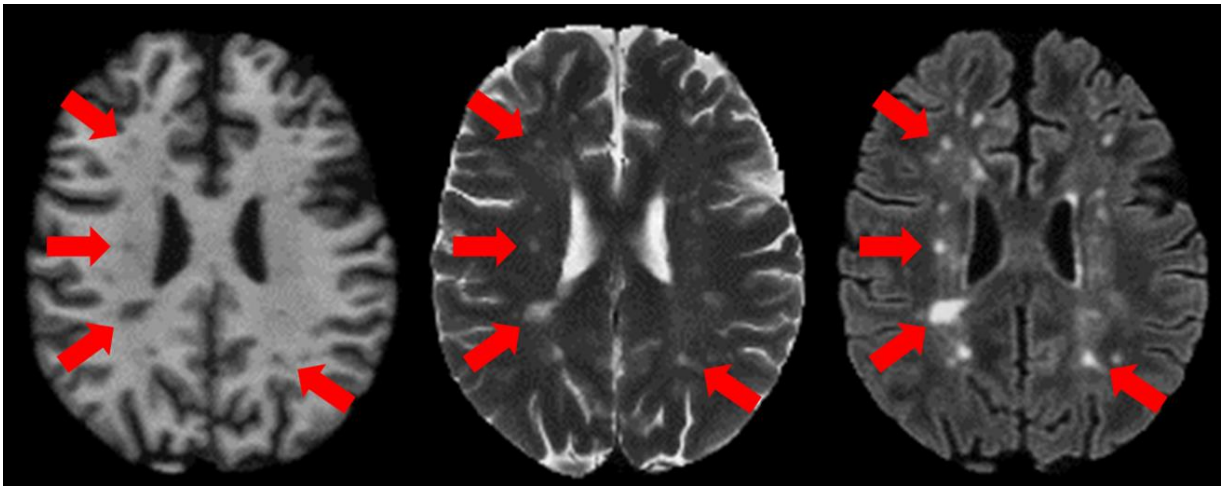

Figure 2.3: Conventional brain MRI from an MS patient. The images represent T1-weighted, T2-weighted, and T2-FLAIR MRI (left to right) offering in vivo visualization of neural changes such as atrophy and lesions (arrows). Lesions are visible with differential proximity to corticospinal fluid (CSF) and cortical regions supporting potential inference of functional outcomes.

Conventional imaging

T1-weighted (T1-w) imaging is based on T1 relaxation achieved by short echo times (TE) and short repetition times (TR). T1-w contrast is brighter in tissues with more fat content. The CSF regions appear dark while white matter regions appear bright, with gray matter regions having an intermediate look. T1-w images are useful in detecting brain volume changes, and presence of tissue loss as observed with T1-w hypointense lesions (black holes) that generally indicate myelin and/or axonal loss, or oedema (42,50). On T1-w images, myelin and axonal loss decreases the fat content of a tissue, and oedema increases the water content. Both changes increase the T1 relaxation time and so decrease T1-w signal (22,70). The presence of chronic black holes have been found to be related to patient disability, and the number of black holes is predictive of EDSS score after 10 years of disease development (71).

With use of gadolinium (Gd) contrast, the T1-w (T1-Gd) images serve as an ideal method for detecting acute inflammation associated with MS lesions. Lesion enhancement in T1-Gd imaging suggests acute inflammatory activity that disrupts the blood brain barrier (BBB). This process causes the gadolinium to infiltrate lesioned regions resulting in a hyperintense appearance on T1-Gd MRI (14,22). The enhancement will resolve with resolution of BBB disruption at future timepoints. In T1-w MRI, these lesion areas may change from hypo- to iso-intense, and such a change in image intensity is believed to indicate tissue repair (22,70). Axonal loss can lead to persistent signal hypointensities in T1-w MRI, particularly in chronic lesions (70,72).

T2-weighted (T2-w) images show an almost opposite appearance to T1-w images given the hyperintense (bright) appearance of lesions instead. The contrast of T2-w MRI depends on the water content. It is highly sensitive to white matter lesions, and the changes therein may arise from different pathological processes including demyelination, axonal loss, inflammation, and gliosis (50). T2-w MRI appearance of lesions endures beyond that of T1-w, spanning from acute to chronic stages, making this sequence an ideal option for assessing lesion load. According to the literature, lesion load of MS patients at disease onset predicts long-term disability accumulated at 15 – 20 years, but the lesion measure is not as sensitive to neuropsychological changes (14,24). T2 lesion load is generally higher in SPMS than RRMS so T2-w MRI is often highly regarded in assessing treatment impact in MS (22). One caveat of T2-w imaging is the superfluous appearance of hyperintense paraventricular lesions with the cerebrospinal fluid (CSF) due to the bright intensity of both structures, which makes it difficult to distinguish between the two without aid of a different anatomical contrast (70).

T2 fluid-attenuated inversion recovery (FLAIR) images are like T2-w except for their use of CSF signal suppression. This makes FLAIR images more effective than T2-w MRI in detecting periventricular lesions and other ventricle-adjacent inflammatory activities as they appear distinct from the CSF-filled structures (72–74). The increased discernibility of lesions in FLAIR MRI also makes it highly useful for assessing cortical and juxtacortical lesions that are believed to play a key role in MS-led dysfunction (22). Finally, the FLAIR sequence is a critical component in many lesion segmentation methods in research or clinical use (46,75).

Advanced Imaging

Advanced MRI may provide stronger relationships to disease activity than conventional MRI due to increased microstructure specificity (13,23,76–78). There are various advanced MRI methods under development, including myelin water fraction and magnetization transfer ratio commonly used to characterize myelin content (70). Susceptibility weighted imaging (SWI) is often employed to detect iron accumulation, which is related to oxidative stress due to production of free radicals, and an indicator of "iron-laden activated microglia" (29,79). SWI is also used to identify phase rim lesions, which show strong associations with chronic active lesions that in turn are considered a symbol of disease progression in MS (16,79). Magnetic resonance spectroscopy measures the composition of a tissue, including the presence of subcellular metabolic structures such as N-acetyl aspartate and glutamate, as indicators of neuroaxonal damage (70). Diffusion-weighted imaging has shown tremendous potential to detect microstructural changes in different tissues including nerve fiber tracts (70,80,81). There have been several technical advances in diffusion imaging, which have also led to the derivation of multiple new measures that may enhance our understanding of structure-function relationships. Likewise, various promising image post-

processing methods exist. One such example is image texture analysis. In this project, I will focus on both brain diffusion-related MRI and MRI texture analysis as two complementary advanced imaging approaches to probe MS pathology.

2.4 Diffusion MR imaging

Diffusion MRI detects the random movement properties of water molecules. Quantifying water movement along different orientations in a specified time period can inform tissue directional information, which along with assessment of the degree of restriction in diffusion can give insight into the overall architecture of a tissue such as neural tracts (72,82–84). The magnitude and orientation of water movement are critical considerations in the acquisition of diffusion MRI and in building models to estimate the diffusion signal. The models vary in both design and implementation; however, they generally provide metrics that reflect unique combinations of diffusion magnitude and orientation, which serve as an integral estimation of tissue microstructure at millimeter and sub-millimeter scales.

2.4.1 Diffusion Tensor Imaging (DTI)

DTI is a modelling approach based on diffusion imaging acquired at a minimum of six directions regarding the presence and properties of structures that restrict the movement of water (85). The DTI measures have shown considerable potential in MS assessment (86). Signal modeling in DTI uses a second order tensor that reflects the relative magnitude of diffusion in perpendicular directions (82–84). The tensor defines three perpendicular axes of diffusion to form an ellipsoid with primary, secondary, and tertiary diffusion axes based on the relative magnitude of diffusion, with the primary axis (longest axis of the tensor) oriented in the direction of greatest diffusion.

Underlying the tensor model in DTI is the assumption of a single dominant diffusion orientation with the probability of diffusion displacement in other directions, defined by a Gaussian distribution centered at the primary axis of the diffusion tensor. The magnitudes of each axis, eigenvalues of the tensor, are used to calculate scalar diffusion metrics that describe the magnitude and/or alignment of diffusion, ranging from a spherical distribution such as that associated with CSF to a linear ellipsoid distribution, as typically seen in the white matter (Figure 2.4) (73,76,82,87,88).

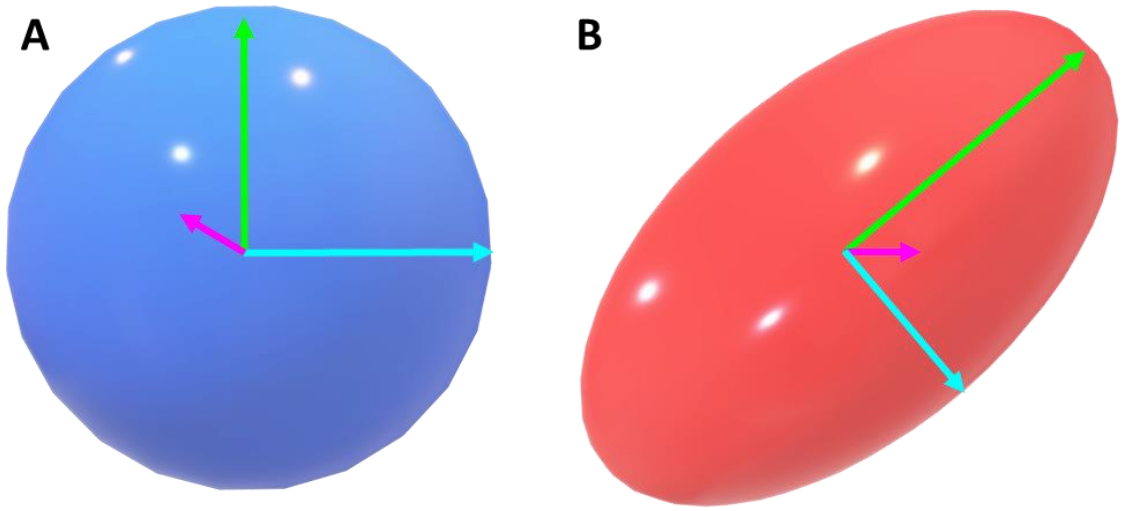

Figure 2.4: Tensor representations of diffusion orientation and magnitude. Diffusion Tensor Imaging represents distributions of diffusion according to second-order tensors that characterize the oriented distribution of diffusion according to three perpendicular axes (green, blue, pink). Isotropic distributions (A) have roughly equal magnitudes of diffusion across the three axes and typically reflect diffusion patterns in CSF regions while anisotropic distributions (B) have unequal diffusion magnitudes with one direction possessing a magnitude greater than the second and third perpendicular orientations resulting in oriented net diffusion typically presenting within uniform white matter structures.

DTI provides several common parameters. Fractional anisotropy (FA) describes the alignment of diffusion in a single orientation (anisotropic), and mean diffusivity (MD) gives the average

diffusion magnitude for the three perpendicular axes of the tensor (84). Other metrics include axial diffusivity (AD) that gives the magnitude of diffusion along the primary diffusion axis, and radial diffusivity (RD) that gives the average diffusion along the perpendicular axes. These parameters have demonstrated various importance in correlating with neural tract properties. FA represents fiber coherence and is a promising measure of tissue damage in NAWM and MS lesions (89). RD correlates with myelin integrity; MD detects early microstructural changes prior to lesion development (90–93); and AD is sensitive to changes in axonal density particularly in tracts of high density and parallel orientations. While with considerable potential, these DTI metrics are not without limitations. FA is noted to have varied responses to microstructure damage as it is a combined measure of neurite dispersion and density which can vary independently. Likewise, the AD and RD can change with the complexity of the underlying tissue architecture, limiting their ability to directly estimate myelin and axonal densities, respectively (94,95).

Another major limitation of DTI is its Gaussian distribution assumption which leads to the modelling of only one major fiber orientation in each voxel. Prior studies have reported that many (30%–90%) voxels in the brain are associated with crossing fibers, which require the representation of multiple diffusion directions in each voxel, a reality that cannot be handled by tensor models (96). Many diffusion MRI investigations have focused on traditional DTI descriptors such as FA and MD. However, due to the limitation of the tensor model in dealing with complex microstructures, these metrics are considered nonspecific as they respond similarly to different microstructure patterns (55,90,92,97). Various evidence support the investigation of new diffusion models to enhance the measurement of complex structures (98–101). One potential diffusion MRI technique that may serve this purpose is high angular resolution diffusion imaging

(HARDI), a method that densely samples the diffusion signal to improve modelling accuracy and specificity to nerve fiber properties (76,102,103).

2.4.2 High Angular Resolution Diffusion Imaging

HARDI samples the diffusion signal at a greater orientational density than what is needed for DTI to more accurately capture the orientation variations in the diffusion signal (Figure 2.5) (102,104). Originally developed to solve the problem of detecting multiple fiber orientations in a single voxel, the acquisition methods of HARDI have expanded to include Q-Ball imaging, diffusion kurtosis imaging, and diffusion spectrum imaging, all of which involve dense orientation samplings, and at times, multiple diffusion weightings (i.e. multi-shell HARDI) (105–107). Single-shell HARDI involves acquiring diffusion imaging with many sampling orientations at a single b-value weighting, the parameter that modulates sensitivity to the magnitude of diffusion in imaging, though multi-shell HARDI acquisition can significantly improve the modelling of the diffusion signal, but it also costs extra scanning time (99). Due to their detailed representation of the diffusion signal, HARDI methods have led to the development of various new analytic techniques that improve upon DTI. These analytic methods fall into two broad categories: 1) Model-free and 2) Mixture models. Model-free methods rely on mathematical descriptors of the diffusion signal over the sphere, and compartment models make assumptions about diffusion properties in unique compartments such as free water and intra-axonal regions.

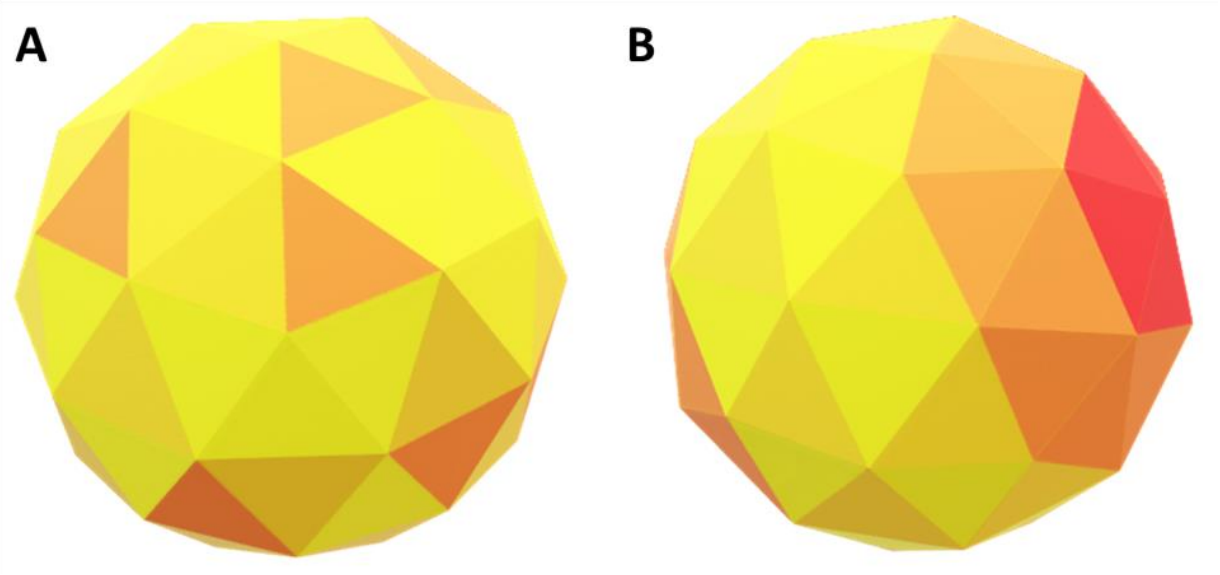

Figure 2.5: Diagram of High Angular Resolution Diffusion Imaging (HARDI) orientation distribution functions (ODF). HARDI models aim to retain sensitivity to local oriented variations in diffusion magnitude (low=yellow, medium=orange, high=red) and capture the complexity of multiple diffusion orientations often using ODFs. Isotropic (A) diffusion distributions can result from mostly equal diffusion magnitudes in all orientations like CSF or can be deciphered with HARDI techniques to relate to the overlap of multiple fiber orientations or unique fiber architectures like fanning fibers identified by orientational modeling of local "hot spots" (orange). Anisotropic (B) diffusion distributions can be related by HARDI techniques to multiple underlying fiber architectures ranging from highly cohesive (highly focal hot spots - red) to dispersed with acquisition schemes supporting delineation of additional properties such as axonal density or diameter.

Model-free methods focus on reconstructing q-space to describe the probability of diffusion across a given distance and direction from the point of origin. These methods have been used primarily for the advancement of tractography techniques given their ability to refine the detection of diffusion in multiple orientations within a single voxel (99,100). Diffusion orientation distribution function (dODF) models are one example of such modeling and are designed to capture the probability of diffusion along individual orientations (88,98,100). Some fiber ODF (fODF) models have been developed to support the detection of neural fiber orientations, where the 3D fiber orientations can be tracked between voxels to produce likely trajectories of major neural tracts

through tractography (103,108). The mean apparent propagator method is another model-free approach that attempts to characterize information from the ensemble average propagator (EAP) (109). The EAP describes the average displacement by diffusion in a voxel over the acquisition time (109). This approach supports the estimation of diffusion behaviours as that measured under slightly modified conditions like alternate b-values (110).

Mixture models are also known as compartment models that assume the presence of multiple compartments, each with unique diffusion behaviours and different contributions to the signals observed within a voxel (111). These models attempt to model the diffusion signal as different volumes of water undergoing diffusion with different spatial restrictions within each compartment. Many HARDI models take such a compartmental approach, but they vary in the complexity of properties to be estimated and assigned to each compartment (77). In neurological tissues, models generally derive estimates for three compartments: intra-axonal, extra-axonal, and isotropic diffusion. As the development is ongoing in this field, the underlying assumptions about diffusion have also been changing , which may involve the number and properties of the compartments, and the methods through which they are derived (77,112). Among some of the promising compartment models are neurite orientation dispersion and density index (NODDI) and ActiveAx (77,78,113–115). Both models take advantage of HARDI and multi-shell techniques in signal sampling, in conjunction with optimization search methods. NODDI is based on a three-compartment model that models intra-neurite diffusion with dispersed sticks, extracellular hindered diffusion with a symmetric tensor, and isotropic diffusion with a spherical tensor. This provides measures of intracellular volume fraction, which relate to the density of neurites and integrity of myelin, isotropic volume fraction, and orientation dispersion index of neurites. ActiveAx is similarly based

on a three-compartment model, with neurites modelled by parallel cylinders with a fixed diameter, extracellular hindered diffusion by a zeppelin, and isotropic diffusion by a spherical tensor. Therefore, ActiveAx indices include the intracellular volume fraction, neurite density, and average neurite diameter. ActiveAx has not been applied to MS, but studies using HARDI models have found increases in axonal diameter within MS lesions (116,117). The NODDI studies have identified decreased ODI and NDI in MS lesions and increased ODI and decreased NDI in the NAWM (118,119). There is also evidence showing correlations of ODI with demyelination in MS and MS-like spinal cord lesions (23,36).

While model-free HARDI methods are generally compatible with both single- and multi-shell HARDI schemes, compartment models typically improve by modelling with multi-shell data. For compartment models, multiple parameters must be investigated for each compartment, so multi-shell diffusion data is better posed for the multiple equations used to derive solutions for outcome parameters. Single-shell data supplied to such models is typically considered underdetermined because there are not enough equations available to solve the parameters. In this regard, model-free HARDI methods can be used to overcome the limitations (110,120). This can include predicting the diffusion signal at alternate gradient directions, or predicting different b-values. Another caveat of compartment models is that the calculations underlying these models are time intensive: it can take hours to days to conduct the model fitting per brain volume depending on the resolution of the images. To improve efficiency, one useful option is accelerated microstructure imaging via convex optimization (AMICO). This method employs linear optimization to increase the speed of calculations and, importantly, it offers quality microstructure-specific parameters similar to those from both NODDI and ActiveAx (121). The AMICO tool has been further

developed as AMICOx to support the modeling of crossing fibers beyond methods established specifically for the compartment models (122).

2.4.3 Tractography

Tractography is another method out of diffusion imaging. It tracks diffusion orientations from voxel to voxel to generate digital streamlines that represent possible neural tract configurations in vivo (123–125). Different methods exist to derive the orientation information for tractography, including the original approaches with orientations derived from the Gaussian DTI primary eigenvector, and current models utilizing HARDI ODF outputs sampled over the sphere (88,98,100,101). HARDI ODF approaches are superior to DTI models for resolving multiple fiber orientations within individual voxels, which can occur in kissing, crossing, and even fanning fiber configurations (80,102,126). The range of tractography models is further expanded by the various settings used in defining the different interpolation methods for orientations between voxels; such settings include maximum angles of curvature between tracking steps, step sizes within voxels, and seeding methods for initiating tracking algorithms. Tractography has been predominantly used to segment white matter tracts for tract-specific analysis, but different analytic methods have been developed to assess structural connectivity and identify anatomic localizations of diffusion metrics. Many tools have been built around tractography with a range of applications. For tract-based analyses where the contribution of distinct tracts is important, new tools have been developed to improve the automaticity and accuracy of tracking (127). Definitions of tract trajectories have been made available through extensive evaluations and have been incorporated into deep learning tools such as TractSeg (Figure 2.6) (128,129).

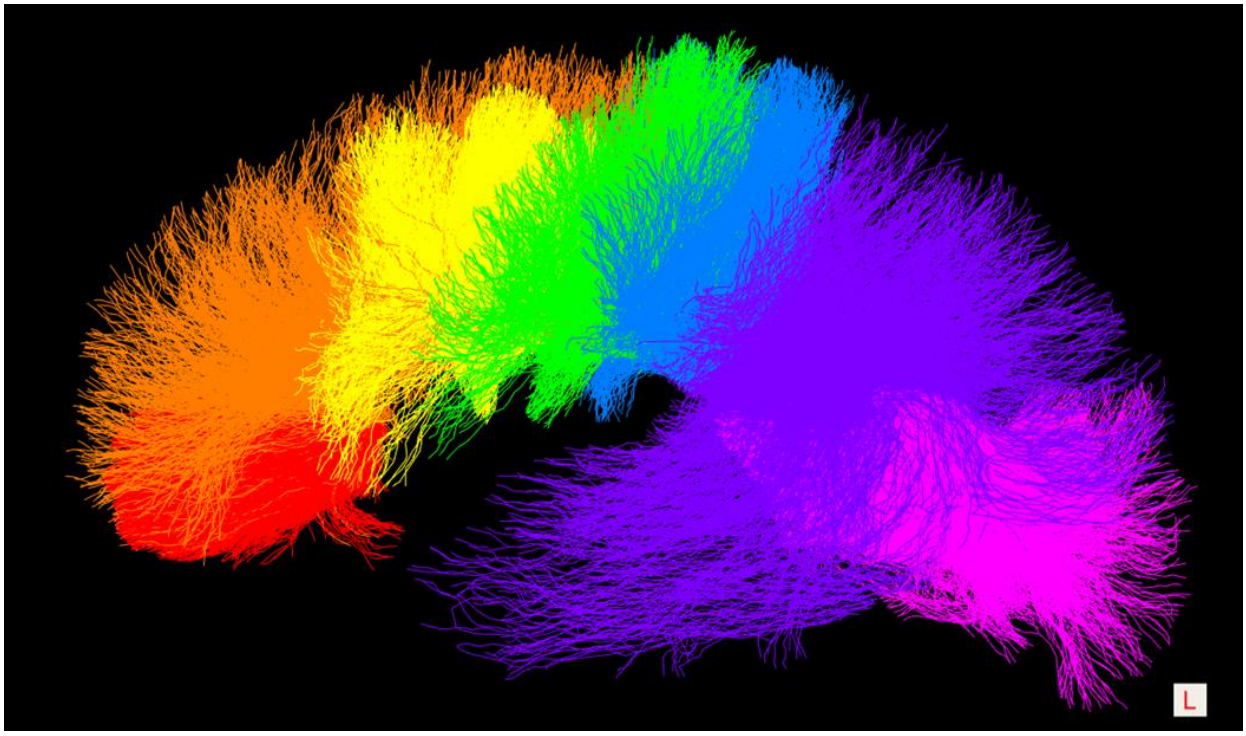

Figure 2.6: Diffusion tractography of the corpus callosum. TractSeg deep learning methods support tracking of multiple cerebral tracts using grey matter connections and likely neural trajectories with a probabilistic tracking algorithm. These methods support segmentation of different neural tract regions that coordinate different functional outcomes.

The utility of tractography in analysing white matter tracts has been shown in many diseases such as MS where white matter is a major target (123,125,130–133). In conjunction with tractography, the analytic tools in diffusion imaging may also enable the measurement of additional parameters along specific white matter tracts for improved understanding of disease activity (80,115,133,134). One critical aspect of tractography that is applicable in this project is developing a means to understand how orientation information relates to MS pathology, given the evidence that tissue pathology disrupts tractography (125,131,135). One approach is the use of tractography in connectomics where anatomical connectivity is inferred based on frequencies of streamline connections between two ROIs and the pathways taken by multiple connections, as measured by streamline abundance and endpoint counts. While this approach provides a global perspective of

neural integrity, the local quantitative potential of tractography has been explored using streamline counts (fiber density index). Fiber density index (FDi) as one of the tractography metrics has been successfully used to assess tractography responses to pathology and microstructural damage (125,131,135). Along-tract statistics is another method for investigating tract-associated changes, which may reveal pathologies not readily detectable with voxel-based analyses (Figure 2.7) (80). With the potential to detect diffusion orientation-based microstructural changes, tractography methods may provide new insight into the mechanisms and evolving patterns of MS pathology (81,131,135).

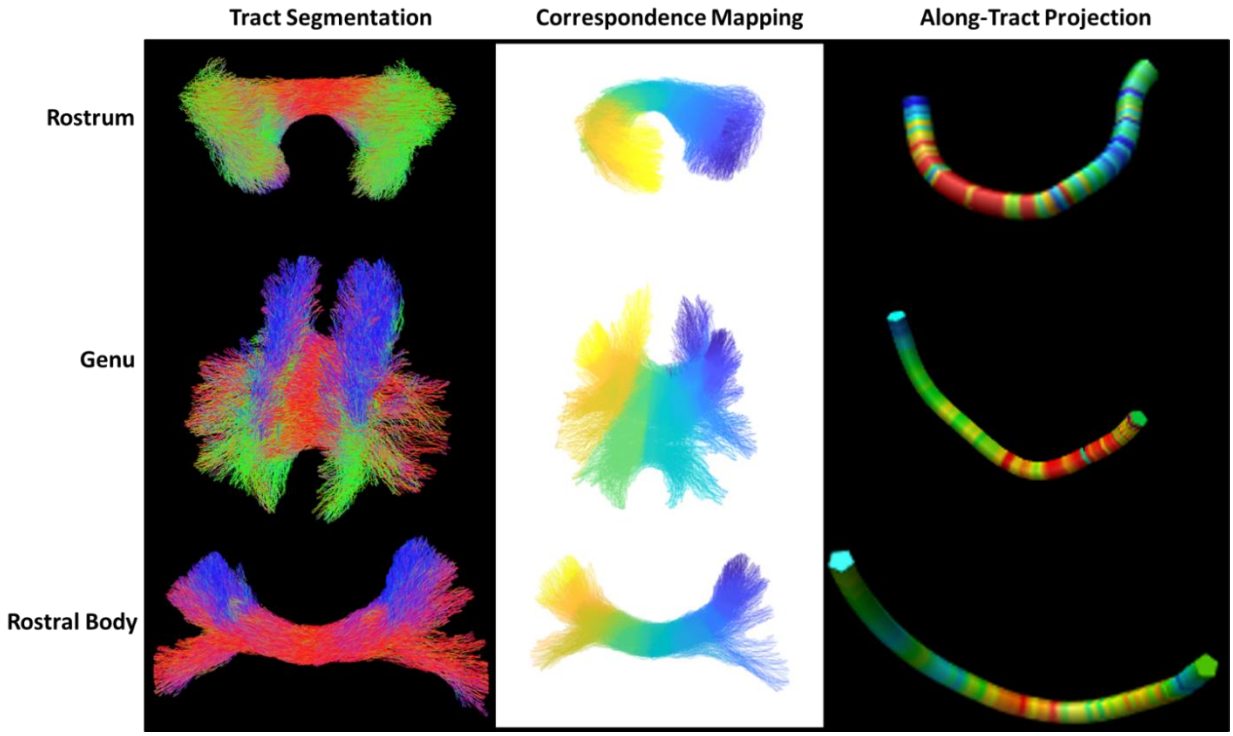

Figure 2.7: Processing pipeline for along-tract statistics in corpus callosum segments. The procedure involves initial tract segmentation (left), grouping of streamline vertices through correspondence mapping (middle), and along-tract projection of investigated measures onto a mean tract geometry (right). This method supports localization of pathological changes that occur in vivo and comparisons of projected measurements between health and disease to investigate the extent of neural damage.

2.5 Phase Congruency as a new Texture Analysis Method

2.5.1 Texture Analysis

Texture is a characteristic defined by the distribution patterns of signal intensity within an image. It can be qualitatively described as organizations of homogeneous to heterogeneous compositions whose component may vary in size, contrast, and other properties. Texture analysis refers to the approach used to uncover features associated with textures, with many approaches providing quantitative measures of texture properties or distributions (136,137). Within images, natural or MRI-based, texture measures can differentiate regions based on their unique patterns and signal qualities (34,136). The features form the building blocks capable of characterizing texture patterns and differentiating regions of interest in many image types and analyses. These features are not easily detectable by visual inspection and so require specialized computation techniques to assist.

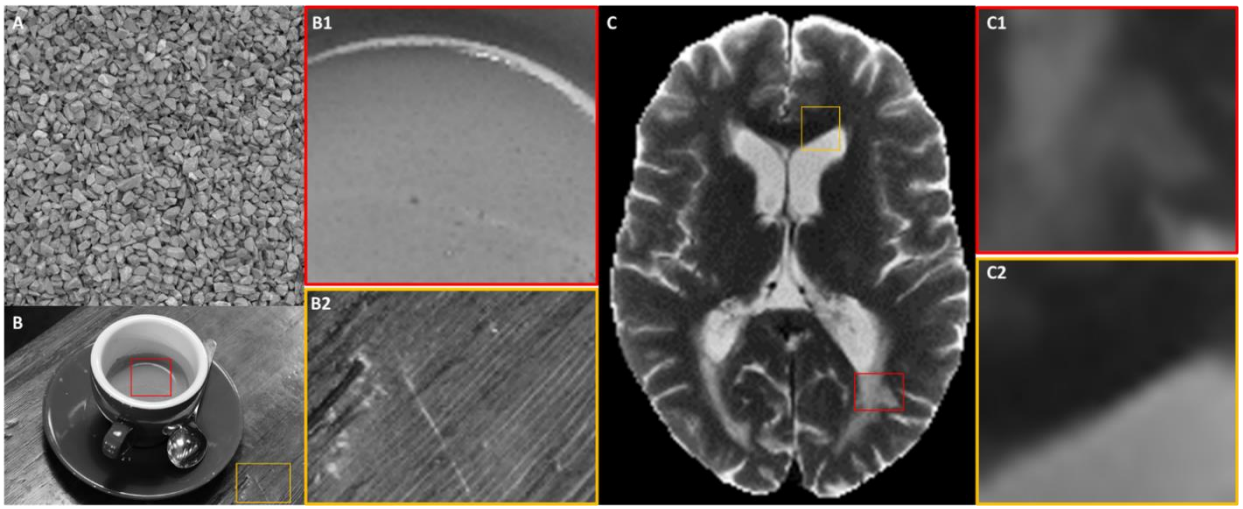

Figure 2.8: Examples of texture properties in natural and MRI images. Larger coarse textures of rocks (A) are contrasted with finer textures of the coffee (B1) neither with regular patterning. In contrast, orientation and linearity features characterize another texture with local variations (B2). In the T2-weighted MR image of an MS brain (C), lesion appear to have heterogeneous intensities and smooth boundaries with surrounding regions (C1) while sharp texture transitions define structural divisions between the NAWM and CSF, each with mainly smooth textures (C2).

Quantitative methods are required for advanced characterization of texture. Common quantitative texture techniques reported in the literature include statistical, transform/frequency-based, model-based, and morphological, which can provide different texture measures useful in medical imaging for a range of applications (136,137). In the literature, statistical and transform/frequency-based methods are most frequently used.

Statistical texture methods can generate features from second order statistics such as those from the grey level co-occurrence matrix (GLCM) technique, where the texture patterns are derived based on spatial arrangement of the signal intensity in images (138). The GLCM method has specifically been successfully employed in tandem with random forest and support vector machine (SVM) machine learning techniques to differentiate normal-appearing and pathological white and gray matter tissues within individuals and between time points (40,139).

Model-based approaches seek to estimate parameters that describe the texture of a signal where the parameters can in turn be applied together with a range of analyses including regression and classification (137). Markov random fields is one such method that models image signals as a function of local surrounding patterns with a general additive model and that has been applied to model de- and re-myelination patterns in a lysolecithin mouse model of multiple sclerosis (39). Morphological texture analysis methods are otherwise rarely used in the imaging setting because they work typically by identification of a fundamental structure whose presence or spatial pattern is expected to indicate qualities of an analyzed region (137). Such fundamental structures are typically difficult to identify even for natural images that are often less complicated than medical

images, though methods associated with edge detection have played a role in some region segmentation approaches (140).

2.5.2 Spatial Frequency Based Texture Analysis

The spatial domain representation of images allows us to observe how signal intensity varies over space within which they are bound. The frequency domain displays how the signal is distributed amongst fundamental waveforms of different frequencies at different phases in their periods. Phase in a sense refers to the location of a point within the cycle of a periodic function. Different methods are available to transform signals between time or spatial domains and the frequency domain. These transform methods employ different basis functions whose frequencies comprise the signal representation in the frequency domain. The Fourier transform serves as a foundation for many of these methods.

The Fourier transform operates with imaginary orthogonal sine and cosine basis function pairs to form a complex-valued frequency transform (141). In addition to temporal signals, the Fourier transform can be applied to images with varying dimensionalities including 2D and 3D images associated with MRI by using multiple convolutions for each dimension. The fundamental implementation of the Fourier transform is intended to represent continuous periodic signals and therefore is limited by its inability to locally characterize frequency compositions, describing when or where they occur (141). The Fourier transform power spectrum has further shown considerable potential to characterize tissue structure alignment and different other properties of MS pathology as seen in animal models of de- and remyelination supported by linear regression (36,142,143).

$$F(\mu) = \int_{-\infty}^{\infty} f(t) e^{-i2\pi\mu t} dt = \int_{-\infty}^{\infty} f(t)[\cos(2\pi\mu t) - i\sin(2\pi\mu t)]dt \qquad (2.1)$$

The short-time Fourier transform (STFT) was developed to address the localization limitation of the Fourier transform by applying a fixed window shape fixed in time to provide signal localization (144,145). This localization can support analysis of unstationary data, having locally varying frequency compositions such as that within MRI. According to the Fourier uncertainty principle, as the width of the window in the time domain is narrowed, frequency resolution decreases while a wider time window decreases temporal resolution but increasing frequency resolution (141). The implementation of the STFT using a fixed Gaussian window is intended to optimize the balance between resolution in the signal and frequency domains and is referred to as the Gabor transform (144).

$$STFT\{f(t)\}(\tau,\omega) \equiv X(\tau,\omega) = \int_{-\infty}^{\infty} f(t)w(t-\tau)e^{-i2\pi\mu t}dt \qquad (2.2)$$

The wavelet transform similarly provides windowed frequency transforms for localized signal analysis; however it improves upon the STFT by supporting multiresolution analysis (141). Wavelets are waveforms that encode bandpass filters in the frequency domain where they can be modulated by a windowing function. Wherein the STFT uses constant bandwidth and positionally fixed signal windows, wavelet transforms implement convolution of varied window sizes to provide multiresolution analyses that similarly support signal localization (141). Following the Fourier uncertainty principle as mentioned above, wavelet analyses typically employ large windows in high frequency regions to improve spatial localization of high-frequency regions while smaller windows in low-frequency areas supporting detection of the corresponding low-resolution spatial signal changes. The scalings and transformations of the mother wavelet are what define the wavelet transform. Wavelet implementation with a Gaussian window similar to the Gabor STFT

optimizes the balance between resolution in both signal and frequency domains and is termed the Morlet wavelet, or Gabor wavelet when specifically references the Morlet wavelet using the complete complex basis functions instead of solely the real component (144,146). Phase congruency uses the Gabor wavelet to support analysis of the phase component of the signal.

$$WT_{\psi}\{x\}(a,b) = \langle x, \psi_{a,b} \rangle = \int_R x(t)\psi_{a,b}(t)\,dt \qquad (2.3)$$

The Stockwell transform advances upon the Gabor wavelet by providing a global representation of phase information and may therefore be referred to as a phase-corrected Morlet wavelet (146,147). It overcomes the STFT limitations regarding the Fourier uncertainty principle by performing multiresolution analysis with scalable gaussian windows correlated to the banded frequencies, similar to the wavelet transform (146,147). By provide globally-referenced phase information, The Stockwell transform improves upon the continuous wavelet transform by providing globally-referenced phase information using the Fourier transform (146). Modifications of this transform have been developed to reduce its computation complexity and improve its applicability to different analytic task. A fast implementation of the Stockwell transform has shown promise for predicting head and neck squamous cell cancers with different tendencies for metastasis using a Bayesian network classifier (148). Further, the polar Stockwell transform has been successfully employed to classify pathological tissue types within MS patients using a random forest model (149).

$$S_x(t,f) = \int_{-\infty}^{\infty} x(\tau)|f|e^{-\pi(t-\tau)^2 f^2} e^{-j2\pi f\tau}\,d\tau \qquad (2.4)$$

Overall, texture analysis methods have proven to be useful in identifying tissue structural changes in different diseases such as MS based on an array of MRI contrasts, including conventional imaging (34,35,40,150).

The phase congruency method employed in this thesis is developed on a modification of the discrete Gabor wavelet transform, though with innovations to improve the computational complexities; similar implementations may be sought with the Stockwell transform. Phase congruency has shown promise in applications to analyze medical imaging including discriminating the presence and type of lung disease based on chest radiographs with linear discriminant analysis (151). The concepts underlying spatial frequency analyses and the phase congruency approach will be explored with further detail.

2.5.3 Phase Congruency

Phase information obtained from transformation of images into the frequency domain have been found to retain more pertinent structural information than the corresponding magnitude information. In isolation, phase components of the signal have been found to support independent image reconstruction and capture the dominant portion of image features. The interaction of phases of different frequencies at any point in an image contribute to notable features central to image perception including edge geometries. Specifically, the Local Energy Model suggests the regions where phases of multiple frequency components are most in phase are where most features are observed (152). The points at which frequency components are maximally in phase can result in different feature appearances such as sharp transitions in intensity associated with square waves or indicating peak points of local gradient intensity (Figure 2.9).

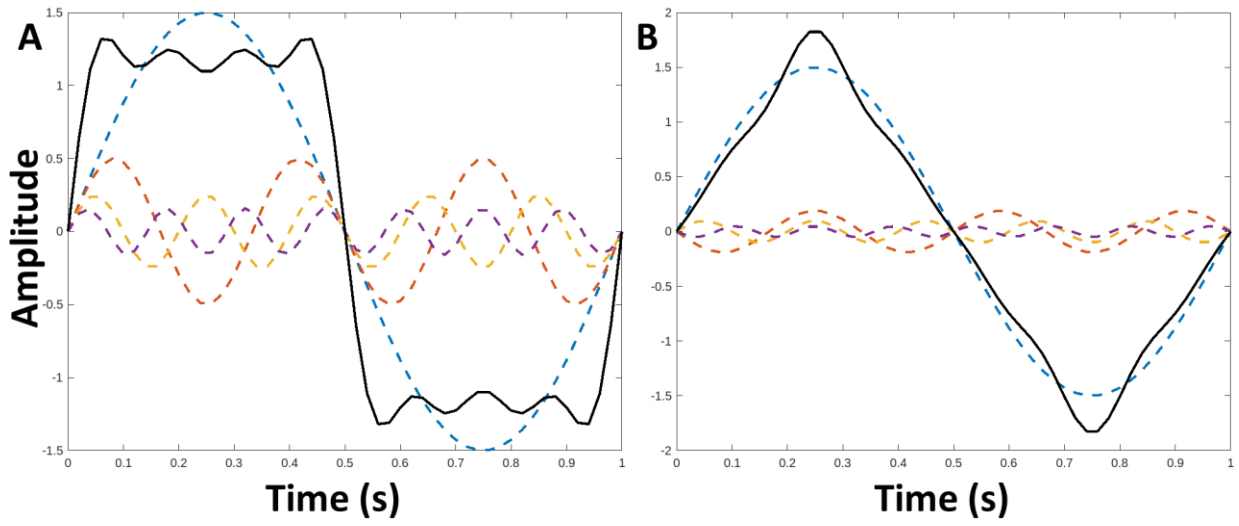

Figure 2.9**:** Alignments of phase characterize a range of feature types. Points of phase alignment across multiple frequencies are noted in A) a square wave at the points of the step ups and downs notable for sharp transitions in images and in B) a triangular wave at the peak and trough.

Phase congruency is a frequency-based texture analysis technique based on the local energy model that focuses on representing features according to the degree to which the frequency components are in phase (37,153,154). In association with structural edge features, phase congruency can also be classified as a structural texture method. Compared to many other local energy techniques, phase congruency is unique as it is highly robust to variations in image contrast and illumination, a common challenge in medical imaging (154,155). It further offers high spatial localization of features at different scales by employing a high pass filtering approach to the addition of frequency filters (156).

Phase congruency in its application to image processing is a spatial frequency technique calculated based on how phases calculated from wavelet filters are distributed around their average. A sensitive measure (PC_2) of this distribution is obtained by combining both the cosine and sine

phase deviations of local Fourier components weighted by their amplitudes across frequency filters scaled to different central frequencies. This formulation was found to improve feature localization beyond original formulations based solely on cosine deviations and is not based on the overall signal magnitude making it invariant to brightness and contrast. The measure is then refined by subtracting the estimated noise contribution (T) according to the Rayleigh distribution, weighting ($W(x)$) with a sigmoid curve according to the range of frequencies ($s(x)$) contributing to the calculation, and then summed over multiple orientations. As phase congruency is applied to varying architectures of phase associated with gradients or steps, these characteristics of features can be described by the weighted mean phase ($\bar{\phi}(x)$) to offer more characterization of feature properties.

$$PC_2(x) = \sum_o \frac{\sum_n W(x)\left\lfloor A_n(x)\left\lfloor \cos\left(\phi_n(x) - \bar{\phi}(x)\right) - \left|\sin\left(\phi_n(x) - \bar{\phi}(x)\right)\right|\right\rfloor - T\right\rfloor}{\sum_n A_n(x) + \varepsilon} \qquad (2.5)$$

Kovesi's phase congruency implementation uses the discrete Log-Gabor wavelet to provide spatially localized analysis that better fit patterns in the statistics of natural images relative to the Gabor wavelet (157). Log-Gabor wavelets are also implemented on the basis that spatial filters of the visual system may be symmetric in the logarithmic frequency domain, and beyond Gabor wavelets, supporting wider bandwidth filters and removing the contribution of the average signal intensities (DC component) (157). Gaining these properties trade off with the optimal balance between frequency and spatial widths offered by the Gaussian window with Log-Gabor wavelets having a positively skewed distribution in the linear frequency domain.

To address the loss of the optimal trade-off between frequency and spatial localization offered by Gaussians, Kovesi empirically determined the relationships between Log-Gabor filter widths and

spatial localization (156). It was determined filter bandwidths between 1 and 3 octaves offered optimal spatial localization. The choice of filter bandwidth in turn influences other steps of parameter selection to define filter bank properties including frequency and orientation coverage.

$$\mathcal{G}(\omega) = e^{\left(\frac{-(\log(f/f_0))^2}{2(\log(\sigma/f_0))^2}\right)} \quad (2.6)$$

When working with images, the transform space is a function of both frequency and orientation. The windowing and tiling of filters across orientations can be performed using uniformly-spaced gaussians organized in a rosette with appropriate angular widths determined by their bandwidth and correspondingly, their standard deviation (σ_θ) (157).

$$\mathrm{G}(\mathrm{f},\theta) = \mathcal{G}(\omega)\, e^{\left(\frac{-(\theta-\theta_0)^2}{2\sigma_\theta^2}\right)} \quad (2.7)$$

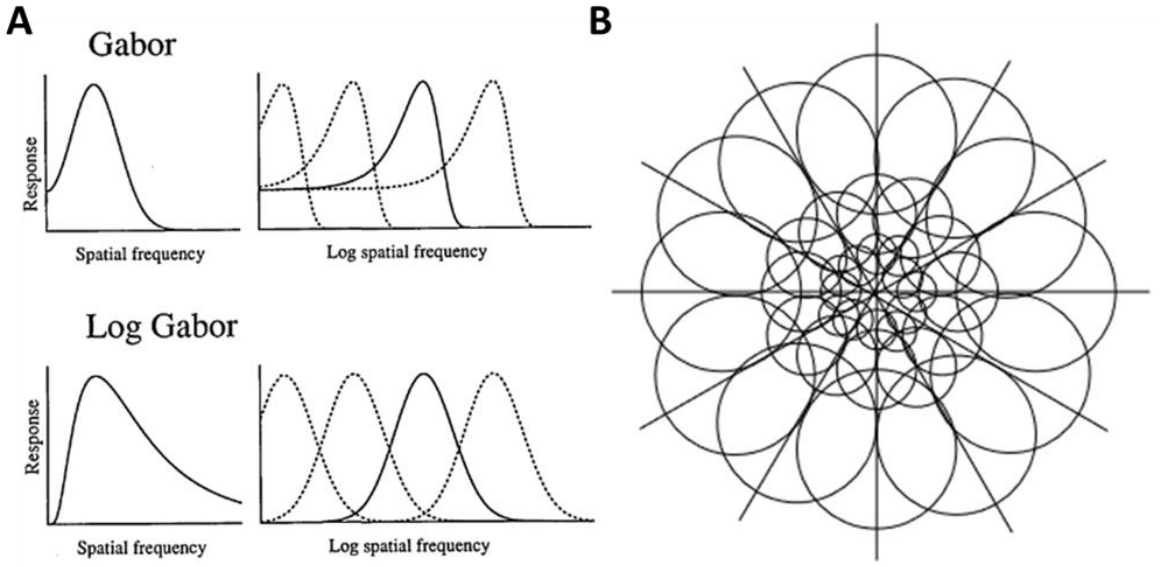

Figure 2.10: A visualization of frequency-shifted and oriented Gaussian filters. A) The Gabor function shows a symmetric Gaussian distribution in the linear frequency axis while log Gabor show this pattern on the log frequency axis which corresponds to a positively-skewed distribution on the linear frequency axis. (Adapted from Field, 1987) (157). B) Gaussian filters are tiled in a 'rosette' formation in the frequency domain to provide optimal coverage of the spectrum. The combination of filters shifted in the frequency domain and tiled in across orientations forms filter banks for image processing and analysis (Adapted from Kovesi, 1996) (156).

To provide coverage of the full frequency spectrum, filters with constant octave bandwidth (β) are defined by maintaining the ratio between the standard deviation of the window (σ_f) and the filter central frequency (f_0) for each wavelet filter ($\eta_\beta = \frac{\sigma_f}{f_0}$) (158). This constructs filters that are wider for high frequencies and narrower for lower frequencies to benefit frequency localization. Modulating the overlap of adjacent wavelet filters varies the net sensitivity and its balance across the full spectrum to different frequency scales. This balance is controlled by identifying a multiple of central frequencies that defines the spacing between adjacent filters and the resulting sum of their sensitivities to specific frequencies for a given octave bandwidth. Finally, to balance orientational sensitivities based on the angular filters, a ratio between the angular separation of filters and the standard deviation of the window can be imposed to scale according to filter positions (156).

Following calculation of phase congruency in multiple orientations across different frequency scales, the contribution of noise (T) to each calculation is removed then the resulting values are further processed with multiplication by a weight ($W(x)$) that penalizes values based on the distribution of frequency responses. The noise contribution is calculated as a function of the filter responses at the highest frequency using the median or mode ($[A'_0]$) according to the Rayleigh distribution for non-negative random variables (156). They are then scaled based on the influence of spatial width on the estimated noise response according to the scaling between successive central frequencies (m) (156). The weighting for frequency spread is performed on the basis that phase congruency is more notable when present over a wide range of frequencies. To this end, the range of frequencies contributing to phase congruency is determined by a width ($s(x)$) function based on relative filter responses normalized by the number of wavelet scales analyzed. A sigmoid

curve is then applied to differentially weight narrow and wide widths modulated by the steepness (g) and shift (c).

$$T = \frac{k[A_0'](1-(\frac{1}{m})^N)}{1-\frac{1}{m}} \quad (2.8)$$

$$W(x) = \frac{1}{1+e^{g(c-s(x))}} \Big| s(x) = \frac{1}{N}\left(\frac{\sum_n A_n(x)}{A_{max}(x)+\varepsilon}\right) \quad (2.9)$$

Notably, phase congruency requires the declaration of multiple parameter values best suited for target analyses. Phase congruency use of the discrete Log-Gabor wavelet requires definition of the number of wavelet scales where each serves as a filter of certain frequency components whose responses are used in the calculations. Most studies have resorted to manual optimization; however, that is difficult to translate across studies and is time consuming; there is strong evidence showing the possibility of automatic optimization of the model parameters for both natural and MR images (159). However, as parameters are tuned, the interpretation of measured outcomes will change accordingly, so there is a need for robust and straightforward approaches to optimize the method to promote its applications.

Given its ability to detect the resonance points of image phases, phase congruency analysis outputs multiple feature characteristics including phase congruency for each assessed orientation, the summed phase congruency across all orientations, weighted mean phase, and the feature orientations. The phase congruency method is highly sensitive to the ‘edge and corner’ features of tissue structures and may be an ideal candidate to detect visually silent pathologies in the NAWM of MS patients, the tissue type showing strong relevance to the progression of the disease. Phase congruency has demonstrated the potential to differentiate lung diseases including cancers. It is not highly used in the study of MS, though it has been previously explored in this lab to detect

lesions in brain white matter, characterize NAWM damage differentiating RRMS and SPMS subtypes, and detect gray matter abnormalities (151,160,161). Phase congruency will be employed not to expand on diffusion MRI but to explore its potential to provide complementary information for the analysis of MS.

2.6 Data Analysis Augmentation with machine learning

Machine learning is an area of AI aiming to support decision making using computerized algorithms. Based on patterns and trends learned from existing data, machine learning can predict outcomes for new unseen data central to a variety of data science activities. In particular, machine learning has been instrumental in supporting various imaging driven tasks ranging from data acquisition to data pre- and post-processing. Specifically related to this thesis, data post-processing and analysis would be the focus of interest. In this direction, the following paragraphs will briefly introduce the most relevant components including the common formats and associated applications of machine learning, and its potential for optimizing feature selection processes. Given the complexity of MS pathology and the high number of variables expected to be generated in disease characterization, integration of the associated machine learning techniques would be encouraging.

2.6.1 Common Formats of Machine Learning

Supervised and unsupervised modelling highlight two common options of machine learning (38). Supervised learning works with labeled data. The goal is to establish a relationship between input and output data based on the known labels for each. In this regard, the output is modelled as a function of the patterns measured from the input variables or images. With this approach, the predicting variables are typically selected based on prior hypotheses about the relationship with

the outcomes being investigated. Unsupervised learning comes into play when there is no labeled data available. In other words, this method is used to detect patterns and trends within data that are not previously known or completely understood. In medical applications, supervised learning is commonly used because labels are often available, it generally performs better than unsupervised learning, and it can be implemented through various approaches (162). The description here involves 2 main types: statistical machine learning and neural networks/deep learning.

2.6.2 Statistical Machine Learning

This method is also known as classical machine learning that refers to learning from existing or user engineered variables at input. Regression and classification are supervised machine learning paradigms used to model data, with the goal of predicting continuous or categorical outcomes. A range of statistical machine learning methods exist. Linear models are a fundamental machine learning approach as represented by the regression-related techniques, where ridge regression specifically aims to improve model generalizability in relating continuous variables. Other techniques include random forest models, which employ ensemble learning to improve model performance, and support vector machines, which identify multidimensional hyperplanes that separate identified groupings underlying the data (163–165). This thesis makes use of different machine learning algorithms to characterize MS pathology and regress functional outcomes.

2.6.3 Support Vector Machine

Support vector machines (SVMs) can be used for both classification and regression tasks, though the focus in this thesis centers on classification. The method is aimed at separating classes using a hyperplane embedded within a multidimensional feature space (Figure 2.11) (166). This is

implemented with the goal of optimizing the tolerance of classification to local variations around the decision plane due to noise, and therefore sample points closest to the hyperplane are identified as support vectors (166). The separation of sample points from different classes across the hyperplane is called the margin, and the SVM hyperplanes are designed to maximize these margins to improve generalization to new samples. The identified hyperplane is defined by normal vectors (weights — w) and a separation from the origin (bias — b), which show how it splits each feature dimension to obtain its discriminative ability. The optimization of hyperplane separations can be tuned for specific data samples and investigations by adjusting the permissibility of the hyperplane to misclassifications through regularizations (165,166). Instead of a hard-margin approach aimed at eliminating all errors during training, a soft-margin approach allows tuning of regularization parameters to allow more errors in the training samples to improve model generalizability (166).

$$w^T x + b = 0 \qquad (2.10)$$

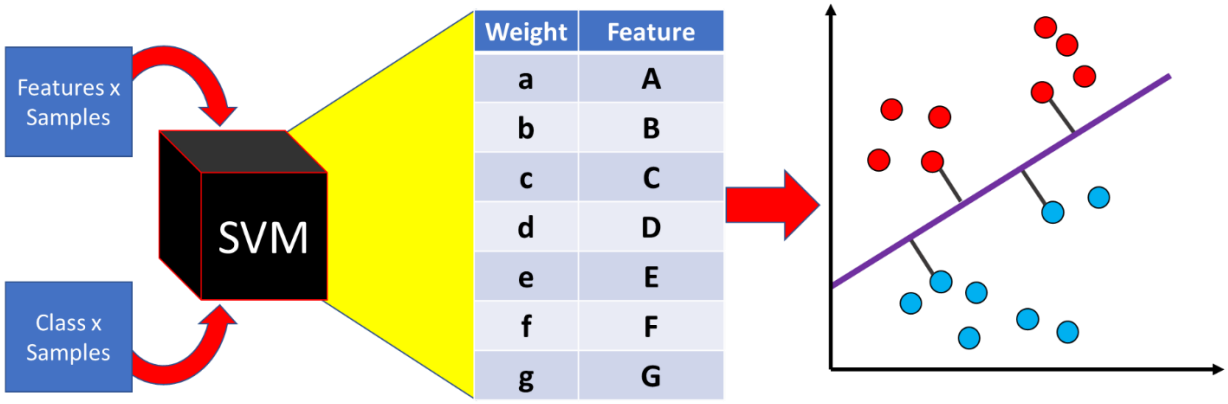

Figure 2.11: Support vector machine (SVM) classification. SVMs assign weights to modelled features to define multidimensional hyperplanes (purple) that separate different classes of data (red and blue) based on key data samples (support vectors). Here a linear SVM is shown however nonlinear hyperplanes support classification amidst more complex distributions. Soft-margin classifications allow for errors close to the hyperplane while optimizing the separation of classes.

The use of a linear hyperplane is most beneficial when the classes are linearly separable based on the selected features. This implementation is employed in this thesis to facilitate more direct interpretation of the coefficients relative to input features. Where this is not a clear linear separability based on input features, SVMs can employ kernel functions to map samples from the original input feature domain to a higher dimensional space ($\phi(x)$) in which linear separability may be better achieved (166). The hyperplane in these transformed dimensions may reflect as nonlinear in the original feature space. Routinely investigated kernels include the linear, polynomial, Gaussian/radial basis function (RBF), Laplacian, and sigmoid kernels (166).

$$w^T \phi(x) + b = 0 \qquad (2.11)$$

2.6.4 Neural Networks and Deep Learning

Deep learning is a subset of machine learning based on the concept of neural networks in the brain, so the methods are also known as artificial neural networks. This type of method aims to train weights of successive layers to learn patterns in an increasingly abstract way, and therefore they are particularly useful for learning complex relationships among data. Once the algorithms are trained, they will be used to predict outcomes similarly to that in statistical machine learning. The neural networks can be shallow or deep depending on the application. Based on cutting-edge technologies in this field such as convolutional neural networks (CNNs), deep learning has shown enormous promise in a range of tasks in the realm of image processing and analysis, including classification of disease pathology and subtypes (167,168). In addition, with limitations in imaging time in clinical settings, neural network models including CNNs have been developed to predict unacquired images based on subsampled imaging data. In this way, both predicted and initially acquired can be modelled together to provide desired outcomes but without the cost of extra

acquisition time. The strategy has been shown to be particularly useful in augmenting diffusion MRI data as seen in this thesis (169).

2.6.5 Feature Selection Assisted by Machine Learning

In addition to the above, machine learning approaches can also help reduce the dimensionality of features used in modeling processes. Multiple methods are available to reduce feature dimensionality, including recursive feature elimination (RFE) (165). This method works by iterative identification of the best-performing subsets of predictors. Machine learning methods typically construct models by assigning weights to different features, commensurate with their contribution to model performance. These weight coefficients rank the importance of each feature in the associated machine learning tasks. Regarding RFE, it works on the premise that more important features will have larger weights. By removing the lowest-ranked features gradually, the subset of features contributing the most to the best overall model performance is retained (165). This method is versatile and can be implemented in tandem with many machine learning methods with appropriate modifications, including use cases in this thesis.

2.7 Summary

MS is a complex disease characterized by different pathological changes leading to different disease severity and functional deficits among individuals. Conventional MRI alone is insufficient to overcome these challenges. Advanced MRI improves upon conventional MRI, particularly regarding its specificity to tissue pathology, but there is still a lack of established methods in MS evaluation and management. Diffusion MRI is a promising method for detecting microstructural properties, and various new imaging and modeling techniques have emerged that may improve the

power of diffusion imaging. MRI texture analysis appears to be a competitive pattern recognition method. It is compatible with conventional MRI and with phase congruency, it also seems to be robust to the variations in image contrast and signal intensity. Currently there are different measures of functionality in people with MS. However, clinical measures are often limited by their sensitivity to early or short-term changes. MRI is highly capable of detecting subclinical MS activities but methods that predict functional outcome are yet to be discovered. Machine learning has shown tremendous potential in various image processing and analysis tasks. Combining machine learning with advanced brain diffusion MRI and phase congruency methods may prove to be a valuable approach for improved study of both disease activity and functional outcomes for people with MS. To this end, different new develop and innovation activities have been implemented and are summarized in Chapter 3 of this thesis that follows.

Chapter 3: Technical Developments and Innovations Associated with This Thesis

As mentioned in previous Chapters, diffusion imaging is one of the most promising advanced MRI methods for characterizing tissue microstructural properties. However, the DTI method is limited by its ability to resolve crossing fiber diffusivities as commonly seen in the brain. The HARDI methods aim to overcome this challenge by offering more specific and sensitive measures than DTI. But it is not always practical to acquire diffusion datasets that support HARDI analysis in clinical imaging due to time constrains. Further, regarding diffusion MRI datasets acquired using different protocols or different scanners, direct combination that is necessary in testing impactful hypotheses is likely not feasible without standardization. Regarding phase congruency, despite its novelty and robustness to variations in imaging contrast and brightness, this method involves up to a dozen variables. Manual refinement as done with prior implementations is time consuming and subject to the availability of effort and expertise. To this end, several advances have been made in this thesis to innovate the analysis and use of these methods. The new areas range from innovative use of single-shell diffusion MRI to data optimization, harmonization and creation for diffusion MRI. For phase congruency, the areas involve both parameter optimization and interface implementation as detailed in this Chapter below.

3.1 New Developments Associated with Diffusion MRI

3.1.1 Advanced Analysis of Diffusion MR Imaging Using HARDI-like Models

Diffusion MRI forms a critical part in MS research, and DTI measures are sensitive to a broad range of pathological changes in MS. But the specificity of DTI is limited in comparison to HARDI

outcomes due to the adoption of multi-compartmental modelling of the latter. Unfortunately, HARDI data acquisition is time-consuming especially regarding multi-shell HARDI and is limited in many study protocols. My research in this direction is to provide mitigation strategies that minimize the issue related to simple diffusion MRI acquisitions. Specifically, this research treats the acquired data as single-shell HARDI and then fits multi-shell models to the single-shell HARDI through algorithm investigations and adjustments. To be able to use this approach, the number of diffusion orientations is suggested to be ≥45, which fits directly to our own datasets applied (111). In this way, competitive measures of neurite properties such as orientation dispersion index (ODI) equivalent to HARDI can be derived that are otherwise impossible based on simpler acquisitions alone. In this thesis, diffusion analyses by modelling with single-shell HARDI is validated using a 45-directional b=1000 s/mm^2 dataset in Chapter 4 with encouraging results found in the associated study scenarios. With development, single-shell HARDI methods may support advanced analysis of changes in tissue microstructure as expected during demyelination and neurodegeneration in MS.

3.1.2 Novel Metrics Derivation Based on Advanced Diffusion Orientation Modelling

In the literature, diffusion orientation modelling approaches have been developed alongside diffusion compartment models (88,98,100). These orientation modeling methods have been applied primarily to support tractography-based segmentation of neural tracts. The orientation information in tractography is rooted in the direct relationships between magnitudes of diffusion in different orientations drawn from raw acquisitions and is therefore somewhat susceptible to changes in tissue structure properties (95). As these magnitudes may change in response to MS pathology, they would reflect the presence of pathology instead of the fundamental anatomy.

Therefore, my hypothesis is that pathology changes will reflect alterations in eigenvector orientations that will be deflected from the ground truth. DTI tractography based on the primary eigenvector is expected to be particularly susceptible to these pathology-driven deflections, which in turn would result in discontinuous tracking between voxels. Example consequences include premature or inaccurate terminations or improbable trajectories. Further exploration of the above hypotheses is also prompted by the encouraging results obtained from the existing DTI tractography outcomes including fiber density index (FDi) (Chapter 4), based on a common tractography algorithm known as fiber assignment by continuous tractography (FACT) (131,135,170). The purpose of my new development is to originate a robust and automatic analytic approach related to the FDi. In the FACT algorithm, several tracking criteria are set manually including maximum deflection angles, FA stopping criteria, and step sizes which variably influence FDi. Eventually, my effort has led to the use of apparent fiber density (AFD) which is completely model-free in its derivation from the fODF (171). As a more data-centric version of FDi, the AFD is used in the thesis after Chapter 4.

In addition, inspired by the orientational aspect of FDi and the possibility of generating ODI using single-shell diffusion MRI, I have focused on the development of another orientation-related measure, which is relatively independent of the long model-fitting procedures of HARDI compartment models. This endeavour starts by modelling the diffusion orientation distribution function (dODF) which reflects the probability of a water molecule being displaced along a certain orientation. The dODF was calculated using a spherical harmonics approximation (100,172). I have discovered that by calculating the probability of diffusion in any of the sampled orientations and fitting these probabilities to a normal distribution, the energy of the probabilities ($\sum \ln(p^2)$),

namely, ODF energy, can be calculated. This parameter is fast to calculate and can serve as a novel measure of orientational complexity localized per voxel, which is evaluated in Chapters 4, 5, and 6 of the thesis.

3.1.3 Diffusion Harmonization

Common to many clinical studies, the imaging data may not always be acquired from the same machine or using the exact same protocol, leading to comparison issues. In this project, some of the patient cohorts involve different studies, where diffusion MRI were acquired using slightly different protocols. To improve the quality of the analyses, two diffusion datasets as part of Chapter 5 were investigated for harmonization employing the linear rotationally invariant spherical harmonics (RISH) method (173,174). This method performs voxel-wise correction of dataset differences based on spherical harmonic features. For optimal outcome, two harmonization steps regarding b-value and angular resolution, respectively, were performed prior to application of the RISH method. This method will be employed in Chapter 5 to test feasibility of using two study datasets. Most other methods available in the literature are limited to harmonization applications on data after processing and deriving measurements while the methods mentioned herein address this challenge by directly working with 'raw' data. Therefore the current approaches can be translated into clinical settings where acquisitions using different protocols or scanner systems are common.

B-value Regression

The basis of b-value harmonization stems from the modelling of diffusion signals with a monoexponential decay. This approach corresponds to the gaussian distribution model of diffusion

in DTI and is believed to be a good fit for data within the b-value bounds of 500 s/mm^2 and 1500 s/mm^2 (Figure 3.1) (106,175). Based on the Stejskal-Tanner equation:

$$S = S_0 e^{-bD}, \qquad (3.1)$$

I can then regress the initial diffusion data to new data of different b-values within the above range (176). Despite the large span of the acceptable b-value range, at 1000 s/mm^2, this study limits the application of this technique to a b-value difference of 200 s/mm^2 given b-values of 800 s/mm^2 and 1000 s/mm^2 from the 2 datasets tested here, falling in the middle of the bounds.

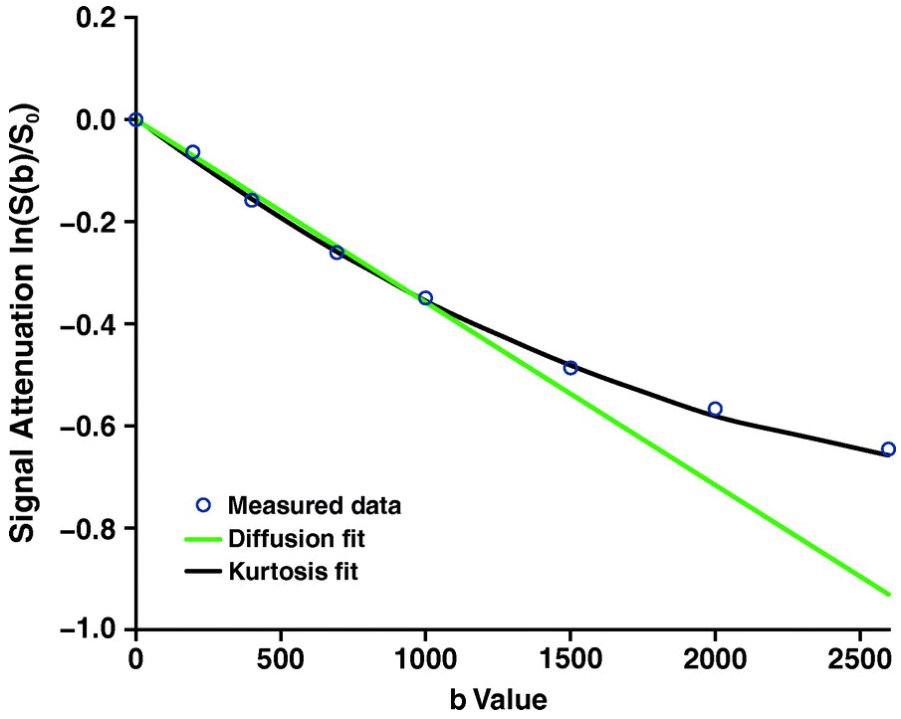

Figure 3.1: Monoexponential and Kurtosis modeling of diffusion signal attenuation. A gaussian monoexponential model (Diffusion fit) has a limited good-fit range to measured data relative to Kurtosis models (Kurtosis fit). (Adapted from Steven *et al*., 2014) (175).

Angular Resolution Adjustment

High angular resolution is a major benefit of HARDI analyses because it supports a more nuanced analysis of local variations in the diffusion signal. While new information cannot be added to diffusion MRI once acquired, modelling the diffusion signal with spherical harmonics allows artificial enhancement of diffusion angular resolution. This approach is employed in some tractography algorithms which use the dODF to support tracking between voxels at multiple angles with a finer sampling than original acquisitions. Just as this supports smoother tracking, for diffusion acquisitions with low angular resolution, I propose that it may improve the numerical stability of HARDI modeling. In contrast to tractography approaches which employ increased angular sampling of the dODF, the spherical harmonic representation supports an inverse calculation whereby the original diffusion signal can be resampled (Figure 3.2) (100). Not only does this approach target improved model stability, it also supports data harmonization by allowing different datasets to be resampled to identical gradient orientations. Further exploration of the spherical harmonic modelling of the dODF indicated that it supported an inverse calculation that recovers the original diffusion signal with arbitrary angular resolution.

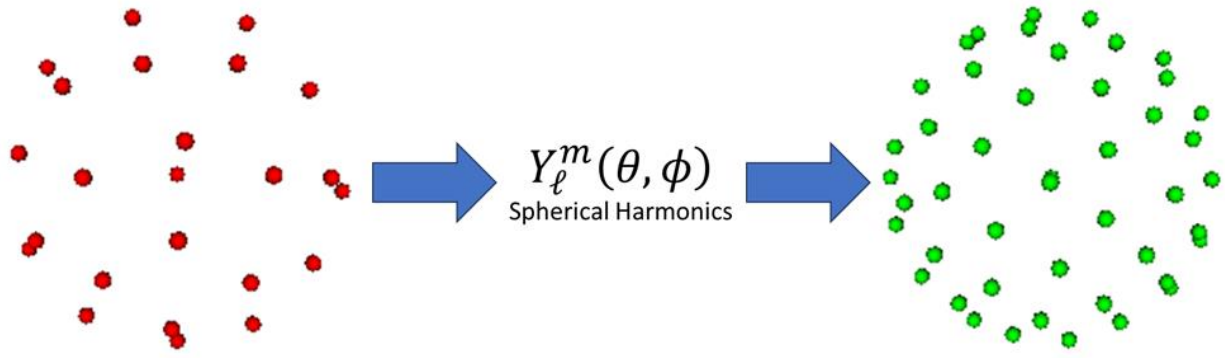

Figure 3.2: Spherical harmonic approximation of the diffusion signal. Spherical harmonic modelling was employed to resample a 23-direction diffusion signal (left) to a 45-direction diffusion signal (right).

3.1.4 Robust Neural Network Models for Data Creation in Diffusion MRI

The fitting of HARDI models to single-shell diffusion datasets is promising but also considered underdetermined because the number of data points measured is lower than the number of variables to be solved. In Chapter 4, this limitation was side-stepped by fitting simpler HARDI models that appeared to be compatible with the single-shell diffusion data. To take advantage of the improved specificity offered by multi-shell HARDI models, my goal here was to develop novel deep learning neural network models such that new diffusion datasets can be predicted using existing datasets. In this way, complete fitting of truly multi-shell HARDI models becomes possible based on both the initial and predicted datasets. This approach is used in Chapters 5 and 6, done by predicting the b=2000 s/mm^2 diffusion data using the corresponding b=1000 s/mm^2 acquisition (Figure 3.3).

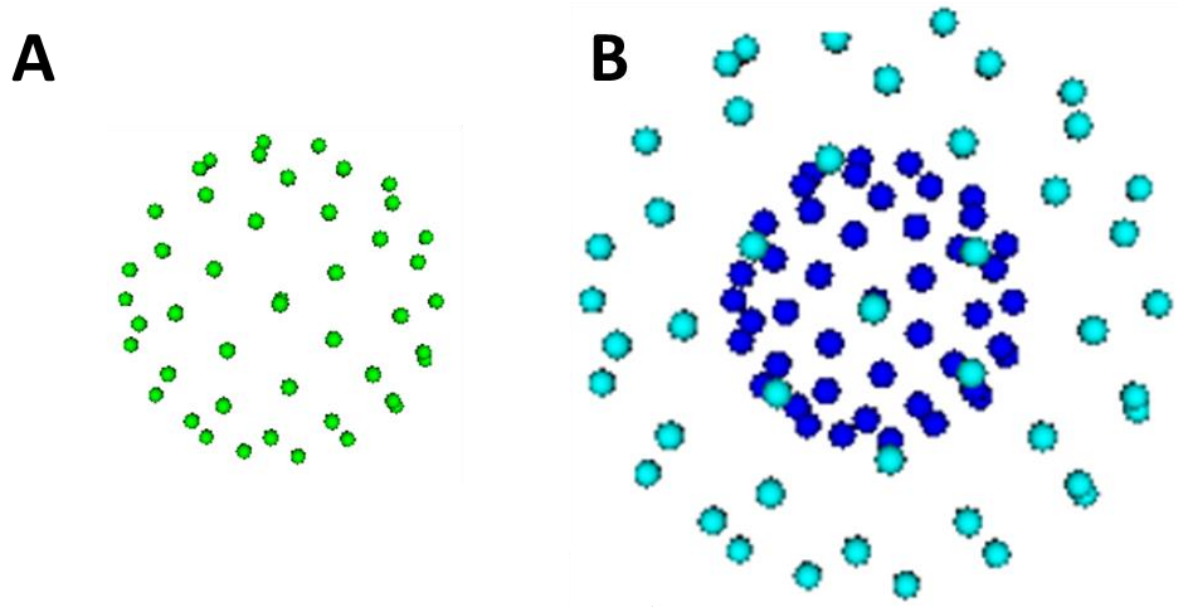

Figure 3.3: Diagram of spherical coordinates defining diffusion acquisition schemes. Shown are an example scheme of a diffusion MRI dataset acquired as a single b=1000 s/mm^2 shell (A), which is used to predict a second shell with a higher b-value of b=2000 s/mm^2. Together they form a multi-shell HARDI dataset (B).

Together with lab mate (Mr. Murray), two neural network models were established. The initial model was developed based on an architecture known as a multi-layer perceptron (MLP). After refinement, the MLP model was integrated into a CNN model. Both models were trained and validated step-wise to optimize hyperparameters, based on multi-shell brain diffusion MRI scans from healthy subjects as part of the Human Connectome Project (HCP) datasets freely available online (177). The final model architectures were obtained by training and testing again using local 2-shell brain diffusion MRI data acquired from people with MS. The results of this work were published as a manuscript with myself as a co-first author (Murray and Oladosu *et al*., *Magnetic Resonance Imaging*, April 2023) (169) (Figure 3.4). These methods can be applied to simplify the diffusion MRI acquisitions in clinical settings where full data coverage costing double time and resources would otherwise be required to obtain comprehensive HARDI outcomes, thereby advancing the disease monitoring and measurement abilities in clinical practice.

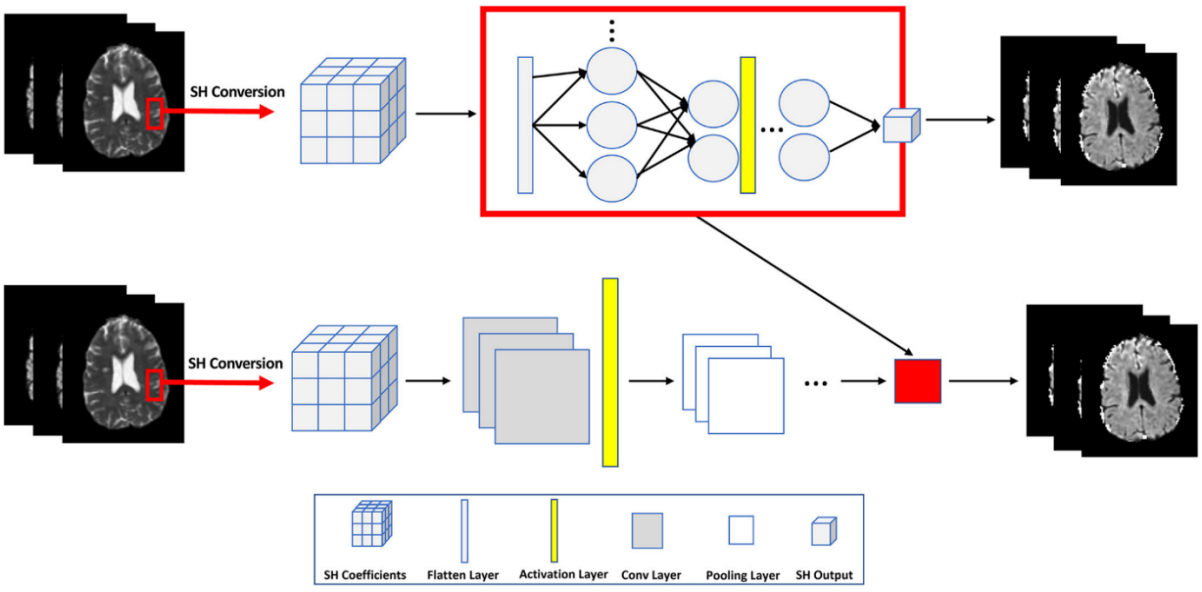

Figure 3.4: High b-value diffusion MRI prediction network. This multilayer perceptron (top) and convolution neural network (bottom) show the fundamental structures of the developed neural networks for predicting b=2000s/mm^2 diffusion data. (Adapted from Murray and Oladosu *et al*., 2023) (169).

3.2 A Novel Framework for Optimizing Textural Phase Congruency Analyses

Clinical management of MS primarily engages with conventional MRI such as T1-weighted, T2-weighted, and T2-FLAIR MRI, so it is important to investigate phase congruency by starting with these imaging sequences. However, while promising, phase congruency presents with some challenges in its use for image analysis, including: 1) the large number of parameters involved; and 2) the expertise and effort needed to fine-tune the parameters. To overcome the limits, I have implemented a graphic user interface that allows fine tuning of all key phase congruency parameters intuitively (Figure 3.5). The following sections introduce three optimization areas as part of my new development, along with the theory and conceptualization of phase congruency that is critical for its understanding and use.

3.2.1 Conceptualization and Workup

Initial tools to implement phase congruency have been provided within MATLAB by the initial author of the methods (Peter Kovesi) in an online code repository (178). Phase congruency has been mainly applied for image segmentation or feature identification in 2D images. To align phase congruency measures with the structure of MRI data, this thesis developed a custom 3D python implementation of phase congruency based on available scripts on 3D with C++ and on 2D with python by others (158,179). 3D phase congruency supports balancing of information from multiple horizontal and vertical orientations. For conventional display purposes, outcomes of phase congruency in this thesis are shown axially.

Phase congruency calculation requires the setup of multiple parameters to define the wavelet frequency filter banks employed in analysis and how the calculations are subsequently processed.

Parameters to construct the filter banks include the width and separation of filters in the linear frequency scale, the minimum wavelength (maximum frequency) and number of filter scales to cover the desired frequency range, and the number of filter orientations. In phase congruency computation, the penalty for frequency spread is modulated by a sigmoid curve with gain (scale) and cutoff (shift) parameters, and the method for identifying and processing noise information. Default settings have been proposed in the original implementation; however, the study-specific parameters are typically set based on visual appearance heuristics of calculated outcomes (159). Certain optimization methods such as maximal contrast between regions of interest have been proposed to improve the quality of output but the value of these settings varies according to study goals (159). In this thesis, the goal was to assess local structural differences, contrasting segmentation or feature identification done in prior studies. The thesis purpose here also entailed the generation of feature maps out of conventional MRI scans to enhance the detection of "hidden" patterns concealed in the investigated images.

Given the number of parameters required by phase congruency in the calculation process, I undertook a thorough investigation of the relationships between the parameters and how each of them influenced phase congruency outcomes. Collectively, phase congruency was conceptualized as the result of variations in several key settings including spectral coverage, spectral sensitivity, and modulation of frequency spread (Figure 3.5).

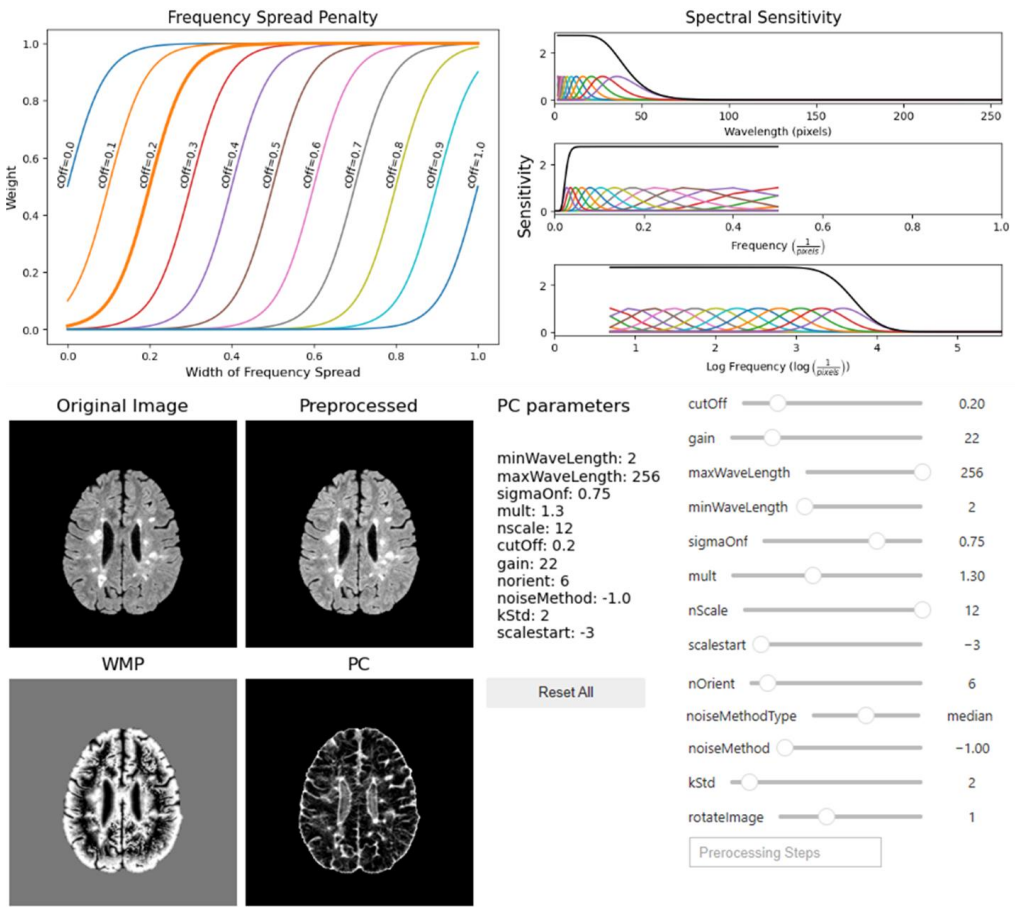

Figure 3.5: Phase Congruency calculations and parameter tunings. Phase congruency calculations are dependent on multiple parameter settings that vary the sensitivity to phase information from different spectral regions, the penalty for frequency spread, and the coverage for different feature orientations. Here plots for the frequency spread sigmoid and spectral sensitivity illustrate the combined influence of most phase congruency parameters.

3.2.2 Angular Resolution of Phase Congruency Measurements

To provide an unbiased isotropic representation of phase congruency, the filter bank includes frequency assessments across multiple orientations. For this reason, enough orientations must be sampled for either 2D or 3D phase congruencies to reduce orientational bias. As this work uses 3D phase congruency analysis, I had the orientation sampling approach innovated by using a convenient 23-direction diffusion gradient sampling scheme available from the Measures of Corpus Callosum Function dataset. The diffusion gradient scheme in terms of imaging is designed

to provide uniform orientational coverage of the spherical sampling space. This approach replaced the need for selection of several orientations in a spherical grid-like approach to save time for measurement collection (158). Based on diffusion MRI results, a minimum of ~20 directions are needed to properly capture variations in the diffusion signal for reconstruction of DTI, so the use of this 23-direction scheme targets a minimum sufficiency in the orientation sampling scheme for phase congruency outcomes (180). Moreover, this scheme supports minimization of variations in angular spacing between orientations. Following the calculation of phase congruency, Gaussian windows are applied at each identified orientation with their bandwidths adjusted to balance orientational coverage and sensitivity. The standard deviation of the Gaussian is defined according to a ratio of 1.2 between the average oriented filter angular separation and the standard deviation of the Gaussian as identified by Kovesi for balanced orientational weighting (156).

3.2.3 Spectral Modulation

Spectral modulation involves the balancing of multiple parameters to provide full coverage of the frequency spectrum for an image of given size and an appropriate balance of sensitivity across the frequency range. This aspect of phase congruency is primarily modulated by the minimum wavelength, the number of filter scales used per orientation, the width of those scales in the frequency domain and their separation defined as the multiple (mult – m) that shifts their central frequencies. Starting with individual filters, their coverage is regulated by their bandwidth modulated by the sigmaOnf (η_β) parameter, the ratio of the window function's standard deviation to its central frequency. However, to cover the full spectral range, multiple filters must be spaced in a way such that the total sensitivity they provide to a given point is equal across the spectrum. Empirical determinations of points on the sigmaOnf-mult curve were plotted based on published

findings (178). The relationship was found to best fit a power curve, so I identified 2 equations. One was derived by solving the power relationship (Equation 2) and another based on the theory that the value of mult would be a function of the filter bandwidth (β) as determined by sigmaOnf (η_β). The power relationship was chosen for further investigations due to simplicity and the approximate nature of the approach, though a precise equation may be ascertained in direct relation to the bandwidth through minimization of the sum of squared filter responses (Figure 3.6).

$$m = \eta_\beta^{\,ln\left(\frac{\pi}{20}\right)} \tag{3.2}$$

$$m = 2^{2\sqrt{\frac{2}{ln(2)}}(\|ln(\eta_\beta)\|)*x} \mid x = \frac{\pi}{4} \tag{3.3}$$

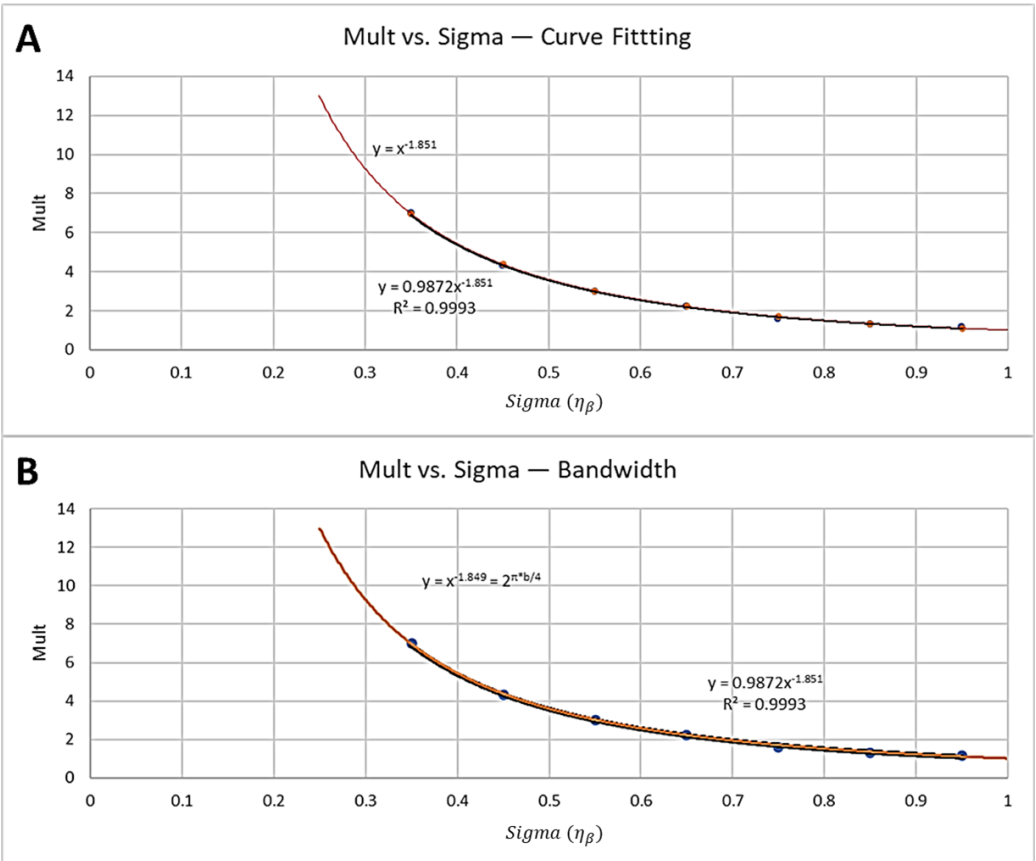

Figure 3.6: Equations for calculating the scaling by mult (m) of central frequencies between successive filters. Mult is formulated based on fitting of empirical data with a power function (A) and a power function constructed around the filter bandwidth (B) as defined by sigmaOnf (η_β).

The importance of this spacing is that with enough filters ($nscale$), full coverage of the spectrum with even sensitivities can be achieved. If the spacing is increased, the sensitivity undulates over the course of the spectrum without a defined interpretation. However, if the spacing is reduced, more weighting is given to high frequency, localized information with wide frequency bandwidths to support localization (Figure 3.7). Therefore, the 'multiple' for scaling successive filters was defined according to the inequality:

$$m \leq {\eta_\beta}^{ln\left(\frac{\pi}{20}\right)}. \qquad (3.4)$$

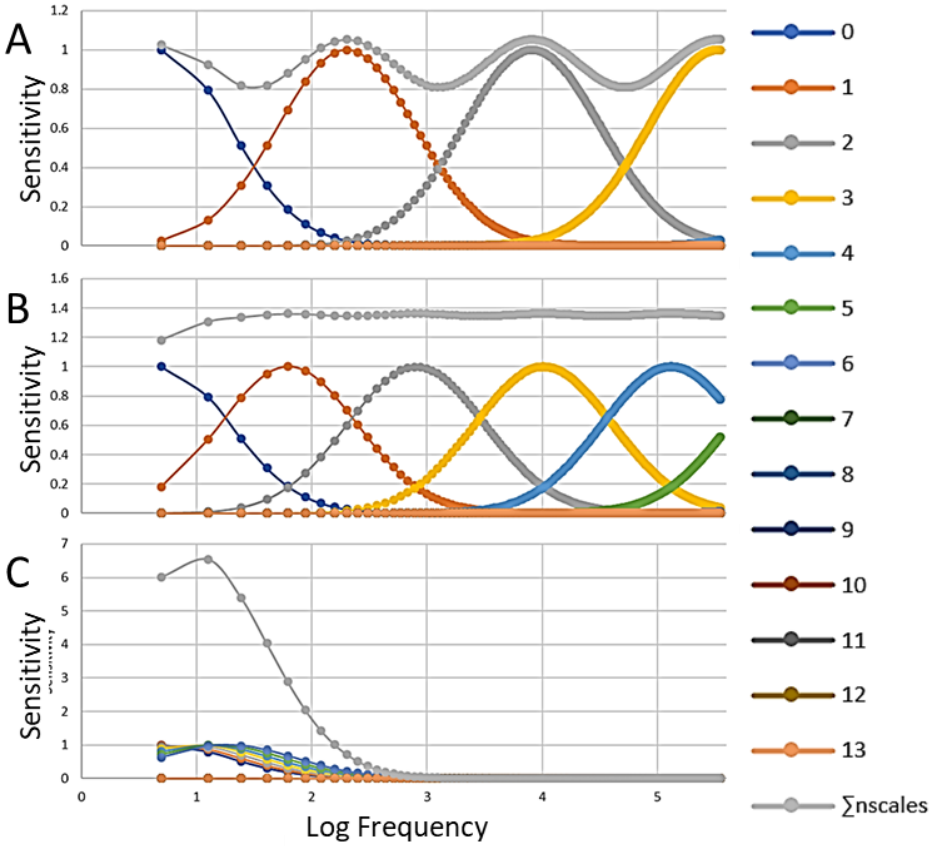

Figure 3.7: Spectral sensitivity modulated by filter scaling with mult (m). Variations in the spectral sensitivity of phase congruency were plotted for a sigmaOnf value of 0.55 against log frequency with mult (m) taking values of A) 5.00, B) an optimal mult value of 3.024 according to equation 3.2, and C) 1.70. Mult values higher than the calculated maximum cause undulating sensitivities while lower values result in greater sensitivities to higher frequency regions due to the high-pass approach to the addition of successive filters.

With the optimized sigma-mult relationship, I ventured to assess what value of nscales would provide full spectrum coverage for image analysis with a defined minimum and maximum wavelength without unnecessarily increasing computation time (Figure 3.8). This was defined based on the number of filters required to cover the distance between the maximum and minimum wavelengths plus an additional 3 filters (Scalestart parameter) to adjust for overlaps of filters at the edges of the spectrum. Because this was a Log-Gabor filter bank, the equation was adjusted accordingly.

$$nscale = \left\lfloor \frac{ln\left(\frac{max_{wavelength}}{min_{wavelength}}\right)}{ln\left(\eta_\beta{}^{ln\left(\frac{\pi}{20}\right)}\right)} \right\rfloor + 3 \qquad (3.5)$$

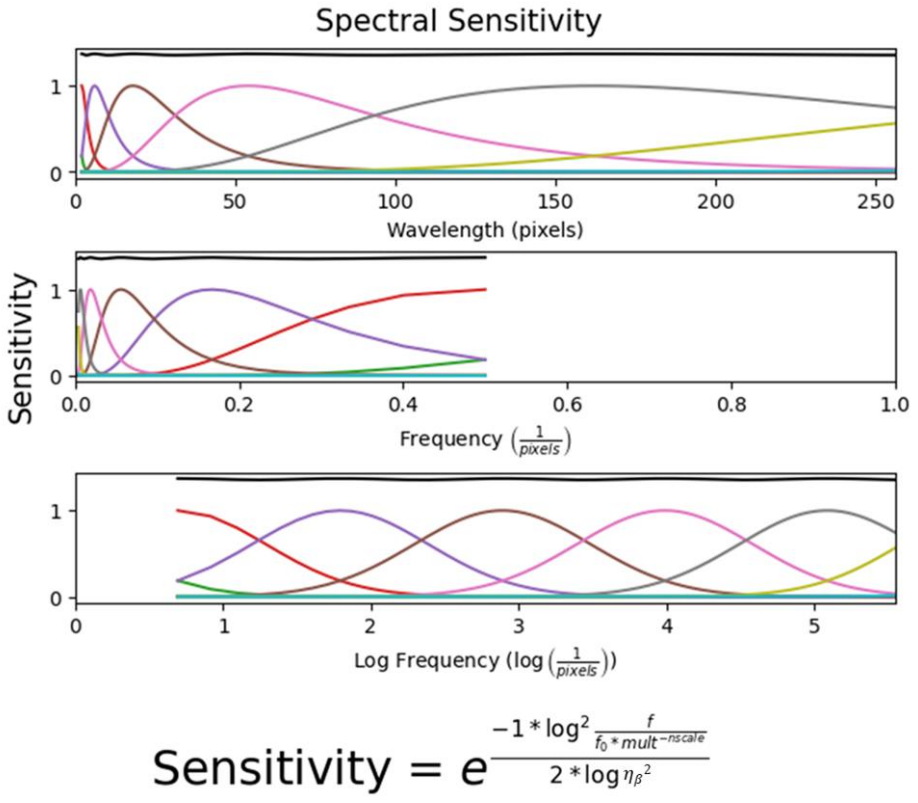

Figure 3.8: Spectral sensitivity of phase congruency. Spectral sensitivity is modulated to provide full spectral coverage with a minimum wavelength of 2 voxels (2 mm) and a maximum wavelength of 256 voxels (256 mm). A sigma value of 0.55 is used with a mult and nscale value calculated according to their respective equations.

3.2.4 Frequency spread

Phase congruency is based on a range of frequencies and therefore it would be more meaningful to favor congruency across multiple frequencies over a few frequencies. For modifying the corresponding gain and cutOff values of the penalizing sigmoid curve, the relationships between certain parameters can guide the manipulation of phase congruency parameters as follows. The width of frequency spread is influenced by the number of filter scales employed in analysis (Figure 3.9). As the number of filters increase by similarly increasing the value of η_β, the effective width of the frequency distribution decreases meaning that similar information now experiences a greater penalty. With knowledge of these relationships, the modulation of phase congruency patterns is ultimately simplified with adjustment of the cutOff having the greater impact.

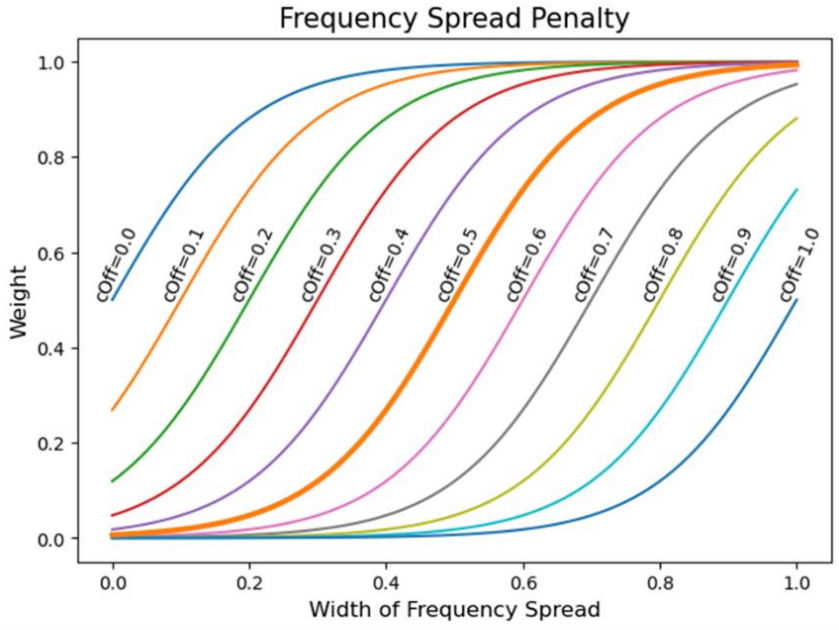

Figure 3.9: Frequency spread penalty modulation. The inflection point (cutOff) and rate of transition (gain) for the sigmoid curve determine penalties for frequency spread. The width of frequency spread is also inversely proportional to the number of filter scales required to cover the spectrum as influenced by the sigma property of applied filter scales.

3.2.5 Implementation

For this thesis, we sought a balanced sensitivity across the included frequencies and focused on analysis of three scales of feature sizes that pertain to MS lesions. To implement this, we set the spatial resolution range marked by a minimum wavelength of 2mm and maximum wavelength of 8 mm, 16 mm, and 32 mm, corresponding to minimum spatial frequencies of 0.125 mm^{-1}, 0.0625 mm^{-1}, and 0.03125 mm^{-1} and a maximum spatial frequency of 0.5 mm^{-1}. We employed a sigmaOnf of 0.55 corresponding to filter bandwidths of 2 octaves and a calculated mult value of 3.02 to equalize sensitivity to all included frequency bands. The number of filter scales was similarly calculated according to the derived equation for each minimum frequency cutOff. The calculated images were accepted so no further changes were made to the frequency spread weightings using the default gain of 10 and cutOff of 0.5. As mentioned previously, a 23-directioned gradient set was employed for analysis with an average angular separation of approximately 30°. The whole-brain phase congruency outputs of both the sum of phase congruency across all orientations and the weighted mean phase were included in the analyses as presented in Chapters 4, 5, and 6. With these settings, there would be opportunities for further experiments including increasing the value of sigma to increase the number of filter scales. This work up may improve the capacity of feature localization with more scales expected in the designated spectral regions; however it will require reduction of the frequency spread cutOff to reduce sparsity of the output. The full extent of phase congruency outputs is not analysed besides the selected parameters for the purpose of studies in this thesis, though future work may seek to understand the tradeoffs associated with such parameter modifications.

3.3 Summary

In summary, this thesis involves considerable innovations in several aspects particularly regarding brain diffusion MRI and phase congruency based on clinically-feasible data acquisitions. Advances in diffusion MRI facilitated the generation of HARDI-like metrics of enhanced sensitivity and specificity to tissue microstructure using single-shell diffusion data, as well as robust harmonization of diffusion samples obtained with unequal protocols, valuable for large sample deserving studies. Further, innovative modelling of diffusion data also enabled the creation of new diffusion MRI measures including ODF energy, and prediction of unavailable diffusion data for comprehensive HARDI analysis. Regarding phase congruency, my new development is also multifold, including the origination of novel approaches for parameter optimization, and implementation of an easy-to-use graphic user interface for improved understanding, evaluation, and application of this new technique. Intuitive parameter tuning facilitated by the implementation is important for defining feature sensitivity according to the scales required for optimal analysis of local structural properties, such as that relating to MS lesions. Combined outcomes would be invaluable for advanced analysis of the associated imaging data as seen in the follow up Chapters, and for future studies outside of this thesis.

Chapter 4: Brain diffusion MRI and texture analysis along with machine learning provide new sensitive measures of MS pathology

As mentioned in previous chapters, significant advances have been made in MS research over the past decades. Various new MRI technologies have also been developed and new imaging initiatives are emerging constantly. However, the MS community is still in need of established measures of MS pathology, which nonetheless is crucial for disease understanding, assessment, and management. To this end, based on cutting-edge image modeling and analysis techniques, I have developed several new methods to improve our disease characterization capabilities, especially pertaining to brain diffusion MRI and phase congruency-based texture analysis. The goal of this chapter is to investigate whether and how these methods detect subtle MS pathology as those related to lesions versus non-lesion areas such as NAWM, and to intra-lesion heterogeneity, assisted by a supervised machine learning method known as support vector machine. A majority of this Chapter has been published as a manuscript as mentioned in the Preface (Oladosu et al, Frontiers in Neuroscience, *Frontiers in Neuroscience 15 (May 7, 2021)*.

4.1 Introduction

Ongoing tissue damage in lesions and NAWM is believed to play a major role in the relentless progression of disability in people with MS. But the nature of tissue damage is complex, requiring measurements beyond conventional analysis (8). Diffusion brain MRI and phase congruency methods may serve as valuable opportunities to provide multi-dimensional analysis of MS pathology including that associated with critical white matter tracts (181).

Several studies using DTI have shown that the mean diffusivity (MD) and fractional anisotropy (FA) detect demyelination and axonal loss in MS, which differentiates lesions from the normal-appearing white matter (NAWM) (182). Within the lesion context, there is evidence showing increased MD in the lesion core versus perilesional white matter (183). However, there are no systemic studies of core versus periphery of lesions in MS. Further, using a single tensor model in DTI, which does not provide compartmental information, it is challenging to detect specific processes of neuronal pathology. The HARDI models such as ActiveAx and neurite orientation dispersion and density index (NODDI) that enable intra-voxel analysis of tissue microstructure may provide an opportunity to overcome these challenges (113,114). However, acquiring multi-shell HARDI data is not always practical due to time constraints, particularly in a clinical setting. An alternative approach is modeling densely sampled diffusion data (orientations ≥45) based on acquisition of only one diffusion weighting, namely, single-shell HARDI (ssHARDI) (184,185). But the utility of ssHARDI for characterizing neurite properties such as orientation requires further investigation (119,185,186).

In addition to advances in diffusion modelling, there have also been considerable improvements in tractography-based investigations in dMRI (187). Traditionally, individual white matter tracts (e.g. corticospinal tract) traced by streamlines of tractography form the mainstay for localized analysis of diffusion metrics. However, the local orientation information represented directly by the streamlines may be also critical indicators of tissue properties, including streamline counts and streamline termination frequency, providing a new dimension of microstructural measurements (135).

Texture analysis represents an alternative way of image analysis that characterizes the distribution pattern of imaging elements generated by the underlying tissue (34,136). Phase congruency provides localized spatial frequency analysis with use of a wavelet transform to identify image features (153,154). These features reflect the coherency of local frequency components and therefore characterize the spatial relationship of tissue structures in an imaged area. Building upon previous studies showing the potential of phase congruency applied to different medical imaging approaches (e.g. CT, MRI), our own pilot work demonstrates the utility of this method in differentiating MS lesions from NAWM using conventional T2-weighted brain MRI (151,158,161). Here we investigate how phase congruency works with other imaging sequences and how it characterizes different types of MS pathology. Further, given the theoretical nature of phase congruency, it may provide comparative and complementary information to diffusion MRI in tissue coherence analyses.

The purpose of this study was to test the feasibility of ssHARDI using clinically available dMRI and investigate how advanced metrics from ssHARDI and DTI tractography compare to traditional DTI measures in assessing MS pathology. Furthermore, phase congruency texture analysis is investigated in parallel to compare the three most common conventional MRI sequences in MS: T1-weighted, T2-weighted, and FLAIR scans. The investigations used a machine learning technique, support vector machine (SVM), to evaluate feature importance through several tissue classification tasks. Specifically, based on 3D regions of interest (ROIs), there were 2 classifications within individual patients: 1) lesion versus the corresponding contralateral NAWM, to obtain a basic understanding of the sensitivity of the features to MS pathology; and 2) lesion core versus shell, to evaluate the detectability of intra-lesion pathology by the features. Between

patients, there were also 2 analyses: lesion comparisons, between patients having high (top 25%) and low (bottom 25%) lesion counts as a surrogate for disease activity; and NAWM comparisons, between the same subject groups.

4.2 Materials and Methods

4.2.1 Sample

This study evaluated brain MRI scans from a convenience sample of 52 participants with relapsing-remitting multiple sclerosis (RRMS) who were screened for participation in a clinical trial of domperidone as a potential myelin repair agent (ClinicalTrials.gov Identifier: NCT02493049). Participants required at least one gadolinium-enhancing lesion on a screening brain MRI to be eligible for randomization to treatment in the clinical trial. In the present study, we utilized the screening brain MRI scans of participants who were not eligible to continue in the trial as they did not contain any enhancing lesions. In addition, all MRI pulse sequences used in this study were conducted before gadolinium use, and therefore no contrast interference. Written informed consent was obtained from all participants following study approval by the Conjoint Health Research Ethics Board of the University of Calgary.

4.2.2 Imaging protocol

All participants had brain anatomical and diffusion MRI undertaken at a 3T scanner (GE Healthcare, Discovery MR750, Milwaukee, USA). Anatomical MRI included T2-weighted (T2-w) and FLAIR images with repetition time (TR) = 6000/7000, echo time (TE) = 100/126ms, matrix = 512x512, and slice thickness = 3mm without gap; and T1-weighted images with TR/TE = 8.2/3.2ms, matrix=256x256, field of view (FOV) = 25x25cm, and slice thickness = 1mm. The

dMRI acquisition used an echo planar sequence where b=1000, 3 b0 volumes, and 45 directions; TR/TE = 8000/61ms; matrix = 120x120, with $2mm^3$ isotropic voxels; and FOV = 24x24cm.

4.2.3 3D ROI Development

To improve the analysis of contextual information, we derived 3D ROIs for all tissue regions, done initially using anatomical MRI (Fig. 1).

Lesion ROIs

Using the FSL library (Oxford, UK), all MRI volumes were skull-extracted, and the T2-w and FLAIR images were then rigid-body co-registered to T1-w images to optimize quality and alignment (188–190). Lesion segmentation focused on brain white matter, using an automatic toolbox (LST, v3.0.0, SPM12) (75). Initially, the LST generated a whole-brain lesion map per subject based on co-registered FLAIR and T1-w volumes. The lesion map then underwent manual correction using ImageJ (NIH, v1.52j) by referencing the co-registered FLAIR and T1-w images to remove areas that overlapped with cerebrospinal fluid or with the NAWM. Any area that contained a confluent lesion, showing signal inhomogeneity but with pixels staying connected, was considered a single ROI. Subsequently, lesion ROIs were colocalized across slices using the 'cluster' command in FSL with 26-connectivity to obtain 3D ROIs, which were further sorted by ROI size.

Contralateral NAWM ROIs

The NAWM ROIs were essentially the mirror image of the lesion ROIs established above. To ensure validity, we applied several quality-control steps. The first step was lesion-filling (191) in

the referencing T1-w MRI, followed by creation of a left-right flipped mirror image of the volume. The accuracy of volume flipping was ensured through a cross-correlation-based nonlinear co-registration process between the reference and mirror T1 volumes, using the 'SyN' option in the ANTs software (192), from which a left-right transformation was obtained. Applying the transformation to the generated lesion masks made the latter geometrically matched to the mirror volume of the reference T1. After left-right flipping, the transformed lesion masks became the 'raw' contralateral NAWM ROIs. The next step was refinement of the NAWM ROIs, including eliminating areas overlapping with any lesion region. This step ensured that each 3D NAWM ROI corresponded to each unique 3D lesion ROI with no contamination by tissues of the other type (see Figure 4.1).

Lesion Core and Shell ROIs

The core-shell segmentation focused on lesion ROIs with identified contralateral NAWM that were large enough to encapsulate a 3x3x3 cube of voxels. Specifically, defining a lesion core ROI used a 3D volumetric erosion process applied to an eligible lesion mask, which allowed to retain only the central voxels not in contact with any non-lesion background area. Then, subtracting the core from the full lesion ROI produced the single-voxel-thick shell ROI for each lesion.

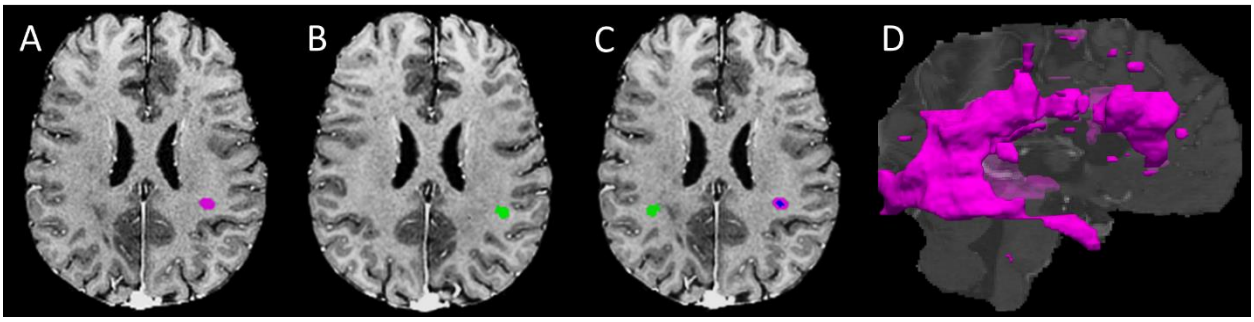

Figure 4.1: Regions of interest development. (A) An example lesion region of interest (ROI) in the T1- FLAIR MRI space (purple mask); (B) A mirror-image of the T1-weighted MRI for developing the contralateral normal appearing white matter (NAWM) ROI (green mask) of the lesion shown in panel A; (C) the finalized contralateral NAWM ROI of the lesion produced using (panel A,B), along with converse co-registration between the corresponding image volumes; the blue and purple areas within the lesion represents the core and shell ROIs, respectively; and (D) 3D whole brain lesion masks produced by grouping adjacent ROI voxels within and between slices.

4.2.4 dMRI Analysis

Pre-processing and DTI Analysis

The dMRI data first underwent eddy current correction (193). To limit variations, we averaged the 3 b0 volumes and then co-registered the mean volume to the T1-w structural space. The resulting mean b0 volume acted as a reference in transforming all calculated diffusion maps to the same T1-w space prior to quantitative evaluations. DTI calculation used the FDT procedure in FSL, which provided 4 classical outcomes: MD, FA, axial diffusivity (AD), and radial diffusivity (RD).

ssHARDI Analysis

Given the relatively high angular nature of our dMRI acquisitions, we also explored ssHARDI modeling. In particular, to improve computing efficiency, we used a new modeling method: Accelerated Microstructure Imaging via Convex Optimization (AMICO), which generated equivalent measures to ActiveAx and NODDI (121). Our AMICO outcomes included axonal diameter, axonal density, and intracellular volume fraction (ICVF) from ActiveAx, and orientation

dispersion index (ODI) from NODDI (113,114). In addition, to further probe intravoxel orientation information beyond ODI, we calculated the orientation distribution function (ODF) of diffusion (100). This in turn enabled us to generate a new parameter termed ODF energy (Fig. 2), which referred to the energy of diffusion oriented at individual directions. The energy was calculated as $log(p^2)$, where p represented a collection of probabilities of diffusion magnitude observed at all possible directions. The probabilities were obtained by fitting the diffusion magnitude values from each direction to a normal distribution.

In addition, to test the feasibility of using AMICO to evaluate ssHARDI, we performed an additional experiment to compare outcomes from different datasets. This included: 1) single-shell, 2-shell, and 3-shell HARDI data freely available online from the Human Connectome Project (HCP) (194); and 2) single-shell data from our own study. The comparisons were done both visually and quantitatively with a concentration on 3 ssHARDI measures out of AMICO ActiveAx: axonal diameter, axonal density, and ICVF. NODDI ODI had been shown to be similar between calculations of single- and multi-shell data (113). In quantitative assessment, we computed the variance of the aforementioned measures at a regional level in 10 example white matter structures bihemispherically: forceps minor, forceps major, genu and splenium of the corpus callosum, and posterior limb of the internal capsule. Each ROI was sized 4x4 pixels, which was the maximal uniform dimension that could be fitted within these structures. Statistical analyses were conducted using one-way ANOVA followed by correction for multiple comparisons where applicable.

DTI Tractography Analysis

We performed tractography based on DTI eigenvectors using a Diffusion Toolkit (MGH GCRC, USA) (195), which applied a deterministic algorithm, fiber assignment by continuous tracking (FACT) (195). Streamline propagation followed a 35° angular threshold as recommended.

Using the rigid-body transformation matrix derived above from FSL, we also aligned the tractography to the T1-w structural space. Based on the TrackVis method (v0.6.1) (195), we evaluated 2 main tractography measures (Figure 4.2): streamline density index (FDi) and streamline endpoint index (FTi), indicating the counts of streamlines passing through or terminating in each voxel, respectively. Our in-house experiment showed that tractography features based on DTI were similar to ssHARDI, so we focused on DTI only here.

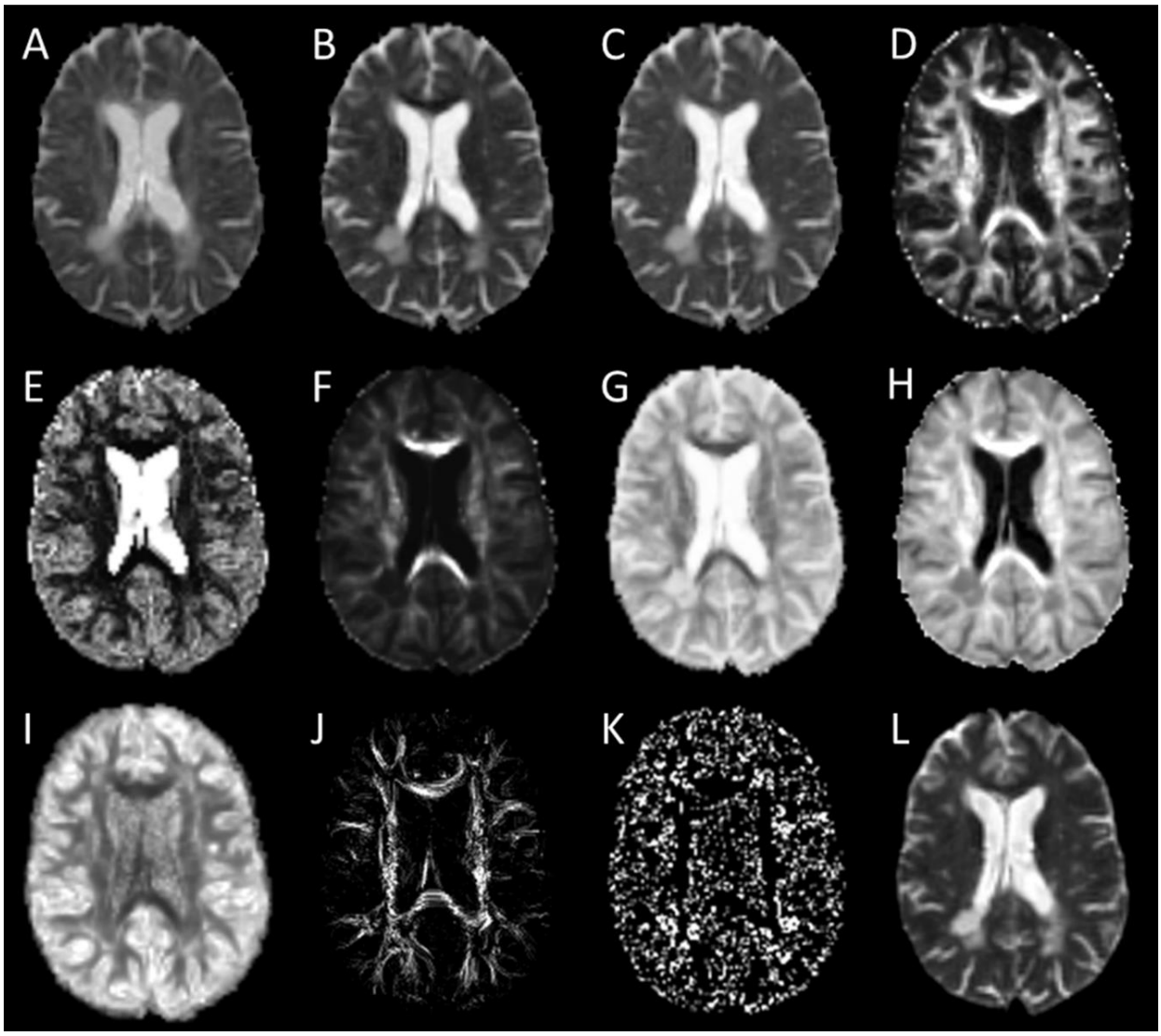

Figure 4.2: Sample diffusion metrics based on DTI, ssHARDI, and DTI tractography models. Shown are measures from DTI: (A) axial diffusivity, (B) radial diffusivity, (C) mean diffusivity, and (D) fractional anisotropy; ssHARDI: (E) orientation dispersion index, (F) density, (G) diameter, (H) intracellular volume fraction, and (I) orientation distribution function (ODF) energy; and DTI tractography: (J) fiber density index and (K) fiber termination index. Shown in (L) is an example b0 image from DTI for reference.

4.2.5 Phase Congruency Analysis

Texture analysis with phase congruency focused on T1-w, T2-w, and FLAIR MRI commonly used in the clinical imaging of MS. These images were preprocessed with a contrast-limited adaptive histogram equalization approach to enhance local feature characterization. In addition, to optimize

the detection of local features associated with lesions, maximum wavelengths of phase congruency were set at scales similar to the most common lesions sizes seen in MS, including 8, 16, and 32mm in diameter. Accordingly, each WMP and PC calculations had three feature scales. This resulted in 18 phase congruency measures (3 MRI sequences X 2 parameters X 3 scales per parameter) in total (Figure 4.3).

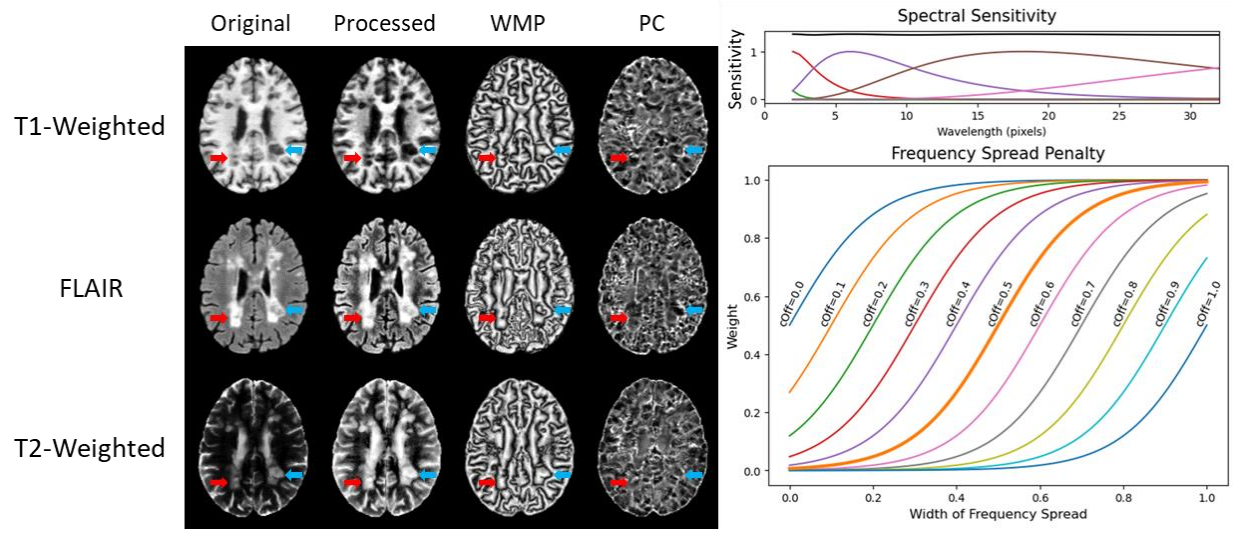

Figure 4.3: Example phase congruency outcomes using conventional brain MRI with a 32 mm maximum wavelength. Shown are the equal sensitivity (black line) of the analysis to features at different frequencies (bottom right, top panel) and assigned penalties for different frequency spreads with a 0.5 cut-off and a gain of 10 (bold orange) (bottom right. Bottom panel). Two lesions (red and blue arrows) are shown to vary in presentation across the phase congruency (PC) and weighted mean phase (WMP) outcomes.

4.2.6 SVM Analysis

In feature ranking, we split the whole dataset randomly into 10 folds (portions), using 9 folds at a time, and repeated 10 times. In classifications, 10-fold cross-validation was performed, with 9 folds for training, and the 10^{th} held-out fold for testing, in each iteration. As a standard practice, we also normalized all feature outcomes to the range 0-1.

We applied a linear SVM to rank the diffusion features through recursive feature elimination (SVM -RFE) (165), with the regularization term fixed to 1 for optimal model generalization. The squared weights of each attribute of the SVM served as the ranking criteria such that a feature with the smallest weight ranked the lowest. The average ranking of a feature from all model constructions (100 in total) represented the final ranking of the feature.

To assess the contribution of each feature to model classifications, we developed another linear SVM with iterative construction (SVM-IC), achieved by adding features to the model one-by-one from the highest to the lowest rankings. With each feature added, the model is reconstructed through 10-fold cross validation. This provided data to build the rank aggregated receiver operating characteristic (ROC) curves for each combination of successively-ranked features, and compute evaluation metrics including the area under the ROC (AUROC) and accuracy, averaged from all tests.

4.2.7 Participant Stratification

To explore how the imaging features relate to disease severity, we also did subgroup analyses. Disease severity was represented by lesion burden based on lesion counts following the LST segmentation. Participants were ranked in percentiles by their respective lesion numbers. To maximize the likelihood of detecting potential imaging feature differences, our analysis focused on 2 groups that had the most possible differences in lesion number: one with the most lesions ($\geq$35) that ranked above the 75%^{ile}, and the other with the least lesions ($\leq$15) that ranked below the

25%^{ile}. Group comparisons were done for both the lesion (whole lesion ROIs) and NAWM regions, using similar SVM strategies as described above for feature ranking and tissue classification.

4.2.8 Statistical Analysis

Assessment of all outcomes used the Scikit-Learn package in Python (v0.22.1) and R (v3.6.3). Comparing model performance used the McNemar's test (196) for accuracy, and DeLong's test (197) for AUROC, including model against chance, and between models successively generated.

4.3 Results

4.3.1 Sample Characteristics

Of the 52 participants, the age range was 18 – 60 years, Expanded Disability Status Scale was 0 – 5.5; 36 were women. In total, we identified 2139 lesion ROIs, 4 to 169 per subject; 1560/2139 lesions had matching contralateral NAWM ROIs, 1 to 119 per subject. Among the 1560 lesions, 243 had core-shell analysis (Table 4.1). In addition, 13 participants had ≥35 lesions, totaling 818 lesions, and 12 participants had ≤15 lesions, totaling 119 lesions. Similarly, there were 818 and 119 matching contralateral NAWM ROIs in each patient group respectively. Further, example outcomes from ssHARDI modeling appeared similar to that from multi-shell data, including the measures from our own diffusion scans (Figure 4.4). Quantitatively, there were no significant differences in variance for diameter, density, or ICVF ($p=0.75$, 0.18, and 0.11, respectively) between the different shell calculations using HCP data or data from our own study (Table 4.2). Further exploration using paired Student's t-tests showed that there were also no significant differences ($p>0.05$) between the 1-shell measures from HCP and our diffusion data in variance of

any of the assessed variables following ssHARDI modeling. In total, there were 11 features calculated from all diffusion models.

Table 4.1: Lesion counts and volumes by analyzed tissue class.

Lesion ROIs	**Number**	**Lesion Volume (mm^3)**			
		Mean	Standard Error	Min	Max
All	2139	256.21	25.65	3.81	16443.64
NAWM-paired	1560	45.41	1.86	3.81	929.88
Core-shell	243	158.14	8.34	35.29	929.88
Shell	--	144.89	6.93	34.33	735.35
Core	--	13.25	1.79	0.95	243.20

Note: ROI: regions of interest; NAWM: normal appearing white matter.

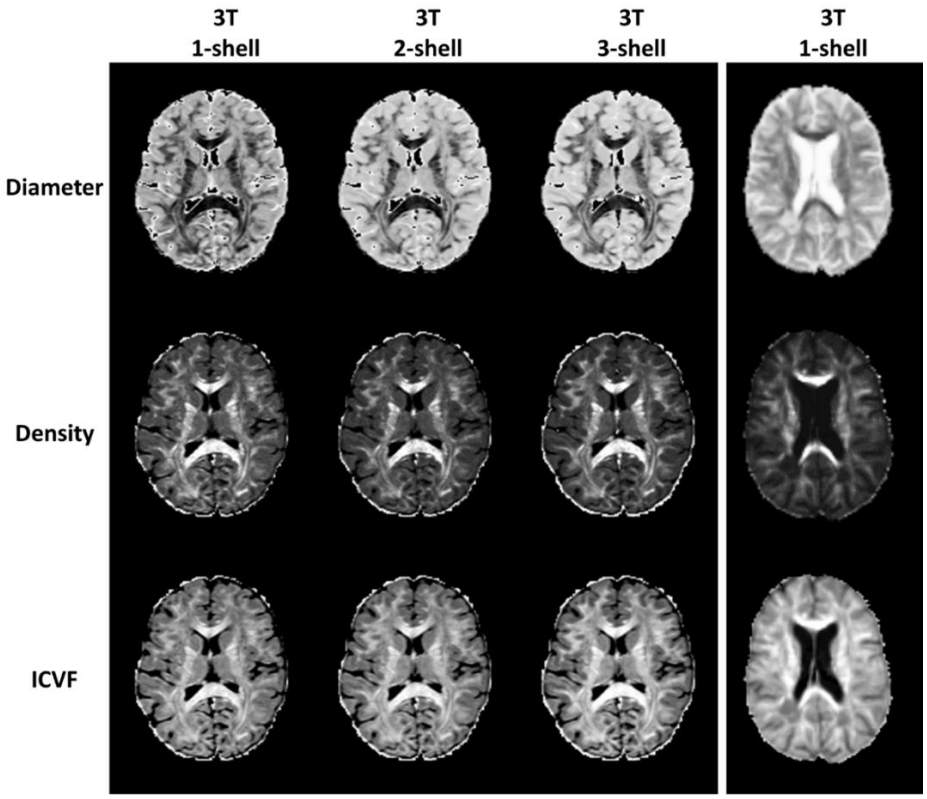

Figure 4.4: Outcome comparison between single-shell and multi-shell acquisitions. Shown are sample HARDI outcomes based on the ActiveAx model implemented in AMICO using the online Human Connectome Project data (left columns): b=1000 s/mm^2, b=1000 and 2000 s/mm^2, and b=1000, 2000, and 3000 s/mm^2 for the 1-, 2-, and 3-shell, respectively; and using our own diffusion data in this study based on ssHARDI (right column), with b=1000 s/mm^2. All represent in vivo datasets.

Table 4.2: Comparison of variances between measures from different shells and datasets.

	HCP1	HCP2	HCP3	In-house	ANOVA p-value	ssHARDI p-value
Diameter	1.416713	1.313007	1.449823	0.939283	0.749132	0.131976
Density	3.62E-06	2.94E-06	3.69E-06	8.1E-06	0.175857	0.192801
ICVF	0.006766	0.006788	0.006341	0.001743	0.114337	0.050831

Note: HCP1-3: Human connectome project data from 1-3 shell acquisitions; In-house: our own '1-shell' diffusion data; ssHARDI p-value: Student's t-tests for variances between HCP1 and In-house data.

4.3.2 Lesion-NAWM analysis

Outcomes based on brain diffusion MRI

Tissue alignment metrics ranked higher than magnitude metrics. Specifically, the top 3 rankings were: HARDI ODF energy, DTI FA, and HARDI ODI (Figure 4.5). Tractography FDi (4^{th}), DTI AD (5^{th}), and tractography FTi (6^{th}) all ranked within the top half of the 11 features, relatively higher than the other DTI and ssHARDI features.

Further assessments using the classification model revealed similar trends. Essentially, combining all top 3 features (ODF energy, FA, and ODI) in the SVM-IC model achieved a 0.65 accuracy and 0.71 AUROC (Figure 4.6 & Figure 4.7). McNemar tests showed that model accuracy with ODF energy alone significantly outperformed chance ($p<2.2e-16$) and improved further with addition of FA ($p<2.2e-16$). ROC analysis mirrored these results. The AUROC was significantly better using ODF energy alone ($p=2.95e-6$) than chance and improved with FA ($p <2.2e-16$). Further, the AUROC peaked at 0.71 with both ODI and FDi added but did not change significantly with further inclusion of the remaining features. Model accuracy peaked at 0.66 with all but the lowest-ranked feature (DTI RD) included.

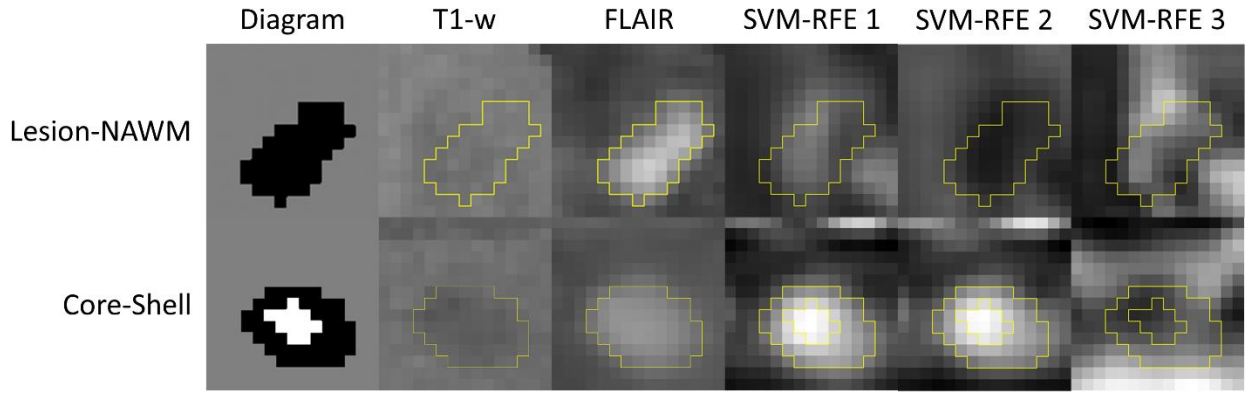

Figure 4.5: Example lesion regions and top diffusion metrics identified in the tissue separation processes. Shown are diagrams for a whole lesion (black, top) and a core-shell lesion (white and black, bottom) used for the lesion versus NAWM and core versus shell classifications, as well as corresponding appearances in the T1-weighted and FLAIR MRI (columns 1–3). The other columns (4–6) demonstrate the top three diffusion features selected by the recursive feature elimination algorithm (SVM-RFE) in respective classification tasks, which are orientation distribution function energy, fractional anisotropy, and orientation dispersion index (top); and mean diffusivity, radial diffusivity, and fractional anisotropy (bottom).

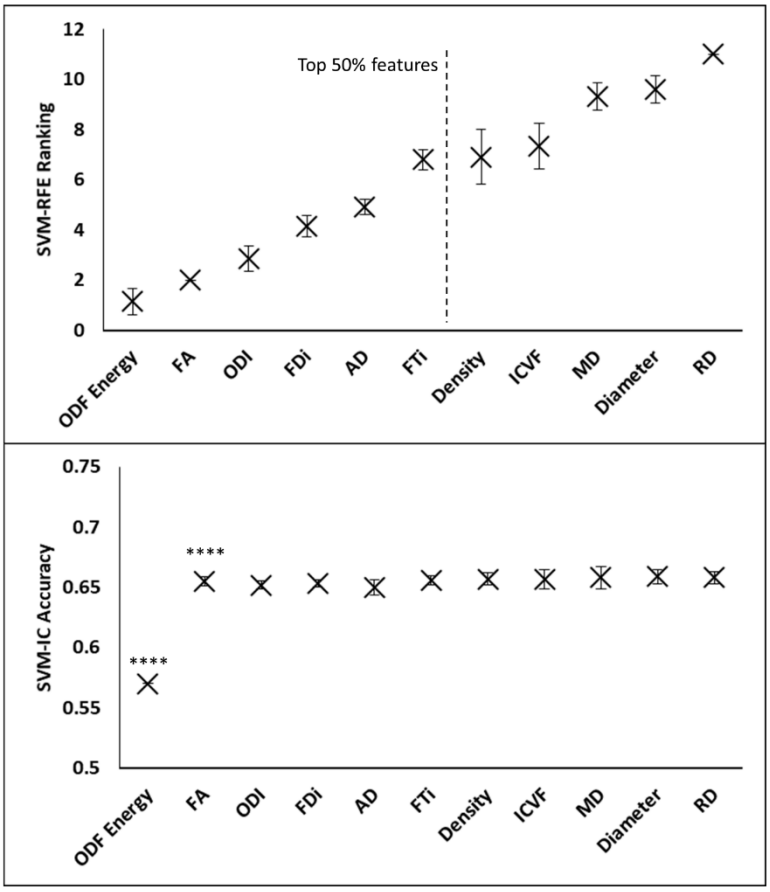

Figure 4.6: Feature ranks and classification accuracy in lesion-NAWM analysis. Top panel: The mean (standard deviation) rankings of the 11 diffusion features based on the linear recursive feature elimination (RFE) algorithm in SVM. Bottom panel: Accuracy of the classification models (SVM-IC) obtained by adding features one at a time, starting from the highest to the lowest rankings. The stars indicate features that contribute to significant improvement in classification accuracy (****$p < 0.0001$).

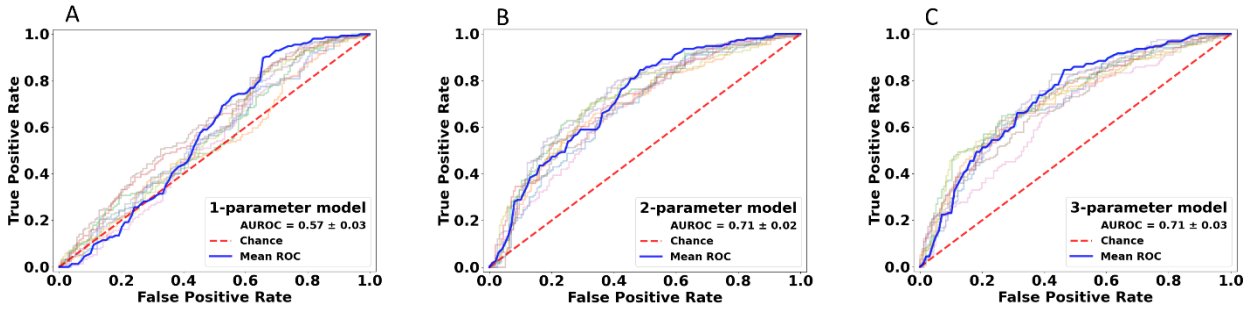

Figure 4.7: Performance comparison of the classification models in lesion versus NAWM analysis. Shown are the ROC curves for models constructed from the top three ranked diffusion features: A) orientation distribution function (ODF) energy alone, B) ODF energy + fractional anisotropy (FA), and C) ODF energy + FA + orientation dispersion index. ROC: receiver operating characteristics; AUROC: area under the ROC curve.

Outcomes based on Phase *Congruency*

Feature ranking for phase congruency models showed the competency of texture features based on FLAIR MRI. The associated features occupied 4 of the top 5 ranking positions (except position #4). All of the 4 FLAIR phase congruency features were WMP, and both the top 2 features were based on 16 mm and 32 mm maximum wavelengths (Figure 4.8).

Classification analysis showed that the top 5 features contributed largely to model performance. The highest ranked feature, WMP16_FLAIR, alone led to a 0.78 accuracy significantly better than chance ($p<2.2e-16$), and an 0.833 AUROC ($p<2.2e-16$). The addition of the 2nd through 4th features resulted in an increased accuracy of 0.88. Further, the top 12 features collectively contributed to a peak accuracy of 0.90, which was not significantly better than the single feature model with WMP16_FLAIR ($p>0.05$). In comparison, the top 13 features formed a model with an AUROC of 0.89 that was significantly better than the single feature model ($p=5.48e-10$; Figure 4.9).

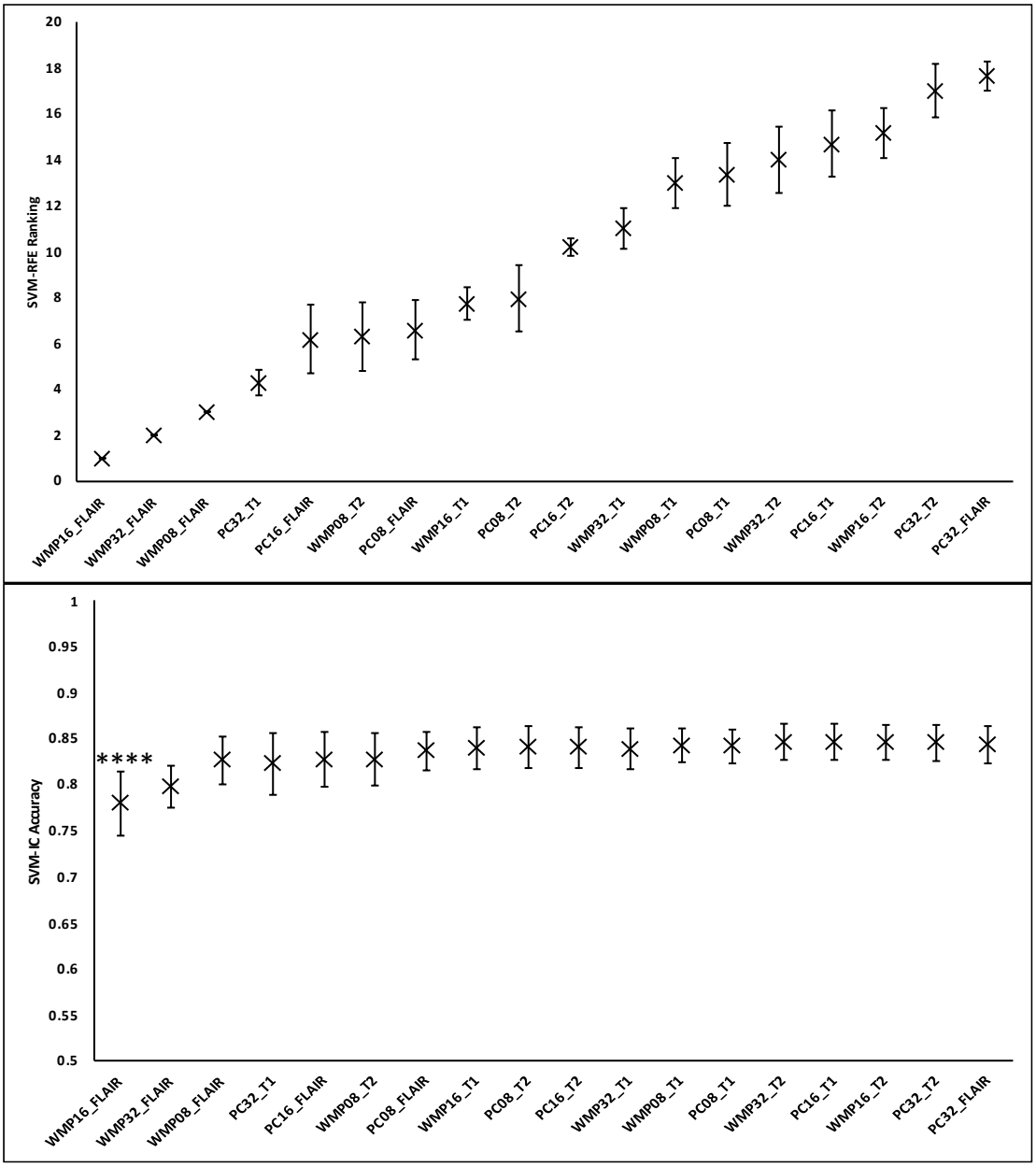

Figure 4.8: Feature ranks and classification accuracies in lesion-NAWM analysis. Top Panel: The mean (standard deviation) rankings of the 18 texture features used in this analysis based on the linear recursive feature elimination (RFE) algorithm in SVM. Bottom Panel: Accuracy of the classification models (SVM-IC) achieved by adding features one at a time, starting from the highest to the lowest rankings. The stars indicate features that contribute to significant improvement in classification accuracy (****$p<0.0001$).

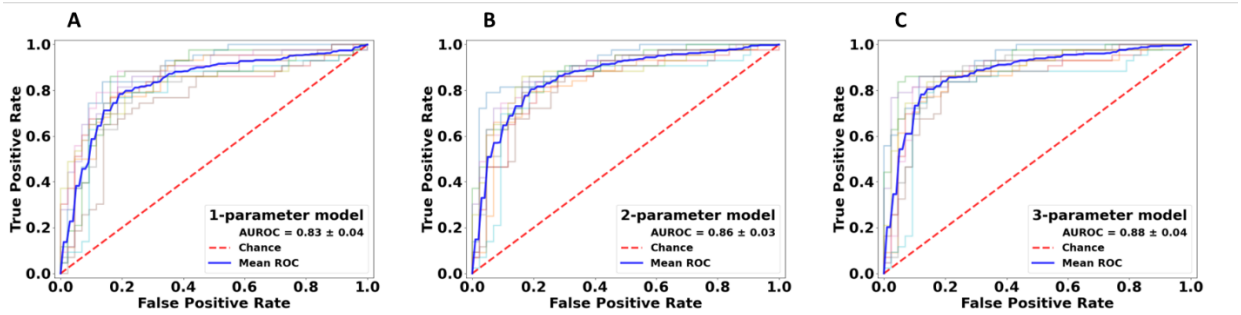

Figure 4.9: Performance comparison of the classification models in the lesion-NAWM analysis. Shown are the ROC curves for models constructed from the top three ranked texture features: A) FLAIR weighted mean phase with a 16 mm maximum wavelength (WMP16_FLAIR) alone, B) WMP16_FLAIR + FLAIR weighted mean phase with a 32 mm maximum wavelength (WMP32_FLAIR), and C) WMP16_FLAIR + WMP32_FLAIR + FLAIR WMP with an 8 mm maximum wavelength (WMP08_FLAIR). ROC: receiver operating characteristics; AUROC: area under the ROC curve.

4.3.3 Core-Shell analysis

Outcomes based on Brain Diffusion MRI

Feature ranking in this assessment used 9 of the 11 diffusion features, with tractography FDi and FTi excluded due to their sparse representation in relatively small ROIs. The top 3 ranked metrics were: DTI MD, RD, and FA. HARDI ODF energy and DTI AD followed in ranking, slightly better than the other HARDI measures, which ranked at 6th-9th (ICVF, Density, ODI, and Diameter).

Classification analysis further revealed the importance of top-ranked metrics in core-shell analysis. The highest-ranked feature, MD, alone accounted for a classification accuracy of 0.59, significantly greater than chance (p=4.98e-5; Figure 4.10). Adding features up to the 5th one (AD), the classification accuracy peaked, at 0.60 (p=3.86e-6). In addition, the model with MD alone achieved an AUROC of 0.59, which improved to the peak at 0.60 when combining with the top 2nd to 4th features (RD, FA, ODF energy), but the AUROC values were not significantly different from chance (p=0.088; Figure 4.11).

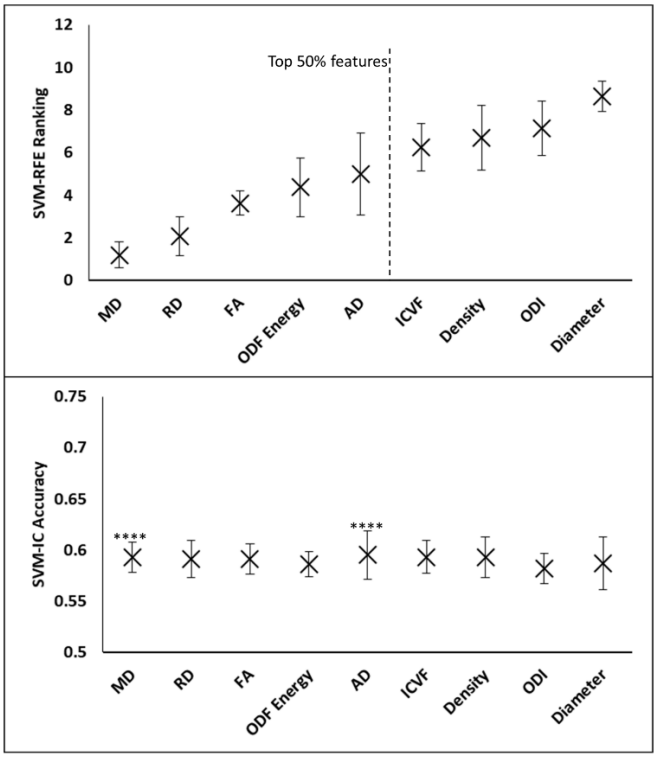

Figure 4.10: Feature ranks and classification accuracies in lesion core-shell analysis. Top Panel: The mean (standard deviation) rankings of the 9 diffusion features used in this analysis based on the linear recursive feature elimination (RFE) algorithm in SVM. Bottom Panel: Accuracy of the classification models (SVM-IC) achieved by adding features one at a time, starting from the highest to the lowest rankings. The stars indicate features that contribute to significant improvement in classification accuracy (****p<0.0001).

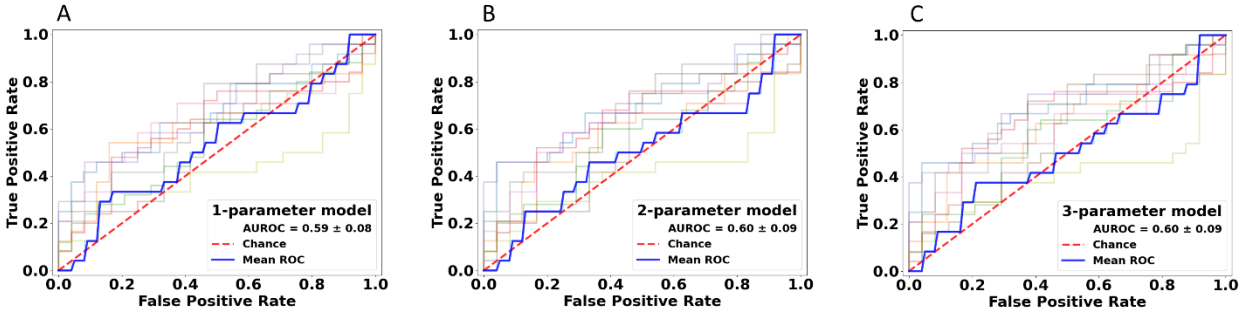

Figure 4.11: Performance comparison of the classification models in the lesion core versus shell analysis. Shown are the ROC curves for models constructed from the top three ranked diffusion features: A) mean diffusivity (MD) alone, B) MD + radial diffusivity (RD), and C) MD + RD + fractional anisotropy. ROC: receiver operating characteristics; AUROC: area under the ROC curve.

Outcomes based on Phase Congruency

In contrast to lesion-NAWM analysis models, the top-ranked phase congruency features were similarly distributed among the three conventional MRI sequences. Specifically, among the top 6 positions, two were based on FLAIR (1^{st} & 4^{th}), two on T2-w MRI (2^{nd} & 3^{rd}), and two on T1-w MRI (5^{th} & 6^{th}). Five of these (except the 4^{th}) were WMP features, where two of the top three features were calculated with a 32 mm maximum wavelength, three with a 16 mm and 1 (one) with an 8 mm maximum wavelength respectively (Figure 4.12).

Classification analysis again demonstrated the importance of top-ranking metrics listed above. In core-shell analysis, the highest-ranked feature, WMP32_FLAIR, achieved an accuracy of 0.74 significantly better than chance (p=5.24e-11; Figure 4.13). The top 9 features contributed to peak performance with an accuracy of 0.85, and the top 13 features led to a peak AUROC of 0.88 (p=2.75e-8), both better than chance.

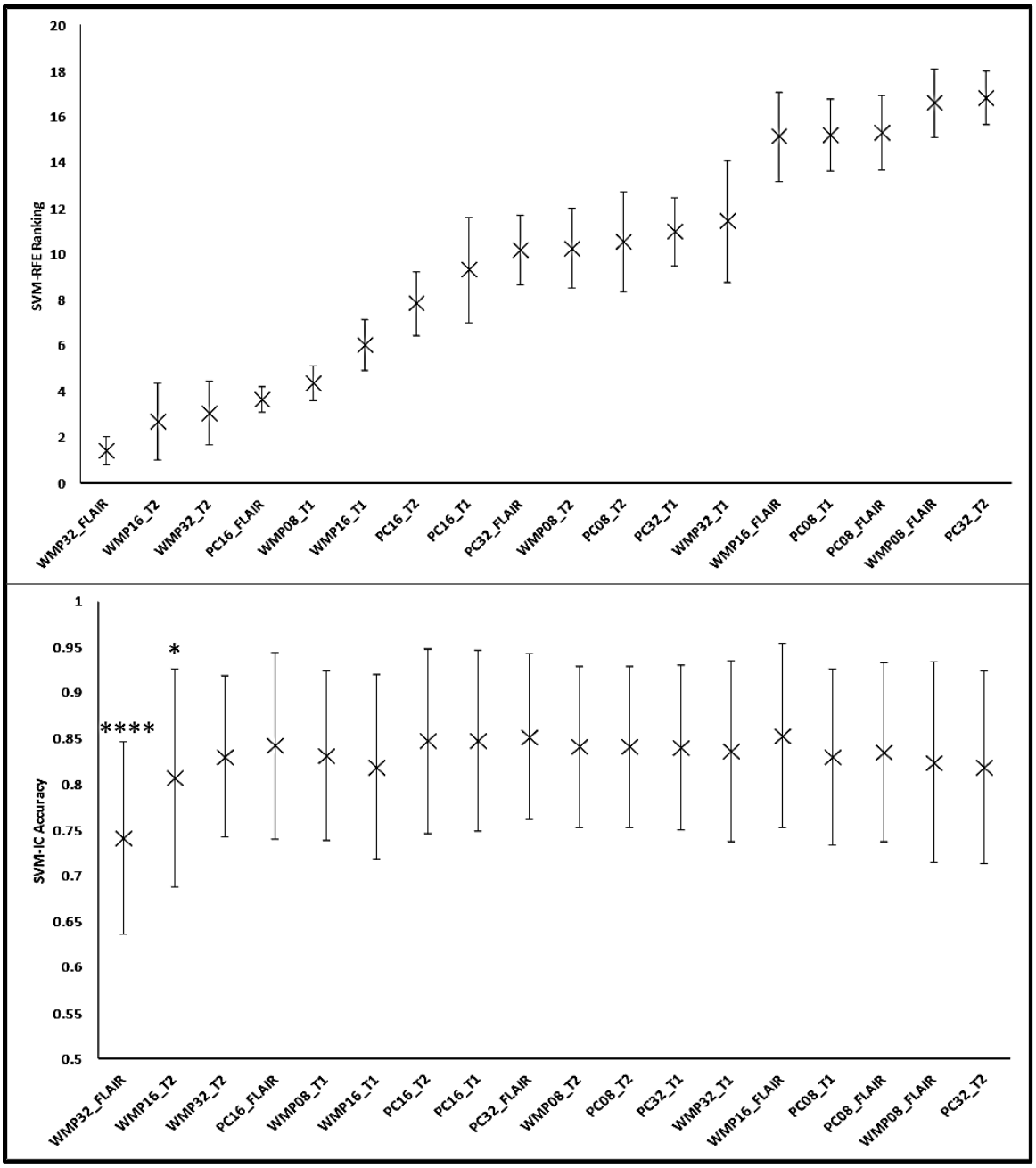

Figure 4.12: Feature ranks and classification accuracies in lesion core-shell analysis. Top Panel: The mean (standard deviation) rankings of the 18 diffusion features used in this analysis based on the linear recursive feature elimination (RFE) algorithm in SVM. Bottom Panel: Accuracy of the classification models (SVM-IC) achieved by adding features one at a time, starting from the highest to the lowest rankings. The stars indicate features that contribute to significant improvement in classification accuracy (*$p<0.05$, ****$p<0.0001$).

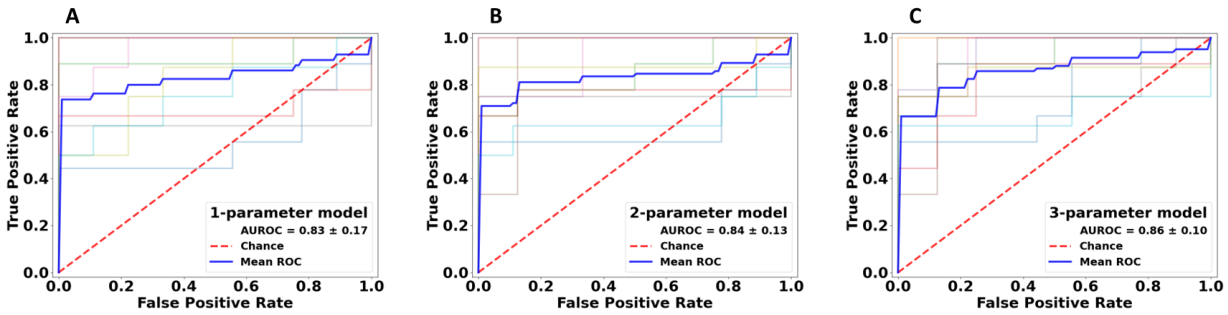

Figure 4.13: Performance comparison of the classification models in the lesion core versus shell analysis. Shown are the ROC curves for models constructed from the top three ranked texture features: A) FLAIR weighted mean phase with a 32 mm maximum wavelength (WMP32_FLAIR) alone, B) WMP32_FLAIR + T2-w weighted mean phase with a 16 mm maximum wavelength (WMP16_T2), and C) WMP32_FLAIR + WMP16_T2 + T2-w WMP with a 32 mm maximum wavelength (WMP32_T2). ROC: receiver operating characteristics; AUROC: area under the ROC curve.

Table 4.3: The AUROC of the linear SVM diffusion classification models.

Lesion vs NAWM			Core vs Shell		
Features	AUROC	Standard Deviation	Features	AUROC	Standard Deviation
ODF energy	0.568	0.030	MD	0.594	0.080
FA	0.707	0.023	RD	0.597	0.088
ODI	0.710	0.026	FA	0.598	0.092
FDi	0.713	0.026	ODF energy	0.600	0.083
AD	0.710	0.029	AD	0.594	0.081
FTi	0.711	0.028	ICVF	0.595	0.081
Density	0.710	0.028	Density	0.598	0.082
ICVF	0.711	0.028	ODI	0.595	0.086
MD	0.710	0.028	Diameter	0.593	0.086
Diameter	0.710	0.028			
RD	0.710	0.028			

Note: AUROC— area under the receiver operating characteristic curve.

Table 4.4: The AUROC of the linear SVM texture classification models.

Features	Lesion vs NAWM		Features	Core vs Shell	
	AUROC	Standard Deviation		AUROC	Standard Deviation
WMP16_FLAIR	0.833	0.037	WMP32_FLAIR	0.835	0.167
WMP32_FLAIR	0.861	0.031	WMP16_T2	0.835	0.135
WMP08_FLAIR	0.879	0.036	WMP32_T2	0.860	0.104
PC32_T1	0.882	0.035	PC16_FLAIR	0.880	0.110
PC16_FLAIR	0.887	0.035	WMP08_T1	0.869	0.112
WMP08_T2	0.891	0.032	WMP16_T1	0.857	0.124
PC08_FLAIR	0.892	0.034	PC16_T2	0.861	0.127
WMP16_T1	0.894	0.033	PC16_T1	0.867	0.125
PC08_T2	0.900	0.033	PC32_FLAIR	0.871	0.121
PC16_T2	0.900	0.032	WMP08_T2	0.875	0.126
WMP32_T1	0.901	0.028	PC08_T2	0.875	0.126
WMP08_T1	0.905	0.028	PC32_T1	0.874	0.121
PC08_T1	0.904	0.028	WMP32_T1	0.879	0.130
WMP32_T2	0.903	0.028	WMP16_FLAIR	0.879	0.129
PC16_T1	0.904	0.027	PC08_T1	0.878	0.122
WMP16_T2	0.904	0.027	PC08_FLAIR	0.877	0.118
PC32_T2	0.903	0.027	WMP08_FLAIR	0.879	0.119
PC32_FLAIR	0.902	0.027	PC32_T2	0.867	0.117

Note: AUROC— area under the receiver operating characteristic curve.

4.3.4 Lesions and NAWM analyses between subjects

These analyses used all of the 11 diffusion features as applied in assessing whole lesion pathology. In comparing the lesion tissue between subjects who had 75%^{ile} high versus 25%^{ile} low lesion load, FA ranked the highest, which alone had an accuracy of 0.589 and AUROC of 0.620. Combining FA with the 2nd-4th features, AD, ICVF, and Diameter, slightly increased the accuracy, which reached the peak at 0.605; further addition of FTi as the 5th feature led to the peak AUROC of 0.638, but no models performed significantly better than chance (p=0.200) in this analysis. In contrast, ODF energy ranked the best in classifying the matching NAWM regions between the same patient groups. Specifically, ODF energy alone achieved a near-peak accuracy of 0.616 and AUROC of 0.662, considerably better than chance (p=0.020). Adding the second-best parameter,

neurite density, achieved the peak values for accuracy at 0.617 and for AUROC at 0.662, almost identical to the ODF energy alone results. There was no further improvement with addition of any other parameters (Figure 4.14 & Figure 4.15).

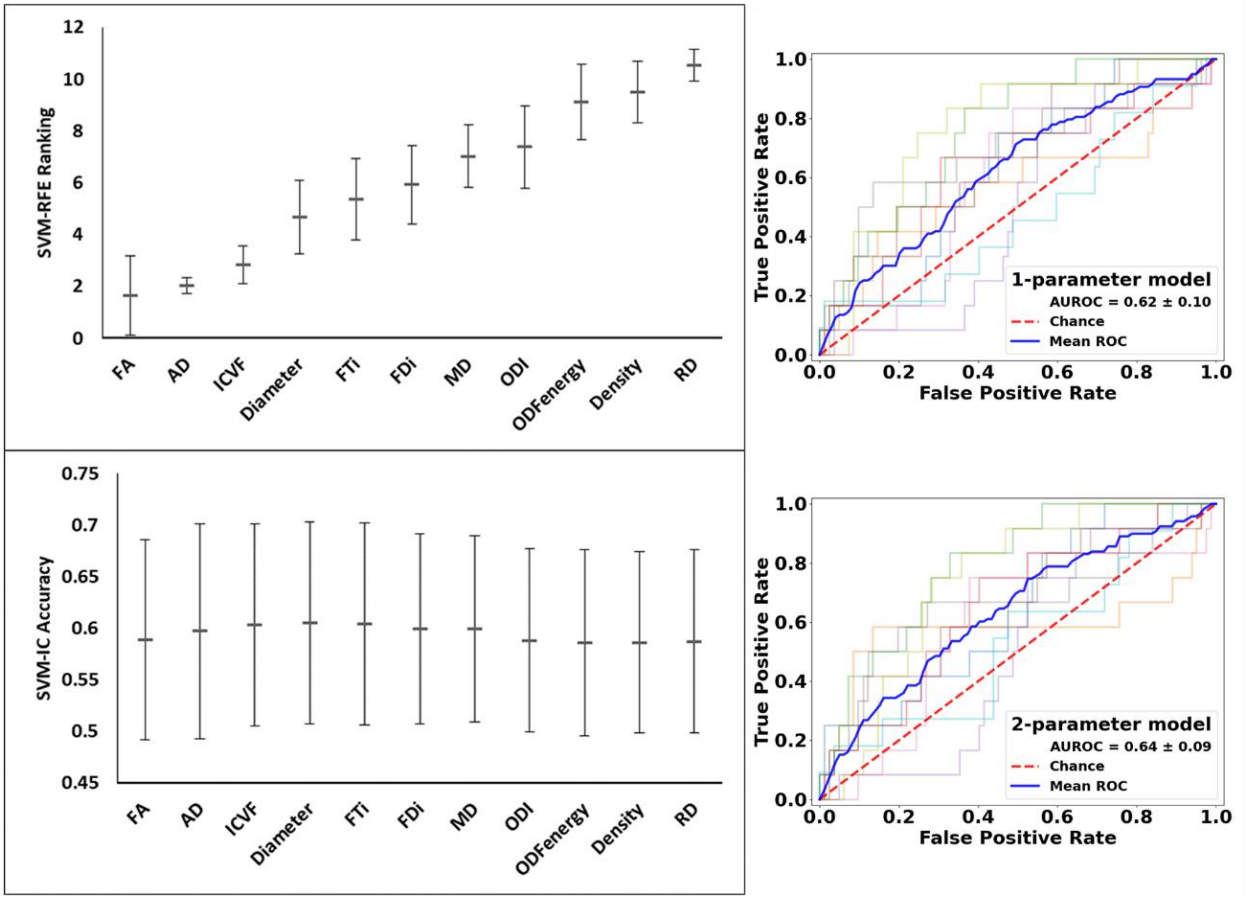

Figure 4.14: Feature ranks and performance comparison in the classification of lesion tissue between high and low disease patients. Top Left Panel: The mean (standard deviation) rankings of the 11 diffusion features used in this analysis based on the linear recursive feature elimination (RFE) algorithm in SVM. Bottom Left Panel: Accuracy of the classification models (SVM-IC) achieved by adding features one at a time, starting from the highest to the lowest rankings. Right Panel: ROC curves for models constructed using the top two ranked diffusion features: top) fractional anisotropy (FA) alone, and bottom) FA + axial diffusivity (AD). ROC: receiver operating characteristics; AUROC: area under the ROC curve.

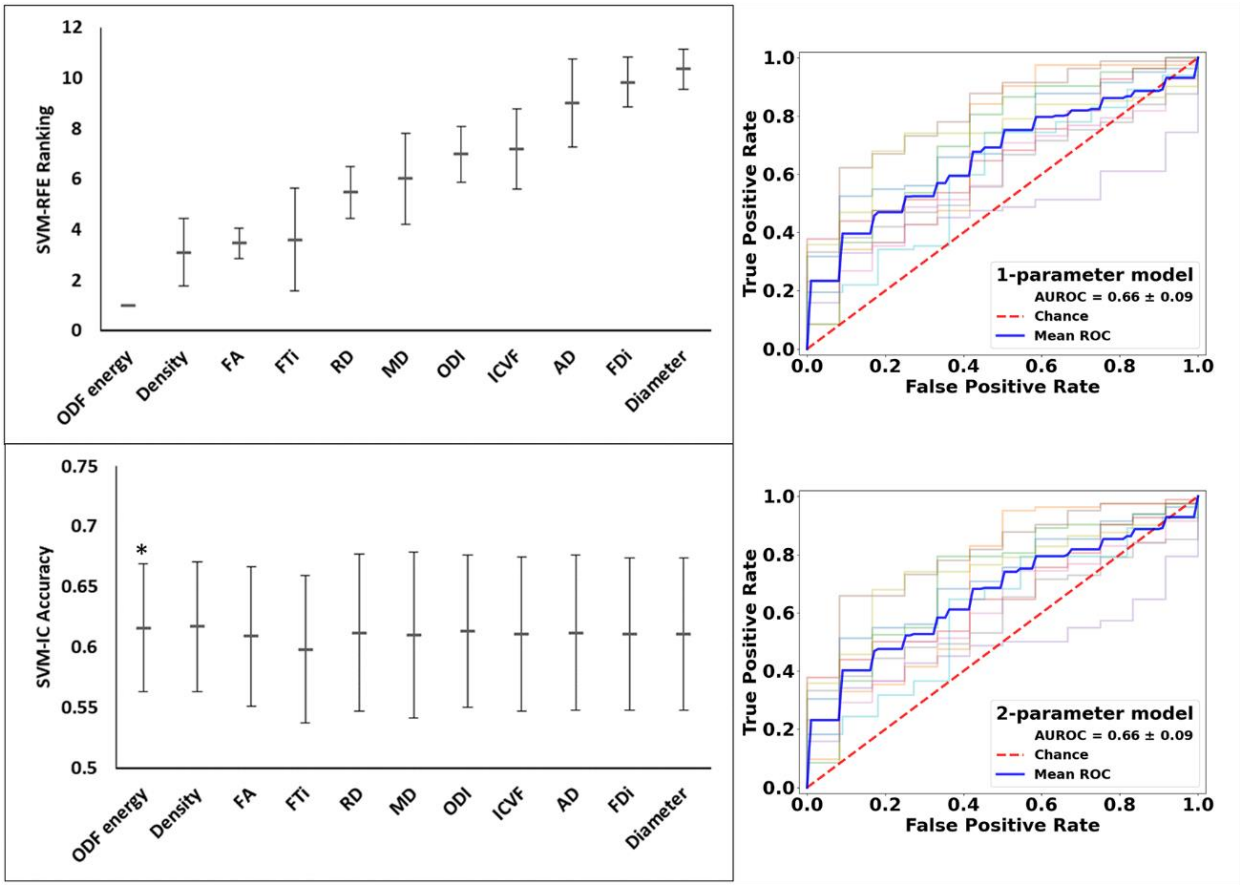

Figure 4.15: Feature ranks and performance comparison in the classification of NAWM tissue between high and low disease patients. Top Left Panel: The mean (standard deviation) rankings of the 11 diffusion features used in this analysis based on the linear recursive feature elimination (RFE) algorithm in SVM. Bottom Left Panel: Accuracy of the classification models (SVM-IC) achieved by adding features one at a time, starting from the highest to the lowest rankings. Right Panel: ROC curves for models constructed using the top two ranked diffusion features: top) orientation distribution function (ODF) energy alone, and bottom) ODF energy + Density (AD). ROC: receiver operating characteristics; AUROC: area under the ROC curve. The stars indicate features that contribute to significant improvement in classification accuracy (*p<0.05).

Similar to the above analyses using brain diffusion MRI, phase congruency-based models were also implemented to compare individuals who had 75%^{ile} high versus 25%^{ile} low lesion load. According to lesion-based outcomes (Figure 4.16), the T2-w PC feature at 32 mm maximum wavelength (PC32_T2) ranked the highest and this measure alone had a 0.593 accuracy ($p<0.0001$) and 0.624 AUROC ($p>0.05$). Accuracy peaked at 0.618 with 6 features and AUROC peaked at

0.677 with 7 features. According to NAWM-based outcomes from the two groups of high and low lesion load (Figure 4.17), the top-ranked feature was PC08_T1 that showed an accuracy of 0.61 (p=6.99e-4) better than chance and an AUROC of 0.64 (p=8.64e-3). In fact, both the top 2 features were calculated using an 8 mm maximum wavelength, with the second one being PC08_T2. A peak accuracy of 0.64 was achieved with 8 features and a peak AUC of 0.67 with 7 features. Only peak accuracy was significantly better than the single-parameter models (p=1.26e-7).

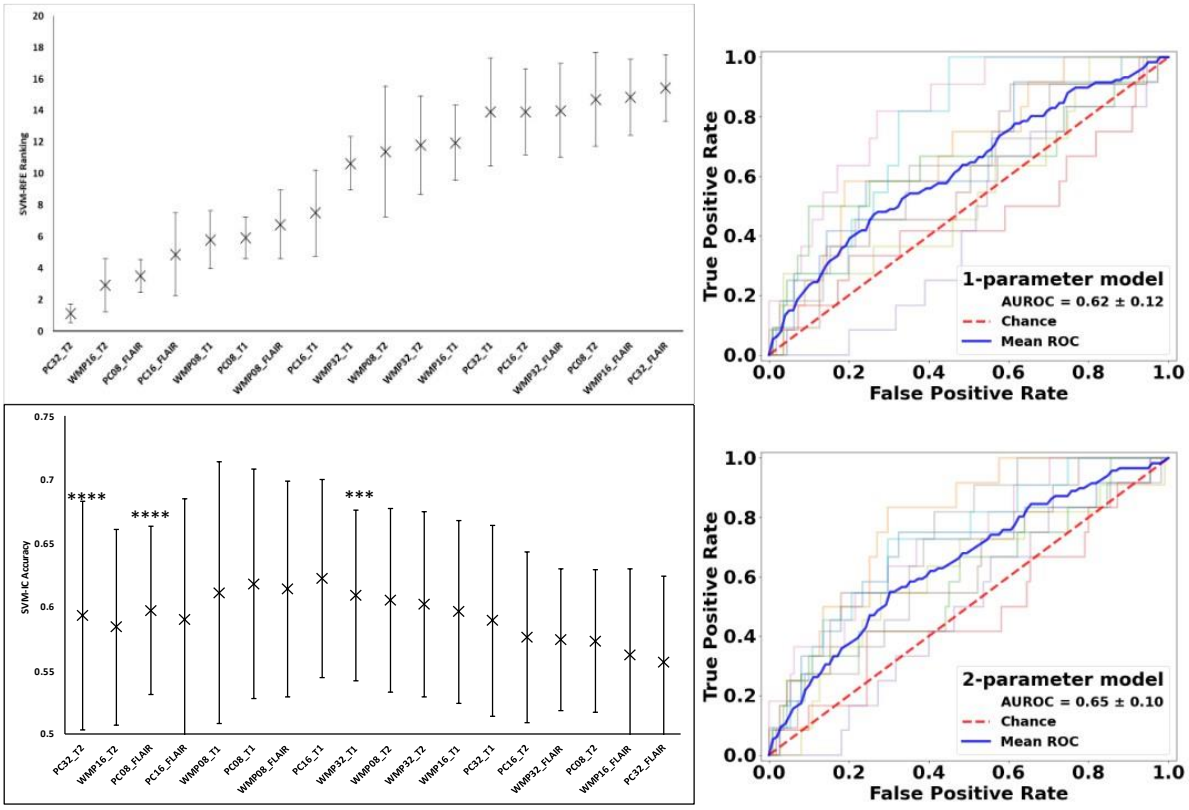

Figure 4.16: Feature ranks and performance comparison in the classification of lesion tissue between high and low disease patients. Top Left Panel: The mean (standard deviation) rankings of the 18 texture features used in this analysis based on the linear recursive feature elimination (RFE) algorithm in SVM. Bottom Left Panel: Accuracy of the classification models (SVM-IC) achieved by adding features one at a time, starting from the highest to the lowest rankings. Right Panel: ROC curves for models constructed using the top two ranked texture features: top) T2-w phase congruency with a maximum 32 mm wavelength (PC32_T2) alone, and bottom) PC08_T1 + T2-w weighted mean phase with a maximum 16 mm wavelength (WMP16_T2). ROC: receiver operating characteristics; AUROC: area under the ROC curve. The stars indicate features that contribute to significant improvement in classification accuracy (***p<0.001, ****p<0.0001).

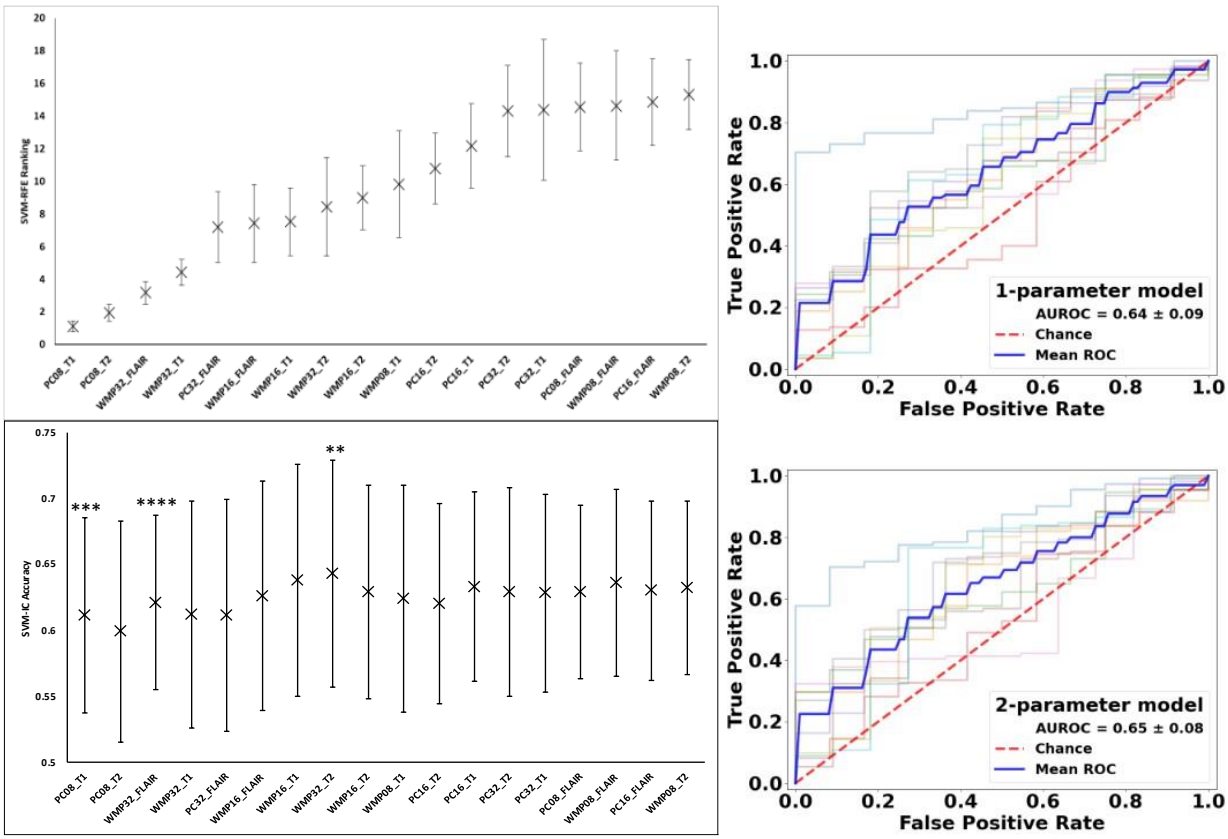

Figure 4.17: Feature ranks and performance comparison in the classification of NAWM tissue between high and low disease patients. Top Left Panel: The mean (standard deviation) rankings of the 18 texture features used in this analysis based on the linear recursive feature elimination (RFE) algorithm in SVM. Bottom Left Panel: Accuracy of the classification models (SVM-IC) achieved by adding features one at a time, starting from the highest to the lowest rankings. Right Panel: ROC curves for models constructed using the top two ranked texture features: top) T1-weighted phase congruency with a maximum 8 mm wavelength (PC08_T1) alone, and bottom) PC08_T1 + T2-weighted phase congruency with a maximum 8 mm wavelength (PC08_T2). ROC: receiver operating characteristics; AUROC: area under the ROC curve. The stars indicate features that contribute to significant improvement in classification accuracy (**p<0.01, ***p<0.001, ****p<0.0001).

4.4 Discussion

Using commonly available dMRI data, we showed the feasibility of conducting ssHARDI analysis and the complementary value of parameters from different diffusion models for assessing MS pathology. It appears that tissue alignment and orientation measures from ssHARDI and DTI are particularly sensitive to the existence of lesions in a patient, and to subtle structural differences

between NAWM areas (specifically the ODF energy metric) between patients with high versus low disease activity. In contrast, tissue diffusivity and alignment metrics from DTI are the best in distinguishing intra-lesion pathology, and in separating lesion activity between high and low disease patients, especially MD and FA. Similarly, phase congruency measures showed the ability to differentiate tissue types in both classification scenarios. Phase congruency measures based on FLAIR ranked highest in models differentiating lesion vs NAWM but were joined by T2-w measures in the core vs shell analysis in the high-ranking features.

The ability to evaluate sub-voxel-based tissue properties through ssHARDI modeling would be important in a clinical setting. However, ssHARDI studies often face the challenge of not obtaining enough diversity of measures for evaluation, unlike multi-shell models. To compensate, a prior study applied a partial, 2-compartment model and showed that both neurite density and dispersion indices from ssHARDI decreased in the NAWM of MS patients, and the reduction in the right internal capsule correlated with MS duration (186). In the present study, we undertook an alternative approach with the assistance of an efficient modeling method, AMICO. This provided several sub-voxel measures of neurite diameter, density, and dispersion. Both visual and quantitative analyses show that the variances at a ROI level are equivalent between these measures derived using either 1-shell or multi-shell data and using either online or own diffusion data in ssHARDI modeling. In addition, based on the distribution of diffusion at all sampling directions in a voxel, we also created a new measure of tissue organization, ODF energy, to increase the capacity of ssHARDI.

To maximize the understanding of diffusion metrics in tissue assessment, our study considered several modeling approaches, 3 regarding ssHARDI alone: ActiveAx, NODDI, and diffusion ODF. Multi-model analysis is critical for assessing complex pathologies as observed in MS (8). However, this strategy also led to a large volume of parameters. A caveat of multiparametric approaches (198) is the difficulty of assigning importance to parameters that have overlapping sensitivities. Here we took advantage of SVM, a well-recognized machine learning method. The SVM-RFE has shown to be robust to feature redundancy and model overfitting, and in a linear form, the SVM can assign unique coefficients to each parameter, thereby identifying the specific contribution of a parameter to individual classification tasks (165).

In lesion–NAWM analysis, based on diffusion MRI models, nearly all top rankings were tissue orientation and alignment metrics, particularly the top 3: ODF energy, FA, and ODI. Based on definition, ODF energy measures the orientational complexity of a structure. The higher the value, the more misalignment in the structure. FA detects changes in both axonal density and alignment anisotropy[9], and therefore is partially explainable by ODI. The leading performance of these orientation features in this analysis may indicate that the most critical changes following lesion formation in MS are tissue damage, such as inflammatory demyelination and axonal injury. A direct consequence of this pathology is increased structural heterogeneity, rather than simple alterations in neurite density. This is consistent with prior findings showing decreased FA in nearly all lesion studies in MS compared to the NAWM (181,182), and ODI changes with lesion formation (23,118) and repair (36), although the consistency of ODI changes deserves further validation (199). Notably, optimal classification between lesion and NAWM ROIs in the current study required the addition of FA. Previously, tractography FDi also showed strong correlations

with FA (131,135), supporting the relationship between these highly ranked features. The unique role of tissue alignment and orientation measures may facilitate early detection and even prediction of lesion pathology in future studies, promoting early management.

The core-shell analysis was designed to probe the intra-lesion patterns of pathology as seen in chronic MS lesions. When active, these lesions show demyelinated, hypocellular cores and inflammatory demyelinating shells; while inactive, present with hypocellularity with no active demyelination in lesion territories (2). As such, the expected differences between core and shell are the degree of cellularity, where based on the diffusion MRI models, the hypocellular core should have higher diffusivity than the cell-rich, inflammatory shell. Indeed, the 3 DTI measures (MD, RD, and FA) ranked the highest in our core-shell analysis, and MD played a dominant role. While there is lack of core-shell studies using dMRI in the literature, prior evidence attests the sensitivity of MD to subtle changes in MS pathology. One report showed that MD increased 5 months before the occurrence of active MS lesions, and pre-lesion MD correlated significantly with the MD of the lesions 2 months after active inflammation (31). In the present study, the lack of significance of the MD model in AUROC compared to chance may be due to several reasons, including the small number of such lesions and their heterogeneity in pathology. For instance, chronic inactive lesions may not show significant core-shell differences, and their inclusion may have caused artifacts. Alternatively, robust analysis of core-shell activity in chronic active lesions can improve our understanding of the ongoing pathology and so disease progression in MS patients (200).

Our inter-patient analysis results appear to agree with the findings described above. Between patients who had high versus low disease activity, FA ranked the highest in lesion tissue classifications; while in NAWM classifications, ODF energy was the best. In general, T2-w MRI lesion load reflects disease activity, and in a long-term, it correlates with disability in MS as seen after 20 years of disease onset (60). Therefore, individuals with higher lesion load are expected to have greater tissue damage, likely affecting both neurite density and orientation, and so greater changes in lesion FA between the participant groups. On the other hand, increased disease activity would also implicate increased pathology in the lesion-free areas, such as the NAWM, yet the changes wherein should be much less than in the visible plaques. Indeed, our NAWM analysis suggests that the pattern of differences between high and low disease patients is mainly orientation based, as reflected by ODF energy, deserving further confirmation.

Collective observations from diffusion MRI-based analyses of this study may suggest that MD and FA are important metrics for assessing MS pathology. In particular, they may serve as top options in core versus shell analysis, disease severity comparisons between participants (e.g. lesion FA), and at a lesser extent, lesion versus non-lesion analysis. However, outcomes from the relatively complex models appear to be more competitive in NAWM-associated evaluations than the DTI measures, particularly the orientation-driven metrics (ODF energy and ODI), suggesting the value of multi-model analysis. Emerging hypotheses of MS disease progression support a mechanistic framework where disease outcome appears to be a joint result of the balancing consequences between different pathological processes and their anatomical locations (201). Currently, dMRI is considered one of the most valuable imaging approaches that can potentially evaluate both myelin and axonal properties that are related to MS pathology. At the same time, it is worth noting that a

variety of other associated techniques are underway, including those for myelin mapping using different MRI approaches. For example, myelin estimation based on simultaneous T1/T2 relaxometry and proton density mapping correlated strongly with histological myelin as seen in post-mortem MS brain samples (202). Another study demonstrated that quantitative susceptibility provided additional myelin information in brain NAWM of MS patients, independent of FA and RD (203). Further, pre-operative myelin mapping using T1/T2 ratio showed the potential to predict outcomes of trigeminal neuralgia following Gamma knife radiosurgery, while FA and RD demonstrated similar values in this prediction as estimators of pre-operative axons (204). These findings further support the importance of multi-dimensional analysis of tissue structural changes in MS, including combining multi-model dMRI, and other candidate metrics of myelin and axons.

Phase congruency-based models with top-ranked features showed a similar trend in the classification scenarios discussed above. Phase congruency features with more low-frequency information (higher maximum wavelength) were more highly ranked in both lesion versus NAWM and core vs shell analyses, especially for T2-w and FLAIR MRI. Higher maximum wavelength was set to characterize imaging patterns associated with larger lesions. The higher ranking of these features in lesion-related classifications suggests that larger-scale contextual relationships characterize greater lesion information. In contrast, when comparing groups with different lesion loads using NAWM-related features, higher frequency content from the lower (8mm) maximum wavelength calculations from T1-w and T2-w MRI ranked higher. This observation likely indicates that fine texture information is of increased impact in differentiating tissues with minimal heterogeneity such as the NAWM. This is consistent with our findings showing the relatively low performance of these high frequency features in group-wise analysis based on lesions that are

known for structural heterogeneity (205). Finally, T2-w and FLAIR phase congruency features typically ranked higher than T1-w features. This might be related to the fact that T2-w and FLAIR images are much more sensitive to focal lesion activity than T1-w MRI, among other possible explanations. These results encourage the use of lesion-sensitive imaging sequences in future research of similar directions.

Based on model evaluation metrics, phase congruency-based models appeared to have outperformed diffusion MRI-based models in both lesion-NAWM and core-shell comparisons. This may stem from differences in the building blocks the imaging measures offer for the classification tasks. Phase congruency characterizes the organizing pattern of the imaged tissue structure while diffusion MRI attempts to directly detect the biophysical property of the underlying tissues. Further, the availability and type of diffusion MRI measures also depend on the models used to derive these measures. Ultimately, the texture- and diffusion-based imaging features can provide complementary information deserving further confirmation for their comparable roles.

We note a few limitations in this study. The spatial resolution of our dMRI was moderate. However, we registered all diffusion outcomes to the high-resolution T1-w MRI to mitigate the impact, and our ssHARDI maps appeared similar to those obtained using high resolution dMRI from the HCP both visually and quantitatively. Next, to optimize data quality, we excluded lesions that did not have a ‘clean’ match of contralateral NAWM regions, and lesions not large enough for core-shell analysis, potentially reducing the variance of modelled features. Nonetheless, SVM regularization techniques support model fitting, so the risk of model overfitting is minimal. Further, in phase congruency analyses, only three maximum wavelengths were tested, limiting the

potential of assessing this method to other sizes of lesions. However, the chosen wavelengths matched to a range of lesion sizes most seen in MS MRI. Finally, there were lesions that appeared overlapping and they were segmented as single confluent regions. Given the inhomogeneity of signal intensity in such lesions, it may have somewhat affected the lesion-NAWM results (e.g. underestimation of tissue differences). However, we applied the mean of ROIs in all quantitative analyses, which should have minimized the effect, if any. The impact on core-shell analysis is expected to be less than the above, as regions of inhomogeneity may be included in both lesion portions. In the future, we seek to confirm our findings using higher resolution diffusion MRI together with phase congruency and evaluate people with different types of diseases and lesion pathologies, including datasets with histology-verified lesion activity. Additionally, we also plan to investigate the utility of the top-performing diffusion and phase congruency features in assessing pre-lesion NAWM pathologies, and in predicting the occurrence of MS lesions, to promote clinical applications. The findings of this work can be applied to detect invisible structural changes within relatively large lesions that may indicate their activity or to studies that track longitudinal changes in either small or large lesions for early understanding of disease outcomes.

4.5 Summary

Collectively, using commonly available dMRI data, it is possible to perform competitive ssHARDI modeling. Combining machine learning with robust ssHARDI and DTI metrics may provide advanced assessment of lesion and NAWM pathology, including mean diffusivity for intra-lesion pathology in MS and similar diseases. Furthermore, texture analysis with phase congruency may be a valuable alternative method to advanced MRI in characterizing subtle MS pathology, particularly given the compatibility of phase congruency with clinically standard MRI and the

better performance of models based on this texture analysis method than diffusion MRI. Given the large number of variables investigated in this chapter, only measures that contributed to peak performance of the models were selected to be tested further in the next chapter for their utility to differentiate disease severity. Including only these significant measures will help improve the reliability of outcomes and reduce noise in the next steps of analyses. These significant measures would include several of those from the lesion vs NAWM analysis such as ODF energy, ODI, FA, and FDi. Likewise, measures would be similarly chosen from the core vs shell analysis. It is worth noting that the diffusivity measures of DTI (MD, FA, and RD) ranked the highest in the core vs shell models but given the improved specificity of HARDI-like measures with similar meanings, two such measures including ICVF and Diameter were chosen instead in Chapter 5 investigations. More phase congruency features were investigated, however, T2-w and FLAIR 16 and 32 mm features contributed greatly to peak performance in both analyses and so were chosen for Chapter 5 investigations.

Chapter 5: Advanced diffusion MRI and textural phase congruency detect widespread brain structural differences between RRMS and SPMS

Developing methods that can sensitively detect tissue structural changes is important. But that typically only serves as the first step. To understand the value of these methods for clinical use, it is important to investigate their potential for characterizing disease level characteristics, and that is the goal of this Chapter. Based on advanced analysis of brain diffusion MRI and phase congruency along with machine learning, Chapter 4 has identified an array of advanced imaging measures that differentiate different types of MS pathology associated with lesions and non-lesion areas. Further, my new development as shown in Chapter 3 has led to the innovation of several of such measures. For instance, the prior neurite density measure FDi is replaced with AFD; the latter is model-free and independent of the tracking algorithms used. In addition, to facilitate truly multi-shell HARDI analysis, I have initiated robust neural network models as part of a published paper to predict new diffusion data not typically acquired in clinical studies (Murray and Oladosu *et al*., *Magnetic Resonance Imaging*, April 2023). In this way, multi-compartmental models based on both NODDI and ActiveAx can be calculated, where modelling uses the softwares AMICO and AMICOx, respectively, the latter to overcome the crossing fiber challenges. Based on all of the above discoveries, this chapter aims to interrogate whether and how the tissue abnormality sensitive measures differentiate disease severity at different scales based on RRMS and SPMS, the two continuum and most common phenotypes of MS. A majority of this Chapter has been

published as a manuscript as mentioned in the Preface (Oladosu et al, Frontiers in Neuroscience, *Frontiers in Neuroscience 16 (August 12, 2022)*.

5.1 Introduction

Various studies suggest that SPMS pathology differs from RRMS pathology in a number of ways that involve both microscopic and macroscopic changes from a MRI perspective. However, the exact scope and degree of these changes are still unclear (8,15). Thorough understanding of the tissue structural abnormalities underlying the functional differences between RRMS and SPMS is essential as that can help determine what and where to examine, and what new targets might be in initiating novel intervention and prevention strategies.

Focal lesions remain to be the hallmark of MS pathology (2,4). Nonetheless, the 'invisible' tissue abnormalities as seen in the brain NAWM are also shown to play a critical role in the pathogenesis and outcomes of MS (4,28,203). Based on advanced MRI including diffusion tensor imaging (DTI) and high angular resolution diffusion imaging (HARDI), and myelin water imaging, studies of brain normal appearing white matter (NAWM) in MS have found considerable reductions in neurite density, neurite dispersion, and myelin integrity as compared to healthy control tissues (13,28,199,206). Using texture analysis methods, recent evidence has also revealed extensive MRI texture abnormalities in the brain NAWM of MS (139).

On the other hand, consequences of MS lesions also depend on their location in the central nervous system (207). Based on DTI white matter tractography and magnetization transfer ratio, studies of major brain white matter tracts such as corpus callosum and corticospinal tracts have shown that a

person's dysfunction can be attributed to a single tissue-impacting lesion that resides in a critical anatomical location (208–211). As such, regions of interest (ROIs) studies within white matter tracts may reveal important 'hot spots' associated with disease evolution. Furthermore, changes distant from focal lesions are common in MS due to mechanisms such as Wallerian degeneration (212). Therefore, diffusion MRI-enabled along-tract statistics would be invaluable for probing both lesion and non-lesion pathology. Currently, there are studies related to individual aspects of the pathological spectrum but they are not necessarily integrated as a whole (208,209,211,213).

In addition to the above, recent evidence suggests the importance of chronic active lesions to disease progression in MS (16,58,214). While lesion development is often connected with clinical relapses in RRMS, many lesions in SPMS are chronic and smoldering, causing occult disease progression without signs of evident relapse (8,58). Histologically, chronic active lesions are characterized by inactive hypocellular demyelinated cores and actively inflammatory demyelinating rims, also referenced as mixed active-inactive lesions (58). Characterizing the nature and extent of such chronic active lesions in vivo has become a critical priority to improve healthcare in MS; however, the availability of methods is limited (183,214). Current research has been relying on susceptibility-based imaging methods (79), which define chronic active lesions as having isointense cores and hypointense rims (rim-positive) (215,216). The presence of more rim-positive lesions is associated with earlier disabilities in MS, and the persistence of paramagnetic rims from acute lesions suggests remyelination failure (16). Nonetheless, susceptibility imaging is still under development and there is no evidence showing the ability of these methods to identify other pathologies such as axonal injury that is critical for MS progression.

This study aims to identify new quantitative methods for integrated analysis of brain pathological changes in RRMS and SPMS and compare how and where they are different. The procedures will focus on novel analyses of diffusion MRI and phase congruency image texture in clinical MRI as proposed in this thesis.

5.2 Materials and Methods

5.2.1 Sample

This study used brain MRI scans of 29 subjects with MS (all females), including 20 RRMS and 9 SPMS from 2 datasets as part of an ongoing clinical study (REB14-1926). Established criteria were followed in all diagnoses of MS (217), RRMS (218), and SPMS (219). The first dataset (dataset1) included 10 RRMS and 9 SPMS patients recruited for a study assessing corpus callosum function. The second (dataset2) included 10 RRMS patients as a convenience sample from a clinical trial of domperidone as a myelin repair agent (ClinicalTrials.gov Identifier: NCT02493049). For the latter, participants needed to have at least one gadolinium-enhancing lesion in brain MRI but the current patients were ineligible and therefore did not continue in the trial. Both studies were approved by the institutional research ethics board. Written informed consent was obtained from all participants.

5.2.2 Imaging protocol

3T anatomical and diffusion brain MRI were obtained from each dataset using a research-dedicated scanner (Discovery MR750, GE Healthcare, Milwaukee, USA). The imaging protocol included T1-weighted MRI acquired with a 1-mm isotropic, magnetization-prepared fast-spoiled gradient echo sequence using 6.7-8.0 ms repetition time (TR), and 2.9-3.0 ms echo time (TE). T2-weighted

MRI was acquired with a spin-echo sequence using TR1/TR2 = 6000/5600 ms and TE1/TE2 = 84/100 ms; matrix = 256x256/512x512; field of view (FOV) = 24x24/22x22 cm; and slice thickness = 3 mm. FLAIR MRI was obtained with a spin-echo inversion recovery sequence using TR1/TR2 = 7000/6000 ms and TE1/TE2 = 127/127 ms; matrix = 512x512; and FOV = 24x24 cm. Diffusion MRI was acquired with a spin-echo echo-planar sequence using TR1/TR2 = 8000 ms and TE1/TE2 = 84/61 ms; matrix = 120x120; FOV = 24x24 cm; slice thickness=3/2 mm, 5 b0, with 23 b = 800 s/mm^2 directions for Dataset1, and 3 b0, 45 b = 1000 s/mm^2 directions, and 3 reverse phase-encoded b0 for Dataset2.

5.2.3 Diffusion MRI Processing and Analysis

Preprocessing

Image preprocessing for diffusion MRI involved several steps, which were essentially the same for dataset1 and dataset2 except the step used in susceptibility distortion correction due to the lack of reverse phase-encoded b0 data in dataset1. Briefly, the diffusion MRI scans were denoised, corrected for Gibbs ringing with a sub-voxel shift correction method, and then bias corrected as reported previously (32,220–223). Eddy current and susceptibility distortion corrections were completed using the FSL eddy method (193,224). The latter involved a tool called topup, where dataset1 was not compatible initially due to acquisition confounders as noted above. To compensate, we inverted the signal intensity of T1-w MRI from Dataset1 and rigidly transformed it to the diffusion space. The corresponding b0 volumes were averaged and nonlinearly registered (ANTs SyN) to the processed T1-w MRI in an x-axis constrained transformation to calculate susceptibility distortion (192,225). The distortions were transformed afterwards to a topup-like output format in FSL for correction (226). Dataset2 was processed for susceptibility distortion

correction using topup directly (226). For both datasets, the corrected average b0 volumes were then rigidly registered (FSL epireg) to the corresponding T1-w MRI per patient for further processing (189,190). Next, diffusion images from the two datasets were harmonized for angular resolution by resampling, and for voxel-wise imaging characteristics by using the linear Rotationally Invariant Spherical Harmonics method based on 8 RRMS patients (100,173,174,227). These published accounts indicated that the harmonization approaches were valid if the b value differences between datasets fell between the range of 500 s/mm^2 and 1500 s/mm^2.

To further clarify the suitability of the aforementioned harmonization methods, we calculated the variance and signal-to-noise ratio (SNR) of white matter ROIs and compared them between datasets based on harmonized data. Eight ROIs sized 6x6 pixels each were drawn in the corpus callosum, forceps minor, and forceps major tracts per subject, per examined diffusion measure. The SNR was evaluated relative to the standard deviation of the cerebrospinal fluid of the brain because the calculated maps were masked, which made the background of the maps all zeros. Subsequently, to enable high angular resolution diffusion imaging (HARDI) analysis, new diffusion MRI data at b=2000 s/mm^2 were predicted for both datasets based on their corresponding b=1000s/mm^2 data using an in-house deep learning algorithm (228).

Diffusion Metrics Calculation

Fractional anisotropy (FA) was obtained from diffusion tensor imaging (DTI) in FSL. HARDI analysis applied the ActiveAx method implemented in the accelerated microstructure imaging with convex optimization (AMICO) for crossing fibers (AMICOx) to model axonal diameter and intracellular volume fraction (ICVF), and neurite orientation distribution and density imaging

(NODDI) in AMICO to calculate orientation dispersion (114,121,122). The apparent fiber density (AFD) was obtained using the fiber orientation distribution function (fODF), and ODF energy, a measure of orientational complexity, was obtained from the diffusion ODF computed by q-ball imaging reconstruction (100,103,171). All measures were transformed to the common MNI-152 coordinates for analysis based on T1-w MRI nonlinear MNI transformation with the ANTs SyN method (Figure 5.1a).

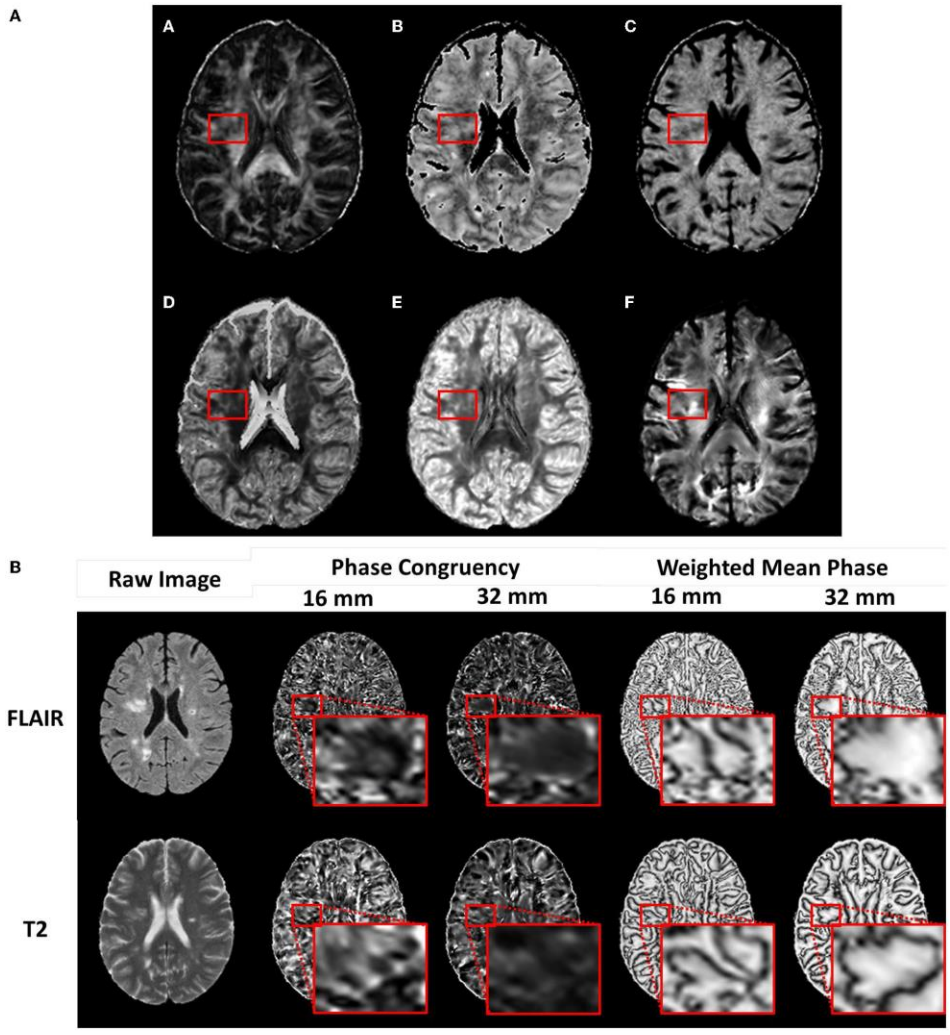

Figure 5.1: Example diffusion and phase congruency texture maps. Shown are: A) Diffusion MRI of a) Fractional Anisotropy, b) axonal diameter, c) Intracellular Volume Fraction, d) Orientation Dispersion Index, e) Orientation Distribution Function energy f) Apparent Fiber Density, and B) phase congruency of (top row) FLAIR MRI and (bottom row) T2-w MRI.)

Diffusion Tractography

The white matter fODF was calculated based on constrained spherical deconvolution using the b=1000s/mm^2 data alone. The resulting orientation distribution was nonlinearly transformed and reoriented to MNI-152 space using diffusion to T1-w rigid and T1-w to MNI nonlinear transformations (103). The peaks of the fODF were calculated and input to a software known as TractSeg to obtain tracts and tract ending segmentations (129,229). Tract orientation mappings were then calculated and tractography generated through probabilistic tracking using iFOD2 and a dilation factor of 2 (Figure 5.2a) (108). The corpus callosum was partitioned into 7 segments according to the Witelson scheme based on locations of cortical intercepts (230). The corticospinal tracts and optic radiations were also segmented bihemispherically.

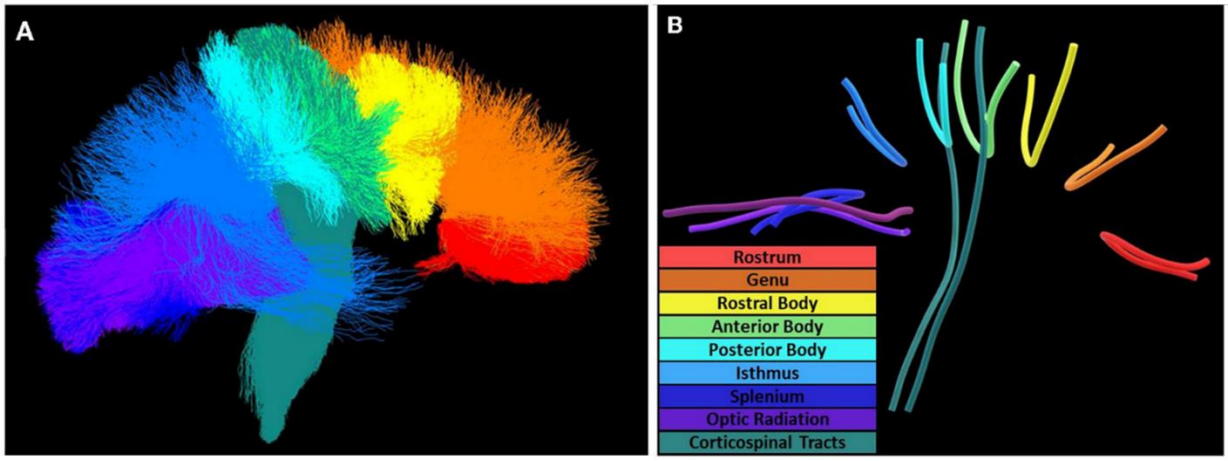

Figure 5.2: Diffusion tractography and tract geometries. Along-tract analysis of the corpus callosum, optic radiation, and corticospinal tracts utilized A) tractography oriented posterior (left) to anterior (right) and B) mean tract geometries for within-tract sampling.

5.2.4 Texture Analysis with Phase Congruency

Texture analysis was done for T2-weighted (T2-w) and FLAIR MRI using a 3D method called phase congruency. It was a frequency-based calculation approach and was shown to be insensitive

to signal intensity differences between images (37). The same image preprocessing pipelines were applied to the anatomical images from dataset1 and dataset2. Essentially, the T1-w, T2-w, and FLAIR MRI were all preprocessed by Gibbs ringing correction, N4 bias field correction, and ANTs template-based brain extraction (231,232). Medial alignment of T1-w MRI was applied and that involved applying a rotation and translation procedure calculated from a rigid body registration to the MNI-152 T1-w reference. T2-w and FLAIR MRI were then rigidly linearly transformed to the same dimensions as T1-w MRI. In addition, T2-w and FLAIR MRI were further processed with contrast-limited adaptive histogram equalization (233) (scikit-image v0.18.3) to enhance feature visibility thereby reducing the potential impact of the slightly different imaging protocols used in acquisitions.

Texture calculation produced 2 metrics: phase congruency, reflecting edge strength based on the alignment of phases, and weighted mean phase, reflecting edge sharpness (Figure 5.1b) (154,158). Optimal calculation of these metrics required fine-tuning of several parameters (Table 4.1). Weighting adjustment for frequency spread used a sigmoid function with the inflection point (cutOff) set at 0.5 and degree of inflection (gain) set as 10.0. Filter bandwidths were regulated by

$$\eta_\beta = \frac{\sigma}{f_0} = 0.55, \qquad (5.1)$$

controlling the filter standard deviations (σ) relative to their central frequencies (f_0) using sigmaOnf (η_β). Central frequencies were separated by a multiple (m) to obtain even spectral coverage. The multiple was empirically determined given by

$$m = \frac{\sigma}{f_0}^{log\left(\frac{\pi}{20}\right)}. \qquad (5.2)$$

By default, the median of the highest frequency filter was used to characterize noise with the noise threshold set at 2 standard deviations. Filters were uniformly oriented on a sphere to balance

orientational coverage according to a diffusion MRI gradient scheme of 23 directions conveniently available in this study. The number of filter scales was determined by

$$n_{scale} = \left\lceil \frac{log\frac{f_{max}}{f_{min}}}{log\, m} \right\rceil + n \quad \Big| \quad f_{max} = \frac{1}{\lambda_{min}}\,,\ f_{min} = \frac{1}{\lambda_{max}},\ \text{n} = 2 \qquad (5.3)$$

including a heuristically determined n=2 additional filters to ensure uniform sensitivity at low frequencies. The frequency domain is bounded by the minimum and maximum wavelengths (λ). For images with a 1 mm^3 voxel resolution, λ_{min} was set at 2 mm and λ_{max} at 16mm and 32 mm to allow analysis of frequencies around the spatial scale of most lesions observed in MS. Increased phase congruency and decreased weighted mean phase suggest increased signal complexity.

Table 5.1. Definition and Impact of Phase Congruency Parameters

Parameter	Symbol	Meaning	Impact
Spectral Coverage			
Minimum Wavelength	λ_{min}	Determines the highest frequency in analysis	Determines the smallest scale features for which patterns are detected
Maximum Wavelength	λ_{max}	Determines the lowest frequency in analysis	Determines the largest scale features for which patterns are detected
Number of scales	nScale	Number of filters to define a filter bank covering the frequency range (λ_{min} , λ_{max})	Defines a set of filters for sensitivity across all feature frequencies
Spectral Sensitivity			
SigmaOnf	η_{β}	Standard deviation of a single filter around its central frequency (f_0).	Regulates the frequency coverage of a single filter
Multiple	m	The factor separating f_0 of successive filters in a filter bank.	Together with σ, regulates how features at each frequency are relatively weighted
Angular Resolution			
Number of orientations	nOrient	The number of filter banks positioned in 3D to detect features in multiple orientations	Provides representation of features at all orientations
Frequency Spread Penalty			
Cut-Off	cutOff	The inflection point of a sigma curve differentiating high and low frequency spread	Weights features with different orientations based on the complexity of their frequency makeup
Gain	g	The sharpness of a sigma curve in contrasting high over low frequency spread.	

5.2.5 Outcome Generation

This analysis focused on four scales of abnormalities associated highly with disease development in MS: whole-brain normal-appearing white matter (NAWM), tract-based regions of interest (ROIs), along-tract changes, and chronic active lesions.

Whole-Brain White Matter

Assessing whole-brain NAWM used a histogram analysis method based on 256 bins. The procedure started with brain tissue segmentation with an open-source software (FSL FAST) using T1-w MRI. Focal MS lesions were segmented based on T1-w and FLAIR MRI as reported previously (32). Eventually, this step provided 3-dimensional ROIs for individual lesions. These lesion ROIs were dilated by one voxel and then subtracted from the FSL-segmented brain white matter to obtain the NAWM for each patient (234). For each investigated imaging measure, the 50^{th} (p50), 75^{th} (p75), and 95^{th} (p95) percentile, and histogram peak were collected.

NAWM and Lesion Regions within Major White Matter Tracts

The 1-mm **ICBM-DTI-81** atlas helped identify major brain white matter tracks, including 3 corpus callosum segments (Genu, Body, Splenium), bihemispheric corticospinal tracts, and optic radiation tracts (128,235,236). The union of ROIs from the corticospinal tract, cerebral peduncle, posterior limb of the internal capsule, and superior corona radiata formed the overall corticospinal tract. NAWM and lesions were defined by intersecting whole-brain NAWM and lesion ROIs respectively with each tract.

Along-Tract Statistics

Tractometry was applied to tractography to obtain measurements for all investigated diffusion metrics at 100 points along the mean geometries of each investigated tract using distance map correspondence (Figure 5.2b) (237,238). Lesion maps were also averaged at each point along a tract giving a measure of the extent of local lesions (lesion extent), with values of 1 (one) indicating complete lesion coverage at that node. Coordinates and measurements at each point in

corresponding mean geometries were further aligned across patients using diffusion profile realignment based on FA (239).

Chronic Lesion Activity Analysis

We proposed a schema to understand the activity of chronic MS lesions based on their core-rim dichotomy (Figure 5.3). Lesions were assigned a z-score based on the relationship between lesion core and rim pathology.

$$Z_{lesion} = \frac{\mu_{Core} - \mu_{Rim}}{\sigma_{Rim}} \quad (5.4)$$

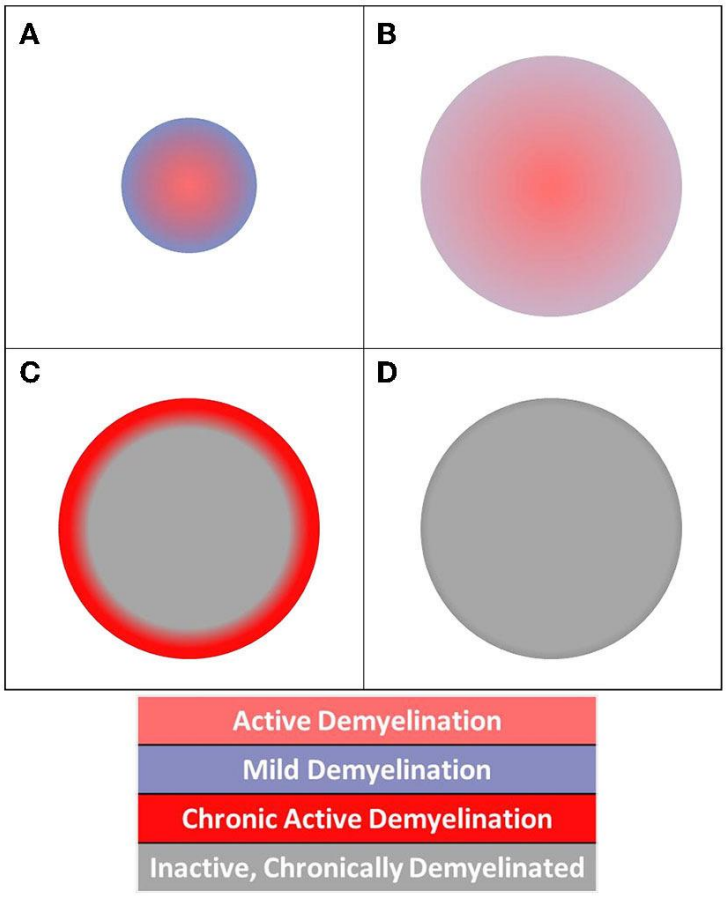

Figure 5.3: Diagram of acute and chronic lesion activity. Different patterns of pathology are visible in A) acute lesion, B) slowly expanding lesion, C) chronic active lesion, and D) chronic inactive lesion structures.

Lesion cores were defined by 26-connectivity erosion of lesion masks. Subtracting the core voxels from full lesion ROIs produced single-voxel-thick rim ROIs for each lesion (32). Lesions without definable cores and rims were excluded in this step of the analysis. With this schema, chronic active lesions would present with z-scores>0 (or <0 based on the investigated measure) highlighting greater core damage. According to literature, pathological changes in MS lesions corresponding to reduced tissue integrity or diseased worsening include reductions in neurite density, increased axonal diameter, and inflammatory demyelination which would be respectively evidenced by negative z-scores for AFD, FA, and ICVF, positive z-scores for axonal diameter, and positive z-scores for ODF energy and ODI (12,31,183,240).

5.2.6 Statistical Analysis

All analyses focused on cohort differences between RRMS and SPMS. Histogram features for each measure were compared using ANOVA then post-hoc tukey correction for multiple comparisons. For tract-based ROI analyses, measures in tracts were compared using ANOVA for combined NAWM and lesion analysis then a linear mixed-effect model with subject as a random effect, including Tukey correction for pairwise comparisons to understand individual group differences. Tract-based means were compared using ANOVA, and along-tract variations were compared with a mixed-effect model and corrected for multiple comparisons using permutation testing. All models included subject age as a covariate. The sex factor was not controlled because all subjects were female. Disease duration was not included as a covariate because it was expected to be different between cohorts given the nature of SPMS being a continuum of RRMS. Analysis of multiple features and tracts were addressed with Benjamini-Hochberg correction. Two-sample comparisons used Student's *t* t-tests, with $p<0.05$ as significance. For chronic active lesion

analysis, the overall lesion percentages, and average counts of lesions per patient at multiple thresholds were graphed and tabulated.

5.3 Results

5.3.1 Sample Characteristics

The mean (standard deviation) age of the participants was 46.9 (11.5) years, which was 40.7 (9.3) years for RRMS and 58.2 (8.9) years for SPMS subjects. The disease duration of the whole cohort was 15.5 (11.8) years, and it was 8.6 (6.5) years for RRMS and 29.3 (8.4) years for SPMS participants. Further, the overall expanded disability status scale (EDSS) score was 3.3 (2.4), which was 1.9 (1.1) and 6.5 (0.5) for RRMS and SPMS subjects respectively. In total, we identified 1026 brain white matter lesions, 1 to 111 per subject. SPMS patients had an average of 48.56 lesions and RRMS patients of 29.45 lesions. Among the 1026 lesions, 275 had core-shell analysis (SPMS: 12.67/pt, RRMS: 8.05/pt). In total, 6 diffusion and 8 phase congruency measures were analyzed. Diameter, ODI, ODF energy, and FLAIR WMP showed higher values in regions of greater pathology such as those in SPMS versus RRMS while AFD, FA, ICVF, and T2 WMP showed the opposite trend, being lower in SPMS than RRMS. In addition, after harmonization of diffusion MRI, there was no significant difference ($p>0.05$) in either variance or SNR of white matter ROIs between dataset1 and dataset2 for any calculated diffusion metrics (Table 5.2).

Table 5.2: The mean (standard deviation) variance and signal-to-noise ratio of white matter regions of interest in RRMS participants from Dataset1 and Dataset2.

Measure	Variance			Signal-to-Noise Ratio (SNR)		
	RRMS1 (μ±s.d.)	RRMS2 (μ±s.d.)	p-value	RRMS1 (μ±s.d.)	RRMS2 (μ±s.d.)	p-value
AFD	0.664 ±0.093	0.696 ± 0114	0.498	19.4 ± 10.9	13.9 ± 4.7	0.166
Diameter	11.3 ± 0.3	11.6 ± 0.3	0.106	12.2 ± 6.8	10.7 ± 7.4	0.636
FA	0.646 ± 0.043	0.613 ± 0.044	0.106	19.4 ± 10.0	16.8 ± 8.4	0.538
ICVF	0.643 ± 0.046	0.601 ± 0.047	0.057	31.8 ± 36.9	25.2 ± 21.8	0.636
ODF Energy	150.3 ± 8.3	152.8 ± 11.9	0.641	2.07 ± 1.19	1.83 ± 0.56	0.560
ODI	0.103 ± 0.014	0.117 ± 0.018	0.059	2.43 ± 6.93	1.11 ± 2.48	0.583

Note: AFD: apparent fiber density; FA: fractional anisotropy; ICVF: intracellular volume fraction; ODF: orientation density function; ODI: orientation dispersion index

5.3.2 Histogram Statistics

ANOVA showed that histogram features differed significantly between RRMS and SPMS for all diffusion and texture measures except T2-w (32mm) phase congruency (Figure 5.4). Diffusion-based AFD ($p<0.0001$) differentiated cohorts across all four histogram features ($p<0.01$); FA differentiated cohorts in all features but p50. Remaining diffusion measures showed cohort difference in only 2 histogram features ($p<0.05$) except for diameter, which only showed significance in histogram peak ($p<0.0001$). T2-w and FLAIR (16mm) phase congruency showed significance in both p75 and p95 ($p<0.05$), while FLAIR (32mm) and T2-w (16 & 32mm) were significant at p50 and p95 ($p<0.05$) in differentiating cohorts.

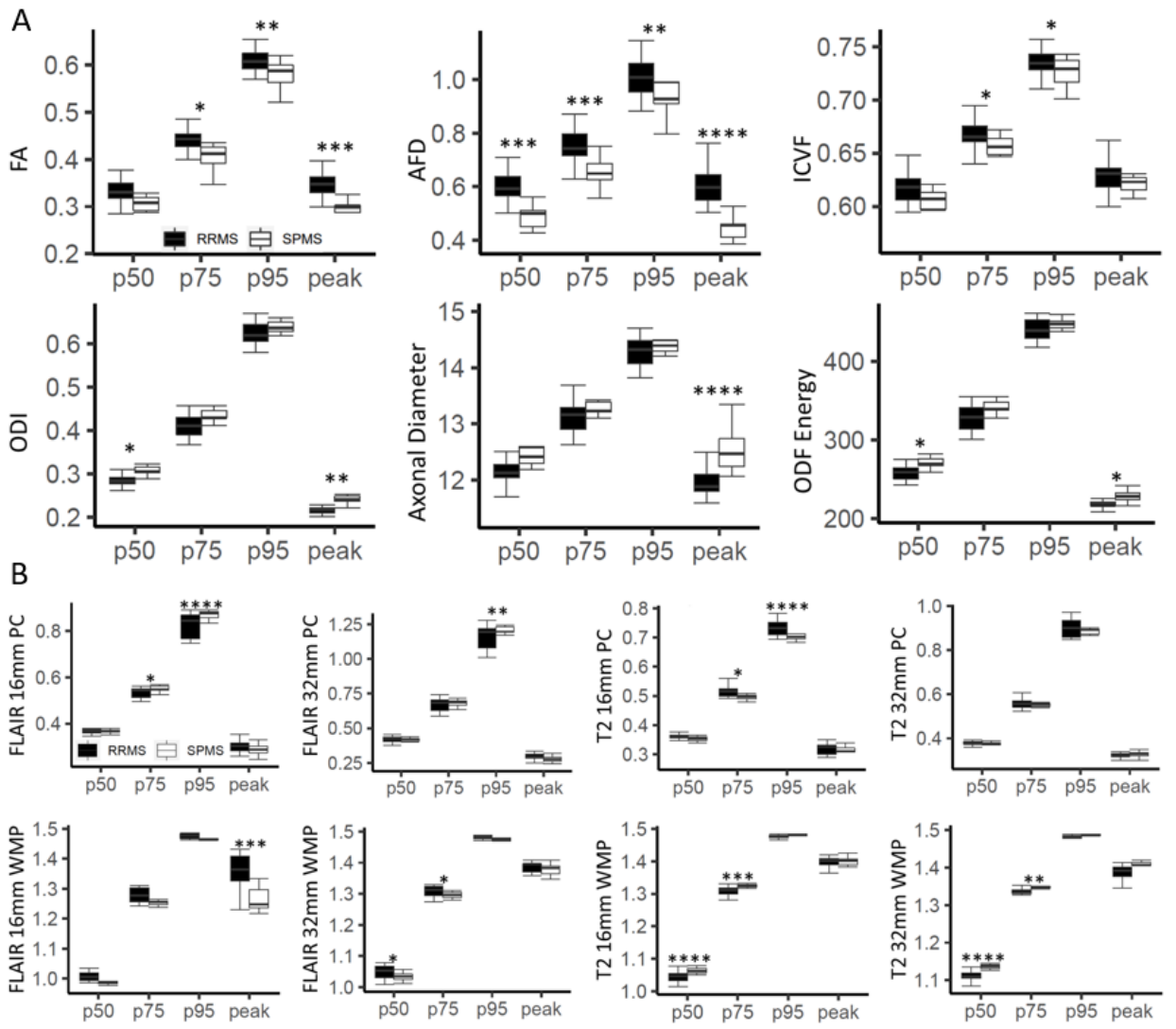

Figure 5.4: Histogram-based outcomes by cohort. Panel A demonstrates results for diffusion measures, and panel B for texture measures from phase congruency. Note: the stars indicate post hoc significance: *p < 0.05, **p < 0.01, ***p < 0.001, ****p < 0.0001. The boxes plot the median, interquartile range (IQR), and 1.5*IQR.

5.3.3 ROI-based Tract-wise Analysis

Following correction of multiple comparisons in ANOVA, 3 diffusion measures, FA, ODF energy, and ODI detected differences between cohorts ($p<0.0026$) (Figure 5.5). All 3 measures showed significance in differentiating lesions ($p<0.001$) and NAWM ($p<0.05$) of the corpus callosum body. ODI and ODF energy were significant for the left (RRMS:0.172, SPMS:0.212) and right

(RRMS:207.64, SPMS:240.49) optic radiations respectively ($p<0.0026$) following ANOVA. Pairwise comparisons highlighted ODI and ODF energy detecting cohort differences in the optic radiations for lesions (RRMS:0.166, SPMS:0.212, $p<0.01$; RRMS:212.15, SPMS:238.15, $p<0.05$) and NAWM (RRMS:0.177, SPMS:0.212, $p<0.05$; RRMS:203.13, SPMS:242.83, $p<0.01$).

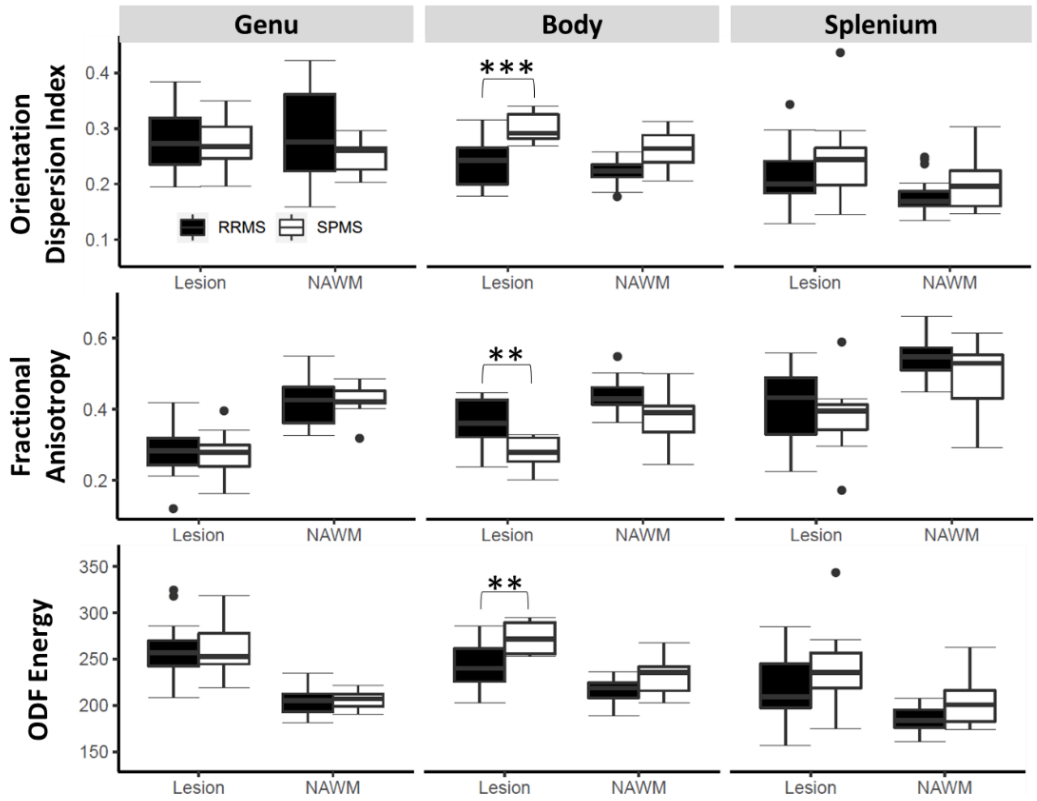

Figure 5.5: Tract ROI-based outcomes by cohort. Shown are findings in 3 diffusion measures on lesions and normal appearing white matter (NAWM) within 3 key regions of the corpus callosum. Note: the stars indicate post hoc significance: *p < 0.05, **p < 0.01, ***p < 0.001. The boxes plot the median, interquartile range (IQR), and 1.5*IQR.

5.3.4 Along-Tract Statistics

There were prominent differences between cohorts in lesion extent when all tract values were averaged (Figure 5.6). With correction for multiple comparisons following ANOVA ($p<0.0024$), lesion extent remained significant in the posterior body, isthmus, and splenium of the corpus

callosum ($p<0.0024$), and optic radiations in both hemispheres ($p<0.0001$). T2-w (16mm) phase congruency was significant in the left but not right corticospinal tract ($p<0.0024$). Lesion extent showed notable along-tract differences at major bihemispheric peaks appearing higher in SPMS than RRMS patients; however, T2-w (16mm) phase congruency showed constant along-tract cohort differences. FA, ICVF, and ODI did not survive correction for multiple comparisons following ANOVA, but indicated whole-tract differences in the genu, rostral body, and both hemispheres of the optic radiation with significant along-tract differences in the callosal segments.

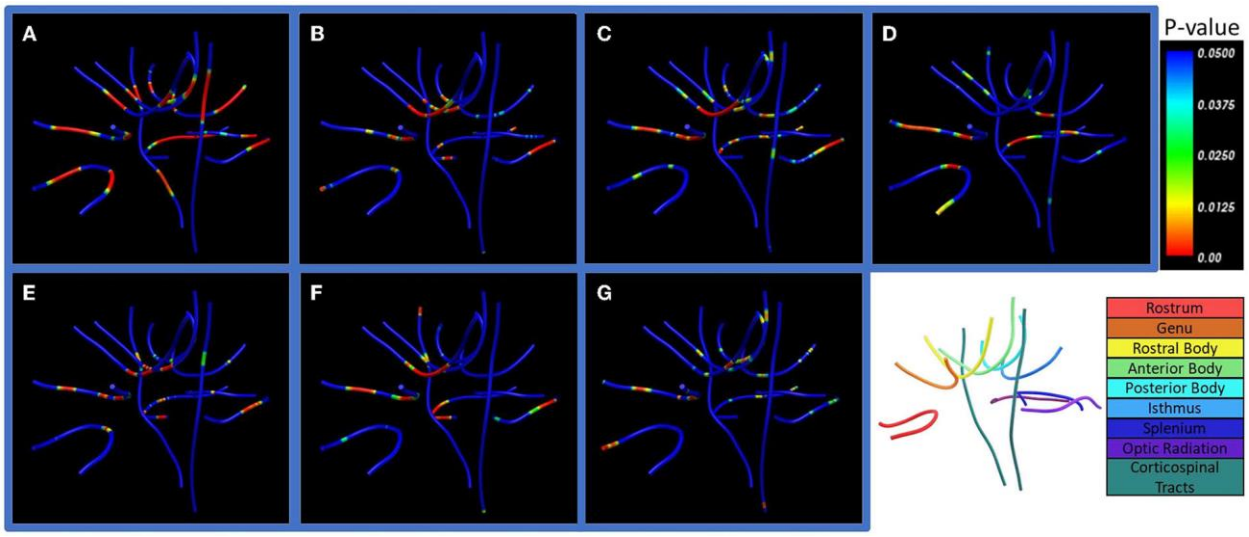

Figure 5.6: Along-tract Statistics between cohorts. Shown are: A) lesion extent, B) orientation dispersion index (ODI), C) fractional anisotropy (FA), D) apparent fiber density (AFD), E) axonal diameter, F) intracellular volume fraction (ICVF), and G) orientation distribution function (ODF) energy. The p-value indicates significance of pointwise cohort differences prior to multiple comparison corrections. Bottom right: Labels of the 7 corpus callosum segments, optic radiation, and corticospinal white matter tracts examined in the study.

5.3.5 Chronic Lesion Analysis

Lesions defined as chronic active had z-scores ranging from 0 to 2.0 (or 0 to -2.0 depending on the investigated measures) based on core versus rim pathology analyses. SPMS patients showed a

14.1%, 18.1%, and 13.2% that corresponded to an average of 3.44, 3.84, and 3.33 more chronic active lesions in SPMS than RRMS patients at z-scores between 0.5 and 1.5 according to axonal diameter, FA, and ICVF (Figure 5.7). In the 0.5 to 1.0 z-score range, the percentage of chronic active lesions in SPMS patients were increased by 18.0%, 12.2%, and 4.9% according to axonal diameter, FA, and ICVF respectively. This corresponded to an average of 3.28, 2.73, and 1.61 more chronic active lesions per SPMS patient than RRMS. According to axonal diameter, FA, and ICVF, 80% – 85% of the measured lesions were chronic active; using AFD, ODF energy, and ODI, 40% – 65% of the measured lesions were chronic active. Examining the number of chronic active lesions based on z-score thresholds, a 0.5 threshold showed cohort differences for all measures, and a threshold of 1.0 showed differences primarily with ICVF, which indicated an average lesion count of 4.56±1.67 for SPMS and 2.17±1.79 for RRMS (Table 5.3).

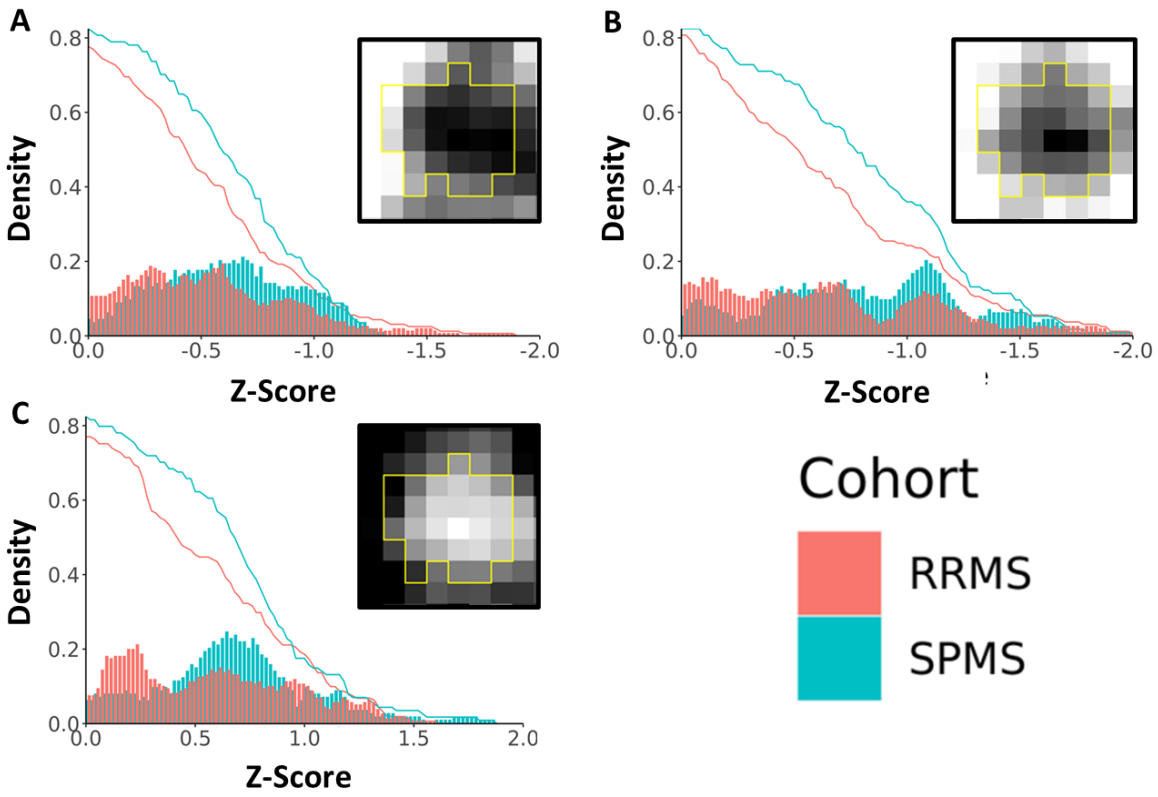

Figure 5.7: Density plot of chronic active lesions per cohort based on a common range of z-scores of diffusion metrics. Shown are results based on A) fractional anisotropy (FA), B) intracellular volume fraction (ICVF), and C) axonal diameter. The histograms (bin size = 0.02) represent the percentage of chronic active lesions, and the red and blue curves represent the accumulated probability of the lesions with equal or more extreme z-scores. The boxed images show example lesion maps of the corresponding diffusion measures.

Table 5.3: The percentage and number of chronic active lesions in each cohort based on z-score definitions

Measures		**RRMS**				**SPMS**			
		>0.5	>1.0	0.5-1.0	0.5-1.5	>0.5	>1.0	0.5-1.0	0.5-1.5
Diameter	% of total	45.3	18.6	26.7	44.7	62.3	17.5	44.7	58.8
	$\#_{lesion}$/pt Mean (s.d.)	4.06 (3.19)	1.67 (1.24)	2.39 (2.45)	4.00 (3.12)	7.89 (2.20)	2.22 (1.56)	5.67 (1.58)	7.44 (1.94)
FA	% of total	44.1	12.4	31.7	41.6	59.6	15.8	43.9	59.7
	$\#_{lesion}$/pt Mean (s.d.)	3.94 (3.33)	1.11 (1.23)	2.83 (2.60)	3.72 (3.23)	7.56 (2.92)	2.00 (1.41)	5.56 (2.92)	7.56 (2.92)
ICVF	% of total	50.9	24.2	26.7	44.7	67.5	36.0	31.6	57.9
	$\#_{lesion}$/pt Mean (s.d.)	4.56 (3.33)	2.17 (1.79)	2.39 (2.23)	4.00 (3.18)	8.56 (3.00)	4.56 (1.67)	4.00 (2.12)	7.33 (2.78)

5.4 Discussion

Through advanced analysis of diffusion and anatomical brain MRI, we have detected significant differences between RRMS and SPMS participants in different scales of tissue pathology. The SPMS individuals show greater NAWM damage across nearly all diffusion and phase congruency-based texture measures of the whole brain. Similarly, increased tissue damage in SPMS is also manifest in both lesions and NAWM within 2 of the 3 critical brain white matter tracks as detected by orientation-informed FA, ODF energy, and ODI diffusion measures. Further, along-tract statistics highlighted significant differences in lesion extent within several callosal segments among others. This is accompanied by dramatically increased percentage and number of chronic active lesions in SPMS compared to RRMS subjects.

It is well known that NAWM plays an important role in disease progression in MS (13,28). However, the exact patterns of change during the process are unclear. Our findings indicate that there is increased tissue damage in the NAWM of SPMS at both micro- and macroscopic levels as shown by advanced diffusion MRI and phase congruency measures. Further, the damage may vary by brain region or tissue type. The observation that the SPMS NAWM shows lower ICVF at p95, greater axonal diameter at p50, and greater orientation dispersion index at p50 histogram regions than RRMS suggest that high density white matter bundles with small diameter and low dispersion are most susceptible to NAWM damage. Texture measures also detected significant differences between RMS and SPMS primarily at sharper structure transition points, as reflected by high phase congruency and low weighted mean phase values. The increase in FLAIR phase congruency and decrease in weighted mean phase may reflect an increased variation in local tissue structure. In contrast, the decreased phase congruency and increased weighted mean phase of T2-w MRI may

reflect increased signal homogeneity due to different factors including reduced axonal packing or density. In this regard, T2-w phase congruency textural sensitivity may concur with ICVF and ODI integrity, deserving further verification. Pinning down the specific patterns of differences in pathology between RRMS and SPMS would permit targeted analysis of brain NAWM thereby increasing the efficiency in the search of non-lesion mechanisms of disease progression in MS.

In contrast to whole brain NAWM analysis, tract-based ROI analysis focused on major white matter tracts known to impact patient function (209,241,242). The corpus callosum plays a significant role in interhemispheric communication. Therefore, it is not surprising to observe significant increases in diffusion damage in the body of corpus callosum of SPMS compared to RRMS in both the NAWM and lesion areas. Cohort differences in the corticospinal tract were also detected by a few diffusion measures showing worsening in SPMS than RRMS but were unilateral and focused on lesions only within the tract. These findings indicate the severity of tissue damage in critical brain regions of SPMS, as all the associated regions of the white matter tracts are important regulators of motor functions (210). Further, current evidence may also highlight that lesion damage within major white matter tracks remain to be critical contributors of advanced disease in MS (243).

Along-tract analysis offered an opportunity to analyze tissue structure properties along the entire length of white matter tracts. Lesion extent appears to be the most significant measure that differentiates SPMS from RRMS, showing increased quantity in SPMS patients in all tracts detected, especially the posterior regions of the corpus callosum and optic radiation. Lesion extent herein measures the percentage of image voxels belonging to lesion areas versus NAWM. While

the findings again highlight the critical role of lesions, consistent with results from ROI-based tract analysis above, lesion extent provides a different measure of pathology in the context of tracts. Lesion extent showed significant cohort differences at symmetric regions between hemispheres, presenting with greater lesion burden than adjacent regions for all tracts. The symmetrical changes in lesion extent between hemispheres are different from the changes in FA, ICVF, and ODI, which showed cohort differences mainly in the midsagittal regions of the brain, such as the genu and rostral body of corpus callosum, warrantee further investigation.

Taking advantage of the sensitivity of diffusion MRI measures to microstructural changes, we have also investigated the activity of chronic MS lesions through the core-rim framework. The dichotomy of the lesion core and rim has been investigated in chronic active lesions previously by others to show DTI sensitivity to regional differences (183,244). In this study, we expanded the lesion core and rim examinations through the z-score framework across a range of diffusion microstructure measures, allowing detailed understanding of individual lesions in both RRMS and SPMS. In this study, cohort differences in the distribution of chronic active lesions over the 0.5 – 1.5 range of z-scores may highlight a critical threshold territory useful for identifying progression from RRMS to SPMS. A z-score of 0.5 indicates a reasonable degree of pathological differences between the core and rim, which may serve as an appropriate threshold to define chronic-active lesions, deserving further verification. ODI, ODF energy, and AFD did not show clear core-rim differences. This may result from their dependence on diffusion orientation models, which may be influenced by reductions in axonal density resulting from pathological damage (118).

There are some limitations in this study. The sample size is relatively small and imbalanced with much fewer persons with SPMS than RRMS. The limited availability of SPMS data is not uncommon in the field because at this stage the disease is mainly driven by insidious progression of disability, such that for where there is no effective treatment frequent imaging is hardly justifiable (245). This imbalance of sample size limits the generalizability of the present findings; however, significant differences were found in different measures between RRMS and SPMS suggesting the viability of the study. Additionally, the high b-value diffusion data used in HARDI analysis is derived from the predicting neural network models rather than data collected directly from participants. While this approach is subject to further confirmation, our pilot results using predicted data demonstrates validity (228), and such approach can be extremely beneficial to clinical scenarios where imaging acquisition time is limited. Further, our diffusion measures present with similar patterns to those shown in the literature, and prior research has found that the outcome measures are equivalent between single-shell and multi-shell HARDI (32). Another limitation is the use of two different datasets. Nonetheless, the impact of dataset combination appears to be mitigated by the similarity of their acquisition protocols, our use of tested techniques to harmonize datasets, and our integration of robust image preprocessing strategies. Specifically, the difference of b values between the two datasets used in our study is 150 s/mm^2, which is well within the allowed threshold (500 s/mm^2 and 1500 s/mm^2) in performing harmonization of diffusion MRI (173). Further, our quantitative results on both the variance and SNR of ROIs in brain white matter confirm the feasibility of our harmonization approaches. Likewise, our use of the contrast-limited adaptive histogram equalization method in phase congruency-based texture analysis should have also helped minimize the impact of corresponding protocol differences. In the future, we seek to validate our findings using additional datasets, extend the z-score paradigm

for chronic active lesion analysis to images with different resolutions and with smaller lesions, and investigate the relationship between chronic active lesion activity and patient function in MS with or without progression.

5.5 Summary

In summary, using advanced diffusion MRI and image texture analysis methods, we found significant differences between RRMS and SPMS subjects across a wide range of measures of brain microstructure. The SPMS participants appear to have increased NAWM pathology at both micro- and macroscopic degrees compared to RRMS participants. Moreover, lesion pathology seems to still play a critical role in disease development in MS, as highlighted by both within-tract and along-tract analyses. Further, using advanced diffusion MRI measures, this study has also developed a novel method for defining the activity of chronic active lesions, a much-needed dimension in understanding functional decline in MS. Overall, this study may provide a useful foundation for future studies of disease progression in MS, as represented by joint analysis of different scales of tissue pathology.

In addition to the above, this Chapter serves as a critical step in the pipeline of developing robust imaging measures for improving disease management for people with MS. In theory, all identified brain diffusion MRI and phase congruency measures that have shown significance in differentiating disease severity between RRMS and SPMS will be carried forward to the next Chapter. However, in both histogram analysis of whole brain NAWM and along-tract analysis, only a few variables are identified. As such, only significant variables out of the tract-based analysis will be evaluated in Chapter 6. This approach will include both lesions and non-lesion

regions within the tracts, and include all three critical brain white matter tracts commonly impacted in MS. Therefore, the current tract-based outcomes are thought to be reasonable representations of the whole brain MS pathology investigated. Finally, the analytical approach developed to characterize chronic active lesions based on diffusion MRI in this Chapter also appears to be valuable but needs further confirmation and therefore will not be brought forward to Chapter 6.

Chapter 6: Advanced brain imaging measures based on diffusion MRI and texture analysis predict functional outcomes in MS and control participants

Structure determines function. In a complex pathological condition such as MS, different types of structural measures may relate to different categories of functional outcomes, depending on the location and severity of tissue injury. Assisted by advanced image analysis technologies, this thesis has discovered several new measures of brain pathology in the context of MS. Specifically, in Chapter 4, I have identified several diffusion MRI and MRI phase congruency measures that are sensitive to brain MS pathology, including measures differentiating different portions of individual lesions. The top-performing measures are then confirmed for their potential to distinguish disease severity (e.g. RRMS vs SPMS) in Chapter 5. Despite the promising results, the relationship of the identified imaging measures with function is not fully understood in people with MS. The goal of the current Chapter is to assess how the identified imaging measures that show significance in Chapter 5 relate to functional outcomes in MS participants and matched controls. To improve understanding, the investigation has included functional metrics from physical, cognitive, and affective domains. Further, given the importance of injury type and location, as well as the relevance of key white matter tracts of the brain with patient function, this Chapter focuses on tract-based measures from Chapter 5, in both lesion and NAWM regions. Furthermore, using a machine learning approach known as Ridge Regression, different prediction models have been built. This process characterizes which and how the identified imaging measures are associated with each functional outcome, and how the models compare with each other.

6.1 Introduction

The ultimate consequence of tissue injury in MS is functional decline that may involve different domains spanning physical, psychological, and neurocognitive areas (17), causing severe health and socioeconomic burden. Clinically there are a variety of measures present for assessing functional outcomes in MS but these measures are not sensitive to short-term changes or to subclinical disease activity, limiting the opportunity for early intervention and prevention. Advanced MRI is an ideal candidate for characterizing invisible changes in neural structure and has the potential to identify pathology processes that underlie early functional impairment (246). However, the utility of advanced MRI for predicting functional outcomes in MS is largely unknown.

Diffusion MRI is one of the promising advanced MRI techniques able to detect subtle structural changes in a neural tissue through characterization of biophysical signals resulting from the diffusion phenomenon of water protons within a tissue. With collection of these signals across multiple orientations, diffusion MRI assesses both the magnitude and orientation of water movement, supporting in-depth tissue structure analyses (111,247). Assisted by relevant modeling strategies, diffusion MRI offers several competitive estimates of axonal and myelin integrity. DTI is a signal model which reflects the orientation and magnitude of diffusion along 3 perpendicular axes. DTI fractional anisotropy (FA) in brain white matter tracts specific to phonemic processing has demonstrated a moderate correlation with verbal fluency in people with MS (248). Nonetheless, DTI has limitations especially that it assumes the presence of a single-fiber group in a modelled voxel, which is not the case in many brain regions and which makes the method difficult to employ for modelling complex neural fiber architectures.

High angular resolution diffusion imaging (HARDI) is an advancement of diffusion MRI. With improved characterization of diffusion orientation and compartmental complexity, HARDI measures are sub-voxel-based and therefore are expected to be more sensitive and specific than the voxel-based DTI to nerve structure characteristics (111). The apparent fiber density (AFD) is an example HARDI measure that estimates intra-axonal water content (171), which has similarities in concept to FA but has increased specificity to axonal density (249). In addition, different biophysical models, such as neurite orientation dispersion and density index (NODDI), can be applied to HARDI for multiple compartmental tissue analysis (113). In people with MS, the NODDI orientation dispersion index (ODI) measured in brain lesions is associated with global cognitive impairment (250). However, the relationship between HARDI measures and functional outcomes in MS is largely unexplored. While not completely clear, one critical reason could be the long imaging time required by HARDI as it typically demands multiple copies of diffusion acquisition, which is not always feasible in clinical settings. As shown in previous Chapters, we have implemented novel deep learning methods for bridging this gap (33,169). By using data from only a single b-value acquisition of diffusion MRI, which saves 50% of the imaging time, I have derived measures equivalent to full-acquisition HARDI. Using the customized approach, my tract-based measures have shown the strong potential in differentiating RRMS from SPMS (33). These tested time-saving HARDI approaches will be applied in this Chapter.

In addition to advanced MRI, advanced analysis of conventional MRI has also shown the promise for robust characterization of neural structure, such as texture analysis (251,35). Similar to the diffusion MRI outcomes, tract-based phase congruency indices in lesions and NAWM based on conventional MRI have significantly differentiated RRMS and SPMS cohorts (Chapter 5) (33).

But the functional correlates of phase congruency measures are unclear in either healthy or MS conditions.

Functional impairment in MS can be manifest in different areas ranging from clinical to neuropsychological outcomes (25,50,62). Expanded disability status scale score (EDSS) is a common assessment of physical disability although not without limitations, including its insensitivity to lower limb function (6,21,50,63). The multiple sclerosis functional composite (MSFC) may improve upon EDSS as it includes tests of both upper limb and lower limb function, as well as cognitive function, namely working memory (62,63,252). The minimal assessment of cognitive function in MS (MACFIMS) represents a dedicated suite of neurocognitive examinations but while each measure has its value, their capability to explain the variance of functional measures in MS varies (6,63,66). Moreover, although considerable efforts have been made, conducting functional assessments are still time consuming and subject to human errors.

The goal of this chapter is to establish models that best predict functional outcomes of people with MS manifest in different domains based on significant diffusion MRI and phase congruency measures of the brain as derived in previous Chapters. Given the recognized connections between critical brain white matter tracts and functional measure of an individual, the investigations are driven by tract-based analysis, in both MS and matched healthy control people for comparison.

6.2 Materials and Methods

6.2.1 Sample

This study takes advantage of a set of archived data acquired from a previous clinical study with the initial goal of identifying functional measures of repair in MS using the corpus callosum model. This dataset includes 19 people with MS and 19 age-, sex- and education-matched healthy controls (167). Of the 19 MS participants, ten have RRMS with disease duration less than ten years, EDSS ≤ 3.0, and age 38.7 (28–53), and nine have SPMS defined by EDSS ≥ 6.0, where disease duration was 17 – 37 years, and age 58.2 (49–75) years. Individuals who had received steroid treatments or chemotherapy within the past two years or experienced optic neuritis within the past year were excluded. Functional examinations were performed, following MRI on the same day. The study was approved by the Conjoint Health Research Ethics Board of the University of Calgary, and written informed consent was obtained from all participants.

6.2.2 Imaging Protocol and Image Processing

All participants had undergone 3T MRI (Discovery MR750; GE Healthcare, Milwaukee, USA) at the Seaman Family MR Research Centre, Foothills Hospital, Calgary. Imaging protocol included both anatomical T1-weighted, T2-weighted, and FLAIR MRI and single b-value diffusion MRI of the brain. As mentioned in Chapter 5, T1-weighted MRI was acquired with a fast-spoiled gradient echo sequence with isotropic voxels sized $1mm^3$; T2-weighted MRI was acquired with a spin-echo sequence with a 2mm isotropic in-plane resolution and 3mm slice thickness; and FLAIR MRI was acquired with a spin-echo inversion recovery sequence with an isotropic resolution of 0.469 mm. In addition, diffusion MRI was acquired using a spin-echo echo-planar sequence where the in-plane resolution was 2mm; slice thickness was 3mm; and b-value was 850 s/mm^2, with 23

diffusion directions and 5 b0 volumes (33). The same protocol was applied to both MS participants and healthy controls. Image preprocessing was done as detailed in Chapter 5 for both anatomical and diffusion MRI (33). Briefly, the steps included Gibbs ringing correction, N4 bias field correction, brain extraction, and MNI-152 rigid body alignment. To enable thorough analysis of diffusion MRI, a new dataset with b=2000 s/mm^2 was predicted per subject using our established neural networks (169). Predictions were done based on the b=1000 s/mm^2 diffusion data, which in turn was obtained by regressing the original b=850 s/mm^2 diffusion MRI.

6.2.3 Diffusion Outcome Calculation

Calculating diffusion MRI metrics used the same approaches as described in previous Chapters. The specific measures to be calculated were determined based on findings in Chapter 5, which was also a reflection of significant information discovered in Chapter 4. Specifically, only diffusion MRI (and phase congruency measures) that showed significance in differentiating RRMS and SPMS in tract-based analysis were used in this Chapter. The three major white matter tracts of the brain (corpus callosum, CST, optic radiation) underlie many functional presentations in health and disease, and by including both lesion and non-lesion areas (NAWM) wherein, the tract-based assessments serve as a reasonable representation of the whole brain pathology as studied in Chapter 5. Briefly, this Chapter computed DTI FA using FSL, NODDI orientation dispersion index (ODI) using the accelerated microstructure imaging with convex optimization (AMICO) (121) implementation, intracellular volume fraction (ICVF) and axonal diameter based on the ActiveAx model from AMICOx (114,122), and apparent fiber density (AFD) (171) and our customized orientation distribution function (ODF) energy from advanced modelling of diffusion orientation and strength (33).

6.2.4 Textural Phase Congruency Outcome Calculation

Phase congruency analysis also followed the tract-based approach as described above with a focus on measures that differentiated RRMS and SPMS in Chapter 5. The calculation included 2 parameters: sum of phase congruency (PC), which is a measure of edge strength, and weighted mean phase (WMP), which is a measure of edge sharpness. These outcomes were calculated for T2-weighted and FLAIR MRI as they typically show more abnormality than T1-weighted MRI, using a 3D implementation of the method. The computing settings were optimized to obtain even spectral coverage, define a slowly-transitioning sigmoid function (gain=10.0, cutOff=0.5) to weight for frequency spread, and define evenly oriented filters using a convenient 3D orientation scheme borrowed from the diffusion data with 23 directions. Further, each metric was calculated with maximum wavelengths of 16mm and 32mm that permitted to focus on imaging features having a similar scale to MS lesions.

6.2.5 Tract-based Analysis

All diffusion MRI and phase congruency measures were measured using the ICBM-DTI-81 white matter atlas to identify the specific tracts of interest. These included: genu, body, and splenium of the corpus callosum, as well as the bilateral corticospinal and optic radiation tracts (235,236). Lesions and NAWM were independently measured within each of the analyzed tracts. Measurements within corticospinal and optic radiation tracts were averaged across the two hemispheres as preliminary data showed few differences between them.

6.2.6 Functional Measurements

All functional measures were conducted by a neuropsychologist associated with the initial clinical study (63,66). Overall, 14 clinical and neuropsychological assessments generated 20 functional measures, where one was specifically investigated in MS. Nine assessments were drawn from the MSFC and MACFIMS batteries, and five from common and alternative MS examinations (66,68,253–255). Based on the nature of the tests and for ease of descriptions, the identified assessments were categorized into 3 groups: Physical, Cognitive, and Affective (Table 6.1). In addition, to maximize the understanding of impact, only functional outcomes that were significantly different ($p<0.05$) between the MS and control cohorts were used in subsequent analyses.

Table 6.1: Assessments of physical, cognitive, and affective measures of MS disease severity

Assessment	Abbr.	Testing Battery	Investigated outcome	Function Involved	Function Domain
Timed 25-Foot Walk	T25FW	MSFC	Best time (s)	Ambulatory function	Physical
Nine-Hole Peg Test	NHPT	MSFC	Average time (s)	Upper limb function	Physical
Expanded Disability Status Scale	EDSS	———	Score	Clinical disability	Physical
Purdue Pegboard	———	———	# of pins inserted	Upper limb function	Physical
Paced Auditory Serial Addition Test	PASAT	MSFC/ MACFIMS	Total correct	Processing speed and working memory	Cognitive
Symbol Digit Modality Test	SDMT	MACFIMS	Total correct	Processing speed and working memory	Cognitive
Brief Visuospatial Memory Test	BVMT	MACFIMS	Immediate and delayed recall	Learning and memory	Cognitive
California Verbal Learning Test-II	CVLT-II	MACFIMS	Immediate, short delay, and long delay recall	Learning and memory	Cognitive
Delis-Kaplan Executive Function System (D-KEFS) Sorting Test	DST	MACFIMS	Free recall correct sorts and description score	Executive functions	Cognitive
Judgement of Line Orientation	JLO	MACFIMS	Total correct	Visual perception and spatial processing	Cognitive
Controlled Oral Word Association Test	COWAT	MACFIMS	Total # of words	Language skills	Cognitive
Tactile Temporal Threshold	TTT	———	Total and component times	Signal and information processing	Cognitive
Modified Fatigue Impact Scale	MFIS	———	Total score	Fatigue	Affective
Beck's Depression Inventory	BDI	———	Total score	Depression	Affective

6.2.7 Development of Function Predicting Models

Ridge regression was employed as the backbone of the prediction models as the method has shown an improved generalization ability to unseen data and robustness to multicollinearity (256). Based on chosen diffusion MRI and phase congruency measures confined in the three white matter tracts (corpus callosum, corticospinal, and optic radiation tracts), three series of prediction models were established, each per study group: MS alone, healthy control alone, and together (All). In each

group, one unique model was implemented for each functional outcome that served as the dependent variable, and the most relevant imaging measures served as independent variables or predictors. In addition, depending on the white matter tract type involved, the imaging measures were further grouped as NAWM-based, and NAWM plus lesion-based (Figure 6.1).

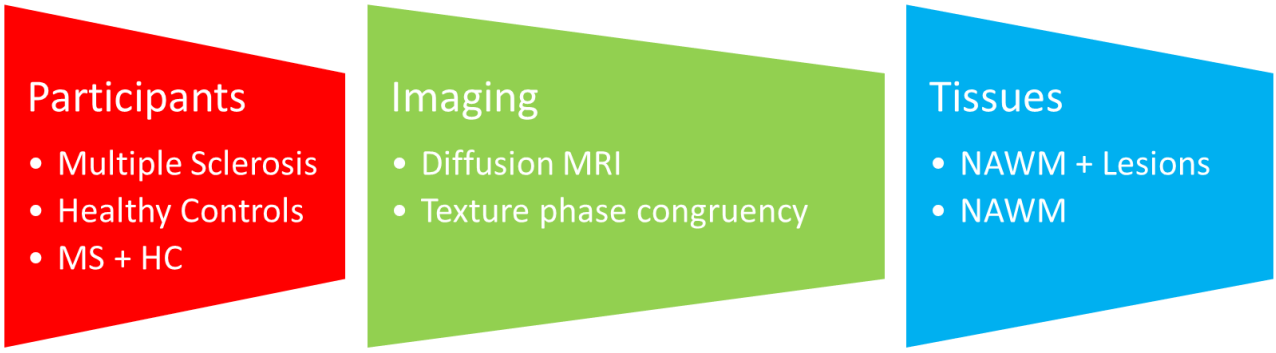

Figure 6.1: Parameters involved in the ridge regression models constructed to predict individual functional outcomes. There were 3 participant groups, 2 imaging types, and 2 tissue types available in the predictor toolbox. Healthy control models were only constructed with NAWM-based measures.

The model implementation process included 2 steps: feature selection, and function prediction. Each involves a 5-fold cross-validation (CV) approach to improve validity. Initially, the data from an individual participant group was 5-fold split into train (4 folds) and test (1 fold) portions (step 1). The train portions were combined and further split with 5-fold CV into train and test partitions again for feature selection (step 2). This step was achieved using a recursive feature elimination (RFE) method in tandem with the ridge regression implementation of the glmnet (v.4.0_2) package. During analysis for each iteration of train portions, RFE provided a ranking of all imaging variables and age and education covariates used as input, and the list of variables that contributed to the peak performance of the relevant model. Eventually, an average ranking across all CV training combinations of RFE was obtained for each peak performance-contributing variable sets.

These variables together formed the base of the predicting measures for step 3. The RFE analyses were achieved with minimization of the root mean squared error (RMSE).

In developing the function prediction models, the RFE-selected variables from step 2 mentioned above were fit to combined train folds of step 1. The resulting models after each cross-validation iteration were employed to predict individual clinical outcomes using the corresponding test folds. Functional prediction performance was assessed using the RMSE and r-squared (coefficients of determination) indices obtained at each prediction; their average across 5 predictions was derived for further analysis. In addition, the RMSE was normalized by the standard deviations of the corresponding functional measure to allow optimal comparison between models. Finally, predicted results were compared with the observed results for all individual functional outcomes, and the presence of correlation as well as the correlation strength were used as estimates of the prediction ability of the applied imaging features. All analyses used the caret package in R (v.3.6.3).

6.2.8 Statistical analysis

Two-sample comparison used a paired t-test or Wilcoxon signed-rank test for normally or non-normally distributed data. Data normality was evaluated using the Shapiro-Wilk test. Pearson correlation was used to assess the relationship between predicted and observed functional outcomes, where the effect size of the model predictions for each functional assessment was also investigated, which was defined as weak ($0.1 \leq r < 0.3$), moderate ($0.3 \leq r < 0.5$), or strong (≥ 0.5) irrespective of significance. Further, Fischer's z-transformation was applied to compare Pearson's r between prediction models.

6.3 Results

6.3.1 Sample Characteristics

This study included 19 MS participants (10 with RRMS and 9 with SPMS; all being right-handed women), and 19 age- and sex-matched healthy control people. The average age was 47.9 ± 13.0 (mean ± sd) years for MS participants, and 50.5 ± 12.0 years for controls. Age ranged from 25 to 75 years per group. Years of education ranged from 12 – 23 years for those with MS and 12 – 19 years for healthy individuals. Those with MS had an average lesion load of 18.0 ± 21.4 mL (Table 6.2).

Table 6.2: Demographics of the MS and control (HC) participants.

	Age (%ile)	Education (%ile)	Disease Duration (%ile)	EDSS	Lesion Load (mL)	HC Age (%ile)	HC Education (%ile)
MS1	50	50	70	6.5	9.893	70	40
MS2	70	0	60	6.5	24.691	80	40
MS3	60	10	80	7.5	25.335	70	20
MS4	20	50	0	2	26.301	30	20
MS5	70	50	60	6.5	19.003	80	90
MS6	90	20	70	6	13.364	90	10
MS7	70	90	20	3	6.440	80	50
MS8	40	80	20	0	3.997	50	0
MS9	20	50	20	3	1.228	40	20
MS10	80	0	90	6	34.730	80	10
MS11	50	20	90	6.5	93.484	60	90
MS12	80	40	50	7	14.051	80	50
MS13	100	20	80	6	18.681	90	0
MS14	10	40	10	1	0.035	20	50
MS15	0	50	50	1	5.790	0	80
MS16	0	20	20	2.5	34.017	10	80
MS17	10	0	0	2	0.782	20	50
MS18	30	50	20	2	6.480	50	10
MS19	30	50	40	0	3.848	40	0

Note: MS — Multiple Sclerosis; HC — Healthy Controls

6.3.2 Functional Assessments in MS versus Controls

There were nine measures showing significant differences between MS and healthy controls (Figure 6.2; Table 6.3). These included both affective assessments (BDI and MFIS), four cognitive assessments (BVMT, COWAT, SDMT, and TTT), and three physical assessments (NHPT, Purdue Pegboard, and T25FW. These nine measures each served as the dependent variable in corresponding functional prediction models per participant group in the follow up sections. In addition, as EDSS was only available in MS participants, this outcome was not compared but modelled as well to gain further understanding.

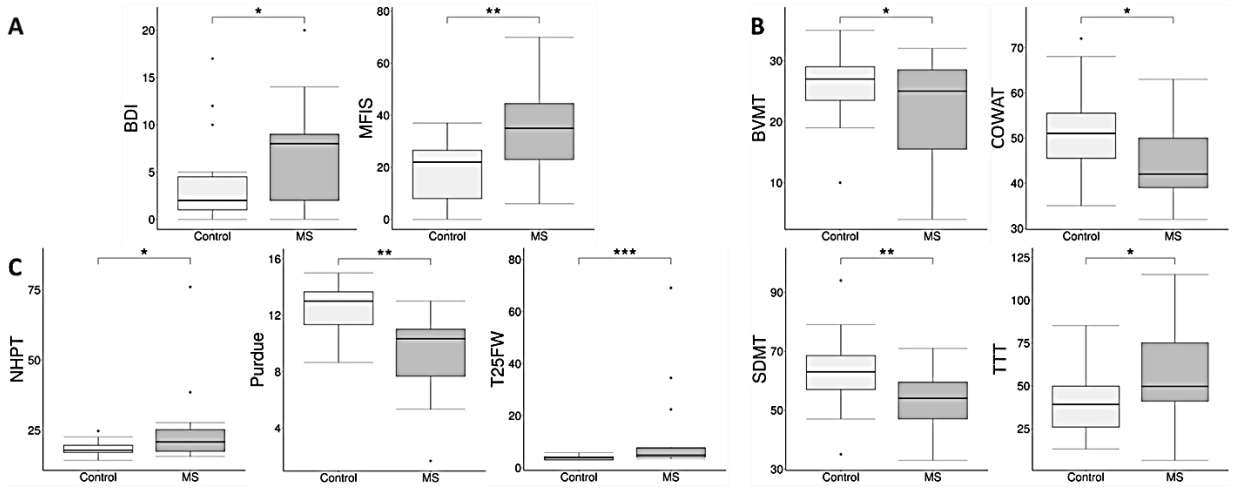

Figure 6.2: Comparison of functional outcomes between MS and matched healthy participants. Note: the stars indicate significance: *p < 0.05, **p < 0.01, ***p < 0.001. The boxes plot the median, interquartile range (IQR), and 1.5*IQR.

Table 6.3: Comparison of functional assessment scores between MS and control participants

Assessment	Outcome	MS		HC		p-value	Cohen's d
		Mean	S.D.	Mean	S.D.		
Purdue Pegboard	Pins inserted (#)	9.35	2.86	12.40	1.84	0.001	0.897
TTT	Total and sub-times (ms)	57.96	30.35	39.11	17.05	0.023	0.632
T25FW	Best time (s)	11.31	16.45	3.80	0.78	0.000	0.457
NHPT	Average time (s)	24.65	13.63	18.39	2.54	0.018	0.436
SDMT	Total correct (#)	52.47	11.29	63.26	12.69	0.002	0.846
BVMT	Immediate recall total correct (#)	22.05	8.73	26.26	5.76	0.014	0.663
	Delayed recall total correct (#)	8.84	3.56	10.42	1.95	0.019	0.577
COWAT	Total words (#)	44.26	8.38	51.58	10.38	0.029	0.545
MFIS	Total score (#)	33.74	15.74	19.11	11.10	0.007	0.702
BDI	Total score (#)	7.00	5.23	3.84	4.55	0.050	0.444

Note: MS — Mulltiple Sclerosis; HC — Healthy Controls

6.3.3 Feature selection outcomes based on RFE

Across all participant group analyses, approximately 50% of the input imaging features contributed to peak performance of the RFE models and were selected for use in subsequent predictions of functional outcomes. For diffusion-based NAWM models, AFD in the corticospinal and splenium tracts, FA in the corpus callosum body, and ICVF and Axonal Diameter in the optic radiation were frequently selected for all participant groups. Similarly, for diffusion-based NAWM+Lesions models, AFD and FA were again frequently selected along with ICVF of the optic radiation NAWM. Measures in CST lesions were also routine additions to the prediction models (Figure 6.3 & Figure 6.4; Supplementary Figures).

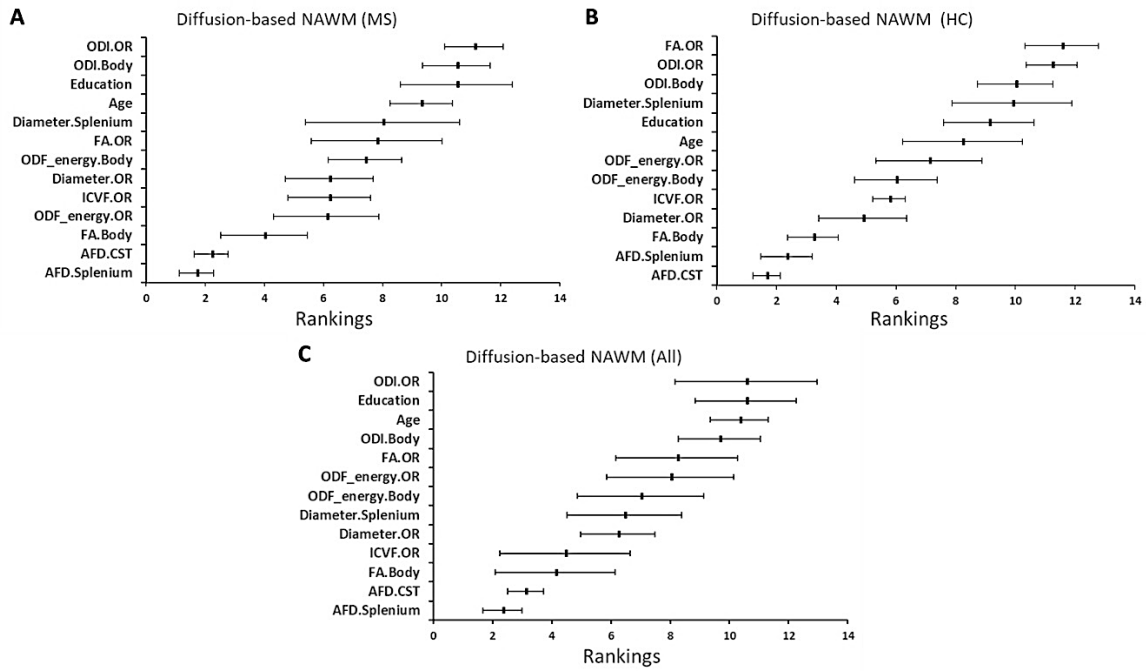

Figure 6.3: Diffusion-based NAWM feature rankings across all assessments. Shown are average feature rankings with 95% confidence intervals derived from ridge regression recursive feature elimination. Features are listed on the y-axis as measurement-tract combinations for A) MS, B) healthy control, and C) all participant analyses.

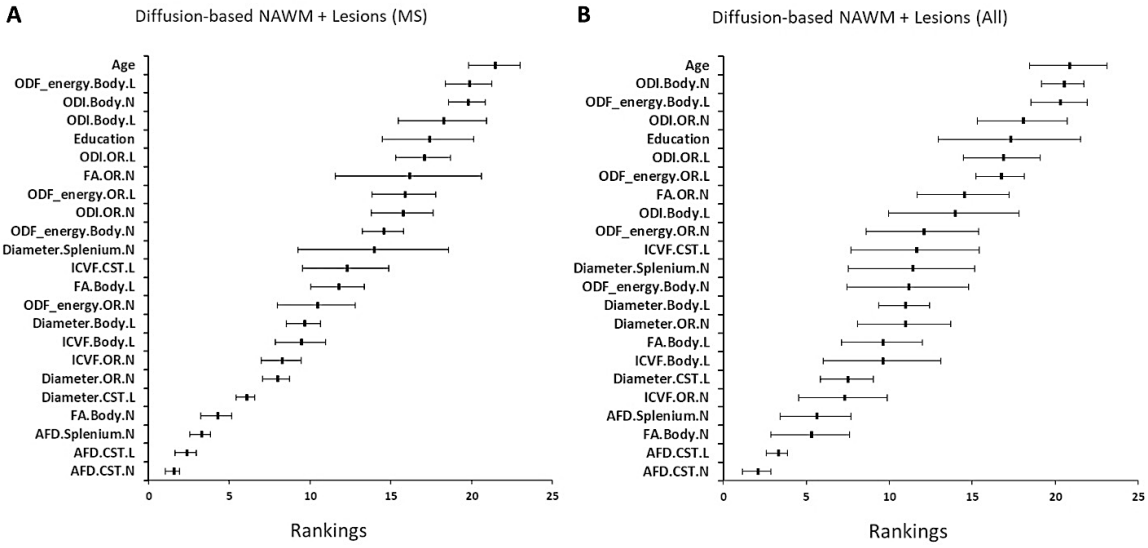

Figure 6.4: Diffusion-based NAWM+Lesions feature rankings across all assessments. Shown are average feature rankings with 95% confidence intervals derived from ridge regression recursive feature elimination. Features are listed on the y-axis as measurement-tract-tissue combinations for A) MS and B) all participant analyses.

Similar to diffusion models, approximately 50% of input imaging features based on phase congruency analyses were selected by RFE. The most frequently selected features were: high-frequency PC of the optic radiation and lower frequency WMP of the corpus callosum body, followed by WMP32. For the NAWM+Lesions models, 50% of the phase congruency features were typically selected, which included higher frequency T2-w and FLAIR PC from tract lesions. In addition, the covariates age and education were also selected frequently. To understand specifically how the texture imaging features impact the functional prediction models subsequently, the covariates were excluded and RFE rankings were found to be similar with and without covariates (Figure 6.5 & Figure 6.6).

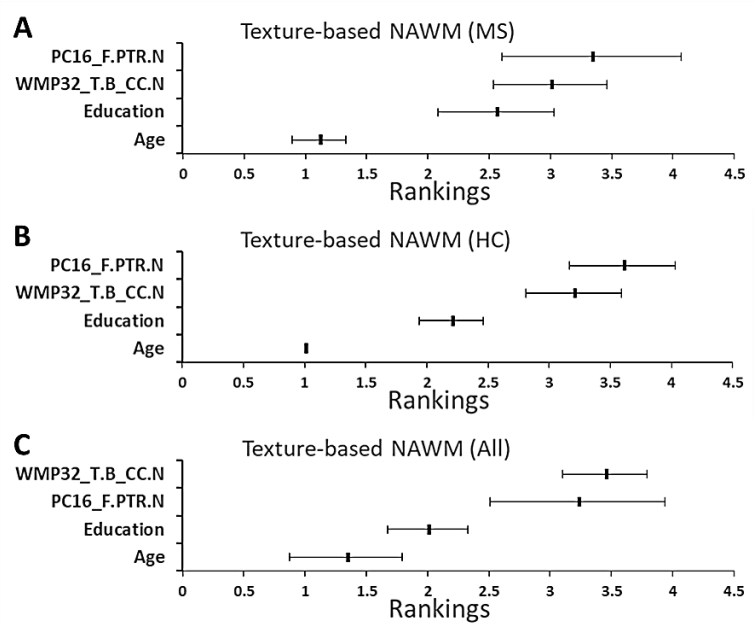

Figure 6.5: Textural phase congruency-based NAWM feature rankings across all assessments. Shown are average feature rankings with 95% confidence intervals derived from ridge regression recursive feature elimination. Features are listed on the y-axis as measurement-tract combinations for A) MS, B) healthy control, and C) all participant analyses.

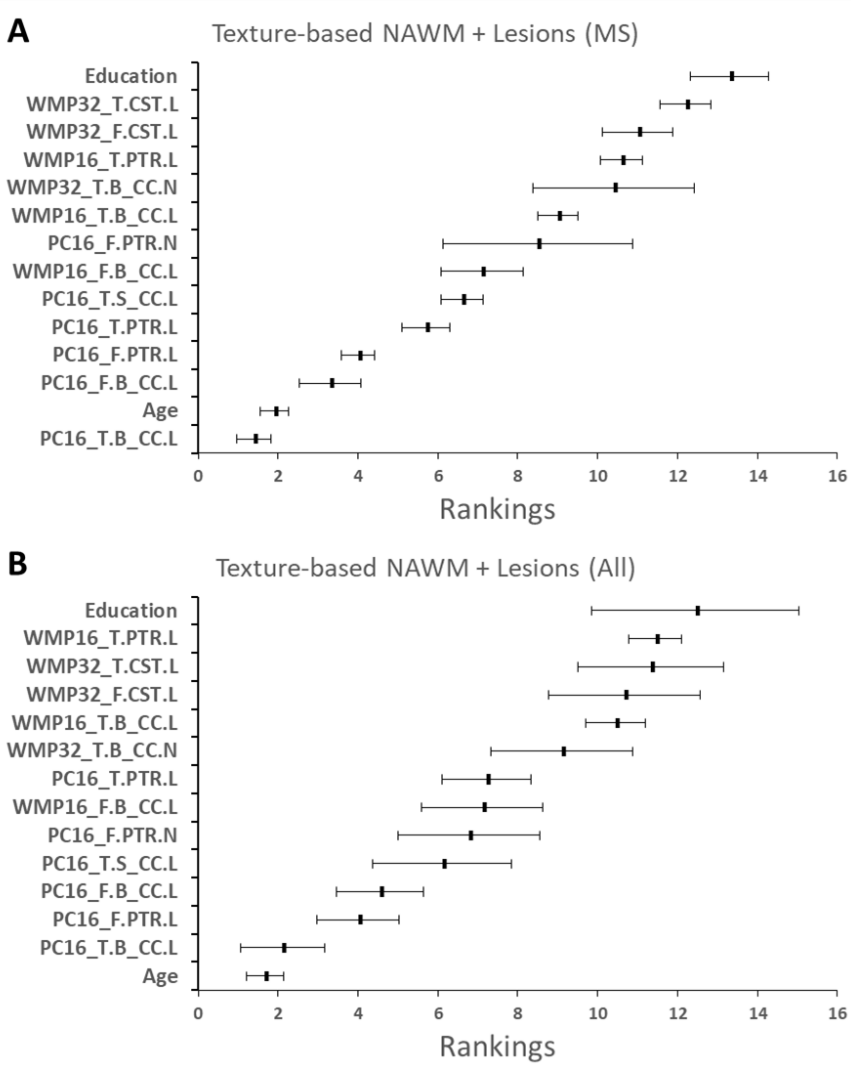

Figure 6.6: Textural phase congruency based NAWM+Lesion feature rankings across all assessments. Shown are average feature rankings with 95% confidence intervals derived from ridge regression recursive feature elimination. Features are on the y-axis listed as measurement-tract-tissue combinations for A) MS and B) all participant analyses.

6.3.4 Prediction model Outcomes

Prediction models were constructed using RFE-chosen features from diffusion MRI and phase congruency in tract NAWM or NAWM+Lesions areas. The model results below are divided by the type of functional outcomes and participant group.

Physical Assessments

For MS participants, predicted EDSS results using diffusion-based NAWM measures (RMSE=0.78sd, R^2=0.65; p<0.0001) and NAWM+Lesions measures (RMSE=1.05, R^2=0.52; p<0.0001) were strongly and moderately correlated to observed outcomes, respectively. Similarly, predictions with texture-based NAWM measures (RMSE=0.60sd, R^2=0.77; p<0.0001) and NAWM+Lesions measures (RMSE=0.84sd, R^2=0.66; p<0.0001) were strongly and moderately correlated to observed findings, respectively. Predicted results using diffusion-based NAWM measures for NHPT (RMSE=0.98sd, R^2=0.56; p<0.05) and Purdue pegboard (RMSE=1.29sd, R^2=0.40, p>0.05) were weakly correlated to the corresponding observed outcomes. Predicted results for NHPT by diffusion-based NAWM+Lesions measures (RMSE=0.96sd, R^2=0.48; p<0.01) were moderately correlated with the observed outcomes. Regarding phase congruency measures, predicted NHPT by texture-based NAWM measures (RMSE=0.71sd, R^2=0.76; p<0.0001) and NAWM+Lesions measures (RMSE=0.83sd, R^2=0.63; p<0.0001) each were strongly correlated with the observed outcomes. In contrast, predicted results for Purdue pegboard by texture-based NAWM measures (RMSE=0.91sd R^2=0.41; p<0.01) showed a weak correlation with the observed outcomes. For T25FW, the predicted results by both diffusion-based NAWM (RMSE=0.83sd, R^2=0.86; p<0.0001) and texture-based NAWM measures (RMSE=0.58, R^2=0.87; p<0.0001) were strongly correlated with the observed outcomes (Figure 6.7 & Figure 6.8).

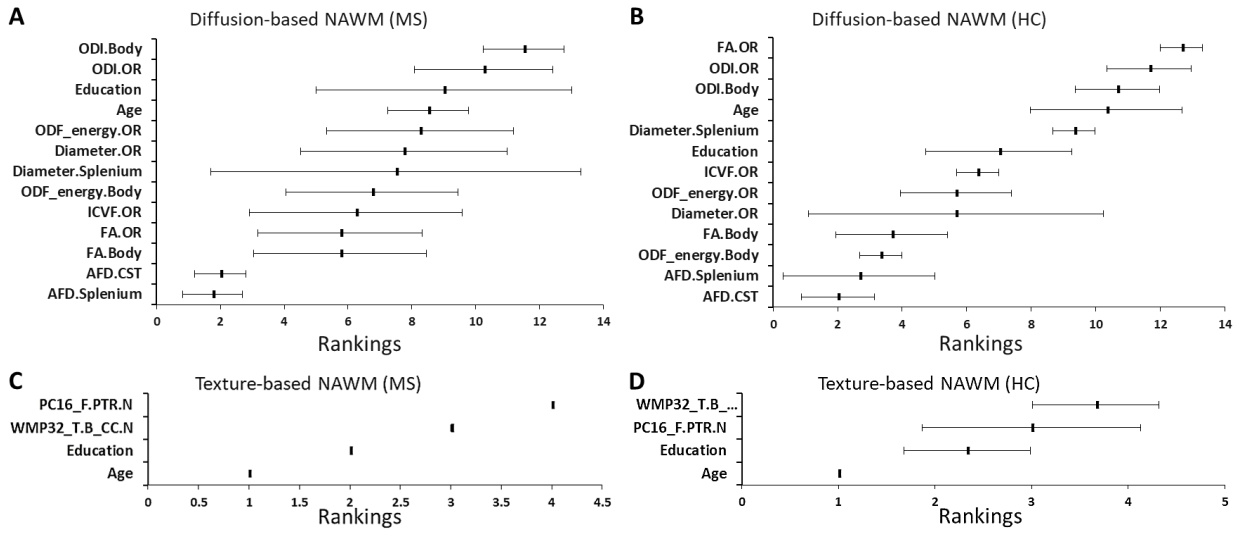

Figure 6.7: Diffusion- and Textural phase congruency-based NAWM feature rankings across physical assessments. Shown are average feature rankings with 95% confidence intervals derived from the recursive feature elimination process of ridge regression. Features are listed on the y-axis as measurement-tract combinations for A,C) MS and B,D) healthy control participant analyses.

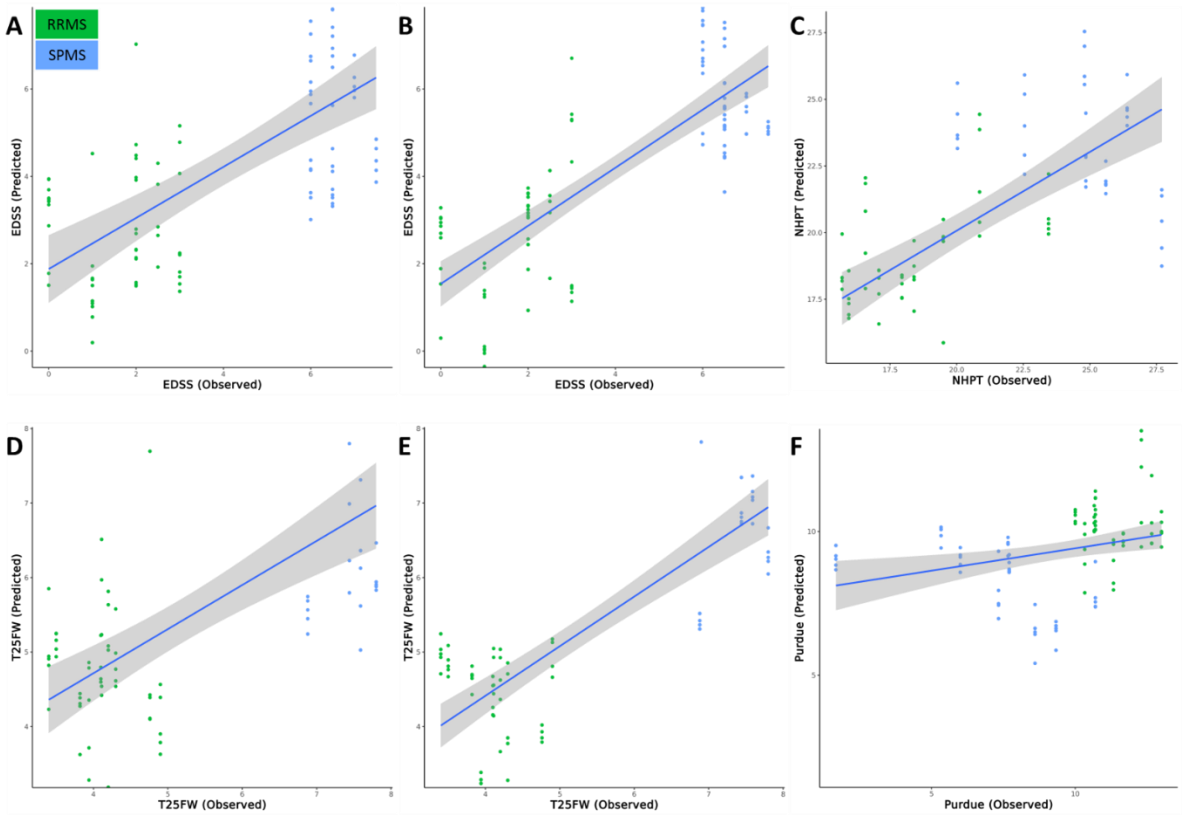

Figure 6.8: Predicted versus observed values for physical assessments of MS participants. Shown are Pearson Correlations between observed and predicted affective outcomes, with the latter derived using diffusion-based NAWM measures regarding EDSS (A), NHPT (C), T25FW (D) and Purdue pegboard (F), respectively, and texture-based NAWM measures regarding EDSS (B) and T25FW (E), respectively. Note: EDSS: Expanded Disability Status Scale; NHPT: Nine-Hole Peg Test; T25FW: Timed 25-Foot Walk; Purdue: Purdue pegboard.

For healthy controls, all correlations between predicted and observed results were non-significant for NHPT. For Purdue pegboard, the predicted results by NAWM-based measures from both diffusion MRI (RMSE=1.00sd, R2=0.43; $p<0.001$) and phase congruency (RMSE=0.93sd, R2=0.43; $p<0.01$) were moderately correlated with the observed outcomes with comparable performance. Further, for T25FW, the predicted results by diffusion- and texture-based NAWM measures (RMSE=0.82/0.82sd, R^2=0.53/0.53; $p<0.0001$) were comparable; both showed a moderate correlation with the observed outcomes (Figure 6.9).

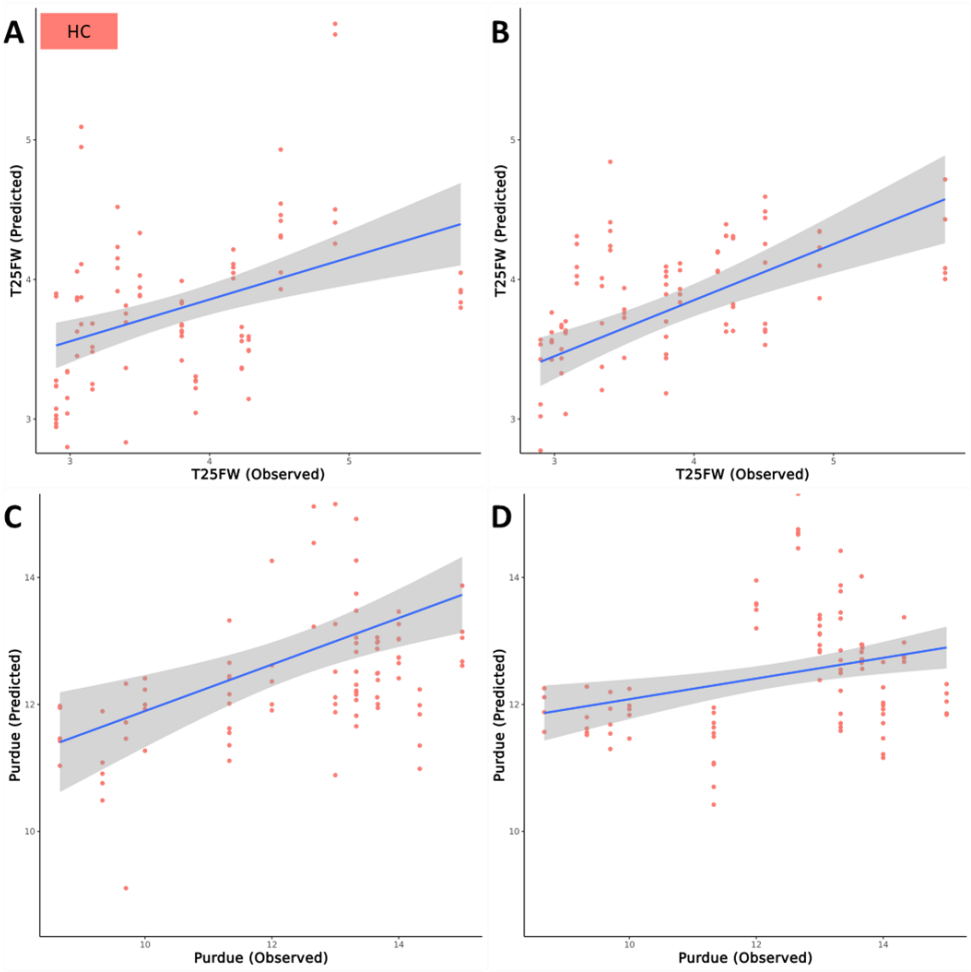

Figure 6.9: Predicted versus observed values for physical assessments of healthy participants. Shown are Pearson Correlations between observed and predicted affective outcomes, with the latter derived using diffusion-based NAWM measures regarding T25FW (A) and Purdue (C), respectively, and texture-based NAWM measures regarding T25FW (B) and Purdue (D), respectively. Note: T25FW Timed 25-Foot Walk; Purdue: Purdue pegboard.

For MS and control participants combined, the predicted results for NHPT based on diffusion-based NAWM (RMSE=0.94sd, R2=0.33; $p<0.0001$) and NAWM+Lesions (RMSE=1.17sd, R2=0.24; $p<0.05$) measures were moderately and weakly correlated with the observed outcomes, respectively. In comparison, the predicted NHPT by texture-based NAWM (RMSE=0.81, $R^2=0.38$; $p<0.0001$) and NAWM+Lesions (RMSE=0.83, $R^2=0.35$; $p<0.0001$) measures were both strongly correlated to the observed results. For Purdue pegboard, the predicted results by diffusion-

based NAWM (RMSE=0.93sd, R^2=0.49; p<0.0001) had a moderate correlation with the observed findings. In contrast, the predicted results by texture-based NAWM+Lesions measures (RMSE=0.79sd, R^2=0.48; p<0.0001) correlated strongly with the observed data, and the correlation was also significantly better than predictions using texture-based NAWM measures (RMSE=0.88sd, R2=0.23; p<0.0001) alone (p<0.01). Regarding the T25FW, the predicted data by diffusion-based NAWM (RMSE=0.76sd, R^2=0.56; p<0.0001) and texture-based NAWM+Lesions (RMSE=0.80sd, R^2=0.49; p<0.0001) measures were both strongly correlated with the observed findings with a similar strength (Figure 6.10 & Figure 6.11).

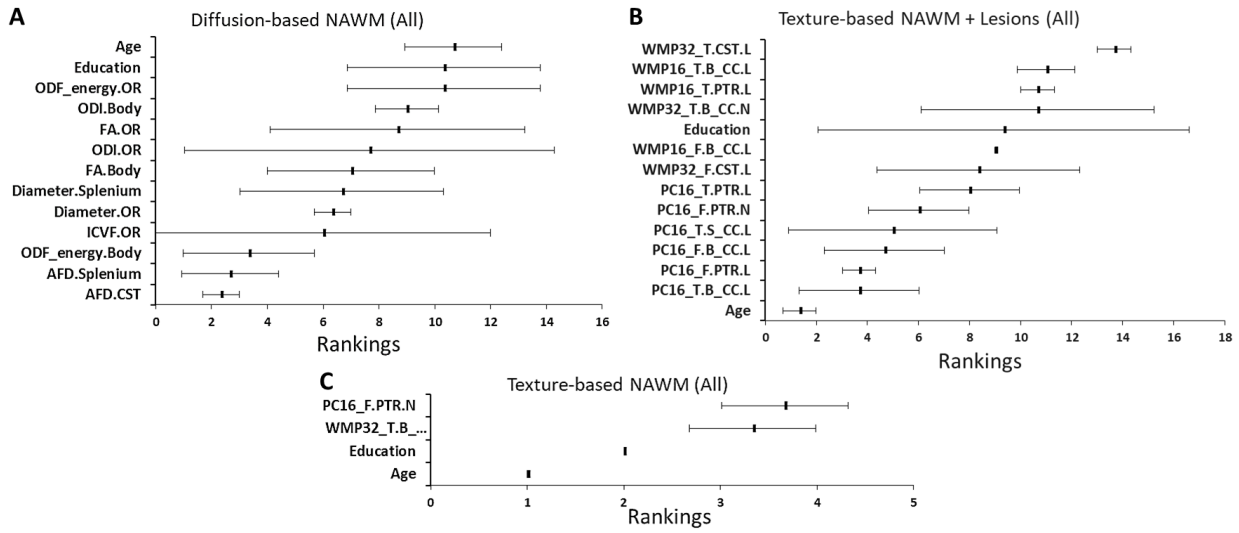

Figure 6.10: Diffusion- and Textural phase congruency-based NAWM and NAWM+Lesions feature rankings across physical assessments. Shown are average feature rankings with 95% confidence intervals derived from the recursive feature elimination process of ridge regression. Features are listed on the y-axis as measurement-tract combinations for all (MS+HC) participant analyses.

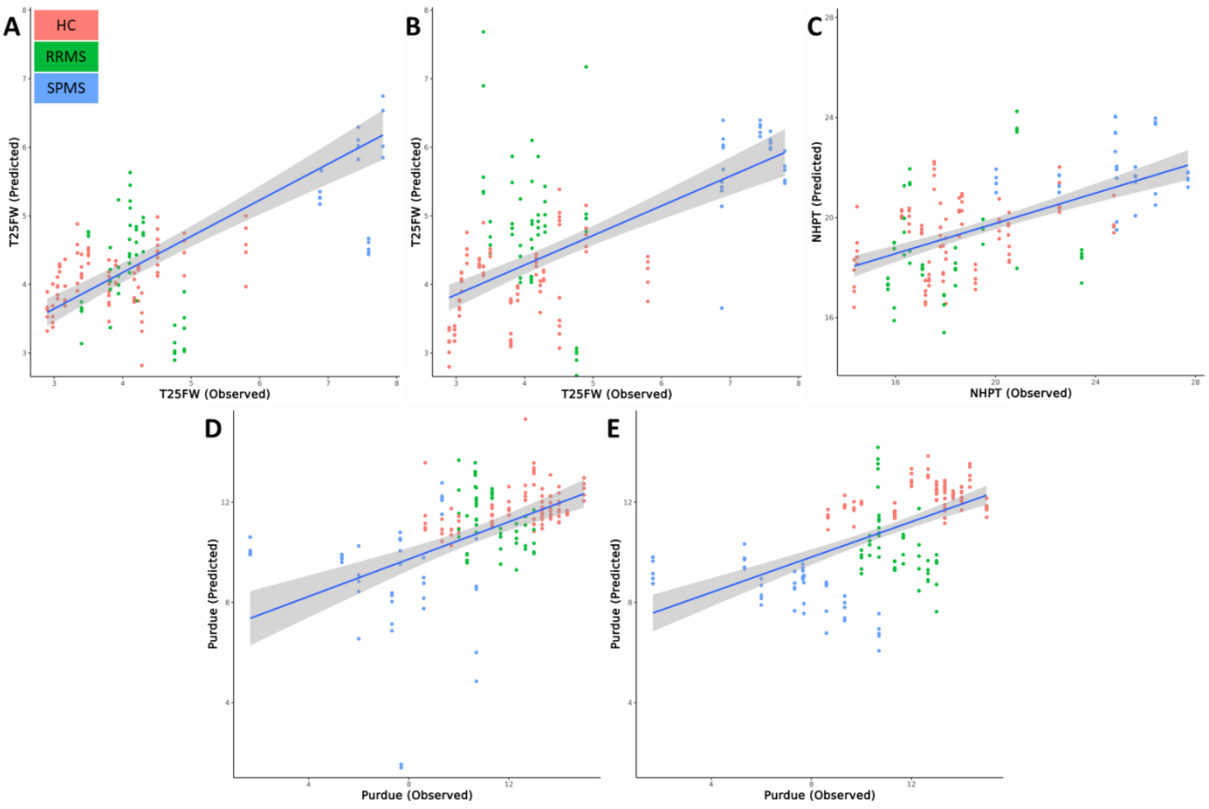

Figure 6.11: Predicted versus observed values for physical assessments of all participants. Shown are Pearson Correlations between observed and predicted affective outcomes, with the latter derived using diffusion-based NAWM measures regarding T25FW (A), and Purdue (D), respectively, texture-based NAWM+Lesions measures regarding T25FW (B) and Purdue (E), respectively, and texture-based NAWM measures regarding NHPT (C). Note: T25FW Timed 25-Foot Walk; NHPT: Nine-Hole Peg Test; Purdue: Purdue pegboard.

Neurocognitive Assessments

For MS participants, predicted SDMT with diffusion-based NAWM measures (RMSE=0.91sd, R^2=0.38; p<0.01) were moderately correlated with the observed outcomes. These observed findings were also weakly correlated with predicted SDMT by diffusion-based NAWM+Lesions measures (RMSE=1.10, R^2=0.40; p<0.05). In addition, predicted SDMT by texture-based NAWM measures (RMSE=0.73sd, R^2=0.65; p<0.0001) and NAWM+Lesions measures (RMSE=0.77sd, R^2=0.59; p<0.0001) were both strongly correlated to the observed findings. Further, predicted results for BVMT by both diffusion models (NAWM (RMSE=0.93sd, R2=0.5; p<0.001) and

NAWM+Lesions (RMSE=0.99sd, R2=0.48; p<0.0001) measures) were moderately correlated with observed outcomes with no significant textural predictions. Furthermore, predicted COWAT by diffusion-based NAWM measures were moderately correlated (RMSE=0.97sd, R^2=0.37; p<0.001) with the observed outcomes (Figure 6.12 & Figure 6.13). Predicted TTT by texture-based NAWM measures (RMSE=0.84sd, R^2=0.46; p<0.001) exhibited moderate correlations with the observed findings.

For healthy controls, the predicted results for SDMT by texture-based NAWM measures were strongly correlated with observed outcomes (RMSE=0.77sd, R^2=0.51; p<0.0001). No other predicted results were significantly correlated with the observed findings for SDMT, BVMT, COWAT, or TTT (Figure 6.13).

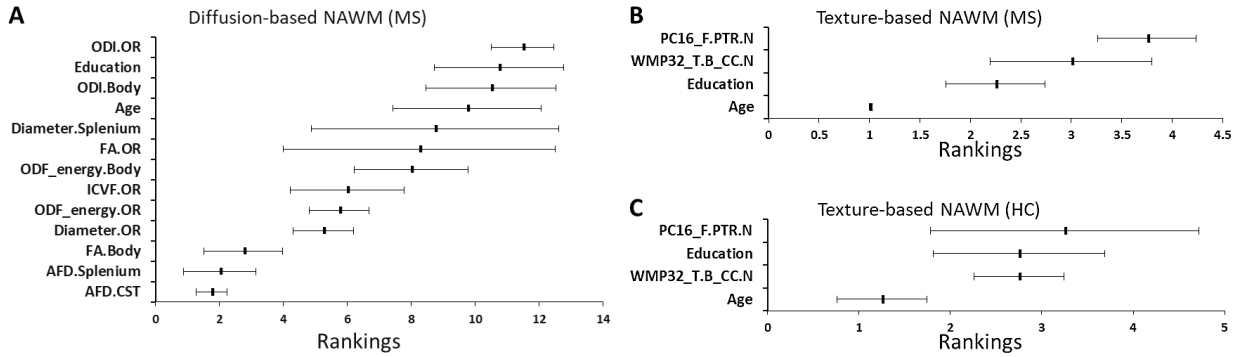

Figure 6.12: Diffusion- and Textural phase congruency-based NAWM feature rankings across neurocognitive assessments. Shown are average feature rankings with 95% confidence intervals derived from the recursive feature elimination process of ridge regression. Features are listed on the y-axis as measurement-tract combinations for A,B) MS and C) healthy control participant analyses.

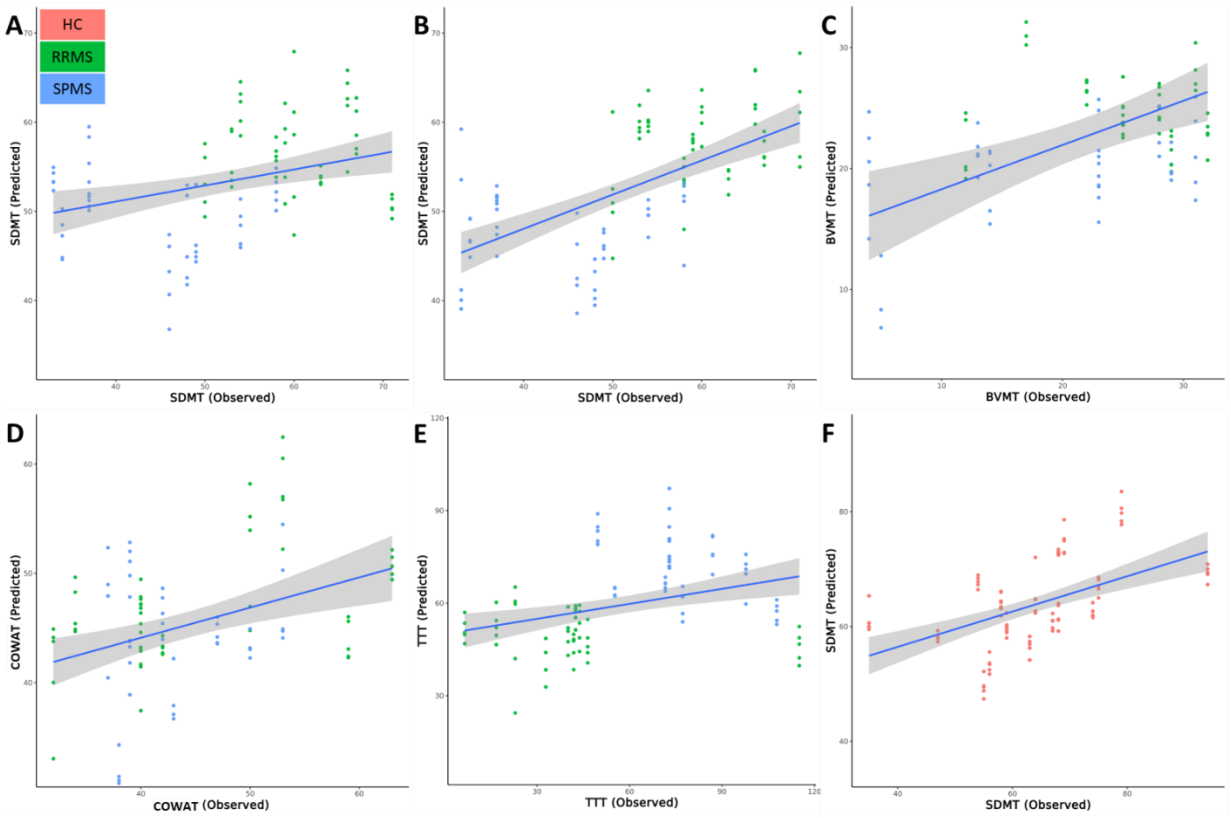

Figure 6.13: Predicted versus observed values for neurocognitive assessments. Shown are Pearson Correlations between observed and predicted affective outcomes, with the latter derived using diffusion-based NAWM measures for MS participants regarding SDMT (A), BVMT (C), and COWAT (D), respectively; texture-based NAWM measures for MS participants regarding SDMT (B) and TTT (E) respectively; and texture-based NAWM measures for healthy control participants regarding SDMT (F) and BDI (D), respectively. Note: SDMT: Symbol Digit Modality Test; BVMT: Brief Visuospatial Memory Test; COWAT: Controlled Oral Word Association Test (COWAT); TTT: Tactile Temporal Threshold.

For both participants groups combined, predicted results for SDMT by diffusion-based NAWM measures and NAWM+Lesions measures were moderately (RMSE=0.85sd, R^2=0.38; p<0.0001) and weakly (RMSE=1.10sd, R^2=0.29; p<0.01) correlated with observed outcomes, respectively. Further, these observed outcomes of SDMT were also strongly correlated with predicted results based on both texture-based NAWM measures (RMSE=0.82sd, R^2=0.40; p<0.0001) and NAWM+Lesions measures (RMSE=0.76sd, R^2=0.51; p<0.0001). In addition, predicted COWAT

by diffusion-based NAWM measures (RMSE=0.98sd, R^2=0.15; p<0.05) and texture-based NAWM+Lesions measures (RMSE=0.97sd, R^2=0.16; p<0.05) were each weakly correlated to the observed outcomes. Likewise, predicted results for BVMT by diffusion-based NAWM (RMSE=0.9sd, R2=0.3; p<0.0001) and NAWM+Lesions (RMSE=0.85sd, R2=0.3; p<0.0001) measures were each moderately correlated with the observed outcomes. Only predicted TTT from texture-based NAWM+Lesions measures (RMSE=0.98sd, R^2=0.21; p<0.01) were weakly correlated with the observed values (Figure 6.14 & Figure 6.15).

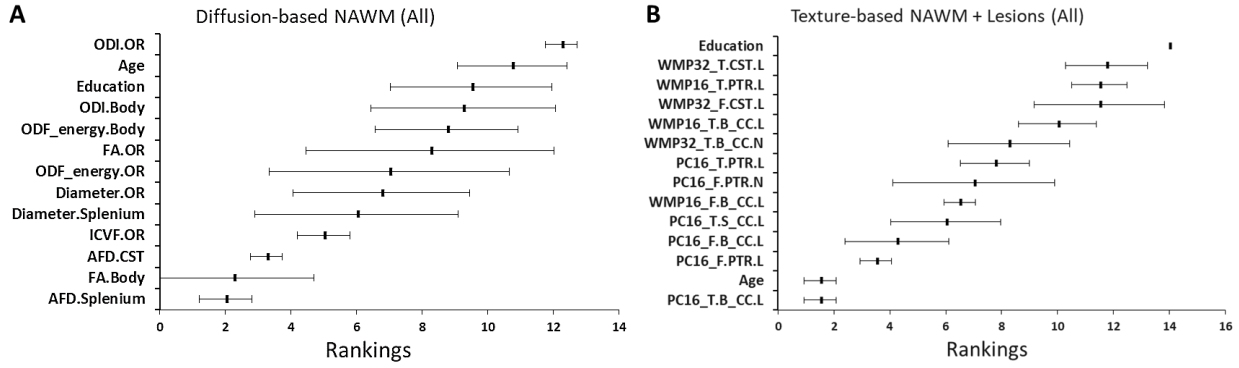

Figure 6.14: Diffusion- and Textural phase congruency-based NAWM and NAWM+Lesions feature rankings across neurocognitive assessments. Shown are average feature rankings with 95% confidence intervals derived from the recursive feature elimination process of ridge regression. Features are listed on the y-axis as measurement-tract combinations for all (MS+HC) participant analyses.

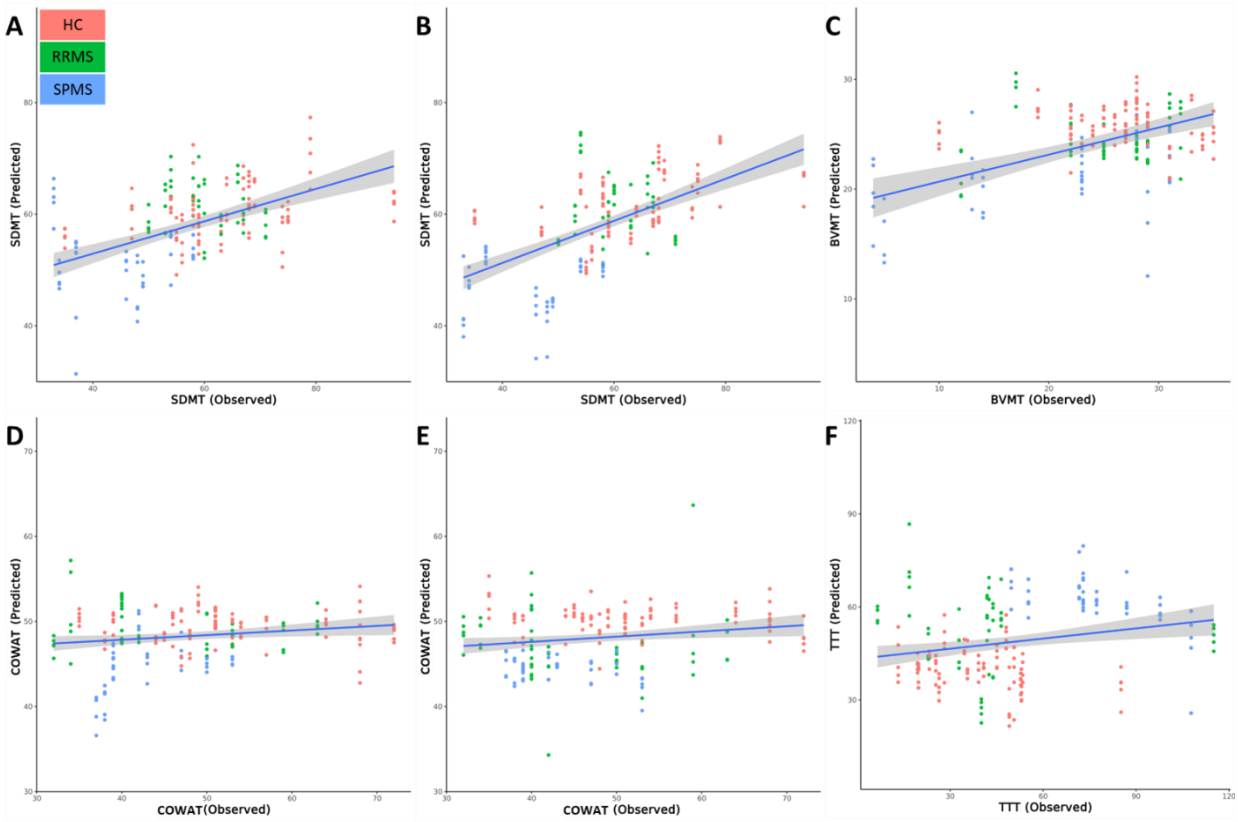

Figure 6.15: Predicted versus observed values for neurocognitive assessments of all participants. Shown are Pearson Correlations between observed and predicted affective outcomes, with the latter derived using diffusion-based NAWM measures regarding SDMT (A), BVMT (C), and COWAT (D), respectively; texture-based NAWM+Lesions measures regarding SDMT (B), COWAT (E), and TTT (F) respectively. Note: SDMT: Symbol Digit Modality Test; BVMT: Brief Visuospatial Memory Test; COWAT: Controlled Oral Word Association Test (COWAT); TTT: Tactile Temporal Threshold.

Affective assessments

For MS participants, the predicted results for MFIS using diffusion-based NAWM measures correlated with observed results (RMSE=0.99sd, R^2=0.42; p<0.001). No other predicted results based on either tract NAWM alone or tract NAWM+Lesions measures correlated with observed outcomes of MFIS, or BDI.

For healthy controls, the predicted results for neither MFIS nor BDI were significantly positively correlated to the observed results.

For all MS and control participants together, the predicted results for MFIS by both diffusion-based NAWM measures (RMSE=0.99, R^2=0.16; p<0.05) and texture-based NAWM+Lesions measures (RMSE=1.00, R^2=0.25; p<0.05) were weakly correlated with the observed MFIS outcomes. Further, predicted results for BDI by texture-based NAWM+Lesions measures (RMSE=0.97sd, R^2=0.18; p<0.05) were also weakly correlated with the observed outcomes of BDI (Figure 6.16 & Figure 6.17).

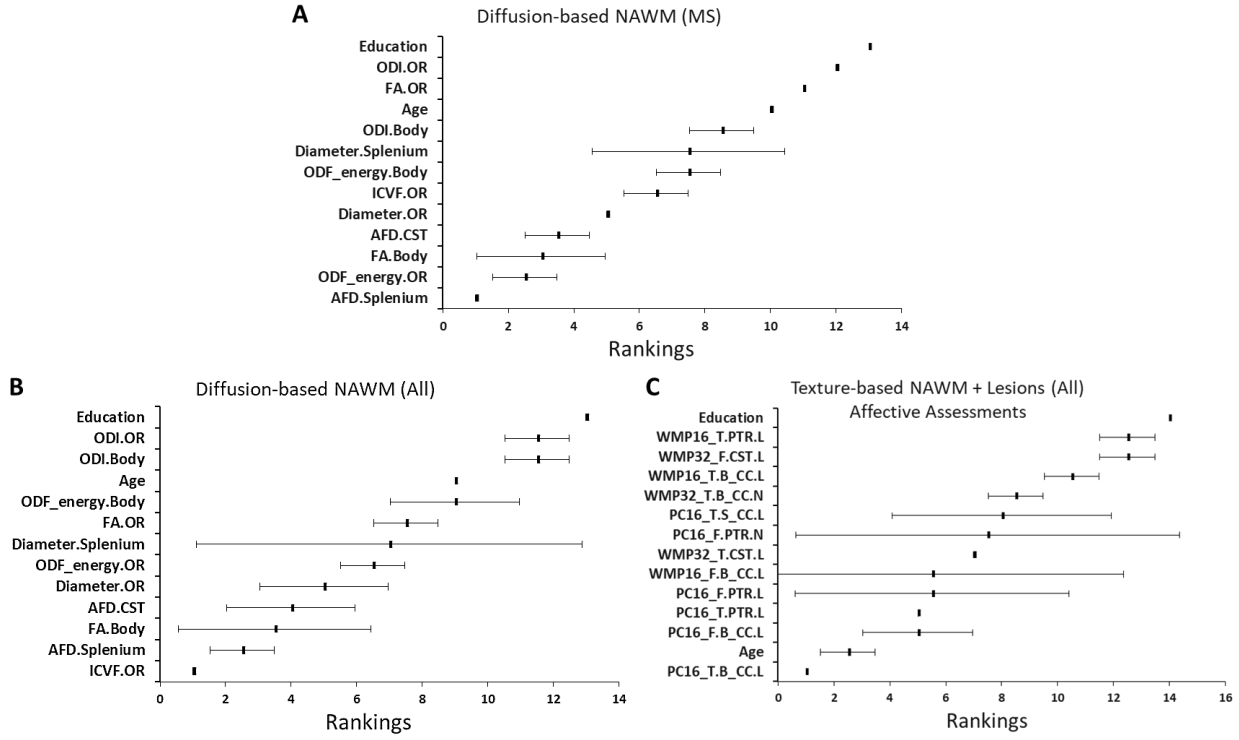

Figure 6.16: Diffusion- and Textural phase congruency-based NAWM and NAWM+Lesions feature rankings across affective assessments. Shown are average feature rankings with 95% confidence intervals derived from the recursive feature elimination process of ridge regression. Features are listed on the y-axis as measurement-tract combinations for A) MS and B,C) all (MS+HC) participant analyses.

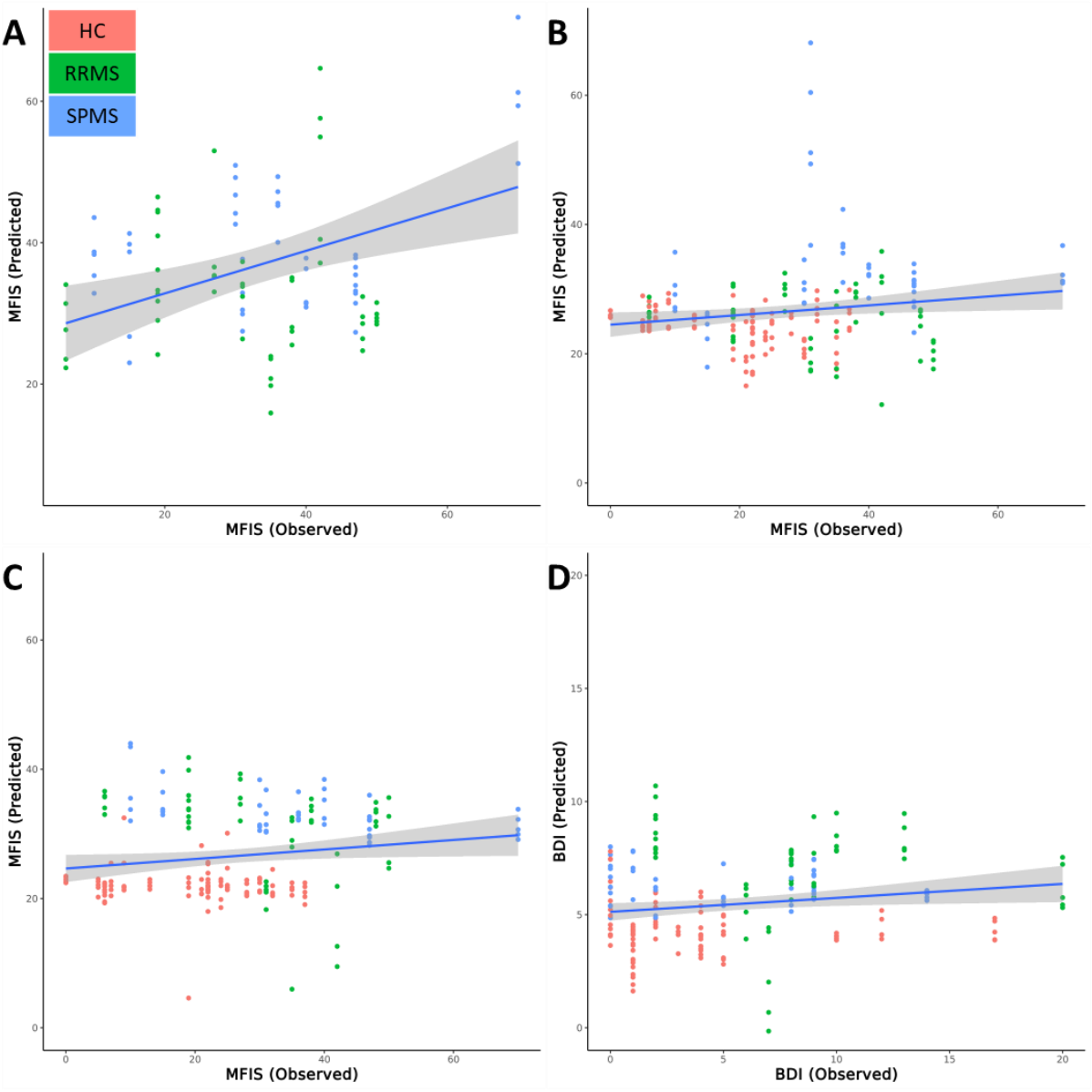

Figure 6.17: Predicted versus observed values for affective assessments. Shown are Pearson Correlations between observed and predicted affective outcomes, with the latter derived using diffusion-based NAWM measures for MS participants (A), diffusion-based NAWM measures for all participants (B), and texture-based NAWM+Lesions measures for all participants regarding MFIS (C) and BDI (D), respectively. Note: MFIS: Modified Fatigue Impact Scale; BDI: Beck's Depression Inventory scores.

Quantitative comparison of the Prediction Models

To further understand the potential of the imaging features for predicting functional outcomes, Fisher's z-transformation of Pearson's Correlation coefficient between imaging-predicted and observed functional measures was done. The assessments included comparisons between prediction models based on NAWM versus NAWM+Lesions measures, diffusion MRI versus phase congruency textural measures, and among participant groups. For control participants, only NAWM models were developed.

For MS participants, models based on NAWM measures from either diffusion MRI or phase congruency typically performed equally or superiorly to that based on NAWM+Lesions measures. In general, the best phase congruency-based models matched or outperformed diffusion-based models (Figure 6.18). For control participants, phase congruency-based models also outperformed diffusion-based models in correlations with observed data for two neuropsychological assessments (Figure 6.19). Comparing model performance between MS and control cohorts based on NAWM predictions, prediction models for the MS cohort were either similarly or better correlated with observed functional outcomes than healthy controls (Figure 6.20).

With both participant groups combined, NAWM models were better for some diffusion-based models while NAWM+Lesions models were generally better for phase congruency-based models. The latter again mostly outperformed diffusion-based models overall, except that the observed BVMT scores were better correlated with diffusion-based than phase congruency-based predictions (Figure 6.21).

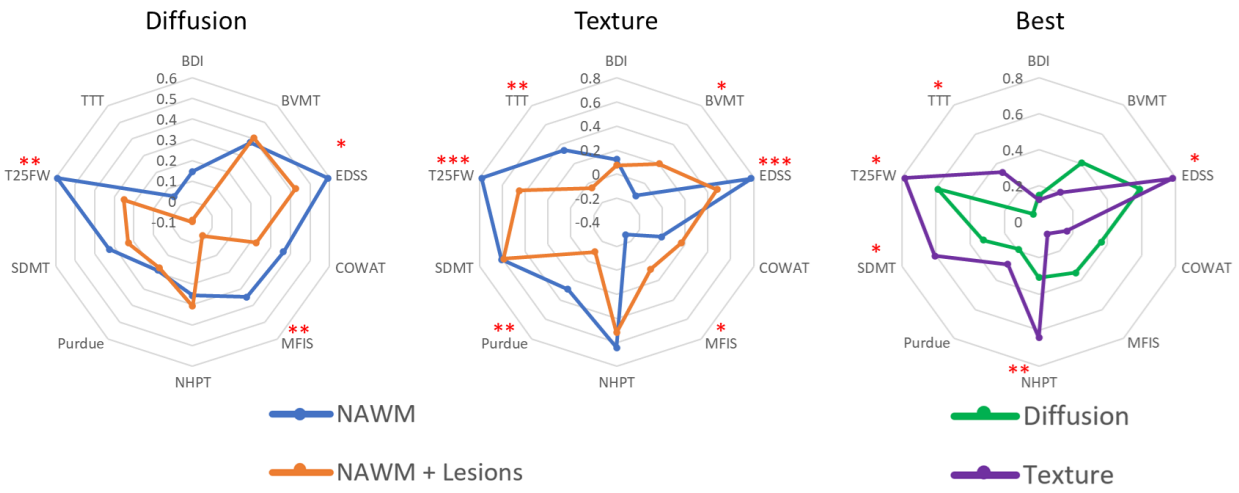

Figure 6.18: Comparisons of correlation strength between predicted and observed functional outcomes by imaging feature type for MS participants. Pearson's correlation coefficients are plotted along the radial axes with a greater distance from the center indicating higher correlations between predicted and observed functional. The stars indicate significantly different results between NAWM (blue) and NAWM+Lesions (orange) or between diffusion MRI (green) and phase congruency texture (purple) measures based on Fischer's transformation of correlations between predicted and observed functional outcomes (*p<0.05, **p<0.01, ***p<0.001, ****p<0.0001).

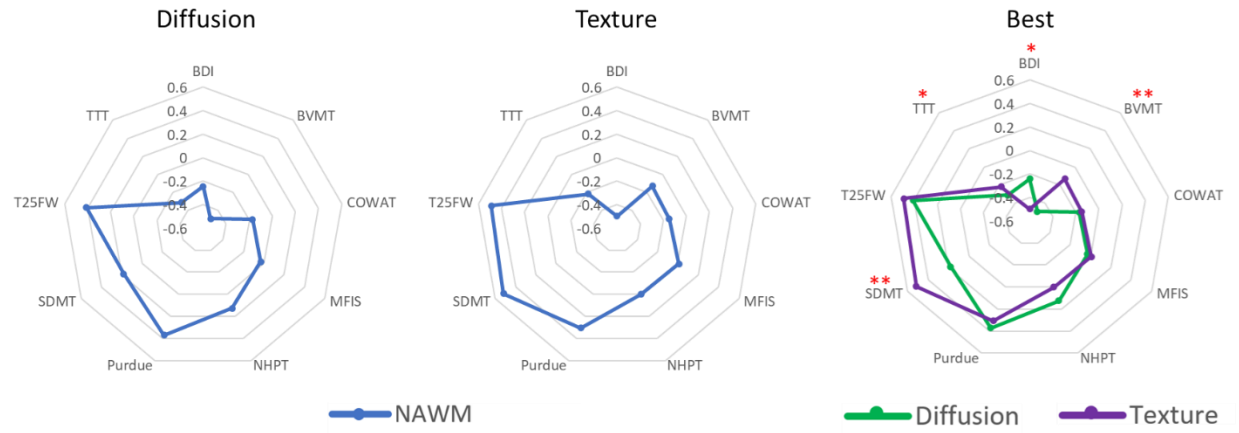

Figure 6.19: Comparisons of correlation strength between predicted and observed functional outcomes by imaging feature type for healthy participants. Only NAWM (blue) performances are shown as Lesions were not available for assessment in healthy controls. Pearson's correlation coefficients are plotted along the radial axes with a greater distance from the center indicating higher correlations between predicted and observed functional outcomes. The stars indicate significantly different results between diffusion MRI (green) and phase congruency texture (purple) measures based on Fischer's transformation of correlations between predicted and observed functional outcomes (*p<0.05, **p<0.01, ***p<0.001, ****p<0.0001).

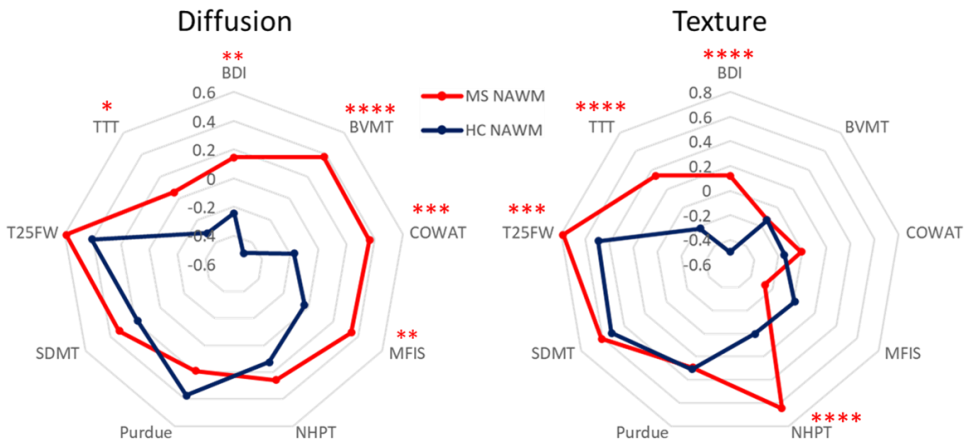

Figure 6.20: Comparisons of correlation strength between predicted and observed functional outcomes by participant group for both diffusion- and texture-based NAWM measures. Pearson's correlation coefficients are plotted along the radial axes with a greater distance from the center indicating higher correlations between predicted and observed functional outcomes. The stars indicate significantly different results between MS (red) and HC (blue) groups based on Fischer's transformation of correlations between predicted and observed functional outcomes (*p<0.05, **p<0.01, ***p<0.001, ****p<0.0001).

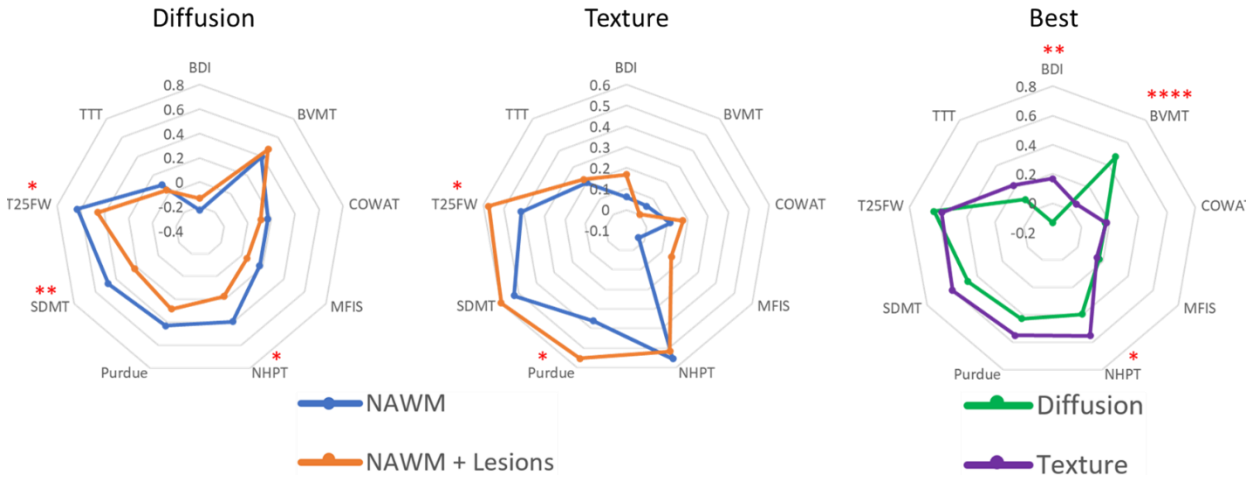

Figure 6.21: Comparisons of correlation strength between predicted and observed functional outcomes by imaging feature type for MS and Healthy control participants combined. Pearson's correlation coefficients are plotted along the radial axes with a greater distance from the center indicating higher correlations between predicted and observed functional outcomes. The stars indicate significantly different results between NAWM (blue) and NAWM+Lesions (orange) or between diffusion MRI (green) and phase congruency texture (purple) measures based on Fischer's transformation of correlations between predicted and observed functional outcomes (*p<0.05, **p<0.01, ***p<0.001, ****p<0.0001).

6.4 Discussion

Using tract-based measures of the brain in both lesion and non-lesion areas, this study investigated the relationship between imaging and functional outcomes in people with MS along with matched controls. Through a series of modeling and analytical processes this study showed that diffusion MRI and texture analysis measures associated with critical brain white matter tracts predict multi-domain functionality in MS and healthy people. Among the three common clinical and neuropsychological domains assessed, physical functions were predicted the best. This was followed by cognitive functions, with the SMDT being predicted the best, showing strong predictions by all imaging measures, and then verbal fluency (COWAT) and visuospatial (BVMT) outcomes that featured moderately correlated predictions by the imaging measures. The affective functions (depression and fatigue) were predicted with the smallest correlations. Between imaging types, the texture-based predictions in general performed similarly or better than diffusion MRI-based predictions.

MS pathology is complex and impacts virtually all brain regions, causing multi-system functional impairment (4). Indeed, out of the 14 functional assessments conducted in the current study, 10 of them showed significant deficit in MS. Brain white matter serves as the physical wire that connects parts of the function drivers, especially the major tracts. Chief among white matter tracts is the corpus callosum, which acts as an information bridge critical to neural coordination of various tasks ranging from sensory to motor and to cognitive functions (230,257). The optic radiation and corticospinal tracts of the brain help govern visual and motor information processing, respectively (209,242). All three groups of white matter tracts are frequently impacted in MS, including regions without visible lesions (NAWM) (211,242,257). Therefore, investigating links between the tract-

based abnormality measures and functional deficits in MS is reasonable. Further, to maximize understanding and impact, this study focused only on functional outcomes that differentiated MS from controls.

As shown in my previous work (Chapters 4 & 5), both diffusion MRI and texture analysis using phase congruency have the potential to detect subtle tissue structural changes and both have shown the utility in differentiating the severity of MS pathology (32,33). Further, in this study, the RFE analyses helped identify the top-ranking imaging measures for subsequent examination, increasing the likelihood of correlation with functional measures. In diffusion MRI-based assessment, the AFD, FA, ICVF, and axonal diameter ranked the highest in the RFE processes. The FA and ICVF are sensitive to structural changes following demyelination and axonal degradation, and the AFD is evidenced to be sensitive to axonal density and swelling that are critical drivers of disease progression in MS (30,258). For the textural phase congruency experiments, the lower-frequency features of WMP were typically ranked high in NAWM-based RFE analyses, while higher-frequency features of PC were often high-ranked in NAWM+Lesions analyses. Through band-wise frequency analysis, the PC and WMP were set to characterize the complexity and sharpness of image patterns, respectively (153). While subject to verification, the ranking difference of these features between RFE models might suggest that texture-based NAWM modeling was mainly driven by subtle pathological changes while modeling together with tract lesions was characterized by complex pathology. Overall, both diffusion MRI- and phase congruency-based assessments have shown the sensitivity to detect invisible MS pathology, setting the foundation for further analysis of their functional relationship.

Machine learning with Ridge Regression facilitated the identification of prediction models for each of the functional measures identified in the present study. Model performance was the best when predicting physical functions, followed by cognitive and then affective functions. Previous studies showed that 66% and 75% of MS patients experience upper limb and lower limb physical impairments, respectively, which contributed to a large range of functional scores that in turn supported the associated model fitting (259), similar to the present study in EDSS of MS participants. For control participants, the predicted results for T25FW and Purdue pegboard predictions were moderately correlated with observed findings, suggesting that variances among healthy sensorimotor functions could also have been well captured by the high-ranking imaging measures associated with the major brain white matter tracts. Also, physical tasks are complex and may demand the integration of multiple systems to conduct tasks including information collection (optic radiation), information processing (corpus callosum), and coordination of motor information (corticospinal tract), especially in individuals with impairments (19,209,211,242). The promising performance in predicting physical outcomes suggests diffusion MRI and MRI texture outcomes showed beneficial sensitivities to tissue structure across multiple tracts. Among the cognitive functions, the SDMT was best predicted followed by BVMT then COWAT. This ordering of prediction performance mirrors the prevalence of impairments in cognitive domains associated with information processing speed, visual memory, and fluency among MS patients (26). The SDMT is a highly regarded cognitive assessment (252). The strong predictability of the imaging measures to this function may have significant clinical implications, deserving further verification (252). The poor performance of imaging predictions for COWAT may be due to the lack of direct link between the investigated white matter tracts and memory and verbal processing centers. Some of these functions exist within the genu of corpus callosum but none of the investigated measures

within this region showed differences between MS cohorts (Chapter 5) (33). Finally, the predictions for affective functions performed the lowest among all examined outcomes. This may suggest that more complex structural underpinnings exist than what is modelled herein using the tracts of interest (65).

Quantitative analysis of the correlation strength between predicted and observed results show that textural phase congruency-based models outperformed diffusion MRI-based models in functional prediction for multiple assessments. Within individual imaging types, the NAWM+Lesions models performed the best for phase congruency-based predictions, and for diffusion MRI-related predictions, the NAWM-based models were better than their NAWM+Lesions counterparts. Biophysically, diffusion MRI reflects the intrinsic properties of the underlying tissue that include microscopic changes. On the other hand, texture analysis characterizes inter-voxel relationships and therefore is sensitive to the patterns of tissue structural organizations not directly observable (35,136). The improved performance of texture-based predictors suggests that certain patterns of tissue abnormalities may be more predictive of functional outcomes than microlevel changes. Similar results have been observed in other studies using different texture analysis methods such as grey level co-occurrence matrix (GLCM) where texture features outperformed advanced MRI measures including FA and magnetization transfer ratio in brain MS pathology classifications (40). Further work is necessary to validate the results associated with phase congruency, but combining diffusion and textural predictors in future investigations may be necessary to provide complementary information.

This study has a few limitations. All investigations were based on archived datasets from a pre-defined study, where the RRMS and SPMS participants had clear separations in disease severity. While promising for initial model development, these sample characteristics limited the diversity of functional outcomes used in model training. Likewise, this study did not have the ability to study other forms of MS, such as PPMS that might otherwise offer further insight into structure-function patterns. Despite these limitations, the study sample was well-characterized and control-matched, providing a valuable opportunity to understand the relationship of the measures from different perspectives. In addition, this study focused only on outcomes from three groups of brain white matter tracts. This may have limited the capacity to study the whole scope of brain pathology, such as those directing to memory and some executive functioning. Nonetheless, the chosen tracts are some of the most impacted regions in MS and indeed, imaging measures from these tracts showed the significant potential for predicting functional outcomes of the participants, deserving future confirmation. Further, generating imaging outcomes involved several image processing and analysis steps, which might impact repeatability for uses with different skill levels. In the future, we plan to test the findings using a larger cohort, including different brain regions other than focused white matter tracts, and implement an integrated image analysis pipeline to foster knowledge translation and exchange.

6.5 Summary

In summary, through comprehensive modeling of an archived cohort of clinical patient data as well as matched controls, this study discovers that both diffusion MRI and textural phase congruency-based imaging measures predict functional outcomes. The prediction strength varies, and is best for physical functions, intermediate for cognitive outcomes, and least for affective

measures. Further, textural phase congruency measures based on conventional brain MRI constantly matched or outperformed diffusion MRI measures in predicting all examined functional outcomes except the visuospatial assessment. This highlights the critical utility of advanced MRI measures of MS pathology, deserving further confirmation. Overall findings will be invaluable for early identification of functional decline in MS participants, thereby enabling early intervention and prevention. Further, given the use of conventional MRI, the texture-based measures can be directly tested for clinical translation after further validation for improved disease monitoring and management in MS and similar diseases.

Chapter 7: Discussion

7.1 Summary and Thesis Contributions

This thesis aimed to develop and evaluate advanced imaging methods based on brain diffusion MRI and phase congruency texture analysis for improved characterization of disease pathology and function in MS. Based on data from well-characterized clinical studies done previously in RRMS and SPMS, several novel methods and technologies were originated (e.g. Chapter 3), which provided a solid foundation in generating new knowledge in subsequent chapters. The follow-up experiments took a stepwise approach, evolved from studies of methods for detecting and differentiating subtle types of MS pathology (Chapter 4), to distinguishing disease severity between two most common forms of MS (RRMS and SPMS, Chapter 5), and to predicting functional outcomes of people with RRMS and SPMS versus controls (Chapter 6). Overall findings suggest that brain imaging measures based on advanced diffusion MRI and phase congruency analyses were highly sensitive to invisible pathology changes that identify MS lesions and within-lesion structural differences, competitive to differentiate disease severity as seen between RRMS and SPMS, and had considerable potential to predict functional performance across multiple domains in MS.

Technical development in this thesis targets exclusively clinically feasible scenarios, datasets, and protocols. Regarding brain diffusion MRI, there were several types of innovations created. For example, using single-shell brain diffusion MRI as is common for DTI, high-quality HARDI-like measures were derived based on image post-processing techniques. Other approaches in the literature have also achieved promising results in this regard based on construction of modified HARDI models but were limited by the lengthy model fitting times as an inheritance of

conventional HARDI implementations (119,186). Simultaneously, ODF energy as a promising parameter in different analysis tasks herein was more quickly calculated (through matrix multiplication) than its 'polymorphism', ODI, computed based on model-based approaches. Further, by applying a dictionary-based modeling method with AMICO, this thesis was able to accelerate the model fitting times, making it possible to elevate the practicability of all the tools and technologies generated. Furthermore, using our robust neural network models, this research was also able to create new/unacquired brain diffusion MRI datasets thereby performing truly multi-shell HARDI analyses with near perfect match with results based entirely on source data (119,121,122). Finally, competitive data harmonization technologies were developed that enabled to both enhance angular resolution of diffusion MRI and improve the scope of analyses with the possibility of combining datasets that were acquired with different imaging protocols.

Similarly, multiple new formulas were developed to improve the affinity of phase congruency as a potentially new method for analysis of MS pathology. A graphic user interface was built for easy visualization and investigation of the multilayered parametric settings of the method. Benefiting from the robustness of phase congruency to artifactual variations in image contrast and signal intensity, a simplified approach was implemented that allowed fine-tuning of different phase congruency parameters for best possible detection of subtle structural changes. With a simplified parameter optimization procedure, the phase congruency method was tuned to focus on specific patterns of signal intensity created by a unique underlying tissue such as MS lesions and the associated pathology (159,260). Further, this study successfully employed 3D analysis to improve feature localization capabilities for all brain regions while addressing limitations in contextualized texture analysis noted in prior 2D applications to MS or other diseases (161).

Single-shell diffusion MRI and phase congruency outcomes were found to be robust in characterizing subtle MS pathology types. The performance of these measures was demonstrated through two scenarios of tissue classification: the basic lesion versus NAWM analysis and an advanced lesion core vs rim comparison. For the lesion versus NAWM models, diffusion orientation-based measures acted as the greatest contributors. Previous studies have found that orientation measures such as ODI may reflect changes in myelin content both during demyelination and remyelination phases in MS-like models (36,261). Therefore, the high ranking of such related measures including ODI, ODF energy, and FA herein suggests that measures sensitive to lesion and NAWM differences may stem from differences in myelination (206). Further, in MS, demyelination is not the only evident pathology; often times it is accompanied by axonal degeneration (206). Many critical patterns of MS lesion pathology are associated with loss of neural density within the lesion core suggesting loss of myelin plus axons (183,262). Investigations of core versus shell pathology found high-ranking measures to be predominantly related to diffusion magnitude. This included sensitive DTI measures such as MD and HARDI-like outcomes of increase specificity based on single-shell diffusion data. The high-ranking of these measures suggest their sensitivity to critical MS pathology patterns related to neurodegeneration as confirmed in studies of chronic active lesions of the optic radiation (183,262). In addition, phase congruency analysis based on the same two tissue classification scenarios showed that FLAIR and T2-weighted MRI outcomes calculated with high and low frequencies (16 mm and 32 mm maximum wavelengths) were routinely high-ranking. Existing literature has not thoroughly investigated the foundation of information offered by phase congruency texture analysis, likely due to the novelty of this method and the availability of

expertise for advanced exploration. However, the competitive results originated in this thesis might highlight the benefits of phase congruency based on T2-based sequences to characterize local patterns within lesion structures, which will be useful for both advanced study of MS pathology and innovate the use of conventional MRI in general.

Both diffusion MRI and phase congruency measures were sensitive to differentiate disease severity between RRMS and SPMS based on pathology detectable at different scales of neurological tissue structure. Histogram analysis of diffusion MRI detected significant differences in whole-brain NAWM between the two MS cohorts, especially in brain regions with high density and highly cohesive NAWM. FLAIR and T2-w texture measures also differentiated cohorts in which FLAIR results aligned with literature showing greater heterogeneity in pathological tissues (36,40). However, the texture results of both FLAIR and T2-w MRI deserve further confirmation, particularly given the relatively scarce use of phase congruency. For tract-based NAWM and lesions, multiple measures detected significant differences within the body of the corpus callosum, most notably diffusion orientation and alignment measures within lesions of this tract. This finding may indicate the sensitivity of diffusion metrics to axon-based pathological changes as greatest axonal loss was found previously in the rostrum and midbody of corpus callosum (263). When assessing chronic active lesion activity defined using diffusion measures via a core-shell z-score framework, SPMS participants had more such lesions than RRMS participants. This finding aligned with evidence showing that MS people with more advanced disability presented with more rim lesions, which were similar to chronic active lesions detected in susceptibility-weighted imaging (16). In this case the potential feasibility of detecting these lesions with methods other than susceptibility-based sequences (e.g. QSM) open a new avenue for future studies. These results

assert the sensitivity of both advanced diffusion MRI and MRI texture outcomes in the investigation of tissue structure differences associated with disease severity in MS.

Tract-based NAWM and lesion measures using advanced diffusion MRI and phase congruency texture analysis predicted physical, neurocognitive, and affective functional outcomes of persons with MS. Physical functions were predicted the best, as represented by the EDSS, upper arm, and lower limb assessments. The improved performance herein may be related to the RRMS-SPMS disparities noted in the body of corpus callosum where notable motor and sensorimotor coordination processes are focused (230,263). Among neurocognitive outcomes, SDMT was the best predicted when considering all participants, followed by BVMT, which supported the literature demonstrating the robustness of these measures (e.g. SDMT) in detecting disability and focus on the frequently affected information processing speed in MS (26). Affective outcomes such as depression and fatigue were not as well predicted compared to other functional outcomes, showing essentially weak predictions. Across functional domains (as per diffusion MRI-based models), measures reflective of axonal density were routinely high ranking, consistent with the literature suggesting that reduction of axonal density was a major determinant of functional decline in MS (16,18). In addition, texture-based models appeared to outperform most diffusion models suggesting that novel analysis of conventional MRI offers a crucial sensitivity to disease severity and functional consequences in MS participants.

7.2 Limitations

The sample sizes were relatively small, especially regarding the SPMS cohort (Chapter 5), limiting broad conclusions. With limited treatment options available for SPMS individuals currently, the

frequency of clinical follow-up including MR imaging is low as compared to RRMS people. However, this thesis had yielded significant results that could stimulate new research ideas and new experiments. Further, the small and inhomogeneous datasets herein had promoted the development of several innovative methods for data optimization, and the inclusion of well-characterized MS participants and matched controls likely had decreased the need for extremely large datasets.

In imaging investigations, two types of methods were focused on: diffusion MRI and phase congruency texture analysis. While not comprehensive, these methods were highly representative, and each showed its own competitiveness as demonstrated in this thesis. Diffusion MRI is one of the few advanced imaging methods capable of providing information on both myelin and axonal integrity, both being critical players in MS pathogenesis and function. Further, diffusion MRI is feasible for various new investigations using models and techniques being developed constantly. Phase congruency is a frequency-based texture analysis method that overcomes different limitations faced by other such techniques including its robustness to imaging variations in brightness. This method is chosen also because its ability to characterize tissue coherency, which is comparable and complementary to diffusion MRI.

In addition, the RRMS and SPMS cohorts analyzed in Chapter 5 represented two different participant groups. Given the continuum of these two disease phenotypes, studying outcomes associated with the same individuals would be ideal, where results could be directly compared to infer disease progression possibilities. This limitation is related to different factors. Importantly, the transition from RRMS to SPMS could take time, up to 10-15 years for nearly half of them.

Committing to a study in such a long timeline is extremely expensive and not possible for many situations. As such, study data from continuum RRMS and SPMS cohorts are rare to achieve. Further, while people with RRMS typically undergo regular clinical and imaging exams on a yearly basis and then every 2-3 years when they start or switch to a new therapy for example, once at the SPMS stage, as disease progresses mostly silently from a clinical perspective, these people do not have frequent exams anymore as compared to RRMS individuals. This further explained the rareness of SPMS datasets in general.

Pathology correlates were primarily based on prior investigations that have sought to establish the histological relationship of the investigated measures in this thesis. These same connections with pathology have yet to be established for phase congruency textural outcomes, specifically. Nonetheless, this lack of direct connection to histology tissue was mitigated by the investigation of three maximum wavelengths of similar size to MS lesions commonly seen on MRI. This is expected to have improved the relationship between the texture measures and the lesion and NAWM features of interest.

This study focused on a small set of white matter structures rather than the entire brain that may have limited the specificity of functional connections to their typical structural foundations. This approach was taken to support an initial exploration of the potential of advanced imaging measures to assess disease activity in known critical structures. Focusing the study on the corpus callosum, corticospinal, and optic radiation tracts allowed this project to focus the analysis on tracts routinely impacted by MS pathology that may in turn hold critical information about the development of pathologies. This approach may be modified in future studies with whole-brain analyses to

improve assessments of the tract-varying relationships between tissue pathology and functional outcomes in different types of MS.

7.3 Future Directions

Confirmation of findings originated from this thesis using a larger sample size would be necessary, especially data from SPMS participants. One option would be extracting data from large-scale, Phase III clinical trials through national and international collaborations. Additional confirmation would also include the new methods and technologies derived in this thesis such as these for data optimization, harmonization, and creation pertaining to diffusion MRI, and those for parameter fine-tuning in phase congruency. In addition, for precise understanding of the mechanisms of disease worsening in MS, future studies should include cohorts that demonstrate actual evolutions in disease trajectory as expected from RRMS to SPMS. Further, to verify utility of the developed imaging measures, additional analysis in other MS phenotype such as primary progressive MS or other neurodegenerative diseases such as amyotrophic lateral sclerosis would be beneficial.

In addition, given the increasingly recognized importance of chronic active lesions for their relevance to disease progression in MS, further studies in this area would be useful. While it is encouraging that this thesis has provided a new way of quantifying this type of lesions based on advanced diffusion MRI measures, the overall investigation is rudimentary and deserves confirmation. Future investigations may include larger sample studies to verify the utility of chronic active lesions identified using the thesis method in differentiating disease severity, as well as correlating the lesion findings with clinical outcomes of MS. To date, susceptibility weighted imaging (SWI) is the method of focus in charactering chronic active lesions in MS, where the SWI

lesions have also shown relationships with disease progression in people with MS. Correlating findings using the thesis-based method with those with SWI will help method confirmation and refinement.

Assisted by machine learning methods, this thesis has identified several advanced imaging measures that differentiate disease activity and predict functional outcomes. These analyses also showcase the importance of critical brain white matter tracts in assessing MS pathology. To further understand usefulness of the identified measures and brain white matter regions, future studies can expand by incorporation with deep learning techniques. Deep learning has shown promise in handling different image processing and analysis tasks. Given the unique learning approach, deep learning methods have the capacity to extract data features automatically from the whole-brain, which may provide new insight into the characteristics of tissue pathology and their relationship with disease outcomes (167), although deep learning is not without challenges. The latter may include the potentially extended training time, requirements of additional image preparation approaches, and intuitiveness of results for understanding.

7.4 Conclusion

Overall, this thesis has originated several advanced imaging methods that are sensitive to subtle pathological differences and disease severity, and are predictive of functional outcomes in people with MS. This is accompanied by technical innovations in different aspects of the studies as highlighted in Chapter 3 of the thesis. In addition, based on knowledge discovered in assessment of disease activity and functional outcomes, the thesis outputs may also help identify risk factors of disease development, which in turn can prompt early intervention and prevention to improve

prognosis. Collective findings should be highly transferrable to different study settings given the use of clinically feasible resources in development and evaluation, including conventional MRI that is the core of routine clinical imaging in MS diagnosis and management. Specifically, the derived methods and measures can be used directly by other clinical researchers with different cohorts of MS to further understand disease pathogenesis and outcomes and to test generalizability. With further confirmation, the imaging outcomes can be also used by clinical trialists as new biomarkers of potential therapies or by clinicians as pilot measures of disease activity during care delivery to inform the potential of future clinical deployment. Finally, while the development focuses on RRMS and SPMS, the current findings should shed light on other phenotypes of MS, as well as similar diseases, deserving further confirmation.

Bibliography

1. Loma I, Heyman R. Multiple Sclerosis: Pathogenesis and Treatment. Current Neuropharmacology. 2011 Sep 1;9(3):409–16.

2. Pittock SJ, Lucchinetti CF. The Pathology of MS. The Neurologist. 2007 Mar;13(2):45–56.

3. Haines JD, Inglese M, Casaccia P. Axonal Damage in Multiple Sclerosis. Mount Sinai Journal of Medicine: A Journal of Translational and Personalized Medicine. 2011 Mar;78(2):231–43.

4. Filippi M, Bar-Or A, Piehl F, Preziosa P, Solari A, Vukusic S, et al. Multiple sclerosis. Nature Reviews Disease Primers. 2018 Dec 8;4(1):43.

5. Compston A, Coles A. Multiple sclerosis. The Lancet. 2008;372(9648):1502–17.

6. Kurtzke JF. Rating neurologic impairment in multiple sclerosis: An expanded disability status scale (EDSS). Neurology. 1983 Nov 1;33(11):1444–1444.

7. Ziemssen T, Bhan V, Chataway J, Chitnis T, Cree BAC, Havrdova EK, et al. Secondary Progressive Multiple Sclerosis: A Review of Clinical Characteristics, Definition, Prognostic Tools, and Disease-Modifying Therapies. Neurology - Neuroimmunology Neuroinflammation [Internet]. 2023 Jan 1 [cited 2023 Jul 4];10(1). Available from: https://nn.neurology.org/content/10/1/e200064

8. Reich DS, Lucchinetti CF, Calabresi PA. Multiple Sclerosis. Longo DL, editor. New England Journal of Medicine. 2018 Jan 11;378(2):169–80.

9. Atlas of MS [Internet]. The Multiple Sclerosis International Federation; 2020 Sep. Report No.: 3rd Edition. Available from: https://www.msif.org/wp-content/uploads/2020/12/Atlas-3rd-Edition-Epidemiology-report-EN-updated-30-9-20.pdf

10. Seewann A, Vrenken H, Van Der Valk P, Blezer ELA, Knol DL, Castelijns JA, et al. Diffusely abnormal white matter in chronic multiple sclerosis: Imaging and histopathologic analysis. Archives of Neurology. 2009;66(5):601–9.

11. Frohman EM, Racke MK, Raine CS. Multiple Sclerosis — The Plaque and Its Pathogenesis. New England Journal of Medicine. 2006 Mar 2;354(9):942–55.

12. Huang SY, Tobyne SM, Nummenmaa A, Witzel T, Wald LL, McNab JA, et al. Characterization of Axonal Disease in Patients with Multiple Sclerosis Using High-Gradient-Diffusion MR Imaging. Radiology. 2016 Jul;280(1):244–51.

13. De Santis S, Granberg T, Ouellette R, Treaba CA, Fan Q, Herranz E, et al. Early axonal damage in normal appearing white matter in multiple sclerosis: Novel insights from multi-shell diffusion MRI. In: 2017 39th Annual International Conference of the IEEE Engineering in Medicine and Biology Society (EMBC). 2017. p. 3024–7.

14. Blumhardt LD, Barbosa S, Roberts N, Betal D, Gratin C, Centre QM, et al. MRI correlates of disease course and activity in multiple sclerosis. Magma: Magnetic Resonance Materials in Physics, Biology, and Medicine. 1994 Oct;2(3):319–22.

15. Ontaneda D. Progressive Multiple Sclerosis. CONTINUUM: Lifelong Learning in Neurology. 2019 Jun;25(3):736–52.

16. Absinta M, Sati P, Masuzzo F, Nair G, Sethi V, Kolb H, et al. Association of Chronic Active Multiple Sclerosis Lesions With Disability In Vivo. JAMA Neurology. 2019 Dec 1;76(12):1474–83.

17. Lublin FD, Häring DA, Ganjgahi H, Ocampo A, Hatami F, Čuklina J, et al. How patients with multiple sclerosis acquire disability. Brain. 2022 Sep 14;145(9):3147–61.

18. De Stefano N. Axonal damage correlates with disability in patients with relapsing- remitting multiple sclerosis. Results of a longitudinal magnetic resonance spectroscopy study. Brain. 1998 Aug 1;121(8):1469–77.

19. Caligiuri ME, Barone S, Cherubini A, Augimeri A, Chiriaco C, Trotta M, et al. The relationship between regional microstructural abnormalities of the corpus callosum and physical and cognitive disability in relapsing–remitting multiple sclerosis. NeuroImage: Clinical. 2015;7:28–33.

20. Grossi P, Portaccio E, Bellomi F, Bianchi V, Cilia S, Falautano M, et al. The minimal neuropsychological assessment of MS patients (MACFIMS): normative data of the Italian population. Neurol Sci. 2020 Jun 1;41(6):1489–96.

21. Healy BC, Engler D, Glanz B, Musallam A, Chitnis T. Assessment of Definitions of Sustained Disease Progression in Relapsing-Remitting Multiple Sclerosis. Multiple Sclerosis International. 2013;2013:1–9.

22. Ge Y. Multiple Sclerosis: The Role of MR Imaging. American Journal of Neuroradiology. 2006;27(6):1165–76.

23. Grussu F, Schneider T, Tur C, Yates RL, Tachrount M, Ianuş A, et al. Neurite dispersion: a new marker of multiple sclerosis spinal cord pathology? Annals of Clinical and Translational Neurology. 2017 Sep;4(9):663–79.

24. Fulton JC, Grossman RI, Udupa J, Mannon LJ, Grossman M, Wei L, et al. MR lesion load and cognitive function in patients with relapsing-remitting multiple sclerosis. AJNR American journal of neuroradiology. 1999;20(10):1951–5.

25. Bakirtzis C, Ioannidis P, Messinis L, Nasios G, Konstantinopoulou E, Papathanasopoulos P, et al. The Rationale for Monitoring Cognitive Function in Multiple Sclerosis: Practical Issues for Clinicians. The Open Neurology Journal. 2018 May 31;12(1):31–40.

26. Chiaravalloti ND, DeLuca J. Cognitive impairment in multiple sclerosis. The Lancet Neurology. 2008 Dec;7(12):1139–51.

27. Zheng Y, Lee J chi, Rudick R, Fisher E. Long-Term Magnetization Transfer Ratio Evolution in Multiple Sclerosis White Matter Lesions. Journal of Neuroimaging. 2018 Mar;28(2):191–8.

28. Vavasour IM, Huijskens SC, Li DK, Traboulsee AL, Mädler B, Kolind SH, et al. Global loss of myelin water over 5 years in multiple sclerosis normal-appearing white matter. Mult Scler. 2018 Oct 1;24(12):1557–68.

29. Haacke EM, Makki M, Ge Y, Maheshwari M, Sehgal V, Hu J, et al. Characterizing iron deposition in multiple sclerosis lesions using susceptibility weighted imaging. Journal of Magnetic Resonance Imaging. 2009 Feb 25;29(3):537–44.

30. De Santis S, Bastiani M, Droby A, Kolber P, Zipp F, Pracht E, et al. Characterizing Microstructural Tissue Properties in Multiple Sclerosis with Diffusion MRI at 7 T and 3 T: The Impact of the Experimental Design. Neuroscience. 2019;403:17–26.

31. Liu Y, Mitchell PJ, Kilpatrick TJ, Stein MS, Harrison LC, Baker J, et al. Diffusion tensor imaging of acute inflammatory lesion evolution in multiple sclerosis. Journal of Clinical Neuroscience. 2012;19(12):1689–94.

32. Oladosu O, Liu WQ, Pike BG, Koch M, Metz LM, Zhang Y. Advanced Analysis of Diffusion Tensor Imaging Along With Machine Learning Provides New Sensitive Measures of Tissue

Pathology and Intra-Lesion Activity in Multiple Sclerosis. Frontiers in Neuroscience [Internet]. 2021 May 7;15. Available from: https://www.frontiersin.org/articles/10.3389/fnins.2021.634063/full

33. Oladosu O, Liu WQ, Brown L, Pike BG, Metz LM, Zhang Y. Advanced diffusion MRI and image texture analysis detect widespread brain structural differences between relapsing-remitting and secondary progressive multiple sclerosis. Frontiers in Human Neuroscience [Internet]. 2022 Aug 12;16. Available from: https://www.frontiersin.org/articles/10.3389/fnhum.2022.944908/full

34. Kassner A, Thornhill RE. Texture Analysis: A Review of Neurologic MR Imaging Applications. American Journal of Neuroradiology. 2010 May;31(5):809–16.

35. Zhang Y. MRI Texture Analysis in Multiple Sclerosis. International Journal of Biomedical Imaging. 2012;2012:1–7.

36. Luo T, Oladosu O, Rawji KS, Zhai P, Pridham G, Hossain S, et al. Characterizing Structural Changes With Evolving Remyelination Following Experimental Demyelination Using High Angular Resolution Diffusion MRI and Texture Analysis. Journal of Magnetic Resonance Imaging. 2019 Jun 19;49(6):1750–9.

37. Kovesi P. Image features from phase congruency. Videre: Journal of Computer Vision Research. 1999;1(3):1–26.

38. Baştanlar Y, Özuysal M. Introduction to Machine Learning. In: Yousef M, Allmer J, editors. miRNomics: MicroRNA Biology and Computational Analysis [Internet]. Totowa, NJ: Humana Press; 2014 [cited 2023 Jul 4]. p. 105–28. (Methods in Molecular Biology). Available from: https://doi.org/10.1007/978-1-62703-748-8_7

39. Pridham G, Hossain S, Rawji KS, Zhang Y. A metric learning method for estimating myelin content based on T2-weighted MRI from a de- and re-myelination model of multiple sclerosis. PLOS ONE. 2021 Apr 5;16(4):e0249460.

40. Hosseinpour Z, Jonkman L, Oladosu O, Pridham G, Pike GB, Inglese M, et al. Texture analysis in brain T2 and diffusion MRI differentiates histology-verified grey and white matter pathology types in multiple sclerosis. Journal of Neuroscience Methods. 2022 Sep;379:109671.

41. Howard J, Trevick S, Younger DS. Epidemiology of Multiple Sclerosis. Neurologic Clinics. 2016 Nov;34(4):919–39.

42. Thompson AJ, Banwell BL, Barkhof F, Carroll WM, Coetzee T, Comi G, et al. Diagnosis of multiple sclerosis: 2017 revisions of the McDonald criteria. The Lancet Neurology. 2018 Feb;17(2):162–73.

43. Gleichgerrcht E, Fridriksson J, Rorden C, Bonilha L. Connectome-based lesion-symptom mapping (CLSM): A novel approach to map neurological function. NeuroImage: Clinical. 2017;16(August):461–7.

44. Zhornitsky S, Wee Yong V, Koch MW, Mackie A, Potvin S, Patten SB, et al. Quetiapine Fumarate for the Treatment of Multiple Sclerosis: Focus on Myelin Repair. CNS Neuroscience & Therapeutics. 2013 Jul;19(10):n/a-n/a.

45. Rolak LA, Fleming JO. The differential diagnosis of Multiple Sclerosis. The Neurologist. 2007;13(2):57–72.

46. Egger C, Opfer R, Wang C, Kepp T, Sormani MP, Spies L, et al. MRI FLAIR lesion segmentation in multiple sclerosis: Does automated segmentation hold up with manual annotation? NeuroImage: Clinical. 2017;13:264–70.

47. Cheng EM, Crandall CJ, Bever CT, Giesser B, Haselkorn JK, Hays RD, et al. Quality indicators for multiple sclerosis. Multiple Sclerosis Journal. 2010 Aug 18;16(8):970–80.

48. Ruggieri S, Fanelli F, Castelli L, Petsas N, De Giglio L, Prosperini L. Lesion symptom map of cognitive–postural interference in multiple sclerosis. Multiple Sclerosis Journal. 2018 Apr;24(5):653–62.

49. Gajofatto A, Benedetti MD. Treatment strategies for multiple sclerosis: When to start, when to change, when to stop? World Journal of Clinical Cases. 2015;3(7):545.

50. Lavery AM, Verhey LH, Waldman AT. Outcome Measures in Relapsing-Remitting Multiple Sclerosis: Capturing Disability and Disease Progression in Clinical Trials. Multiple Sclerosis International. 2014;2014:1–13.

51. Casanova B, Coret F, Valero C, Landete L, Pascual A, Vilchez JJ, et al. High clinical inflammatory activity prior to the development of secondary progression: a prospective 5-year follow-up study. Multiple Sclerosis Journal. 2002 Feb 2;8(1):59–63.

52. Hauser SL, Oksenberg JR. The Neurobiology of Multiple Sclerosis: Genes, Inflammation, and Neurodegeneration. Neuron. 2006;52(1):61–76.

53. Rosti-Otajärvi E, Ruutiainen J, Huhtala H, Hämäläinen P. Cognitive performance profile in different phenotypes of MS with cognitive complaints. Multiple Sclerosis and Related Disorders. 2014 Jul;3(4):463–72.

54. Huijbregts SCJ, Kalkers NF, de Sonneville LMJ, de Groot V, Reuling IEW, Polman CH. Differences in cognitive impairment of relapsing remitting, secondary, and primary progressive MS. Neurology. 2004 Jul 27;63(2):335–9.

55. Petracca M, Margoni M, Bommarito G, Inglese M. Monitoring Progressive Multiple Sclerosis with Novel Imaging Techniques. Neurology and Therapy [Internet]. 2018 Jun 28; Available from: http://link.springer.com/10.1007/s40120-018-0103-2

56. Lassmann H. Relapsing–remitting and primary progressive MS have the same cause(s) – the neuropathologist's view: 1. Multiple Sclerosis Journal. 2013 Mar 20;19(3):266–7.

57. Iezzoni LI. Symptoms and Diagnosis of MS. In: Silver JK, editor. Multiple Sclerosis [Internet]. Santa Barbara, California: ABC-CLIO, LLC; 2010. p. 51–71. Available from: http://ebookcentral.proquest.com/lib/ucalgary-ebooks/detail.action?docID=491950

58. Dutta R, Trapp BD. Relapsing and progressive forms of multiple sclerosis. Current Opinion in Neurology. 2014 Jun;27(3):271–8.

59. Cree BAC, Hollenbach JA, Bove R, Kirkish G, Sacco S, Caverzasi E, et al. Silent progression in disease activity–free relapsing multiple sclerosis. Annals of Neurology. 2019;85(5):653–66.

60. Fisniku LK, Brex PA, Altmann DR, Miszkiel KA, Benton CE, Lanyon R, et al. Disability and T2 MRI lesions: A 20-year follow-up of patients with relapse onset of multiple sclerosis. Brain. 2008;131(3):808–17.

61. Iezzoni LI. Disability and Rehabilitation Therapies. In: Multiple Sclerosis. ProQuest Ebook Central; 2010. p. 15.

62. Uitdehaag BMJ. Disability Outcome Measures in Phase III Clinical Trials in Multiple Sclerosis. CNS Drugs. 2018 Jun 20;32(6):543–58.

63. Polman CH, Rudick RA. The Multiple Sclerosis Functional Composite: A clinically meaningful measure of disability. Neurology. 2010 Apr 27;74(17 Supplement 3):S8–15.

64. Nocentini U, Pasqualetti P, Bonavita S, Buccafusca M, De Caro MF, Farina D, et al. Cognitive dysfunction in patients with relapsing-remitting multiple sclerosis. Multiple Sclerosis Journal. 2006 Feb 2;12(1):77–87.

65. Siegert RJ. Depression in multiple sclerosis: a review. Journal of Neurology, Neurosurgery & Psychiatry. 2005 Apr 1;76(4):469–75.

66. Benedict RHB, Fischer JS, Archibald CJ, Arnett PA, Beatty WW, Bobholz J, et al. Minimal Neuropsychological Assessment of MS Patients: A Consensus Approach. The Clinical Neuropsychologist. 2002 Aug 1;16(3):381–97.

67. Langdon D, Amato M, Boringa J, Brochet B, Foley F, Fredrikson S, et al. Recommendations for a Brief International Cognitive Assessment for Multiple Sclerosis (BICAMS). Mult Scler. 2012 Jun;18(6):891–8.

68. Fisk JD, Pontefract A, Ritvo PG, Archibald CJ, Murray TJ. The Impact of Fatigue on Patients with Multiple Sclerosis. Canadian Journal of Neurological Sciences. 1994 Feb;21(1):9–14.

69. Yoo Y, Tang LYW, Brosch T, Li DKB, Kolind S, Vavasour I, et al. Deep learning of joint myelin and T1w MRI features in normal-appearing brain tissue to distinguish between multiple sclerosis patients and healthy controls. NeuroImage: Clinical. 2018;17(October 2017):169–78.

70. Trip SA, Miller DH. Imaging in multiple sclerosis. Journal of Neurology, Neurosurgery & Psychiatry. 2005;76(suppl_3):iii11–8.

71. Kaunzner UW, Gauthier SA. MRI in the assessment and monitoring of multiple sclerosis: an update on best practice. Therapeutic Advances in Neurological Disorders. 2017 Jun 12;10(6):247–61.

72. Basser PJ, Özarslan E. Introduction to Diffusion MR. In: Diffusion MRI. Elsevier; 2014. p. 3–9.

73. Henry RG, Oh J, Nelson SJ, Pelletier D. Directional diffusion in relapsing-remitting multiple sclerosis: A possible in vivo signature of Wallerian degeneration. Journal of Magnetic Resonance Imaging. 2003 Oct;18(4):420–6.

74. Bitar R, Leung G, Perng R, Tadros S, Moody AR, Sarrazin J, et al. MR Pulse Sequences: What Every Radiologist Wants to Know but Is Afraid to Ask. RadioGraphics. 2006;26(2):513–37.

75. Schmidt P, Gaser C, Arsic M, Buck D, Förschler A, Berthele A, et al. An automated tool for detection of FLAIR-hyperintense white-matter lesions in Multiple Sclerosis. NeuroImage. 2012 Feb;59(4):3774–83.

76. Tournier J. High angular resolution diffusion-weighted imaging (HARDI): beyond the diffusion tensor model. In: MICCAI 2010 Workshop on Computational Diffusion MRI. Beijing; 2010.

77. Panagiotaki E, Schneider T, Siow B, Hall MG, Lythgoe MF, Alexander DC. Compartment models of the diffusion MR signal in brain white matter: A taxonomy and comparison. NeuroImage. 2012 Feb;59(3):2241–54.

78. Assaf Y, Blumenfeld-Katzir T, Yovel Y, Basser PJ. Axcaliber: A method for measuring axon diameter distribution from diffusion MRI. Magnetic Resonance in Medicine. 2008 Jun;59(6):1347–54.

79. Absinta M, Sati P, Fechner A, Schindler MK, Nair G, Reich DS. Identification of chronic active multiple sclerosis lesions on 3T MRI. American Journal of Neuroradiology. 2018;39(7):1233–8.

80. Colby JB, Soderberg L, Lebel C, Dinov ID, Thompson PM, Sowell ER. Along-tract statistics allow for enhanced tractography analysis. NeuroImage. 2012 Feb;59(4):3227–42.

81. Wang JY, Bakhadirov K, Devous MD, Abdi H, McColl R, Moore C, et al. Diffusion Tensor Tractography of Traumatic Diffuse Axonal Injury. Archives of Neurology. 2008 May 1;65(5):619–26.

82. Kingsley PB. Introduction to diffusion tensor imaging mathematics: Part I. Tensors, rotations, and eigenvectors. Concepts in Magnetic Resonance Part A. 2006 Mar;28A(2):101–22.

83. Kingsley PB. Introduction to diffusion tensor imaging mathematics: Part III. Tensor calculation, noise, simulations, and optimization. Concepts in Magnetic Resonance Part A. 2006 Mar;28A(2):155–79.

84. Kingsley PB. Introduction to diffusion tensor imaging mathematics: Part II. Anisotropy, diffusion-weighting factors, and gradient encoding schemes. Concepts in Magnetic Resonance Part A. 2006 Mar;28A(2):123–54.

85. Jones DK, Leemans A. Diffusion Tensor Imaging. In: Magnetic Resonance Neuroimaging [Internet]. 2011. p. 127–44. Available from: http://link.springer.com/10.1007/978-1-61737-992-5_6

86. Tuch DS, Reese TG, Wiegell MR, Van J. Wedeen. Diffusion MRI of Complex Neural Architecture. Neuron. 2003 Dec;40(5):885–95.

87. Wu YC, Field AS, Chung MK, Badie B, Alexander AL. Quantitative analysis of diffusion tensor orientation: Theoretical framework. Magnetic Resonance in Medicine. 2004 Nov;52(5):1146–55.

88. Tuch DS. Q-ball imaging. Magnetic Resonance in Medicine. 2004 Dec;52(6):1358–72.

89. Pulizzi A, Rovaris M, Judica E, Sormani MP, Martinelli V, Comi G, et al. Determinants of disability in multiple sclerosis at various disease stages: A multiparametric magnetic resonance study. Archives of Neurology. 2007;64(8):1163–8.

90. Cortez-Conradis D, Favila R, Isaac-Olive K, Martinez-Lopez M, Rios C, Roldan-Valadez E. Diagnostic performance of regional DTI-derived tensor metrics in glioblastoma multiforme: simultaneous evaluation of p, q, L, Cl, Cp, Cs, RA, RD, AD, mean diffusivity and fractional anisotropy. European Radiology. 2013 Apr 21;23(4):1112–21.

91. Thomas B, Eyssen M, Peeters R, Molenaers G, Van Hecke P, De Cock P, et al. Quantitative diffusion tensor imaging in cerebral palsy due to periventricular white matter injury. Brain. 2005 Nov 1;128(11):2562–77.

92. D'Souza M, Trivedi R, Singh K, Grover H, Choudhury A, Kaur P, et al. Traumatic brain injury and the post-concussion syndrome: A diffusion tensor tractography study. Indian Journal of Radiology and Imaging. 2015;25(4):404.

93. Ontaneda D, Sakaie K, Lin J, Wang X, Lowe MJ, Phillips MD, et al. Identifying the Start of Multiple Sclerosis Injury: A Serial DTI Study. Journal of Neuroimaging. 2014;24(6):569–76.

94. Timmers I, Roebroeck A, Bastiani M, Jansma B, Rubio-Gozalbo E, Zhang H. Assessing Microstructural Substrates of White Matter Abnormalities: A Comparative Study Using DTI and NODDI. Yap PT, editor. PLOS ONE. 2016 Dec 21;11(12):e0167884.

95. Wheeler-Kingshott CAM, Cercignani M. About "axial" and "radial" diffusivities. Magnetic Resonance in Medicine. 2009 May;61(5):1255–60.

96. Schilling K, Gao Y, Janve V, Stepniewska I, Landman BA, Anderson AW. Can increased spatial resolution solve the crossing fiber problem for diffusion MRI? NMR in Biomedicine. 2017 Dec;30(12):e3787.

97. Hasan KM, Gupta RK, Santos RM, Wolinsky JS, Narayana PA. Diffusion tensor fractional anisotropy of the normal-appearing seven segments of the corpus callosum in healthy adults and relapsing-remitting multiple sclerosis patients. Journal of Magnetic Resonance Imaging. 2005 Jun;21(6):735–43.

98. Aganj I, Lenglet C, Sapiro G. ODF reconstruction in q-ball imaging with solid angle consideration. In: 2009 IEEE International Symposium on Biomedical Imaging: From Nano to Macro [Internet]. IEEE; 2009. p. 1398–401. Available from: http://ieeexplore.ieee.org/document/5193327/

99. Descoteaux M. High Angular Resolution Diffusion MRI: from Local Estimation to Segmentation and Tractography. University of Nice-Sophia Antipolis; 2008.

100. Descoteaux M, Angelino E, Fitzgibbons S, Deriche R. Regularized, fast, and robust analytical Q-ball imaging. Magnetic Resonance in Medicine. 2007;58(3):497–510.

101. Wu YC, Alexander AL. Hybrid diffusion imaging. NeuroImage. 2007 Jul;36(3):617–29.

102. Dell'Acqua F. Diffusion Imaging Models 1 : From DTI to HARDI models. OHBM 2017 Educational Course Presentation. 2017. p. 1–20.

103. Tournier J, Calamante F, Gadian DG, Connelly A. Direct estimation of the fiber orientation density function from diffusion-weighted MRI data using spherical deconvolution. NeuroImage. 2004 Nov;23(3):1176–85.

104. Onu M. From Gaussian to non-Gaussian diffusion models in tractography. In: European Society of Radiology. 2013. p. 1–10.

105. Takahashi E, Dai G, Wang R, Wedeen V. Diffusion Spectrum Imaging (DSI) Tractography of Neonatal Cat Brains. In: Proceedings 16th Scientific Meeting, International Society for Magnetic Resonance in Medicine [Internet]. 2008. p. 667. Available from: /MyPathway2008/0667

106. Marrale M, Collura G, Brai M, Toschi N, Midiri F, La Tona G, et al. Physics, Techniques and Review of Neuroradiological Applications of Diffusion Kurtosis Imaging (DKI). Clin Neuroradiol. 2016 Dec 1;26(4):391–403.

107. Granziera C, Benner T, Kumar A, Tuch D, Singhal A, Koroshetz W, et al. A comparison between Diffusion Tensor Imaging and Q-ball MRI in the study of post-stroke plasticity. Proceedings 16th Scientific Meeting, International Society for Magnetic Resonance in Medicine. 2008;Toronto:1862.

108. Tournier J, Calamante F, Connelly A. Improved probabilistic streamlines tractography by 2nd order integration over fibre orientation distributions. In: Proceedings of the International Society of Magnetic Resonance in Medicine. Stockholm: ISMRM; 2010. p. 1670.

109. Özarslan E, Koay CG, Shepherd TM, Komlosh ME, Irfanoğlu MO, Pierpaoli C, et al. Mean apparent propagator (MAP) MRI: A novel diffusion imaging method for mapping tissue microstructure. NeuroImage. 2013;78:16–32.

110. Fick RHJ, Wassermann D, Caruyer E, Deriche R. MAPL: Tissue microstructure estimation using Laplacian-regularized MAP-MRI and its application to HCP data. NeuroImage. 2016;134:365–85.

111. Descoteaux M. High Angular Resolution Diffusion Imaging (HARDI). In: Wiley Encyclopedia of Electrical and Electronics Engineering [Internet]. John Wiley & Sons, Ltd; 2015. p. 1–25. Available from: https://onlinelibrary.wiley.com/doi/abs/10.1002/047134608X.W8258

112. Ferizi U, Schneider T, Panagiotaki E, Nedjati-Gilani G, Zhang H, Wheeler-Kingshott CAM, et al. A ranking of diffusion MRI compartment models with in vivo human brain data. Magnetic Resonance in Medicine. 2014 Dec;72(6):1785–92.

113. Zhang H, Schneider T, Wheeler-Kingshott CA, Alexander DC. NODDI: Practical in vivo neurite orientation dispersion and density imaging of the human brain. NeuroImage. 2012;61(4):1000–16.

114. Alexander DC, Hubbard PL, Hall MG, Moore EA, Ptito M, Parker GJMM, et al. Orientationally invariant indices of axon diameter and density from diffusion MRI. NeuroImage. 2010 Oct;52(4):1374–89.

115. Girard G, Daducci A, Petit L, Thiran JP, Whittingstall K, Deriche R, et al. AxTract: Toward microstructure informed tractography. Human Brain Mapping. 2017 Nov;38(11):5485–500.

116. Huang SY, Nummenmaa A, Witzel T, Duval T, Cohen-Adad J, Wald LL, et al. The impact of gradient strength on in vivo diffusion MRI estimates of axon diameter. NeuroImage. 2015;106:464–72.

117. Fisher E, Chang A, Fox RJ, Tkach JA, Svarovsky T, Nakamura K, et al. Imaging correlates of axonal swelling in chronic multiple sclerosis brains. Annals of Neurology. 2007;62(3):219–28.

118. Schneider T, Brownlee W, Zhang H, Ciccarelli O, Miller DH, Wheeler-Kingshott CG. Sensitivity of multi-shell NODDI to multiple sclerosis white matter changes: a pilot study. Funct Neurol. 2017 Jul 5;32(2):97–101.

119. Grussu F, Schneider T, Zhang H, Alexander DC, Wheeler-Kingshott CAM. Single-shell diffusion MRI NODDI with in vivo cervical cord data. In: Proc Intl Soc Mag Reson Med. 2014. p. 1716.

120. Koppers S, Haarburger C, Merhof D. Diffusion MRI signal augmentation: From single shell to multi shell with deep learning. Mathematics and Visualization. 2017;61–70.

121. Daducci A, Canales-Rodríguez EJ, Zhang H, Dyrby TB, Alexander DC, Thiran JP. Accelerated Microstructure Imaging via Convex Optimization (AMICO) from diffusion MRI data. NeuroImage. 2015 Jan;105:32–44.

122. Auria A, Romascano D, Canales-Rodriguen E, Wiaux Y, Dirby TB, Alexander D, et al. Accelerated microstructure imaging via convex optimisation for regions with multiple fibres (AMICOx). In: 2015 IEEE International Conference on Image Processing (ICIP) [Internet]. IEEE; 2015. p. 1673–6. Available from: http://ieeexplore.ieee.org/document/7351085/

123. Pavuluri MN, Yang S, Kamineni K, Passarotti AM, Srinivasan G, Harral EM, et al. Diffusion Tensor Imaging Study of White Matter Fiber Tracts in Pediatric Bipolar Disorder and Attention-Deficit/Hyperactivity Disorder. Biological Psychiatry. 2009 Apr;65(7):586–93.

124. Schonberg T, Pianka P, Hendler T, Pasternak O, Assaf Y. Characterization of displaced white matter by brain tumors using combined DTI and fMRI. NeuroImage. 2006 May;30(4):1100–11.

125. Torgerson CM, Irimia A, Leow AD, Bartzokis G, Moody TD, Jennings RG, et al. DTI tractography and white matter fiber tract characteristics in euthymic bipolar I patients and healthy control subjects. Brain Imaging and Behavior. 2013 Jun 16;7(2):129–39.

126. Descoteaux M, Deriche R, Knosche TR, Anwander A. Deterministic and probabilistic tractography based on complex fibre orientation distributions. IEEE Transactions on Medical Imaging. 2009 Feb;28(2):269–86.

127. Raffelt DA, Tournier JD, Smith RE, Vaughan DN, Jackson G, Ridgway GR, et al. Investigating white matter fibre density and morphology using fixel-based analysis. NeuroImage. 2017;144:58–73.

128. Wakana S, Caprihan A, Panzenboeck MM, Fallon JH, Perry M, Gollub RL, et al. Reproducibility of quantitative tractography methods applied to cerebral white matter. NeuroImage. 2007;36(3):630–44.

129. Wasserthal J, Neher P, Maier-Hein KH. TractSeg - Fast and accurate white matter tract segmentation. NeuroImage. 2018;183(March):239–53.

130. Granziera C, Benner T, Tuch D, Singhal A, Koroshetz W, Krueger G, et al. Q-ball MR imaging of longitudinal brain rewiring during functional recovery after ischemic stroke. Proceedings 16th Scientific Meeting, International Society for Magnetic Resonance in Medicine. 2008;Toronto:1964.

131. Roberts TPL, Liu F, Kassner A, Mori S, Guha A. Fiber density index correlates with reduced fractional anisotropy in white matter of patients with glioblastoma. AJNR American journal of neuroradiology. 2005 Oct;26(9):2183–6.

132. Acosta-Cabronero J, Nestor PJ. Diffusion tensor imaging in Alzheimer's disease: insights into the limbic-diencephalic network and methodological considerations. Frontiers in Aging Neuroscience. 2014 Oct 2;6(SEP):1–21.

133. Tan WQ, Yeoh CS, Rumpel H, Nadkarni N, Lye WK, Tan EK, et al. Deterministic Tractography of the Nigrostriatal-Nigropallidal Pathway in Parkinson's Disease. Scientific Reports. 2015 Dec 1;5(1):17283.

134. Goodlett C, Corouge I, Jomier M, Gerig G. A quantitative DTI fiber tract analysis suite. In: ISC/NA-MIC/MICCAI Workshop on Open Source Software [Internet]. 2005. p. 1–5. Available from: http://hdl.handle.net/1926/39

135. Ukmar M, Montalbano A, Makuc E, Specogna I, Bratina A, Longo R, et al. Fiber density index in the evaluation of the spinal cord in patients with multiple sclerosis. La radiologia medica. 2012 Oct 28;117(7):1215–24.

136. Castellano G, Bonilha L, Li LM, Cendes F. Texture analysis of medical images. Clinical Radiology. 2004 Dec;59(12):1061–9.

137. Maerka A, Strzelecki M. Texture analysis methods -- a review. INSTITUTE OF ELECTRONICS, TECHNICAL UNIVERSITY OF LODZ. 1998;

138. Haralick RM. Statistical and structural approaches to texture. Proceedings of the IEEE. 1979 May;67(5):786–804.

139. Loizou CP, Pantzaris M, Pattichis CS. Normal appearing brain white matter changes in relapsing multiple sclerosis: Texture image and classification analysis in serial MRI scans. Magnetic Resonance Imaging. 2020;73(March):192–202.

140. Tang H, Wu EX, Ma QY, Gallagher D, Perera GM, Zhuang T. MRI brain image segmentation by multi-resolution edge detection and region selection. Computerized Medical Imaging and Graphics. 2000 Nov 1;24(6):349–57.

141. Gonzalez RC, Woods RE. Digital Image Processing [Internet]. Pearson; 2018. Available from: https://books.google.ca/books?id=0F05vgAACAAJ

142. Sharma S, Zhang Y. Fourier transform power spectrum is a potential measure of tissue alignment in standard MRI: A multiple sclerosis study. Zhang Y, editor. PLOS ONE. 2017 Apr 17;12(4):e0175979.

143. Sharma S, Laule C, Moore GRW, Li DKB, Zhang Y. Correlating new directional measures of myelin and axonal integrity in T2-weighted MRI with quantitative histology in multiple sclerosis. Journal of Neuroscience Methods. 2019 Jan;311(September 2018):369–76.

144. Zhu H, Goodyear BG, Lauzon ML, Brown RA, Mayer GS, Law AG, et al. A new local multiscale Fourier analysis for medical imaging. Medical Physics. 2003;30(6):1134–41.

145. Prabhu K. Application of Windows in Spectral Analysis. In: Window Functions and Their Applications in Signal Processing [Internet]. 1st edition. Taylor & Francis; 2014 [cited 2023 Sep 5]. Available from: https://learning.oreilly.com/library/view/window-functions-and/9781466515840/17-9781315216386_chapter-chap8.xhtml

146. Pridham G, Steenwijk MD, Geurts JJG, Zhang Y. A discrete polar Stockwell transform for enhanced characterization of tissue structure using MRI. Magnetic Resonance in Medicine. 2018;80(6):2731–43.

147. Beuter C, Oleskovicz M. S-transform: from main concepts to some power quality applications. IET Signal Processing. 2020;14(3):115–23.

148. Dang M, Lysack JT, Wu T, Matthews TW, Chandarana SP, Brockton NT, et al. MRI Texture Analysis Predicts p53 Status in Head and Neck Squamous Cell Carcinoma. American Journal of Neuroradiology. 2015 Jan 1;36(1):166–70.

149. Pridham G, Oladosu O, Zhang Y. Evaluation of discrete orthogonal versus polar Stockwell Transform for local multi-resolution texture analysis using brain MRI of multiple sclerosis patients. Magnetic Resonance Imaging. 2020 Oct;72:150–8.

150. Xiong H, He X, Guo D. Value of MRI texture analysis for predicting high-grade prostate cancer. Clinical Imaging. 2021 Apr;72:168–74.

151. Rijal OM, Ebrahimian H, Noor NM, Hussin A, Yunus A, Mahayiddin AA. Application of Phase Congruency for Discriminating Some Lung Diseases Using Chest Radiograph. Computational and Mathematical Methods in Medicine. 2015;2015:1–15.

152. Morrone MC, Owens RA. Feature detection from local energy. Pattern Recognition Letters. 1987 Dec;6(5):303–13.

153. Kovesi P. Edges Are Not Just Steps. In: The 5th Asian Conference on Computer Vision. Melbourne: ACCV; 2002.

154. Kovesi P. Phase congruency detects corners and edges. In: Digital Image Computing: Techniques and Applications DICTA 2003 [Internet]. Sydney; 2003. p. 309–18. Available from: http://books.google.com/books?hl=en&lr=&id=oz-Sinxlj08C&oi=fnd&pg=PT381&dq=Phase+Congruency+Detects+Corners+and+Edges&ots=yXzzHCqVpV&sig=r_J7k8qHa2GRQFpQGZRLAucOJvk

155. Kovesi P. Phase congruency: A low-level image invariant. Psychological Research Psychologische Forschung. 2000 Dec 1;64(2):136–48.

156. Kovesi P. Invariant Measures of Image Features from Phase Information [Internet]. University of Western Australia; 1996. Available from: https://research-repository.uwa.edu.au/en/publications/invariant-measures-of-image-features-from-phase-information

157. Field DJ. Relations between the statistics of natural images and the response properties of cortical cells. J Opt Soc Am A, JOSAA. 1987 Dec 1;4(12):2379–94.

158. Ferrari RJ, Allaire S, Hope A, Kim J, Jaffray D, Pekar V. Detection of point landmarks in 3D medical images via phase congruency model. J Braz Comput Soc. 2011 Jun;17(2):117–32.

159. Alavi SMM, Zhang Y. Phase Congruency Parameter Optimization for Enhanced Detection of Image Features for both Natural and Medical Applications. 2017 May 5;1–10.

160. Oladosu OA, Zhang Y. Statistical analysis of phase congruency detects normal appearing white matter changes associated with disease severity between relapsing remitting and secondary progressive multiple sclerosis. In: ISMRM 27th annual meeting & Exhibition. Montreal; 2019. p. 1–3.

161. Baxandall S, Sharma S, Zhai P, Pridham G, Zhang Y. Quantitative phase and texture angularity analysis of brain white matter lesions in multiple sclerosis. In: Medical Imaging 2018: Image Processing [Internet]. SPIE; 2018 [cited 2023 Jun 2]. p. 350–6. Available from: https://www.spiedigitallibrary.org/conference-proceedings-of-spie/10574/105741E/Quantitative-phase-and-texture-angularity-analysis-of-brain-white-matter/10.1117/12.2293595.full

162. James G, Witten D, Hastie T, Tibshirani R. An Introduction to Statistical Learning [Internet]. New York, NY: Springer; 2013 [cited 2023 Jul 6]. (Springer Texts in Statistics; vol. 103). Available from: http://link.springer.com/10.1007/978-1-4614-7138-7

163. Chen Q, Meng Z, Liu X, Jin Q, Su R. Decision variants for the automatic determination of optimal feature subset in RF-RFE. Genes. 2018;9(6).

164. Bendfeldt K, Taschler B, Gaetano L, Madoerin P, Kuster P, Mueller-Lenke N, et al. MRI-based prediction of conversion from clinically isolated syndrome to clinically definite multiple sclerosis using SVM and lesion geometry. Brain Imaging and Behavior. 2019;13(5):1361–74.

165. Guyon I, Weston J, Barnhill S. Gene Selection for Cancer Classification using Support Vector Machines. Machine Learning. 2002;46:389–422.

166. Zhou ZH. Machine Learning [Internet]. Singapore: Springer; 2021 [cited 2023 Sep 7]. Available from: https://link.springer.com/10.1007/978-981-15-1967-3

167. Zhang Y, Hong D, McClement D, Oladosu O, Pridham G, Slaney G. Grad-CAM helps interpret the deep learning models trained to classify multiple sclerosis types using clinical brain magnetic resonance imaging. Journal of Neuroscience Methods. 2021 Apr;353:109098.

168. Yoo Y, Tang LYW, Li DKB, Metz L, Kolind S, Traboulsee AL, et al. Deep learning of brain lesion patterns and user-defined clinical and MRI features for predicting conversion to multiple sclerosis from clinically isolated syndrome. Computer Methods in Biomechanics and Biomedical Engineering: Imaging and Visualization. 2019;7(3):250–9.

169. Murray C, Oladosu O, Joshi M, Kolind S, Oh J, Zhang Y. Neural network algorithms predict new diffusion MRI data for multi-compartmental analysis of brain microstructure in a clinical setting. Magnetic Resonance Imaging [Internet]. 2023 Apr; Available from: https://linkinghub.elsevier.com/retrieve/pii/S0730725X23000693

170. Mori S, Crain BJ, Chacko VP, van Zijl PC. Three-dimensional tracking of axonal projections in the brain by magnetic resonance imaging. Annals of neurology. 1999;45(2):265–9.

171. Raffelt D, Tournier JD, Rose S, Ridgway GR, Henderson R, Crozier S, et al. Apparent Fibre Density: A novel measure for the analysis of diffusion-weighted magnetic resonance images. NeuroImage. 2012;59(4):3976–94.

172. Garyfallidis E, Brett M, Amirbekian B, Rokem A, van der Walt S, Descoteaux M, et al. Dipy, a library for the analysis of diffusion MRI data. Frontiers in Neuroinformatics. 2014;8(FEB):1–17.

173. Cetin Karayumak S, Bouix S, Ning L, James A, Crow T, Shenton M, et al. Retrospective harmonization of multi-site diffusion MRI data acquired with different acquisition parameters. NeuroImage. 2019;184(August 2018):180–200.

174. Mirzaalian H, Ning L, Savadjiev P, Pasternak O, Bouix S, Michailovich O, et al. Multi-site harmonization of diffusion MRI data in a registration framework. Brain Imaging and Behavior. 2018;12(1):284–95.

175. Steven AJ, Zhuo J, Melhem ER. Diffusion Kurtosis Imaging: An Emerging Technique for Evaluating the Microstructural Environment of the Brain. American Journal of Roentgenology. 2014 Jan;202(1):W26–33.

176. Stejskal EO, Tanner JE. Spin diffusion measurements: Spin echoes in the presence of a time-dependent field gradient. The Journal of Chemical Physics. 1965;42(1):288–92.

177. Van Essen DC, Ugurbil K, Auerbach E, Barch D, Behrens TEJJ, Bucholz R, et al. The Human Connectome Project: A data acquisition perspective. NeuroImage. 2012;62(4):2222–31.

178. Kovesi PD. MATLAB and Octave Functions for Computer Vision and Image Processing [Internet]. Available from: https://www.peterkovesi.com/matlabfns/

179. Muldal, Alistair. Phasepack: a toolkit for phase-based image feature detection.

180. Papadakis NG, Murrills CD, Hall LD, Huang CLH, Adrian Carpenter T. Minimal gradient encoding for robust estimation of diffusion anisotropy☆. Magnetic Resonance Imaging. 2000 Jul;18(6):671–9.

181. Inglese M, Bester M. Diffusion imaging in multiple sclerosis: research and clinical implications. NMR in Biomedicine. 2010 Sep 29;23(7):865–72.

182. Schmierer K, Wheeler-Kingshott CAMM, Boulby PA, Scaravilli F, Altmann DR, Barker GJ, et al. Diffusion tensor imaging of post mortem multiple sclerosis brain. NeuroImage. 2007;35(2):467–77.

183. Klistorner A, Wang C, Yiannikas C, Parratt J, Dwyer M, Barton J, et al. Evidence of progressive tissue loss in the core of chronic MS lesions: A longitudinal DTI study. NeuroImage: Clinical. 2018;17(December 2017):1028–35.

184. Descoteaux M. High Angular Resolution Diffusion Imaging (HARDI). In: Wiley Encyclopedia of Electrical and Electronics Engineering. Hoboken, NJ, USA: John Wiley & Sons, Inc.; 2015. p. 1–25.

185. Taquet M, Scherrer B, Boumal N, Macq B, Warfield SK. Estimation of a multi-fascicle model from single B-value data with a population-informed prior. Medical image computing and computer-assisted intervention : MICCAI. International Conference on Medical Image Computing and Computer-Assisted Intervention. 2013;16(Pt 1):695–702.

186. Magnollay L, Grussu F, Wheeler-Kingshott CAMMM, Sethi V, Zhang H, Chard DT, et al. An investigation of brain neurite density and dispersion in multiple sclerosis using single shell diffusion imaging. In: International Society of Magnetic Resonance in Medicine. ISMRM; 2014. p. 2048.

187. Tournier J. Diffusion MRI in the brain – Theory and concepts. Progress in Nuclear Magnetic Resonance Spectroscopy. 2019;112–113:1–16.

188. Jenkinson M, Beckmann CF, Behrens TEJJ, Woolrich MW, Smith SM. FSL. NeuroImage. 2012 Aug;62(2):782–90.

189. Jenkinson M, Smith S. A global optimisation method for robust affine registration of brain images. Medical Image Analysis. 2001 Jun;5(2):143–56.

190. Jenkinson M, Bannister P, Brady M, Smith S. Improved optimization for the robust and accurate linear registration and motion correction of brain images. NeuroImage. 2002;17(2):825–41.

191. Battaglini M, Jenkinson M, De Stefano N. Evaluating and reducing the impact of white matter lesions on brain volume measurements. Human Brain Mapping. 2012;33(9):2062–71.

192. Avants BB, Epstein CL, Grossman M, Gee JC. Symmetric diffeomorphic image registration with cross-correlation: Evaluating automated labeling of elderly and neurodegenerative brain. Medical Image Analysis. 2008;12(1):26–41.

193. Andersson JLR, Sotiropoulos SN. An integrated approach to correction for off-resonance effects and subject movement in diffusion MR imaging. NeuroImage. 2016 Jan;125:1063–78.

194. Van Essen DC, Ugurbil K, Auerbach E, Barch D, Behrens TEJJ, Bucholz R, et al. The Human Connectome Project: A data acquisition perspective. NeuroImage. 2012;62(4):2222–31.

195. Wang R, Wedeen VJ. Diffusion Toolkit : A Software Package for Diffusion Imaging Data Processing and Tractography. Proc Intl Soc Mag Reson Med. 2007;15:3720.

196. Agresti A. Categorical data analysis. Alan Agresti. Statistics in Medicine. New York, NY: Wiley; 1990. 350–354 p.

197. DeLong ER, DeLong DM, Clarke-Pearson DL. Comparing the Areas under Two or More Correlated Receiver Operating Characteristic Curves: A Nonparametric Approach. Biometrics. 1988 Sep;44(3):837.

198. Cercignani M, Bouyagoub S. Brain microstructure by multi-modal MRI: Is the whole greater than the sum of its parts? NeuroImage. 2018 Nov;182(November 2017):117–27.

199. Spano B, Giulietti G, Pisani V, Morreale M, Tuzzi E, Nocentini U, et al. Disruption of neurite morphology parallels MS progression. Neurology: Neuroimmunology and NeuroInflammation. 2018;5(6).

200. Giorgio A, Stromillo ML, Bartolozzi ML, Rossi F, Battaglini M, De Leucio A, et al. Relevance of hypointense brain MRI lesions for long-term worsening of clinical disability in relapsing multiple sclerosis. Multiple Sclerosis. 2014;20(2):214–9.

201. Kuhlmann T, Moccia M, Coetzee T, Cohen JA, Correale J, Graves J, et al. Multiple sclerosis progression: time for a new mechanism-driven framework. The Lancet Neurology. 2023 Jan 1;22(1):78–88.

202. Ouellette R, Mangeat G, Polyak I, Warntjes M, Forslin Y, Bergendal Å, et al. Validation of Rapid Magnetic Resonance Myelin Imaging in Multiple Sclerosis. Annals of Neurology. 2020;87(5):710–24.

203. Yu FF, Chiang FL, Stephens N, Huang SY, Bilgic B, Tantiwongkosi B, et al. Characterization of normal-appearing white matter in multiple sclerosis using quantitative susceptibility mapping in conjunction with diffusion tensor imaging. Neuroradiology. 2019;61(1):71–9.

204. Li CMF, Hung PSP, Chu PPW, Tohyama S, Hodaie M. Trigeminal neuralgia associated with multiple sclerosis: A multimodal assessment of brainstem plaques and response to Gamma Knife radiosurgery. Multiple Sclerosis Journal. 2020;26(14):1877–88.

205. Granziera C, Wuerfel J, Barkhof F, Calabrese M, De Stefano N, Enzinger C, et al. Quantitative magnetic resonance imaging towards clinical application in multiple sclerosis. Brain. 2021;144(5):1296–311.

206. Rahmanzadeh R, Lu PJ, Barakovic M, Weigel M, Maggi P, Nguyen TD, et al. Myelin and axon pathology in multiple sclerosis assessed by myelin water and multi-shell diffusion imaging. Brain : a journal of neurology. 2021;144(6):1684–96.

207. Bates E, Wilson SM, Saygin AP, Dick F, Sereno MI, Knight RT, et al. Voxel-based lesion–symptom mapping. Nature Neuroscience. 2003 May 21;6(5):448–50.

208. Ngamsombat C, Tian Q, Fan Q, Russo A, Machado N, Polackal M, et al. Axonal damage in the optic radiation assessed by white matter tract integrity metrics is associated with retinal thinning in multiple sclerosis. NeuroImage: Clinical. 2020;27(May):102293.

209. Reich DS, Zackowski KM, Gordon-Lipkin EM, Smith SA, Chodkowski BA, Cutter GR, et al. Corticospinal Tract Abnormalities Are Associated with Weakness in Multiple Sclerosis. American Journal of Neuroradiology. 2008 Feb 1;29(2):333–9.

210. Sechi E, Keegan BM, Kaufmann TJ, Kantarci OH, Weinshenker BG, Flanagan EP. Unilateral motor progression in MS. Neurology. 2019 Aug 13;93(7):e628–34.

211. Tovar-Moll F, Evangelou IE, Chiu AW, Auh S, Chen C, Ehrmantraut M, et al. Diffuse and Focal Corticospinal Tract Disease and Its Impact on Patient Disability in Multiple Sclerosis. J Neuroimaging. 2015 Mar;25(2):200–6.

212. Klistorner A, Vootakuru N, Wang C, Yiannikas C, Graham SL, Parratt J, et al. Decoding diffusivity in multiple sclerosis: Analysis of optic radiation lesional and non-lesional white matter. PLoS ONE. 2015;10(3):1–23.

213. Harrison DM, Caffo BS, Shiee N, Farrell JAD, Bazin PL, Farrell SK, et al. Longitudinal changes in diffusion tensor-based quantitative MRI in multiple sclerosis. Neurology. 2011 Jan 11;76(2):179–86.

214. Bagnato F, Gauthier SA, Laule C, Moore GRW, Bove R, Cai Z, et al. Imaging Mechanisms of Disease Progression in Multiple Sclerosis: Beyond Brain Atrophy. Journal of Neuroimaging. 2020;30(3):251–66.

215. Chawla S, Kister I, Sinnecker T, Wuerfel J, Brisset JC, Paul F, et al. Longitudinal study of multiple sclerosis lesions using ultra-high field (7T) multiparametric MR imaging. PLoS ONE. 2018;13(9):1–16.

216. Filippi M, Preziosa P, Banwell BL, Barkhof F, Ciccarelli O, De Stefano N, et al. Assessment of lesions on magnetic resonance imaging in multiple sclerosis: practical guidelines. Brain. 2019;142(7):1858–75.

217. Polman CH, Reingold SC, Banwell B, Clanet M, Cohen JA, Filippi M, et al. Diagnostic criteria for multiple sclerosis: 2010 Revisions to the McDonald criteria. Annals of Neurology. 2011 Feb;69(2):292–302.

218. Lublin FD, Reingold SC, Cohen JA, Cutter GR, Sorensen PS, Thompson AJ, et al. Defining the clinical course of multiple sclerosis: The 2013 revisions. Neurology. 2014 Jul 15;83(3):278–86.

219. Lublin FD, Reingold SC. Defining the clinical course of multiple sclerosis: Results of an international survey. Neurology. 1996 Apr 1;46(4):907–11.

220. Cordero-Grande L, Christiaens D, Hutter J, Price AN, Hajnal JV. Complex diffusion-weighted image estimation via matrix recovery under general noise models. NeuroImage. 2019;200(June):391–404.

221. Tournier JD, Smith R, Raffelt D, Tabbara R, Dhollander T, Pietsch M, et al. MRtrix3: A fast, flexible and open software framework for medical image processing and visualisation. NeuroImage. 2019;202(August):116137.

222. Veraart J, Novikov DS, Christiaens D, Ades-aron B, Sijbers J, Fieremans E. Denoising of diffusion MRI using random matrix theory. NeuroImage. 2016 Nov;142:394–406.

223. Veraart J, Fieremans E, Novikov DS. Diffusion MRI noise mapping using random matrix theory. Magnetic Resonance in Medicine. 2016 Nov;76(5):1582–93.

224. Andersson JLR, Graham MS, Zsoldos E, Sotiropoulos SN. Incorporating outlier detection and replacement into a non-parametric framework for movement and distortion correction of diffusion MR images. NeuroImage. 2016 Nov;141:556–72.

225. Huang H, Ceritoglu C, Li X, Qiu A, Miller MI, van Zijl PCM, et al. Correction of B0 susceptibility induced distortion in diffusion-weighted images using large-deformation diffeomorphic metric mapping. Magnetic Resonance Imaging. 2008 Nov;26(9):1294–302.

226. Andersson JLR, Skare S, Ashburner J. How to correct susceptibility distortions in spin-echo echo-planar images: application to diffusion tensor imaging. NeuroImage. 2003 Oct;20(2):870–88.

227. Billah T, Cetin Karayumak S, Bouix S, Rathi Y. Multi-site Diffusion MRI Harmonization [Internet]. https://github.com/pnlbwh/dMRIharmoniziation. 2019. Available from: https://github.com/pnlbwh/dMRIharmonization

228. Murray C, Oladosu O, Zhang Y. Prediction of new diffusion MRI data is feasible using robust machine learning algorithms for multi-shell HARDI in a clinical setting. In: International Society of Magnetic Resonance in Medicine 31st annual meeting. London; 2022.

229. Wasserthal J, Neher PF, Hirjak D, Maier-Hein KH. Combined tract segmentation and orientation mapping for bundle-specific tractography. Medical Image Analysis. 2019;58:101559.

230. WITELSON SF. Hand and sex differences in the isthmus and genu of the human corpus callosum: a postmortem morphological study. Brain. 1989 Jun 1;112(3):799–835.

231. Kellner E, Dhital B, Kiselev VG, Reisert M. Gibbs-ringing artifact removal based on local subvoxel-shifts. Magnetic Resonance in Medicine. 2016 Nov;76(5):1574–81.

232. Tustison NJ, Avants BB, Cook PA, Gee JC. N4ITK: Improved N3 bias correction with robust B-spline approximation. In: 2010 IEEE International Symposium on Biomedical Imaging: From Nano to Macro [Internet]. IEEE; 2010. p. 708–11. Available from: http://ieeexplore.ieee.org/lpdocs/epic03/wrapper.htm?arnumber=5490078

233. Zuiderveld K. Contrast Limited Adaptive Histogram Equalization. In: Graphics Gems. Elsevier; 1994. p. 474–85.

234. Zhang Y, Brady M, Smith S. Segmentation of brain MR images through a hidden Markov random field model and the expectation-maximization algorithm. IEEE Transactions on Medical Imaging. 2001;20(1):45–57.

235. Hua K, Zhang J, Wakana S, Jiang H, Li X, Reich DS, et al. Tract probability maps in stereotaxic spaces: Analyses of white matter anatomy and tract-specific quantification. NeuroImage. 2008;39(1):336–47.

236. Mori S, Wakana S, van Zijl PCM, Nagae-Poetscher LM. MRI Atlas of Human White Matter. Amsterdam: Elsevier; 2004.

237. Maddah M, Grimson WEL, Warfield SK, Wells WM. A unified framework for clustering and quantitative analysis of white matter fiber tracts. Medical Image Analysis. 2008 Apr;12(2):191–202.

238. Wasserthal J, Maier-Hein KH, Neher PF, Northoff G, Kubera KM, Fritze S, et al. Multiparametric mapping of white matter microstructure in catatonia. Neuropsychopharmacology. 2020;45(10):1750–7.

239. St-Jean S, Chamberland M, Viergever MA, Leemans A. Reducing variability in along-tract analysis with diffusion profile realignment. NeuroImage. 2019;199(February):663–79.

240. Huang SY, Fan Q, Machado N, Eloyan A, Bireley JD, Russo AW, et al. Corpus callosum axon diameter relates to cognitive impairment in multiple sclerosis. Annals of Clinical and Translational Neurology. 2019;6(5):882–92.

241. Llufriu S, Blanco Y, Martinez-Heras E, Casanova-Molla J, Gabilondo I, Sepulveda M, et al. Influence of Corpus callosum damage on cognition and physical disability in multiple sclerosis: A multimodal study. PLoS ONE. 2012;7(5).

242. Reich DS, Smith SA, Gordon-Lipkin EM, Ozturk A, Caffo BS, Balcer LJ, et al. Damage to the Optic Radiation in Multiple Sclerosis Is Associated With Retinal Injury and Visual Disability. Archives of Neurology. 2009 Aug 1;66(8):998–1006.

243. Martínez-Heras E, Solana E, Prados F, Andorrà M, Solanes A, López-Soley E, et al. Characterization of multiple sclerosis lesions with distinct clinical correlates through quantitative diffusion MRI. NeuroImage: Clinical. 2020;28(September):102411.

244. Klistorner S, Barnett MH, Wasserthal J, Yiannikas C, Barton J, Parratt J, et al. Differentiating axonal loss and demyelination in chronic MS lesions: A novel approach using single streamline diffusivity analysis. PLoS ONE. 2021;16(1 January):1–17.

245. Caseby SCL, Woodhouse FA, Montgomery SM, Kroes MA, Duddy ME. Transition to secondary progressive multiple sclerosis: The consequences for patients and healthcare systems, a healthcare professional survey. Health Sci Rep. 2022 Jan 23;5(1):e474.

246. Ge Y. Multiple Sclerosis: The Role of MR Imaging. AJNR American journal of neuroradiology. 2006 Jun 1;27(6):1165–76.

247. Alexander AL, Lee JE, Lazar M, Field AS. Diffusion tensor imaging of the brain. Neurotherapeutics. 2007 Jul;4(3):316–29.

248. Blecher T, Miron S, Schneider GG, Achiron A, Ben-Shachar M. Association between white matter microstructure and verbal fluency in patients with multiple sclerosis. Frontiers in Psychology. 2019;10(JULY).

249. Gajamange S, Raffelt D, Dhollander T, Lui E, van der Walt A, Kilpatrick T, et al. Fibre-specific white matter changes in multiple sclerosis patients with optic neuritis. NeuroImage: Clinical. 2018 Jan 1;17:60–8.

250. Preziosa P, Pagani E, Meani A, Marchesi O, Conti L, Falini A, et al. NODDI, diffusion tensor microstructural abnormalities and atrophy of brain white matter and gray matter contribute to cognitive impairment in multiple sclerosis. J Neurol. 2023 Feb 1;270(2):810–23.

251. Bharati MH, Liu JJ, MacGregor JF. Image texture analysis: Methods and comparisons. Chemometrics and Intelligent Laboratory Systems. 2004;72(1):57–71.

252. Ontaneda D, Cohen JA, Amato MP. Clinical outcome measures for progressive MS trials. Multiple Sclerosis. 2017;23(12):1627–35.

253. Brown LN, Metz LM. Tactile temporal thresholds detect relapse-related changes in multiple sclerosis: a preliminary study. Mult Scler. 2005 Dec 1;11(6):725–7.

254. Brown LN, Metz LM, Sainsbury RS. Sensory Temporal Thresholds and Interhemispheric Transfer Times in Multiple Sclerosis: A Preliminary Study of a New Outcome Measure. Journal of Clinical and Experimental Neuropsychology. 2003 Sep 1;25(6):783–92.

255. Lawson I. Purdue Pegboard Test. Occupational Medicine. 2019 Aug 22;69(5):376–7.

256. Wan ATK. On generalized ridge regression estimators under collinearity and balanced loss. Applied Mathematics and Computation. 2002 Jul 10;129(2):455–67.

257. Ozturk A, Smith S, Gordon-Lipkin E, Harrison D, Shiee N, Pham D, et al. MRI of the corpus callosum in multiple sclerosis: association with disability. Mult Scler. 2010 Feb 1;16(2):166–77.

258. Beaudoin AM, Rheault F, Theaud G, Laberge F, Whittingstall K, Lamontagne A, et al. Modern Technology in Multi-Shell Diffusion MRI Reveals Diffuse White Matter Changes in Young Adults With Relapsing-Remitting Multiple Sclerosis. Frontiers in Neuroscience [Internet]. 2021 [cited 2023 May 29];15. Available from: https://www.frontiersin.org/articles/10.3389/fnins.2021.665017

259. Pellegrino L, Coscia M, Muller M, Solaro C, Casadio M. Evaluating upper limb impairments in multiple sclerosis by exposure to different mechanical environments. Sci Rep. 2018 Feb 1;8(1):2110.

260. Obara B, Fricker M, Gavaghan D, Grau V. Contrast-Independent Curvilinear Structure Detection in Biomedical Images. IEEE Transactions on Image Processing. 2012 May;21(5):2572–81.

261. Wang N, Zhang J, Cofer G, Qi Y, Anderson RJ, White LE, et al. Neurite orientation dispersion and density imaging of mouse brain microstructure. Brain Struct Funct. 2019 Jun 1;224(5):1797–813.

262. Klistorner A, Wang C, Yiannikas C, Parratt J, Barton J, You Y, et al. Diffusivity in the core of chronic multiple sclerosis lesions. Chen X, editor. PLOS ONE. 2018 Apr 25;13(4):e0194142.

263. Evangelou N, Esiri MM, Smith S, Palace J, Matthews PM. Quantitative pathological evidence for axonal loss in normal appearing white matter in multiple sclerosis. Annals of Neurology. 2000;47(3):391–5.